FREQUENCY-DOMAIN OPTICAL SPECTROSCOPY AND IMAGING OF TISSUE AND TISSUE-SIMULATING MEDIA

By

Brian William Pogue, B.Sc., M.Sc.

A Thesis

Submitted to the School of Graduate Studies

in Partial Fulfilment of the Requirements

for the Degree

Doctor of Philosophy

McMaster University

1996

DOCTOR OF PHILOSOPHY (1996, PHYSICS)

MCMASTER UNIVERSITY
Hamilton, Ontario, Canada

TITLE: Frequency-Domain Optical Spectroscopy and Imaging of Tissue and Tissue-Simulating Media

AUTHOR: Brian William Pogue, B.Sc. Hons. (York University, Canada)
M.Sc. (York University, Canada)

SUPERVISOR: Dr. Michael S. Patterson

NUMBER OF PAGES: 266

ABSTRACT

The goal of this work was to develop and study the use of a diagnostic *in vivo* tissue spectroscopy system based upon frequency-domain light measurements. Intensity-modulated light which is incident upon a scattering sample creates waves of light intensity which propagate through the medium in a manner which is dependent upon the scattering and absorption characteristics of the tissue. Detection of these waves at a point on the surface of the sample can be used to non-invasively estimate the scattering and absorption coefficients. Recovering these optical interaction parameters requires the use of a suitable model of light propagation in tissue, for which diffusion theory has been shown to work. The technical development of this system and the theoretical modelling are examined in this study. Some physiologically important chromophores can be detected within tissue using the spectral discrimination provided by a wavelength tunable source or detector. The quantification of chromophores can be used in dosimetry for therapeutic laser treatments or for diagnostic laser applications such as measuring hemoglobin oxygen saturation.

In addition to reflectance measurements, diffuse fluorescence can be detected from a scattering medium such as tissue if there is an active fluorescent molecule present. The theoretical modeling for diffuse fluorescence signals was developed and experimentally tested in a tissue-simulating phantom. There was excellent agreement between the theoretical model and the experimental tests with a fluorophore in a scattering emulsion. This work suggests that measurements of fluorescence lifetime or quantum yield can be made on a homogeneous tissue volume by deconvolution of the effects of multiple

scattering.

Preliminary work was done on an optical tomography algorithm using measurements of phase and intensity at multiple points on a tissue surface to reconstruct images of the optical properties of the interior. Tomographic imaging is routinely done with x-rays for diagnostic imaging and recent developments suggest that a similar form of imaging can be accomplished with light, albeit with much poorer resolution and contrast. Frequency-domain measurements can provide a method for diffuse optical imaging through relatively thin tissue volumes (i.e. thickness less than approximately 10 cm). The theoretical development of a tomographic imaging system is examined in the final section of this thesis and tested with data from a tissue simulating phantom. The potential medical applications of such a system range from tissue oxygenation imaging to detection of cancerous regions within soft tissue.

Acknowledgements

I would like to express my thanks to Dr. Michael Patterson, without who this thesis would not have been possible. All aspects of this thesis were stimulated by his insight and knowledge, and I cannot express my gratitude enough for the experience I have gained. I would also like to thank Dr. Brian Wilson for providing his guidance and research facilities to work in, and for the gentle 'push out of the nest' at the end of my thesis. I would like to thank Dr. Chettle for kindly accepting me into the Medical Physics program at McMaster under somewhat harried circumstances.

I would like to thank David Moulton, Dr. John Adams, Dr. Tom Chow and Dr. Tom Farrell for the use of their software and subroutines. I would also like to thank the many members of the biomedical optics group at Hamilton, who have helped and hindered in the development of this thesis, and for companionship over the last few years, namely: Steen Madsen, Lothar Lilge, Tom Farrell, Satish Jaywant, Alwin Kienle, Alex Vitkin, Bill Whalen, Malini Oliveo, Patricia Singh, Joe Hayward, Ron Lalonde, Tom Chow, Joshua Fishkin, Joshua Woosley, Huabei Jiang.

I would like to thank my parents for their interest, patience and help through the last few years. Finally I must thank my wife, Jane, for ecouragement and companionship over the years. We have had just the right balance of grounding and chaos which makes it all worth it!

Table of Contents

Chapter 3 : Papers on tissue spectroscopy

Chapter 4: Papers on tissue imaging

Chapter 1

Introduction

1.1 Applications of light in medicine

The use of light in medicine has been rapidly increasing since the development of laser technology. The applications of light can be divided into two major categories: therapeutic and diagnostic. The therapeutic applications utilize photon absorption to deposit energy in the tissue. The energy deposition is a function of how light of that wavelength propagates within tissue, as well as the incident intensity. By changing the wavelength and intensity, the laser can be used for effects such as heating, mechanical shock, ablation or photochemical reactions. For the first three of these effects, the photon absorption is usually due to endogenous chromophores such as water, melanin or hemoglobin which can be strong absorbers and are present in relatively high concentrations in tissue. The absorption spectra of these three molecules are shown in figure 1.1 (Patterson *et al* 1991(d), Boulnois 1985). The optical energy density absorbed by a particular chromophore depends upon the concentration within the tissue, the extinction coefficient at the excitation wavelength, and the local light fluence rate. The summation of the energy absorbed by all the tissue components yields the total energy absorption in the tissue for the given light intensity.

The therapeutic applications of light range from photocoagulation with low

intensities (~1-2 Watts/cm^2) to ablation of tissue with much higher intensities (~10^6 to 10^9 Watts/cm^2). The main goal of photocoagulation is to cause a local heating of the tissue above 60°C over the course of a few minutes, until coagulation of the proteins causes cell death. Photoablative treatment of tissue is usually associated with the explosive removal of tissue by microsecond or nanosecond pulses of light. Ablation with ultraviolet light may be associated with the photochemical breaking of bonds within the irradiated zone causing minimal thermal damage, while ablation with infrared light is associated with a rapid local heating causing the tissue to be explosively removed with a peripheral zone of thermal damage. There is a large body of literature devoted to studying the fundamental mechanisms associated with these photon interactions with tissues (Welch 1984, Boulnois 1985, Senz and Muller 1989). One of the major problems in this area is that the interaction coefficients of tissue are difficult to measure accurately before the procedure. In order to predict the resulting thermal effects within the tissue properly, the interaction coefficients must be known before treatment to predict the energy deposition (Welch *et al* 1991, Gijsbers *et al* 1991) or the treatment must be dynamically controlled in real time. While the latter may provide the best solution for relatively long treatment times, it is still important to roughly predict the energy deposition before treatment. This problem has been examined through the use of diagnostic spectroscopy of tissue and tissue components before and during ablation (Walsh *et al* 1994, Ediger *et al* 1994, Pettit *et al* 1993). An ideal spectroscopy system could allow non-invasive measurements of these values before and perhaps even during the treatment.

Photochemical reactions are also used therapeutically in applications such as photodynamic therapy (PDT), a treatment for tumour destruction (Henderson *et al* 1992, Kessel *et al* 1993, Pass 1993). The death of cancer tumour cells is initiated by injection

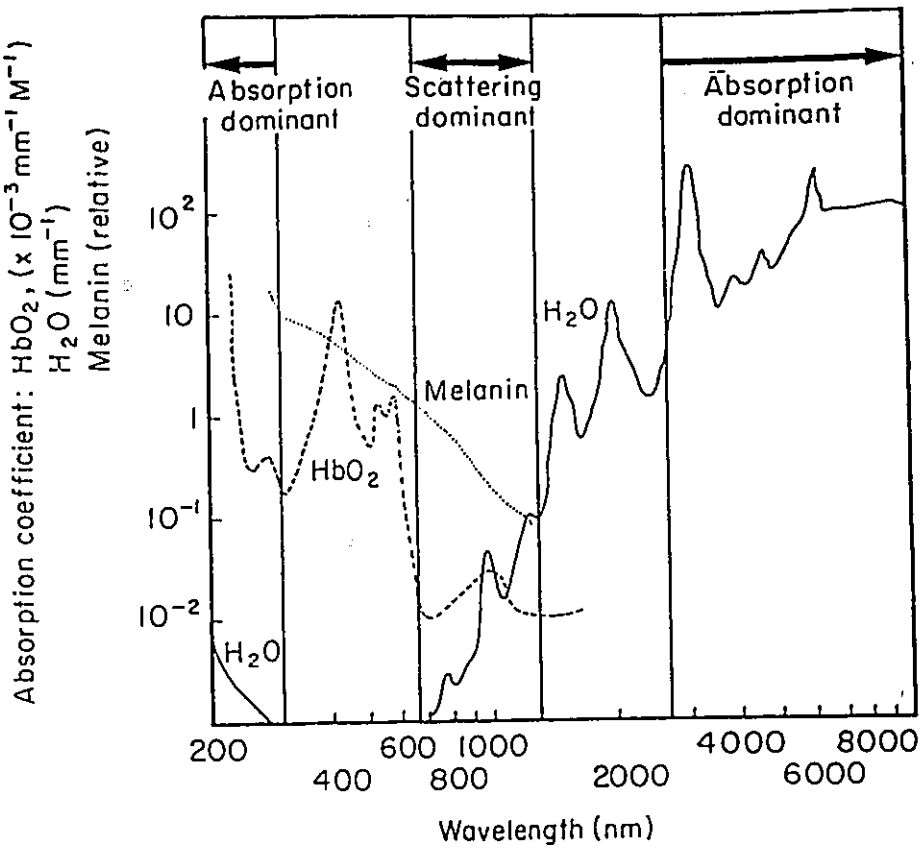

Figure 1.1 Absorption spectra of some important chromophores within human tissue.

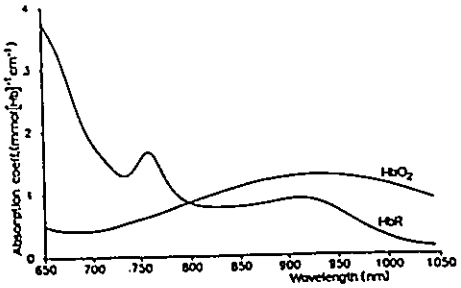

Near-infrared absorption spectra of oxygenated and deoxygenated hemoglobin.

of an exogenous chromophore which is preferentially taken up within some malignant tissues. The electronic excitation of this dye with light is thought to produce singlet oxygen via energy transfer from the excited triplet state dye molecule to ground state triplet molecular oxygen (Keene *et al* 1986, Tromberg *et al* 1990). The resulting reactions with singlet state oxygen can cause both cell death and destruction of blood vessels in the region of the treated area. The precise mechanisms which result in preferential uptake in cancer cells and the sequence of events which lead to cell death are dependent upon the particular sensitizer used and are still under investigation for many different photosensitzers (Kessel 1993).

Photodynamic therapy for various cancer types is currently undergoing clinical trials at many different research centres. The Health Protection Bureau of Canada recently approved the commercial photosensitizer Photofrin for treatment of bladder cancer (Dougherty 1993). The same photosensitizer has been approved in Japan for treatment of oesophageal, endobronchial and stomach cancer. However the optimization of photodynamic therapy may require diagnostic light measurements because the photodynamic effect is quite sensitive to both drug concentration in tissue and to the light fluence delivered to the tissue. Several researchers have been developing systems to measure the concentration of drug in tissue (Wilson *et al* 1990, Sinaasappel *et al* 1993, Andersson-Engels *et al* 1993, Durkin *et al* 1994), as well as the intrinsic optical coefficients of the tissue so that the light fluence within the tissue can be predicted accurately (Wilson *et al* 1993, Madsen *et al* 1994, Arnfield *et al* 1993). Dosimetry for PDT may be one potential application of the system developed in this study.

The diagnostic uses of light have dramatically increased in recent years. It has been shown that light in the red and infrared region of the spectrum travels the furthest

in tissue, since the absorption is the lowest here, see figure 1.1. In this region the attenuation of light is dominated by elastic scattering. Scattering coefficients in typical tissues range from 1 mm^{-1} to 100 mm^{-1}. Light can be transmitted through a few millimetres of tissue quite easily in this spectral region, and measurements through a few centimetres of tissue is possible with equipment such as lasers and photomultiplier tubes. Recently considerable research has been directed towards using near-infrared light for an increasing number of non-invasive diagnostic measurements. Recent claims in the literature suggest that near-infrared tissue spectroscopy may be used in monitoring glucose levels (Maier *et al* 1995, Essenpriess *et al* 1995) or in detecting intracranial hemorrhage in the brain (Benaran *et al* 1994, Chance *et al* 1994). In this thesis, the main applications are thought to be in hemoglobin oxygen saturation measurement, blood volume measurement, cancerous tissue detection, and dosimetry for photodynamic therapy.

One of the most common biomedical uses of near-infrared light is to determine hemoglobin oxygen saturation levels (Mengelkoch *et al* 1994). The oxygen saturation level is an good indicator of respiratory status, and as such can be an inexpensive reliable monitor for patients under study or being treated in hospital. The typical oxygenation monitors (called pulse oximeters) use relative intensity measurements at two wavelengths, along with a empirical calibration curve to calculate the approximate oxygen saturation of arterial blood. One of the goals of the present study is to eliminate the need for empirical calibration, by calculating the exact absorption coefficients of the tissue. Once the exact absorption coefficients of the tissue are known, the concentrations of Hb and HbO_2 can be calculated from their spectroscopically measured extinction coefficients (Wray *et al* 1988). This is examined further, later in the thesis. Also, the ability to recover the exact absorption coefficients with better spatial resolution suggests that

infrared imaging may be possible. Theoretically, blood volume or blood oxygenation within tissue could be mapped with a reconstruction algorithm. This type of imaging is examined further in the final section on this thesis.

Breast transillumination has been used for the detection of cancer tumours for several decades with questionable success (Gros *et al* 1972, Navarro *et al* 1988). More recent work has attempted to determine the basis of contrast for these measurements in order to optimize a detection system (Profio *et al* 1989(a), Peters *et al* 1990). Several groups are currently developing breast cancer imaging/detection systems, based upon either time-resolved (Kang *et al* 1993) or frequency-domain light imaging (Kaschke *et al* 1994). Kaltenbach *et al* (1993) have demonstrated the use of a frequency-domain measurements to differentiate between cysts and tumours, since the phase shift caused by the two objects is quite different. Time-varying light signals may provide the opportunity to improve the resolution, contrast and specificity over traditional steady-state transillumination measurements.

The type of time-varying signals examined in this thesis are depicted in figure 1.2. When the intensity of a light source on a tissue surface is modulated, it sets up a travelling intensity wave in the tissue. The frequency of these waves is determined by the source, and they can be detected at any point if the attenuation is not too great. The properties of these intensity waves is the subject of this thesis. The mathematical theory used to model the propagation of these waves within a highly scattering medium, such as tissue, will be examined first.

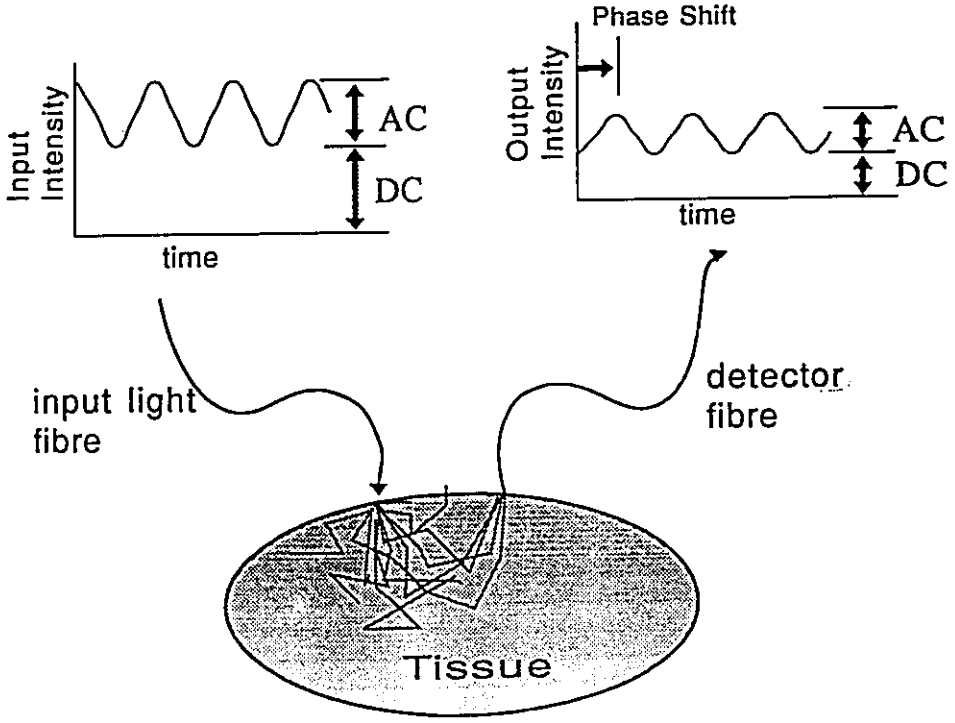

Figure 1.2 Schematic diagram of frequency-domain diffuse light propagation in a scattering medium.

1.2 Light Interaction with Tissue

The two main mechanisms by which optical photons interact with tissue are elastic scattering and absorption. The scattering is thought to be from changes in the refractive index, n, of cellular structures such as membranes and internal organelles such as the mitochondria (Beauvoit *et al*, 1995 and 1993). The absorption within tissue is due to natural chromophores within the tissue such as melanin, hemoglobin, cytochromes and water. The absorption is quite strongly dependent on wavelength, while the scattering tends to be less wavelength dependent. Figure 1.1 shows some of the values of absorption coefficient for several of the most important tissue chromophores, measured *in vitro*. Both the interaction coefficients can vary significantly between different tissue types, as can be seen from the values catalogued by Cheong *et al* 1991.

The fundamental physics used to describe the interaction of light with matter is usually derived from electromagnetic theory. Using the complex dielectric of the material, the propagation of electromagnetic waves in a medium can be described by Maxwell's equations. This formal approach has been quite successful in describing the scattering of light from spherical particles, referred to as Mie scattering (Bohren and Huffman 1983). van Staveren *et al* (1991) have successfully used Mie scattering theory to predict the scattering coefficients of a lipid emulsion with the commercial name Intralipid, which is often used in tissue-simulating phantoms. This emulsion was used throughout the present study as a tissue-simulating medium, and the Mie theory calculations were used as the theoretical estimate for the scattering coefficient. The electromagnetic theory calculations have met with very limited success for tissue, mainly due to the high degree of inhomogeneity of living cells. The scattering in tissue is thought to be a result of the index of refraction changes at the boundary of cellular membranes (Beauvoit *et al* 1993),

but the cellular surfaces are irregular, and cells are closely packed making exact calculations difficult.

An alternative method for modelling light propagation in tissue is to ignore the wave nature of light and treat the individual photons as neutral particles. The definition of macroscopic interaction coefficients allows the equation of radiative transfer to be used to describe the propagation of photons. This approach has had considerable success in predicting the distribution of light in scattering media such as tissue from analytic solutions of this equation (Ishimaru 1978, Star *et al* 1988, Patterson *et al* 1989, Profio 1989). This approach ignores wave phenomena such as polarization and coherence, however for multiply scattered light these are usually not observable.

A useful numerical approach for modelling the light interaction in tissue has been the Monte Carlo technique (Flock *et al* 1989) in which individual photon histories are traced as they travel through the tissue. This type of calculation is very useful and accurate, but it suffers from long computation times when the propagation distance is much larger than the mean free path. This method is often used as a 'numerical experiment' to provide a test of analytic solutions, in the absence of experimental data (Farrell *et al* 1991, Gandjbakhche *et al* 1993, Hielscher *et al* 1995).

The three main parameters which are used to describe the interaction at a given wavelength are the absorption coefficient, μ_a, scattering coefficient, μ_s, and average cosine of the scattering angle, g. The coefficients μ_a and μ_s represent the probability per unit path length of a photon being absorbed or scattered, respectively. Often the angular scattering distribution is described by a scattering phase function, $f(\Omega' \bullet \Omega)$ which is the normalized probability density for the scatter of a photon from angle Ω' to Ω. The average cosine of the scattering angle, g, is the average of $\Omega' \bullet \Omega$ over all angles weighted by the phase

function. The value g is a measure of whether the scattering is forward peaked (i.e. g = $\langle\cos(0^0)\rangle$ = 1.0), or backward peaked (i.e. g = $\langle\cos(180^0)\rangle$ = -1.0). If the scattering is isotropic, it has no net direction (i.e. g = 0). In most tissue types the scattering is highly forward peaked, with typical g values above 0.8 (Cheong *et al* 1991) and in brain tissue the g value can be as high as 0.99 (van der Zee *et al* 1993).

Since most of the scattering in tissue is elastic, the radiance within the tissue can be modelled with the single energy transport equation for neutral particles. The radiance, $\psi(\mathbf{r},\Omega,t)$, represents the photons in solid angle Ω at position $\mathbf{r}$, at time t, within the tissue

(1.1)

$$\frac{1}{c_n}\frac{\partial\psi(\boldsymbol{r},\Omega,t)}{\partial t} + \Omega\cdot\nabla\psi(\boldsymbol{r},\Omega,t) + (\mu_a+\mu_s)\psi(\boldsymbol{r},\Omega,t) = \mu_s\int_{4\pi} f(\Omega'\cdot\Omega)\psi(\boldsymbol{r},\Omega',t)\,d\Omega' + S(\boldsymbol{r},\Omega,t)$$

Where $c_n = c/n$ is the speed of light in the medium, and $S(\mathbf{r},\Omega,t)$ is the source of photons in solid angle Ω at position $\mathbf{r}$ and time t. This is a complicated differential-integral equation which is impossible to solve analytically in all but a few cases. Several different approaches have been used to make use of this equation, ranging from discrete ordinates numerical calculations to more heuristic two flux models (Patterson *et al* 1991(c)). In this study, the diffusion approximation has been used throughout, due to recent success in applying analytic solutions of this equation to tissue spectroscopy (Ishimaru 1978, Patterson *et al* 1989, Patterson *et al* 1991(a)).

1.3 Development of Diffusion Theory

The diffusion approximation to radiative transport theory was developed long ago for modeling photon migration in the outer layers of a star (Milne 1921). More recently

it has been used for modeling the neutron flux in nuclear reactors (Lamarsh 1966). Applications of this approximation to multiply scattered photon propagation in tissue have been relatively recent (Ishimaru, 1978). It is important to understand the assumptions and limitations of the diffusion approximation, so a brief description of the derivation is included here. The radiance and the phase function in equation (1.1) can be expanded into a series of spherical harmonics. By assuming that the radiance is just linearly anisotropic, only the first two terms in the spherical harmonic expansion are retained. The angular dependence of the equation is eliminated by integrating over all angles. This is the P_1 approximation, whereby the equation is rewritten in terms of the photon fluence rate and photon current. Here the photon fluence rate is defined as

$$\Phi(\boldsymbol{r}, t) = \int_{4\pi} \psi(\boldsymbol{r}, \Omega, t)\, d\Omega \qquad (1.2)$$

and describes the number of photons passing through an infinitesimal spherical surface per unit time. The net photon current vector is

$$J(\boldsymbol{r}, t) = \int_{4\pi} \Omega\ \psi(\boldsymbol{r}, \Omega, t)\, d\Omega \qquad (1.3)$$

The resulting equation is the well known equation of continuity, which describes the photon fluence rate at any point as a function of time

$$\frac{1}{c}\frac{\partial \Phi(\boldsymbol{r}, t)}{\partial t} - \nabla \cdot J(\boldsymbol{r}, t) + \mu_a \Phi(\boldsymbol{r}, t) = S_0(\boldsymbol{r}, t) \qquad (1.4)$$

where $S_0(\mathbf{r},t)$ is an isotropic source of photons. In deriving the diffusion equation from the equation of continuity it is also necessary to employ Fick's Law for diffusion, which states that the current is proportional to the gradient of the fluence rate (Lamarsh 1966). Fick's Law can be approximately derived from equation 1.1 by first multiplying by Ω and

then integrating over all angles, to yield the equation

$$\frac{1}{c_n}\frac{\partial J}{\partial t} + \frac{1}{3}\nabla\Phi(r,t) + \mu_t J(r,t) = S_1(r,t) \qquad (1.5)$$

where $S_1(r,t)$ is an anisotropic source term and $\mu_t = \mu_a + \mu_s'$, where μ_s' is the transport (or reduced) scattering coefficient defined as $\mu_s' = \mu_s(1-g)$ and g is the average cosine of the scattering angle. Then the assumption must be made that the first term in equation 1.5, the time derivative of the current, is much smaller than the third term, which is the interaction rate of photons. Assuming there are only isotropic sources, Fick's Law can then be written as

$$J(r,t) = -D\,\nabla\Phi(r,t) \qquad (1.6)$$

The diffusion equation results from combination of (1.6) and (1.4), contains only the fluence rate

$$\frac{1}{c}\frac{\partial\Phi(r,t)}{\partial t} - \nabla D\nabla\Phi(r,t) + \mu_a\Phi(r,t) = S_0(r,t) \qquad (1.7)$$

where D is defined as the diffusion coefficient, $D = [3(\mu_a+\mu_s')]^{-1}$.

The assumptions used in deriving Fick's Law from the equation of radiative transfer are fairly restrictive. There are three main assumptions which will be examined here. First it was assumed that the source is only isotropic. However for a laser beam incident on a tissue surface, the light radiance can be highly anisotropic close to the light source, and so diffusion theory should not be as good at predicting the light propagation in this area. Several studies have investigated the accuracy of diffusion theory close to a light source in tissue simulating materials, and it is established that diffusion theory can be used to model light fluence at distances of 3 to 5 mean free scattering paths from the source (Yoo *et al* 1990, Farrell *et al* 1991). The typical scattering in tissue is highly

forward peaked; after several scattering lengths the fluence pattern will appear to originate from an isotropic source if $\mu_s >> \mu_a$.

A second assumption in deriving Fick's Law was that the time between photon scattering events is much shorter than the time scale of the photon current changes, or

$$\frac{1}{J}\frac{\partial J}{\partial t} << c\mu_t \qquad (1.8)$$

Since μ_t is typically 0.2 to 4.0 mm^{-1} in tissue, then $c\mu_t$ is typically around 10^{11} sec^{-1}, equation 1.8 will be true for most light signals except at the rising edge of ultra-short laser pulses (in the nanosecond to picosecond range) or for modulation frequencies in the GHz range. Fishkin (1994) and Haskell *et al* (1995) have determined that the diffusion approximation is less accurate for light modulated near 1 GHz, due to this approximation. They have developed an analytic solution for the full P1 expansion which is not constrained by equation 1.8. However for most tissue spectroscopy applications with modulation frequencies less that 1 GHz, diffusion theory should be adequate.

The third assumption in derivation of the diffusion equation was that the light radiance be only linearly anisotropic. This assumption requires that the angular dependence of the radiance be relatively small, or that the magnitude of the current be much smaller than the magnitude of the fluence rate, $| J(\mathbf{r},t) | << | \Phi(\mathbf{r},t) |$. In an infinite medium with interaction coefficients similar to tissue, the value of $|\Phi/J|$ is high, confirming that the diffusion approximation is appropriate. When μ_s' is between 2 and .5 mm^{-1}, and μ_a is between 0.005 and 0.04 mm^{-1}, the value of $|\Phi/J|$ ranges from 8 to 41 for CW light. The lower values occur when the absorption coefficient becomes significant in comparison to the scattering coefficient. Haskell *et al* (1995) have examined the ratio of $|\Phi/J|$ as a function of frequency and at the boundary of a scattering medium and air

interface. They found that the ratio would be significantly reduced when the modulation frequency was in the GHz range. Also they demonstrated that the $|\Phi/J| \approx 5$ at a water-air interface. This result suggests that the radiance is highly directional near boundaries, and that diffusion theory may be less accurate here. Unfortunately most diagnostic measurements in tissue are taken at the air-tissue boundary, however diffusion theory still appears to provide a good prediction of the relative fluence at large distances from the source.

1.4 Boundary Conditions

The Green's function solutions to equation 1.7 have been well documented for several regular geometries (Carslaw and Jaeger 1959, Lamarsh 1966, Case and Zweifel 1969). These analytic solutions have been summarized by both Moulton (1990) and Arridge *et al* (1992) for applications in time and frequency-domain tissue spectroscopy. The geometries include the infinite medium, semi-infinite medium, infinite slab, cylinder and sphere. The observed quantity at the surface of a tissue sample is not the fluence, but the current of photons passing through the surface, given by

$$R(\rho, t) = -D\frac{\partial \Phi}{\partial z}(\rho, z, t)\,|_{z=0} \qquad (1.9)$$

for the geometry shown in figure 1.3, where z is the ordinate perpendicular to the tissue surface, and ρ is parallel to the surface, with origin at the source location. This quantity is referred to as the diffuse light signal, which can also be referred to as reflectance or transmittance at a surface.

Moulton (1990) and Patterson *et al* (1991b) have examined different boundary conditions for each of the Green's function geometries, in an attempt to simplify and

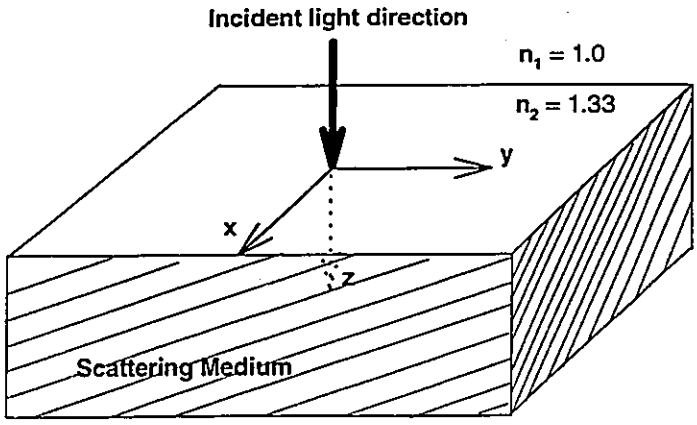

Figure 1.3 Geometry for non-invasive diffuse spectroscopy of scattering media.

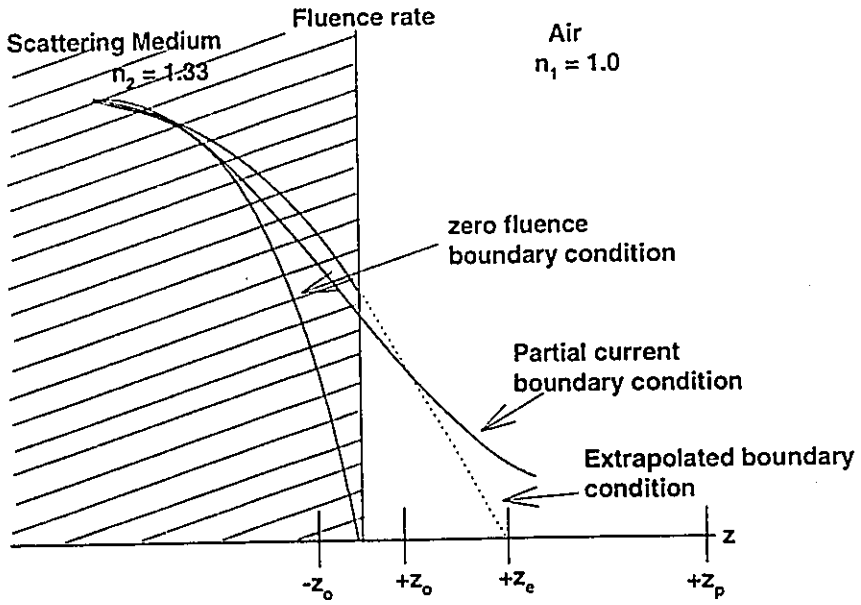

Figure 1.4 Example depiction of fluence rate versus depth for three different boundary conditions.

understand modelling of the boundary effects. The fluence rate is depicted in figure 1.4 for the three types of boundary conditions mentioned here. The most physically accurate boundary condition is a partial photon current at the surface of a scattering volume

$$\frac{\partial \Phi(r,t)}{\partial z} = \frac{2D}{\kappa}\,\Phi(r,t) \qquad (1.10)$$

where κ is a constant which depends on the index of refraction mismatch at the boundary

$$\kappa = \frac{(1-R)(1-\mu_c)}{(1+R)+(1-R)\mu_c^3} \qquad (1.11)$$

(Keijzer *et al*, 1988) and

$$R = \left(\frac{n_1 - n_2}{n_1 + n_2}\right)^2 \qquad (1.12)$$

$\mu_c = \cos(\sin^{-1}(n_2/n_1))$, where n_2 and n_1 are the indices of refraction for the tissue and boundary medium. κ=1 for a matched index, n_1=n_2, and κ=0.4258 for the case of a boundary between water, n=1.333 (or tissue), and air. Unfortunately, the partial current boundary condition leads to an analytic solution which contains an infinite integral for most geometries. Haskell *et al* (1995) has derived the frequency-domain expression for the semi-infinite volume, but the solution contains an integral with no analytic integrand. Both Moulton (1990) and Haskell *et al* (1995) found that the partial current boundary condition can be well approximated by assuming that the fluence rate drops to zero at some extrapolated boundary, a distance z_e beyond the surface, $\Phi(\rho,z=z_e,t) = 0$. Then the method of images can be used to produce a boundary of zero fluence rate between a positive source within the tissue at depth z_o, and a negative photon source outside the tissue, at a distance $z_p = z_o + 2z_e$, see figure 1.4. The source depth is defined as, $z_o = (\mu_s')^{-1}$, one mean free transport pathlength into the sample. In the present study, the

extrapolated boundary condition solution was used with the diffusion extrapolation length set to the diffusion solution value of $z_e = 2D/\kappa$. There are also applications where the simple zero fluence boundary condition will be applied. This condition states that the fluence rate is exactly zero on the boundary. This boundary condition is the simplest to implement and yields a quick approximation to the signal.

Diffusion theory solutions have been used to predict the relative reflectance from tissue-phantom material in several studies (Wilson *et al* 1990, Farrell *et al* 1991, Star *et al* 1988). Patterson *et al* (1989) demonstrated that picosecond pulses of light incident on tissue-phantom material would propagate through tissue and the remitted pulse could be accurately modeled with time-dependent diffusion theory. Madsen (1993) has compared diffusion theory calculations to the pulses remitted from tissue-phantoms with well characterised optical properties. Those studies demonstrated the ability to calculate the absorption and transport scattering coefficients from the time-resolved data measured at any point on the surface of an optically turbid medium. While this method can be very useful, it requires the use of a short pulsed laser and complicated single photon counting equipment. Patterson *et al* (1991(a)) also demonstrated that the same measurements made in the frequency domain could be used to calculate the optical properties of the medium. This study will examine frequency-domain diffuse spectroscopy further, as a method for *in vivo* tissue spectroscopy and imaging.

1.5 Analytic Solutions

Solutions of equation 1.7 in the frequency-domain can be found by Fourier transformation of the time-domain solutions derived by Moulton (1990), or by transforming equation 1.7 and developing Green's functions for this new equation. The

Fourier transform of equation 1.7 is

$$\nabla^2\Phi(r,\omega) - \left(\frac{\mu_a - i\omega/c}{D}\right)\Phi(r,\omega) = S(r,\omega) \qquad (1.13)$$

For simplicity, the coefficient in front of the second term will be defined as the square of the complex effective attenuation coefficient

$$k = \left(\frac{\mu_a + i\omega/c}{D}\right)^{1/2} \qquad (1.14)$$

where $\omega = 2\pi f$, and f is the frequency of light modulation. In steady state measurements the same expression describes the effective attenuation coefficient with $\omega=0$.

Some of the solutions of this equation using the extrapolated boundary condition are given in table 1.1. The geometries for these equations are shown in figures 1.5, 1.6 and 1.7. The first two equations are for the infinite medium 1.15, and the semi-infinite with isotropic source located at a depth z_o below the surface (see figure 1.5) for the zero fluence boundary condition 1.16. The following three equations are all for the extrapolated boundary condition and are written in terms of equation 1.16 for simplicity: semi-infinite medium 1.17 (see figure 1.6), slab reflectance 1.18 (see figure 1.7), and slab transmittance (1.19).

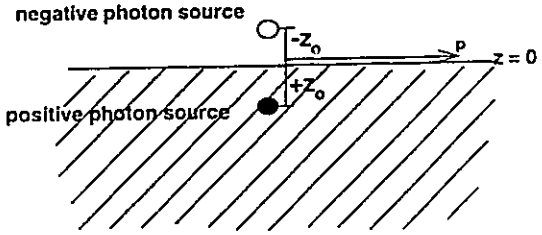

Figure 1.5 Zero fluence boundary condition at the air-tissue interface. semi-infinite geometry

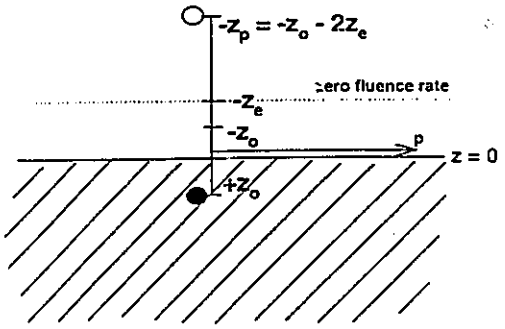

Figure 1.6 Extrapolated boundary condition semi-infinite geometry

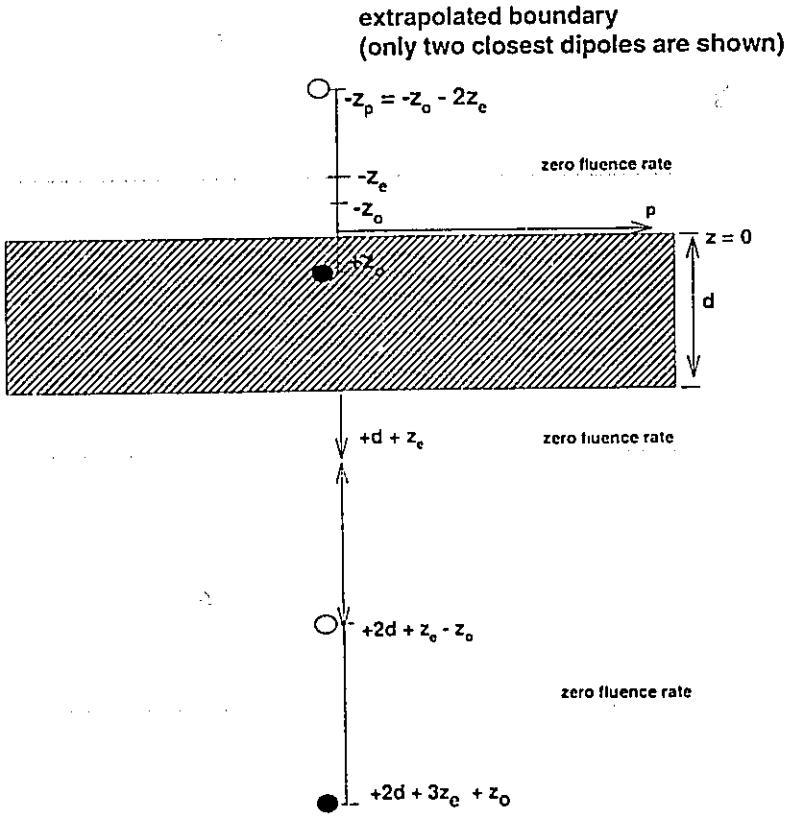

Figure 1.7 Extrapolated boundary condition Slab geometry

Table 1.1

$$R_{\infty}(r,\omega) = \frac{(1+kr)}{2(2\pi)^{3/2}r^2}\, e^{-kr-i\omega t} \qquad (1.15)$$

$$R_{\infty/2}(\rho_o, z_o, \omega) = \frac{z_o(1+k\rho_o)}{(2\pi)^{3/2}\rho_o^{\,3}}\, e^{-k\rho_o - i\omega t} \qquad (1.16)$$

$$R_{\infty/2}(\rho, 0, \omega) = \frac{1}{2}\left[R_{\infty/2}(\rho_o, z_o, \omega) + R_{\infty/2}(\rho_p, z_p, \omega) \right]$$

$$R_{slab}(\rho, z=0, \omega) = R_{\infty/2}(\rho_o, z_o, \omega) + \frac{1}{2}\sum_{n=2\ even}^{\infty}\left[\begin{array}{l} R_{\infty/2}(\rho_{+no}, z_{+no}, \omega) + R_{\infty/2}(\rho_{+np}, z_{+np}, \omega) \\ - R_{\infty/2}(\rho_{-no}, z_{-no}, \omega) - R_{\infty/2}(\rho_{-np}, z_{-np}, \omega) \end{array} \right] \qquad (1.18)$$

$$T_{slab}(\rho, z=d, \omega) = \frac{1}{2}\sum_{n=1\ odd}^{\infty}\left[\begin{array}{l} R_{\infty/2}(\rho_{+no}, z_{+no}, \omega) + R_{\infty/2}(\rho_{+np}, z_{+np}, \omega) \\ - R_{\infty/2}(\rho_{-no}, z_{-no}, \omega) - R_{\infty/2}(\rho_{-no}, z_{-no}, \omega) \end{array} \right]$$

the distance variables have been defined as follows :

$\rho_o = (\rho^2 + z_o^2)^{1/2}$ $\qquad$ $\rho_p = (\rho^2 + z_p^2)^{1/2}$

$z_{+no} = nd + z_o$ $\qquad$ $z_{+np} = nd + z_p$

$\rho_{+no} = (\rho^2 + z_{+no}^2)^{1/2}$ $\qquad$ $\rho_{+np} = (\rho^2 + z_{+np}^2)^{1/2}$

$z_{-no} = nd - z_o$ $\qquad$ $z_{-np} = nd - z_p$

$\rho_{-no} = (\rho^2 + z_{-no}^2)^{1/2}$ $\qquad$ $\rho_{-np} = (\rho^2 + z_{-np}^2)^{1/2}$

These designations for the distance variables are meant to simplify the analytic expressions. It should also be noted that some of these equations and their development have been described by Moulton (1990), Arridge *et al* (1992), Tromberg *et al* (1993), Fantini *et al* (1995) and Fishkin *et al* (1994).

1.6 Numerical Solutions

Recent developments in diffusion theory have focused on finding simple analytic solutions of the diffusion equation to allow fast calculations and recovery of optical properties. Until this point the solutions presented here have all assumed that the optical interaction coefficients were not spatially variant. For the development and analysis of tissue spectroscopy in heterogeneous optical volumes or for irregular geometries, a numerical solution of the diffusion equation was also used.

Some researchers have derived analytic diffusion solutions for inhomogeneous interaction coefficients for imaging applications. Barbour *et al* (1993) and Kaltenbach *et al* (1993) derived solutions for a point scattering or absorbing perturbation within a homogeneous scattering volume. These solutions have been used by several researchers for perturbation based inverse imaging algorithms. Fishkin *et al* (1993) solved for the fluence rate in an infinite medium containing a totally absorbing straight edge. Boas *et al* (1994) derived a solution for an infinite medium containing a spherical inhomogeneity. O'Leary *et al* (1994) have successfully used this solution as a forward calculation to provide an imaging algorithm for frequency-domain optical imaging. The main problem with using analytic solutions for optical imaging, is that they apply only to regular heterogeneities such as a point, sphere or plane.

Generally, a useful solution of the diffusion equation, should allow spatial variation of the optical properties at all points within the volume,

$$\frac{1}{c}\frac{\partial \Phi(\boldsymbol{r}, t)}{\partial t} - \nabla D(\boldsymbol{r})\,\nabla \Phi(\boldsymbol{r}, t) + \mu_a(\boldsymbol{r})\,\Phi(\boldsymbol{r}, t) = S_0(\boldsymbol{r}, t)$$

This equation has spatially varying coefficients $\mu_a(\mathbf{r})$ and $D(\mathbf{r}) = [3(\mu_a(\mathbf{r}) + \mu_s'(\mathbf{r})]^{-1}$. It can be solved numerically either by a finite difference or finite element solution. These

numerical solutions can be much slower than the analytic calculations, especially when the tissue volume being simulated is larger than a few mean free paths, however they provide the flexibility which cannot be achieved with analytic solutions. For the imaging sections of this thesis a fast finite difference solver was used for the forward solution of the diffusion equation. Studies comparing the efficiency of finite difference solutions have demonstrated that multigrid solutions provide the fastest method of solving a finite difference elliptic equation numerically (Press *et al* 1992, Fulton *et al* 1986) at the present time. Further explanation of this method is given in papers 4 and 5 of this thesis.

1.7 Thesis Proposal

The remainder of this thesis describes experiments and theory derived for frequency-domain tissue spectroscopy and imaging. Chapter 2 of this thesis describes the theory and experimental work used to measure frequency-domain light signals transmitted through tissue-simulating phantoms with well characterized optical properties. These measurements were used to test analytic diffusion theory in calculating the average absorption and scattering coefficients of the media. Calibration phantoms were used for optical properties typical of human tissue. The system was then used for non-invasive spectroscopy in applications which are outlined in the following chapters.

In chapter 3, three papers discuss particular areas of near-infrared homogeneous tissue spectroscopy with the frequency-domain system. In the first paper, diffusion spectroscopy is examined on small regular geometry phantoms. The effects of specific boundaries and shapes are examined in order to estimate the errors which could occur *in vivo* due to erroneous assumptions about the geometry. Some general guidelines for *in vivo* frequency-domain spectroscopy with diffusion theory are provided. The applications

of this work are discussed with respect to both photodynamic therapy dosimetry, and tissue oxygenation measurements. This work was published in Physics in Medicine and Biology Volume 39, pp 1157-1180, 1994. The second paper has been submitted to the Journal of Biomedical Optics and addresses the accuracy of a frequency-domain spectroscopy system. The errors associated with random noise, systematic errors and physiologic noise are all considered for a specific system. This paper examines the fundamental limitations of frequency-domain tissue spectroscopy. The third paper examines diffuse fluorescence from a uniformly distributed fluorophore in a tissue simulating medium. Analytic expressions for diffuse fluorescence were developed and tested with experimental measurements. This work is a preliminary step in being able to non-invasively probe a fluorophore distributed within tissue and calculate properties such as concentration, lifetime or quantum yield. Recently there has been considerable interest in the medical applications of fluorescent light as a non-invasive optical biopsy of tissue. This paper was published in Applied Optics Volume 33 (10), pp 1963-1974 (1994).

Chapter 4 of the study examines the use of frequency-domain measurements for heterogeneous tissue. In particular, phase, modulation and intensity measurements are used to examine the detection of absorbing and scattering inhomogeneities within a tissue-simulating medium and the feasibility of these measurements for use in optical tomography. A fast iterative reconstruction algorithm was used along with a fast numerical solution for the diffusion equation to reconstruct images from simulated and measured data. The first tomography paper assesses the resolution, contrast and accuracy of reconstruction, as well as examining some potential applications of the method. This paper was published as part of the SPIE Biomedical Optics Conference proceedings 3489, (1995). The second paper in tomography was published in Physics in Medicine and

Biology **40**, 1709-1729 (1995). This paper addresses the issues of reconstruction stability and accuracy. The effects of random noise and systematic errors were examined. Also in this paper, results of reconstructions from experimental data on tissue phantoms are presented.

The emphasis of this thesis has been to examine frequency-domain measurements and their utility in tissue spectroscopy applications. There are many parameters which can affect the measurements, so this thesis has attempted to consider as many of these parameters as possible without focusing on any one particular application. These studies should provide future researchers with a broad gauge of the benefits and drawbacks of frequency-domain measurements for tissue spectroscopy and imaging.

Chapter 2

Frequency-Domain Diffuse Spectroscopy

2.1 Frequency-Domain Light Propagation

The accuracy of a diffuse spectroscopy system relies mainly upon the modeling used to recover the scatter and absorption coefficients from a detected light measurement. While much of the diffusion theory testing has been well developed in the literature, it is useful to examine some of the fundamental properties of the light signals in order to optimize and understand the system. Frequency-domain light signals in tissue have been referred to as photon density waves which propagate outwards from the source. The solution of the diffusion equation (1.13) in an infinite medium, for a point source, is given by

$$\Phi(r,\omega) = \frac{S_o(r,\omega)\, e^{-kr}\, e^{i\omega t}}{4\pi D r} \qquad \textbf{(2.1)}$$

where k is the complex attenuation coefficient which can be separated into real and imaginary components as

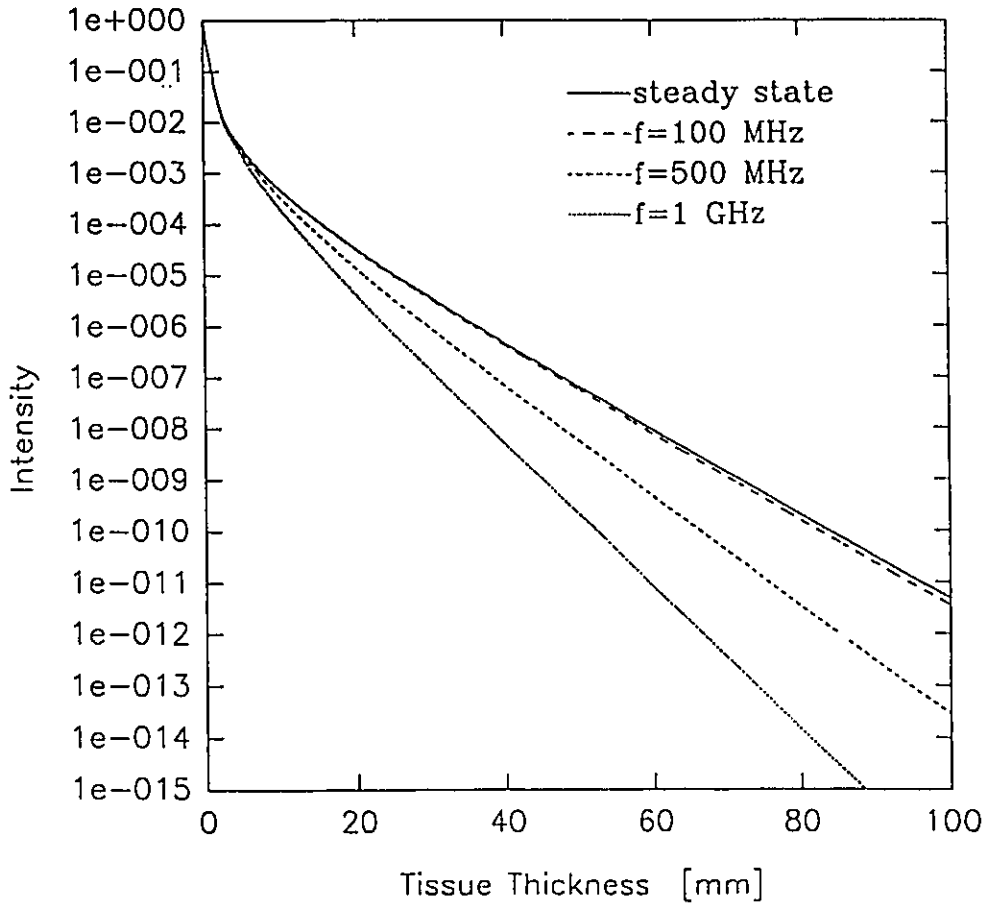

Figure 2.1 Diffusion theory calculation of normalized fluence rate in an infinite medium. Optical properties $\mu_a = 0.01$ mm^{-1}, $\mu_s' = 1.0$ mm^{-1}

$$k_r = \left(\frac{\mu_a^2 + \omega^2/c^2}{D^2}\right)^{1/4} \cos\left(\frac{1}{2}\tan^{-1}\left(\frac{\omega}{\mu_a c}\right)\right) \qquad \textbf{(2.2)}$$

and

$$k_i = \left(\frac{\mu_a^2 + \omega^2/c^2}{D^2}\right)^{1/4} \sin\left(\frac{1}{2}\tan^{-1}\left(\frac{\omega}{\mu_a c}\right)\right) \qquad \textbf{(2.3)}$$

The real part of k represents the exponential damping of the AC intensity wave. The transmitted intensity from a unit source is plotted in figure 2.1 as a function of the distance between source and detector for typical tissue optical properties of $\mu_a = 0.01 mm^{-1}$ and $\mu_s' = 1.0\ mm^{-1}$. The attenuation of the photon density wave is not significantly different from DC attenuation until modulation frequencies in the 100 MHz region are used.

The values of μ_a and μ_s' can significantly affect the wave propagation by changing the wavelength and contributing to the attenuation. The wavelength of oscillation is given as $2\pi/k_i$, and this is plotted in figures 2.2 (a) and (b) for different frequencies and different values of μ_a and μ_s'. In general the wavelength is almost inversely proportional to the square root of the frequency, and is decreased by increasing μ_s' or decreasing μ_a. When the solutions for fluence rate in a semi-infinite medium are required, the method of images can be used to calculate the fluence rate from the infinite medium solution (See section 1.5). The boundary causes a loss of light at the interface and an increase of the average wavelength, or a decrease in the average path length. These calculations of wavelength will be more significant in the imaging section where the presence of an object with different optical properties will cause a localized change in the wavelength as well as the

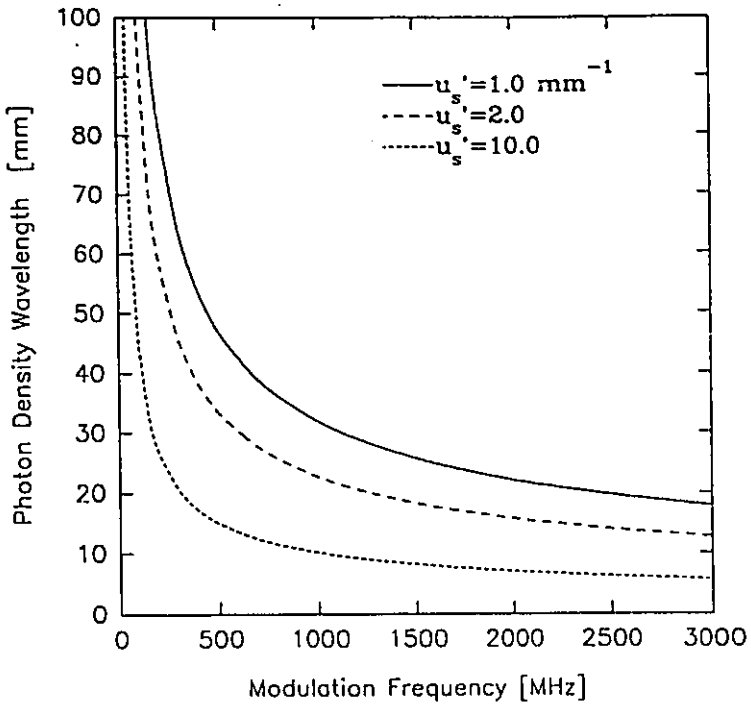

Figure 2.2 (a) Theoretical calculation of modulation wavelength in an infinite medium. Absorption fixed at $\mu_a = 0.01$ mm^{-1}.

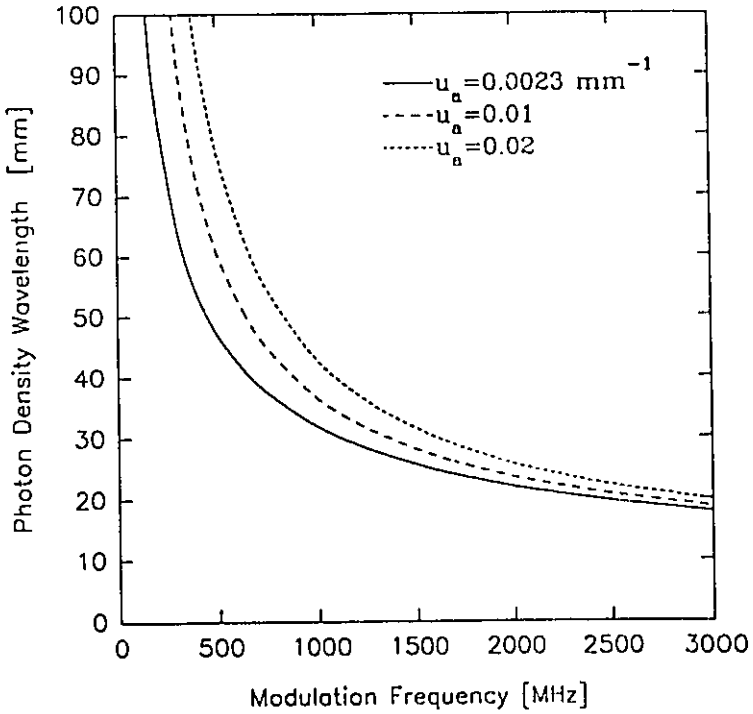

Figure 2.2 (b) Theoretical calculation of modulation wavelength in an infinite medium. Scattering fixed at $\mu_s' = 1.0$ mm^{-1}.

intensity. Changes in the wavelength appear as a phase shift of the wave at the detection location. Most of the treatment of these waves is analogous to highly damped acoustical waves (Coulton 1992) or thermal waves (Carslaw and Jaeger 1959).

2.2 Theoretical Analysis of Parameters

2.2.1 Observable parameters

Before a system is developed for measurements in tissue, it is important to establish the appropriate choice of parameters to be measured. The observable parameters are phase (ϕ), AC intensity (I_{AC}), DC intensity (I_{DC}) and modulation (M) and can be calculated as functions of the interaction coefficients (μ_a and μ_s'), source-detector distance (ρ) and the modulation frequency ($\omega=2\pi f$). The observable parameters were calculated from the equations for reflectance and transmittance, given in equations 1.15 to 1.19. They are

$$\phi(\mu_a,\mu_s',\rho,\omega) = \tan^{-1}\left(\frac{\mathbb{I}m\,[R(\mu_a,\mu_s',\rho,\omega)]}{\mathbb{R}e\,[R(\mu_a,\mu_s',\rho,\omega)]}\right) \qquad (2.4)$$

$$I_{AC}(\mu_a,\mu_s',\rho,\omega) = \left| R^{*}(\mu_a,\mu_s',\rho,\omega)\, R(\mu_a,\mu_s',\rho,\omega) \right|^{1/2} \qquad (2.5)$$

$$I_{DC}(\mu_a,\mu_s',\rho) = \left| R(\mu_a,\mu_s',\rho,\omega=0) \right| \qquad (2.6)$$

$$M(\mu_a,\mu_s',\rho,\omega) = \frac{I_{AC}(\mu_a,\mu_s',\rho,\omega)}{I_{DC}(\mu_a,\mu_s',\rho)} \qquad (2.7)$$

for phase, AC intensity, DC intensity, and modulation respectively.

2.2.2 Detection configurations

In order to map a particular set of phase and modulation measurements onto a set of μ_a and μ_s' values, it is important to understand the range of values expected in soft tissue. Rough estimates of the range of scattering and absorption coefficients expected in tissue in the red and near IR are used for the axes of figure 2.3. The lines of constant phase and modulation are plotted on this graph for a fixed source-detector separation of 20 mm, and a modulation frequency of 140 MHz. These are typical operating conditions for this particular spectroscopy system. The phase measurements in this region are between 0 and 100°, and the modulation values are between 1.0 and 0.85. To put these numbers into perspective, typical noise values are 0.2° in phase, and 0.005 in modulation. From these rough estimates it is obvious that the noise in modulation will be a problem, since the typical noise is almost 1/30 of the dynamic range, while the noise in the phase would be only 1/500 of the dynamic range needed.

An alternative approach is to use 2 detector positions and to measure the intensity ratio and phase difference between them. In figure 2.4 the lines of constant phase difference and intensity ratio are plotted for the same typical tissue values of μ_s' and μ_a, using detector distances of 10 mm and 20 mm, and a frequency of 140 MHz. In this configuration, typical phase measurements would range between 4° and 30°, while the intensity ratio would range between 0.1 and 0.001. The phase noise of 0.2° would probably be the dominant factor here since the intensity measurements would have quite low error associated with them. Both of these configurations have been used in the work in this chapter as well as in the papers included in the following chapters.

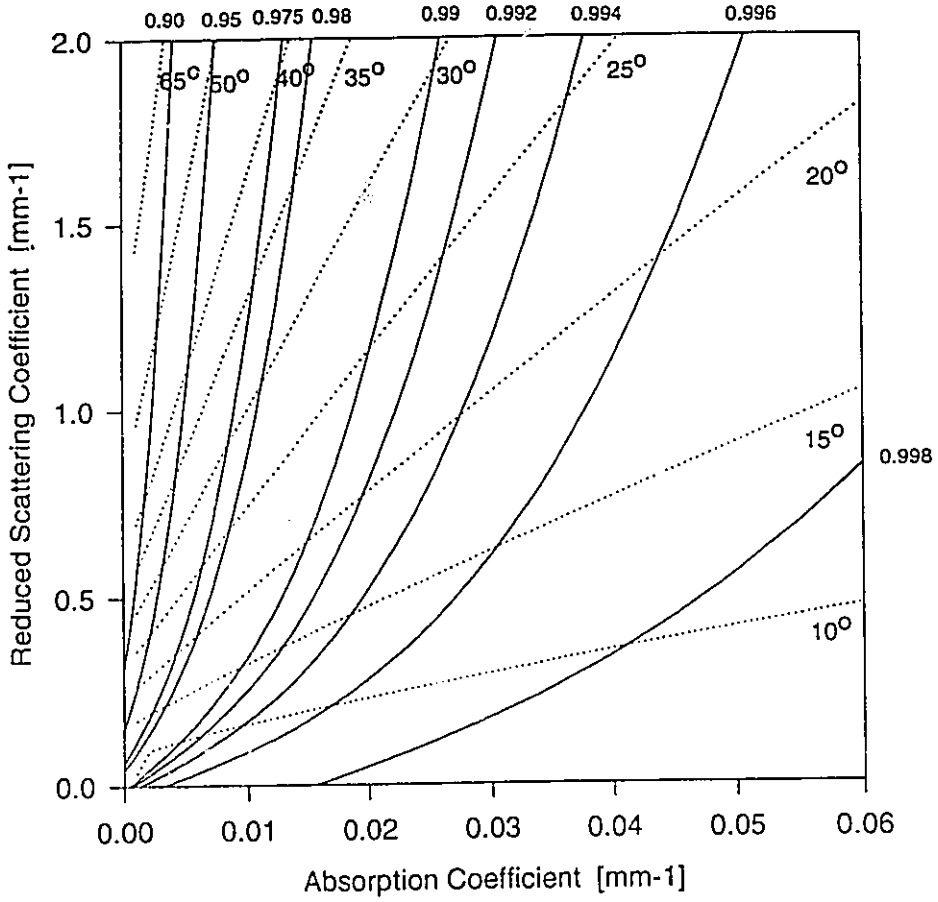

Figure 2.3 Theoretical calculation of lines of constant phase and modulation, as a function of μ_a and μ_s', for extrapolated boundary semi-infinite medium. Modulation frequency was 140 MHz, and source-detector distance was 20 mm.

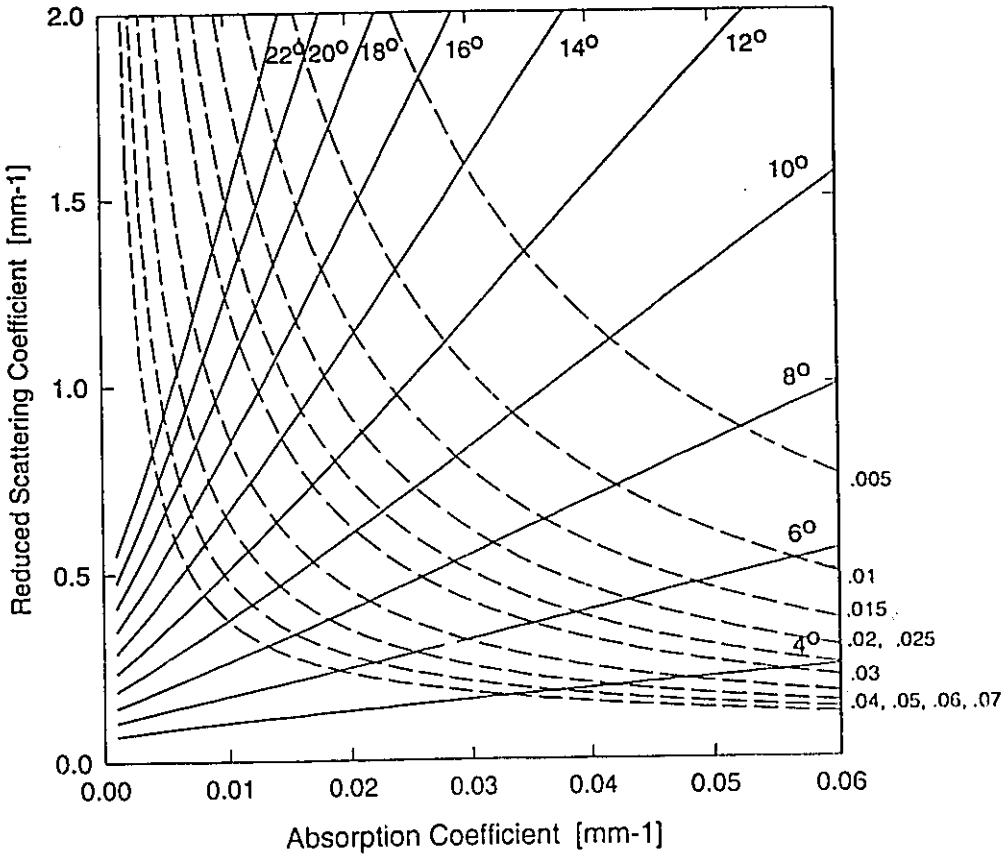

Figure 2.4 Theoretical calculation of lines of constant phase difference and intensity ratio, for two detectors located at 10 mm and 20 mm from the source, for extrapolated boundary semi-infinite medium. The modulation frequency was 140 MHz.

2.2.3 Examination of parameter dependence

The preceding discussion applies only to the specific frequency and distances chosen. In order to illustrate the effects of these parameters, phase and modulation are plotted as functions of frequency in figures 2.5 (a) and (b). Figure 2.5 (a) is plotted for $\mu_s' = 1.24$ mm^{-1}, and $\mu_a = 0.0004$, 0.01, and 0.02 mm^{-1} at a fixed source-detector distance of 10 mm. Figure 2.5 (b) has the same parameters except the distance is 30 mm.

Phase and modulation are non-linear functions of both frequency and distance. Assuming that the optical properties used in this graph are typical for tissue, it can be seen that increasing the distance from 10 mm to 30 mm will increase the dynamic range for both the phase and modulation. The larger dynamic range of these values means that the observable change in phase and modulation is larger for changes in μ_a and μ_s' of the medium. Also, increasing the modulation frequency can increase the dynamic range available, but there is a limit since at high frequency the dynamic range begins to decrease again. The optimum dynamic range is different for each frequency and distance. In general the most useful frequencies will be between 100 MHz and 1 GHz, for typical distances of 10 to 30 mm. A compact high frequency tissue spectroscopy system has been developed by Madsen *et al* (1995), which could be used at smaller distances. In future systems for tissue spectroscopy it is important to use as high a frequency as possible (under 1 GHz), and as large a distance as possible without introducing other boundary problems. However the limitation at higher frequencies is usually the expense of the system.

DC intensity is an easier observable to predict as it is attenuated almost exponentially with distance for distances greater than a few millimetres. Since relative intensity is always measured, the only limitation is that the thickness of tissue must be

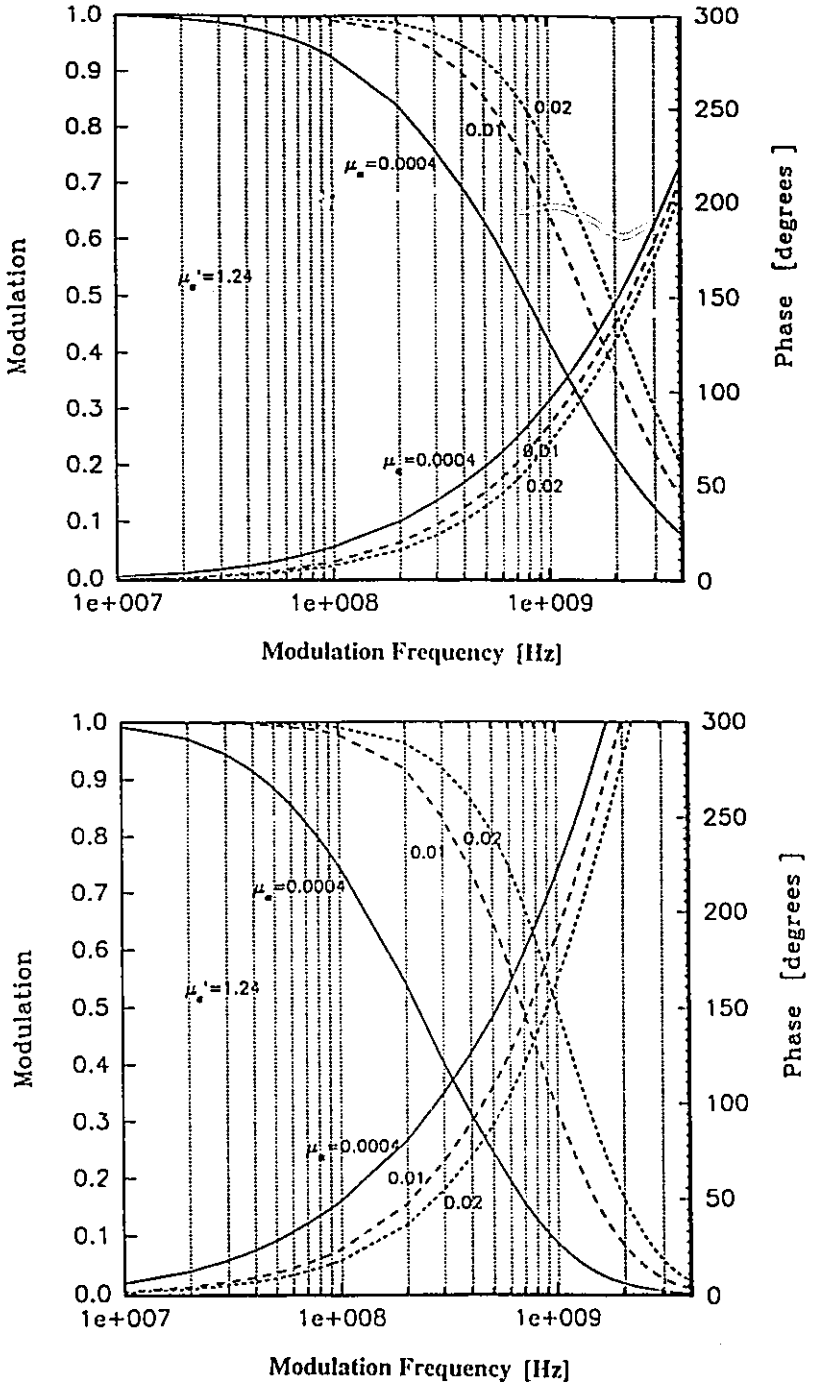

Figure 2.5 Theoretical calculation of modulation and phase for source-detector distance (a) 10 mm, and (b) 30 mm, for extrapolated boundary semi-infinite medium. The scattering coefficient was fixed at $\mu_s' = 1.24$ mm^{-1} for both. The three lines represent different absorption coefficients, $\mu_a = 0.004, 0.01, 0.02$ mm^{-1}.

small enough to allow useful transmission measurements. This thickness limitation is dependent upon the optical properties as well as the input light intensity and the efficiency of the detection system. The maximum tissue thickness can be estimated from the maximum incident light intensity which can be used, the lower limit of detectability, and the typical interaction coefficients of tissue. The intensity limit for near-infrared light exposure to tissue for medical applications is governed by the ANSI standards (Seuss, 1982), with maximum for long term exposure set to 1 W/cm^2. The minimum signal which will provide a useful signal to noise ratio using the Hamamatsu R928 photomultiplier tube corresponds to 10-100 picoWatts at the photocathode (estimated from paper #2 of this thesis). Therefore the attenuation must be 10^{10} or less. Assuming the attenuation predicted by diffusion theory for an infinite medium from equation 2.1, and typical values of μ_a and μ_s', 0.01 mm^{-1} and 1.0 mm^{-1}, respectively, the attenuation through 9 cm is approximately 10^{10}, as seen in figure 2.1. Therefore neglecting losses at the boundaries and losses at the fibres, the thickest tissue which could be probed with near-infrared light would be approximately 90 mm. Changes in the coefficients can increase the depth of penetration to perhaps 100 mm, however in order to observe a range of μ_a and μ_s' values it is probably better to take the more conservative estimate here.

2.3 Experimental system

2.3.1 Optical Source

Measurements of the type depicted in figure 1.2 are achieved with some readily available optical and radio frequency equipment. A schematic diagram of the apparatus used in this study is shown in figure 2.6. Several different light sources were used for excitation: an arc lamp for white light, or lasers for specific wavelengths. In order to

Frequency-Domain Spectroscopy System

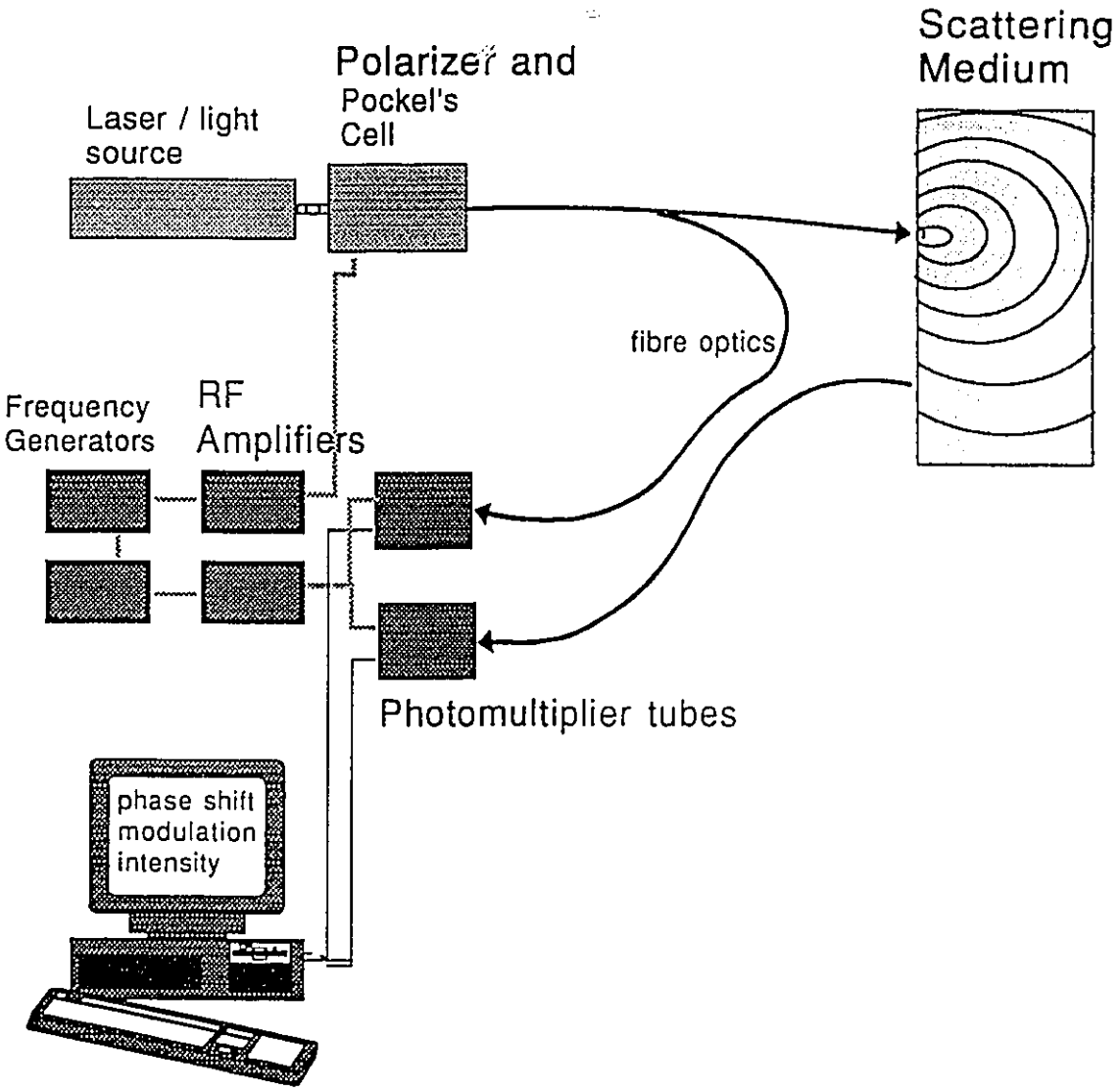

Figure 2.6 Schematic diagram of apparatus in the experimental system.

modulate the light intensity, a system from ISS Instruments (Urbana, Illinois) was used. The system used a Pockel's cell with the voltage modulated by an amplified radio frequency signal (Marconi Model 2022A). The light is polarized before doing a double pass through the Pockel's cell, and then passing through the polarizer again. The Pockel's cell rotates the plane of polarization of the light according to the voltage across the cell. When the light passes through the polarizer the second time, its intensity is modulated at the frequency applied from the RF generator. This light was focused into an optical fibre to illuminate the sample. In order to get a wavelength tunable source, a monochromator and associated optics were inserted before the entrance to the Pockel's cell polarizer system. This system could provide light with approximately 5% to 10% modulation for a white light source and up to 40% modulation for a columnated laser source.

Alternatively a diode laser can be used to generate the intensity modulated light, as it can be directly modulated by varying the current across the junction. The percentage of sinusoidally modulated light can be as high as 100% for a diode laser. Since diode lasers can provide high, stable power, they will likely be a robust method of producing frequency-domain light for clinical apparatus. Madsen *et al* (1995) have demonstrated a diode laser-based system which can operate at up to 1 GHz. Fantini *et al* (1994) demonstrated the use of very inexpensive light emitting diodes for this application, however presently they suffer from power limitations (approximately 1 mW) and relatively low modulation frequency ($f < 80$ MHz). The limitations of both LED's and diode lasers is that they exhibit reduced modulation at higher driving frequencies. The diode laser used in these studies could be modulated to about 300 MHz, with the RF amplifier being the main limitation.

2.3.2 Optical detection

Light was transmitted to and from the tissue phantoms with optical fibre bundles, 3 mm in diameter. Optical detection was performed with infrared sensitive photomultiplier tubes (Hamamatsu, R928) for both the reference channel and the sample channel (see figure 2.6). In order to measure the phase and AC intensity, a heterodyne detection system was used (Gratton *et al* 1983, Fedderson *et al* 1989). A DC bias of 1000 Volts was applied from cathode to anode and AC modulation of the gain was achieved by injecting an RF signal on the second dynode at a frequency 100 Hz greater than the source frequency. In this way, the signal could be detected at the difference frequency of 100 Hz, using a two channel A/D board in the lab computer. The two frequency generators and the A/D board were synchronized to the same 10 MHz clock.

The PMT housings were altered to include a filter wheel, so that attenuation or wavelength selection filters could be introduced between the fibre and the photocathode. The wavelength selection filters were necessary in order to eliminate unwanted fluorescent light in some measurements (see paper #2).

2.3.3 Signal processing

The A/D board (ISS instruments) digitized a 0.5 second segment of the 100 Hz wave train (containing 50 cycles), at 1024 kHz sampling frequency. This record was fast Fourier transformed to yield phase, modulation and DC intensity. In most cases 10 to 30 of these measurements were averaged in order to lower the variance of the measurement. It should be noted that much faster measurements have been made by Gratton *et al* (1995), by increasing the heterodyne frequency to the kHz range.

A thorough noise analysis of this system is presented in the next chapter. The

noise associated with the phase and intensity measurement can be quite small if the light intensity and modulation are high. Under typical conditions the signal to noise ratio is photon limited, so that the noise is proportional to the square root of the number of photons detected. The noise in the phase is inversely proportional to both the square root of the DC intensity and directly to the modulation.

2.3.4 Data inversion

Figure 2.3 demonstrates that for any combination of scattering and absorption coefficients (at a fixed frequency and source-detector distance) there is a unique phase and modulation pair. A similar mapping is true for phase difference and intensity ratio between two fixed detectors. Therefore, using diffusion theory it is possible to calculate the exact absorption and scattering coefficients of the medium from measurements of phase and modulation or phase difference and intensity ratio. In the present study, an iterative routine was used to calculate μ_a and μ_s' from either set of observables (Press *et al* 1992). A Newton-Raphson method was used to solve the non-linear equations for phase and modulation or phase difference and intensity ratio. This method uses an initial guess at the μ_a and μ_s' values and then calculates the appropriate derivatives in order to make the next estimate of μ_a and μ_s'. This routine was able to fit a single set of parameters in less than a second for most cases. The propagation of error from the measurements to the calculated optical properties was non-linear, and this is the subject of the second paper in the next chapter.

2.4 Measurements on Tissue-Simulating Phantoms

2.4.1 Tissue-simulating materials

In recent years there has been interest in developing materials which can be used to simulate the optical properties of tissue (van Staveren *et al* 1991, Flock *et al* 1992, Madsen *et al* 1992, Firbank *et al* 1994). By replacing tissue with a well controlled phantom, the calibration and testing of different optical systems can be done in a methodical way. One very common tissue simulating material has been Intralipid (Kabi Pharmacia, Quebec) or Liposyn (Abbott Laboratories, Montreal). Both of these are phospholipid emulsions in deionized water, manufactured for intravenous infusion. The optical scattering properties of this material are fairly well known and quite consistent between batches (Madsen 1992). A diluted solution of Intralipid was used to yield a transport scattering coefficient which was quite similar to human soft tissue in the near-infrared. The intrinsic absorption coefficient of this suspension in the near-infrared is due almost entirely to water. In order to raise the absorption to that typical of tissue, India ink was added to the solution. India ink has an absorption spectrum which is relatively constant with wavelength in the near-infrared region (Madsen *et al* 1991). In other experiments some molecular absorbers were used to increase the absorption coefficient or to introduce spectral features in the absorption coefficient (i.e. Aluminum Phthalocyanine, Nickel Phthalocyanine).

2.4.2 Experiment versus diffusion theory

Initial measurements were taken on a 1% mixture of Intralipid in a black lucite box of dimensions 20 x 20 x 20 cm. The sides of the box were far enough away to cause negligible boundary effects, and so the medium appeared essentially semi-infinite with

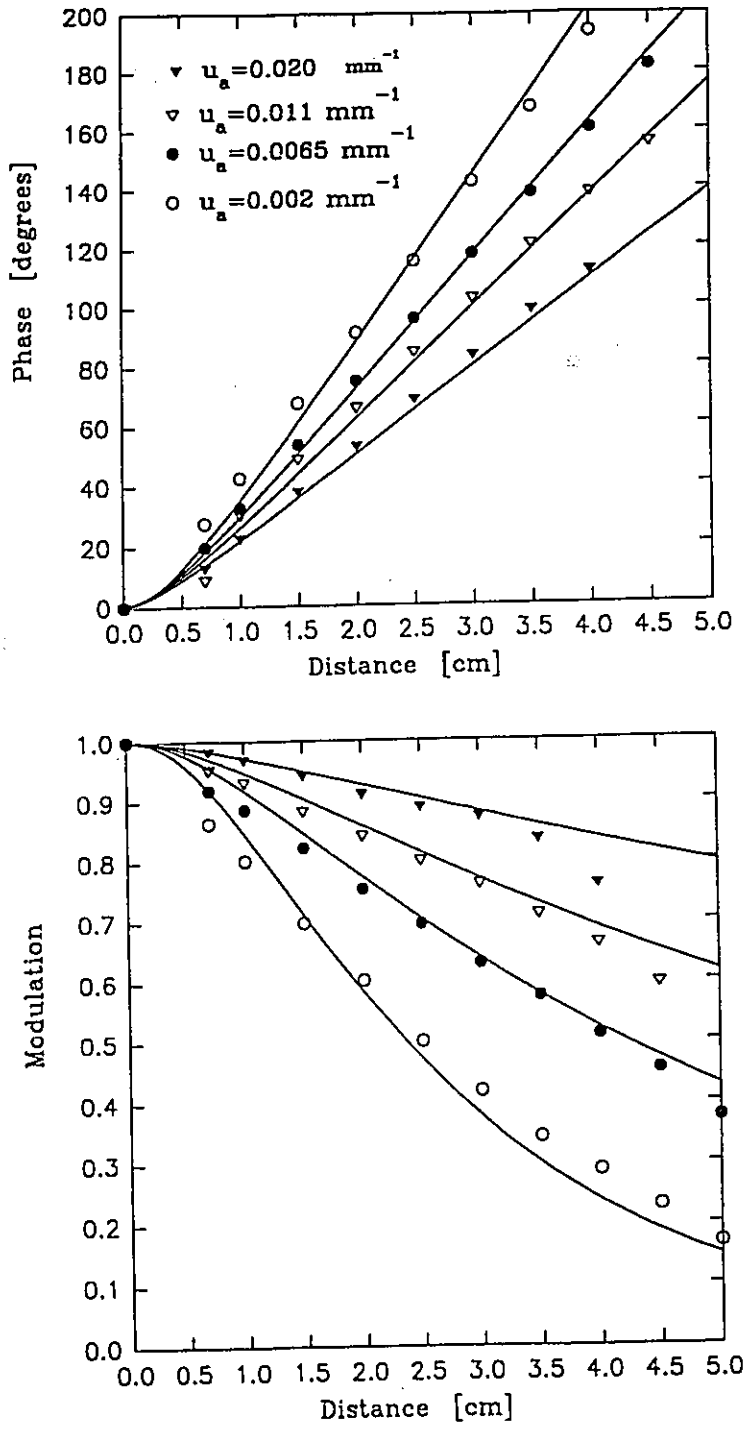

Figure 2.7 Experimental measurements of phase and modulation as a function of distance, along the surface of a 1% Intralipid. Four different concentrations of ink were used, 0, 9 ml, 18 ml, and 36 ml. The lines are best fits from extrapolated boundary semi-infinite diffusion theory.

only the upper air boundary being important. A diode laser, modulated at 300 MHz, was used as the light source at a wavelength of 751 nm, and power of 4.5 mW. Measurements of phase and modulation ratio were taken as a function of distance between the source and detector fibre bundles along the surface of the solution and are plotted in figure 2.7. The same measurements were taken for different amounts of India ink added to the phantom. The lines plotted on the graph are calculations based on the extrapolated boundary solution of diffusion theory, equation 1.17, using a best fit to all the data points. These measurements reaffirmed earlier studies that diffusion theory could be used to predict the phase and modulation measured on the surface of a tissue-simulating phantom (Patterson *et al* 1991a).

2.4.4 Spectral measurements

Spectrally resolved measurements required the use of a wavelength tunable light source, so that the arc lamp and monochromator system was used. The modulation frequency of the Pockel's cell was limited to 150 MHz for these studies, with 5% of the light intensity modulated. The available light could be tuned from 400 nm to 850 nm, with a resolution FWHM of 12 nm, and an output intensity at the fibre of 0.01 mW in the 12 nm bandpass.

Semi-infinite phantoms of 1% Liposyn were used as a subject material. The phase and modulation were measured at a fixed source-detector distance of 10 mm, at 20 nm wavelength intervals. These were used to calculate the values of μ_a and μ_s' based upon the diffusion theory solution, which are plotted in figure 2.8. Similarly, measurements of phase difference and intensity ratio were taken for two detector positions of 10 mm and 20 mm. These values were used to calculate μ_a and μ_s' and are plotted on the same graph.

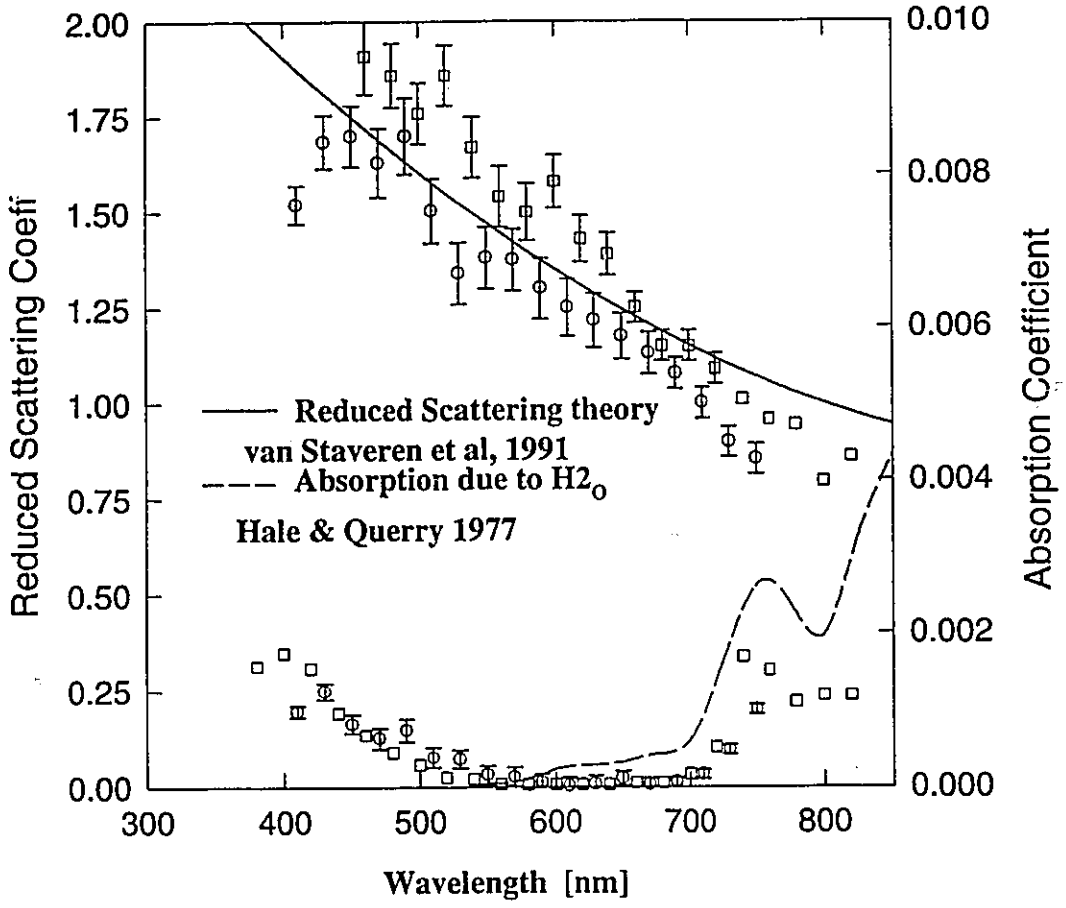

Figure 2.8 Experimental measurements of μ_a and μ_s' versus wavelength, for 1% Liposyn. Measured in the semi-infinite geometry with both phase-modulation (circles) and phase-intensity (squares).

The scattering values predicted by van Staveren *et al* (1991) are plotted on the same graph as a solid line, and the absorption value due to pure water is also included as the dotted line. There was agreement between the different scattering measurements with an estimated error of 15% to 20% overall. The measurement variability between any two spectral measurements was closer to 10%, while the variability between different measurement sets was higher. This systematic difference suggests that there may be differences in the intralipid content of the two batches or that there was a systematic difference in the measurements. Either one of these two problems is possible. The systematic problem associated with the phase and modulation measurement is the normalization of the measurements to the zero distance value. This measurement is taken with the source and detector fibres placed in contact with each other. The major problem with this measurement was that the light has different modulations and phases across the face of the fibre bundle, so that small shifts in the alignment of the two bundles can cause changes in the reference phase and modulation. If the normalization phase and modulation values have an error then this propagates as a systematic shift in all of the measurements. For this reason the two detector system which requires no separate reference measurement is suggested as the more useful geometry.

The other problem with the data in figure 2.8 is that the absorption coefficient of the material is lower than that of pure water, which is clearly not possible if the phantom is 99% water. The general shape of the absorption coefficient spectrum is similar to the theoretical water spectrum of Hale and Querry (1973). The source of this discrepancy has not been conclusively identified, but later measurements made with a totally absorbing mask on the surface had better agreement with the water values. It is possible that light channelling along the surface layer of water had added to the signal. This sort of light

channelling in lipid suspensions has been observed by others such as Fantini *et al* (1994) and Yoo *et al* (1990).

2.4.5 Independent comparisons

Measuring the absolute optical scattering and absorption coefficients is not trivial. While the measurements here seem to be accurate, there is the general problem of knowing whether the values are really correct. Ideally there should be an accepted method of measuring scattering and absorption which could be used as a precise reference. There are several different methods which can be used to estimate these values however each of them may have up to a 10% or more error associated with them. For Intralipid, the accepted theoretical values for the scattering coefficient have been those generalized from the semi-empirical equation derived by van Staveren which is a calculation based on Mie scattering theory. Alternatively samples of polystyrene spheres could be used along with Mie theory calculation, since they are available in well calibrated sizes. The value of the absorption coefficient of India ink was simply taken from repeated measurements of diffuse reflectance and transmittance with a double integrating sphere apparatus (Jaywant *et al* 1992). While this is not the best method for deriving an absolute calibration it is the most practical approach at present. The goal of the next measurements was to compare the inter-system variability in measuring μ_a and μ_s'.

A comparison was made between measured values of μ_a and μ_s' for a series of reference solutions for three different optical systems. The first system was a double integrating sphere system (Jaywant *et al* 1992, Madsen 1993, Pickering *et al* 1993). With this system, a 1.6 mm sample of the material was used and a narrow columnated beam was directed onto one face of the solution. The diffuse reflectance and transmittance were

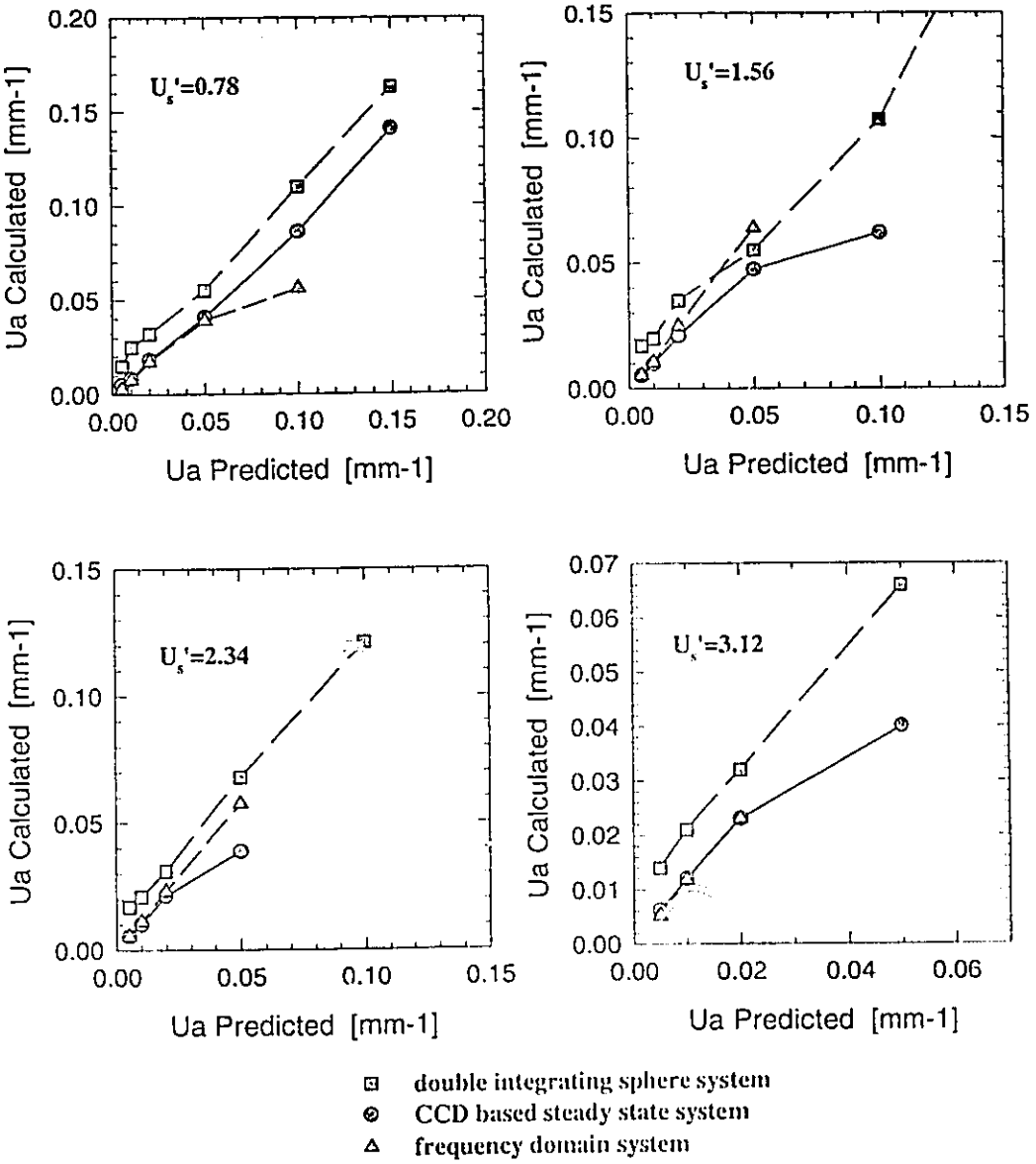

Figure 2.9 (a) to (d) Experimental measurements of μ_a for three different diffuse spectroscopy systems. The predicted value of μ_a was from a previous measurement with the double integrating sphere measurement system. μ_s' was (a) 0.78 mm^{-1}, (b) 1.56 mm^{-1}, (c) 2.34 mm^{-1}, and (d) 3.12 mm^{-1}. The wavelength used was 514 nm.

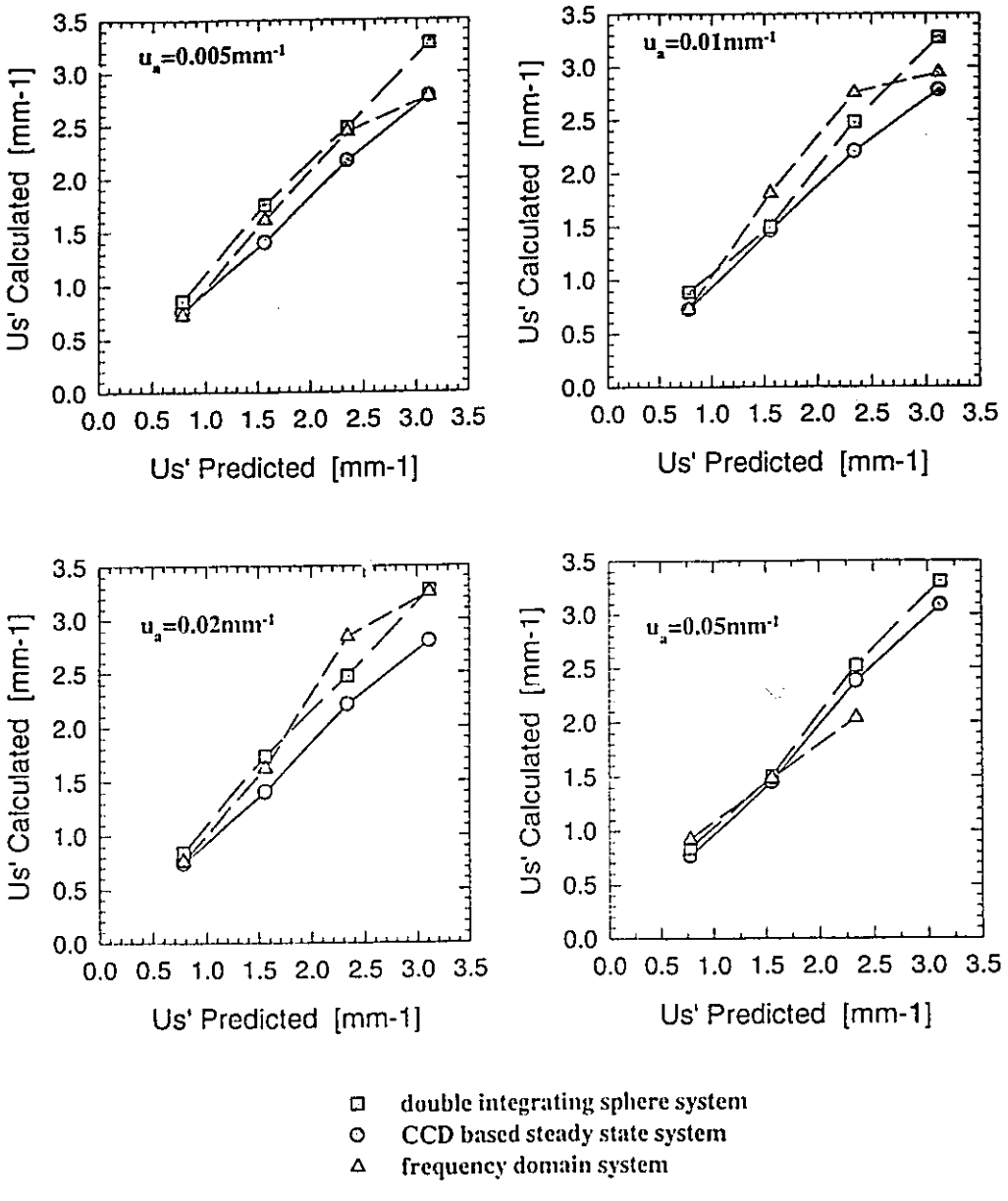

Figure 2.9 (e) to (h) Experimental measurements of μ_s' for three different diffuse spectroscopy systems. The predicted value of μ_s' was from van Staveren *et al* 1991. μ_a was (a) 0.005 mm^{-1}, (b) 0.01 mm^{-1}, (c) 0.02 mm^{-1}, and (d) 0.04 mm^{-1}. Conditions were the same as (a) to (d).

measured with integrating spheres on either side. Using these observed values, the absorption and scattering coefficients can be estimated from a series of Monte Carlo simulations which predict reflectance and transmittance for different μ_a and μ_s' values. The second system measured diffuse reflectance for steady state light at several different distances along the surface of a semi-infinite medium (Farrell *et al* 1991). Measurements are taken from a small probe containing 8 detector fibres at distances up to 10 mm from the source fibre. This system used calculated values of diffuse reflectance from diffusion theory to estimate the optical properties. The third system was the frequency-domain light system using diffusion theory to fit the measurements.

The wavelength was fixed at 514 nm for all three systems. The predicted reduced scattering coefficients were between 0.78 and 3.12 mm^{-1}, with absorption coefficients between 0.005 and 0.05 mm^{-1}. The measured results are plotted in figures 2.9 (a) to (h). Graphs (a) to (d) have the scattering coefficients fixed and show the μ_a predicted vs μ_a calculated for each experiment. Graphs (e) to (h) plot the predicted vs calculated μ_s' data with μ_a fixed.

There was a systematic shift in the double integrating sphere method's estimates of μ_a. Since absolute values of μ_a and μ_s' are difficult to measure for *in vivo* tissue, comparative measurements such as these on tissue-simulating phantoms are important to give some proof of their accuracy. Since all three systems yield similar values independently, it is likely that these values are authentic.

It should be noted that later tests of the same type did show some larger systematic differences between the systems, however each of the systems is quite susceptible to systematic errors in the measurements. One of the major systematic errors for the frequency-domain system was the presence of air bubbles on the surface within

the holes of the mask which is used to hold the fibres. It is difficult to eliminate these bubbles with liquid phantoms, and the use of solid tissue-simulating phantoms in the future will be a major benefit. Another problem with the frequency-domain system is that the Pockel's cell modulation is not spatially uniform, and so different phases are observed across the surface of the excitation source fibre bundle. A major improvement of the system would be to eliminate the Pockel's cell from the apparatus. This was done for many future measurements by using the diode laser.

Introduction to Paper #1

The following paper was a study of boundary effects which may be observed with frequency-domain tissue spectroscopy for finite tissue volumes. The paper was stimulated by the idea that spectroscopic measurements were being used by several groups for tissue oxygenation measurements (Duncan *et al* 1993, Franceschini *et al* 1993) using the semi-infinite expression for analysis of the interaction coefficients. It was not clear at the time how valid this expression would be for finite tissue shapes such as a forearm or a head. This paper was a systematic analysis of the errors which would be incurred in using the simple semi-infinite diffusion model for irregular tissue volumes. The main emphasis was to quantify errors in μ_a and to put limits on tissue thickness and tissue curvature for which the absolute μ_a errors would be acceptable. This type of analysis is essential when transferring a laboratory experiment to a clinical setting to estimate the systematic errors.

The theoretical calculations and experimental work were done by me under the supervision of Dr. Patterson. The diffusion theory calculations of cylinders and spheres in the time domain were completed with programs written by David Moulton. These time-series were then fourier transformed to provide frequency-domain data. The original manuscript was written by me and edited by Dr. Patterson.

Frequency-Domain Optical Absorption Spectroscopy of Finite Tissue Volumes using Diffusion Theory

Brian W. Pogue[1] and Michael S. Patterson[1,2]

1 Hamilton Regional Cancer Centre and McMaster University
699 Concession Street
Hamilton, Ontario, L8V 5C2, CANADA
2 Ontario Laser and Lightwave Research Centre
University of Toronto
Toronto, Ontario, CANADA

Short Title: Frequency-Domain Tissue Absorption Spectroscopy

Frequency-Domain Optical Absorption Spectroscopy of Finite Tissue Volumes using Diffusion Theory

Abstract : The goal of frequency-domain optical absorption spectroscopy is the non-invasive determination of the absorption coefficient of a specific tissue volume. Since this allows the concentration of endogenous and exogenous chromophores to be calculated, there is considerable potential for clinical application. The technique relies on the measurement of the phase and modulation of light which is diffusely reflected or transmitted by the tissue when it is illuminated by an intensity modulated source. A model of light propagation must then be used to deduce the absorption coefficient. For simplicity, it is usual to assume the tissue is either infinite in extent (for transmission measurements) or semi-infinite (for reflectance measurements). The goal of this paper is to examine the+wrrors introduced by these assumptions when measurements are actually performed on finite volumes. Diffusion theory calculations and experimental measurements were performed for slabs, cylinders and spheres with optical properties characteristic of soft tissues in the near infrared. The error in absorption coefficient is presented as a function of object size as a guideline to when the simple models may be used. For transmission measurements, the error is almost independent of the true absorption coefficient, which allows absolute changes in absorption to be measured accurately. The implications of these errors in absorption coefficient for two clinical problems - quantitation of an exogenous photosensitizer and measurement of haemoglobin oxygenation - are presented and discussed.

1. Introduction

Near Infrared Spectroscopy (NIRS) of tissue is a diagnostic tool which has several potential clinical applications. In particular, it has recently been investigated for measuring blood oxygenation (Brazy *et al* 1985, Cope *et al* 1988, Chance *et al* 1988, Sevick *et al* 1991, Ferrari *et al* 1992, Wilson *et al* 1993) and for dosimetry during photodynamic therapy (PDT) of cancer (Wilson *et al* 1993, Patterson *et al* 1990, Wilson *et al* 1990). In both applications, it is important to have methods of measuring the optical absorption in tissue due to endogenous chromophores (such as melanin, haemoglobin and cytochromes) or exogenous chromophores (such as PDT photosensitizers), so that the concentrations of these chromophores can be estimated. Time-resolved or frequency-domain techniques which incorporate a model of light transport can determine absolute scattering and absorption coefficients of uniform tissue from a measurement at a single point (Ferrari *et al* 1992, Wilson *et al* 1993, Patterson *et al* 1990).

Jobsis (1977) first noted that the spectral absorption of both haemoglobin and cytochrome aa_3 (which are affected by oxygen concentration) could be observed *in vivo* with near IR transillumination. Brazy *et al* (1985) showed that this method could be used as a monitor for brain oxygen levels of newborn infants, and since then several groups have measured muscle and brain oxygenation with NIRS. However the absolute absorption coefficient of tissue cannot be directly determined from cw intensity measurements due to the large amount of light scattering in tissue. Delpy *et al* (1988), and Wyatt *et al* (1990) developed a method for quantifying changes in absorption coefficient due to changes in blood oxygen saturation by using a pre-measured differential

pathlength factor to account for the effect of multiple scattering. The use of frequency domain methods may eliminate the need for empirical calibration, or use of a standard pathlength factor for different tissue types. Clinical monitors could provide a relatively inexpensive and stable real-time monitoring system for large tissue volumes using diode laser sources and photomultiplier detection.

A variety of methods have been investigated to recover the absolute values of transport scattering and absorption coefficients, μ_s' and μ_a. Patterson et al (1989) showed that time-dependent diffusion theory accurately described the reflectance of short pulses of light injected into a semi-infinite tissue phantom. Similarly, frequency-domain diffusion theory calculations have been used to predict the reflectance signal resulting from a train of short light pulses (Patterson *et al* 1991a) or intensity-modulated cw light (Tromberg *et al* 1993). Moulton (1990) and Arridge *et al* (1992) have derived time domain diffusion theory solutions for several regular sample geometries, including infinite, semi-infinite, infinite slab, cylinder and sphere. Arridge *et al* have extended this development to provide solutions in the frequency domain.

While diffusion modelling with exact boundary conditions can be quite accurate, a practical problem limiting the use of time and/or frequency dependent tissue spectroscopy is that real tissue volumes are not simple geometries (see Figure 1) (i.e. spheres, cylinders, slabs, semi-infinite, or infinite media). For *in vivo* frequency-domain spectroscopy to be useful in a clinical setting, it is necessary to know when the regular geometric solutions of the diffusion equation can be applied. For example, large volumes of tissue may often be approximated by a semi-infinite medium (Figure 1 a) if all boundaries other than the surface produce a negligible effect on the detected signal, for measurements at the surface (Figure 1 b,c). This assumption may not be appropriate when

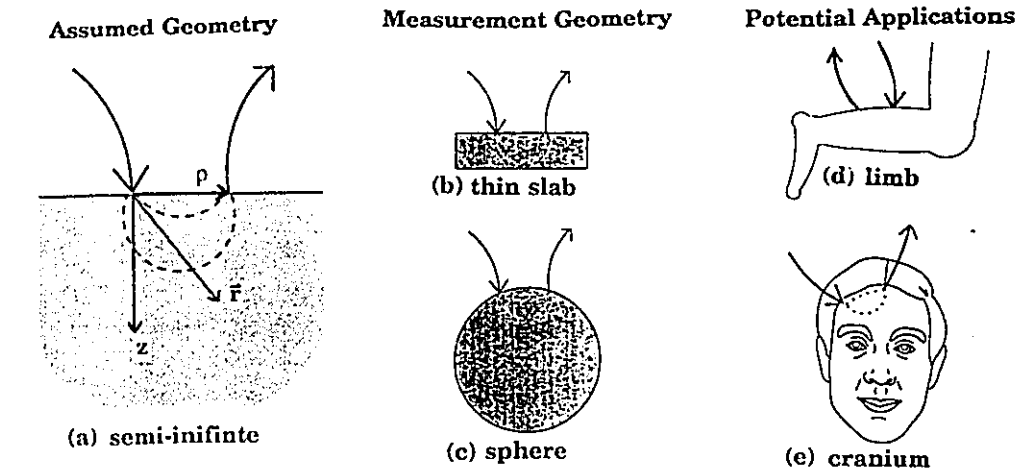

Figure 1 Geometries used in this study for reflectance and transmittance measurements. Reflectance data were generated for both thin slab (b) and sphere (c) geometries and the equations for a semi-infinite medium (a) are used to recover μ_a and μ_s'. This analysis has potential implications for samples such as limb (d) or cerebral measurements (e). Transmittance measurements for slab (h), sphere and cylinder (i) media are used with the equations for infinite (f) and slab (g) geometries. Again potential clinical applications are seen in (j) and (k).

the tissue surface is curved or when the tissue thickness is reduced (Figure 1 d,e). Similarly, when measuring in transmission mode, an infinite slab geometry can often be assumed (Figure 1 g), but for smaller tissue volumes, the lateral boundaries may produce significant effects (Figure 1 h,i,j,k).

In this paper the effects of finite volumes upon the estimation of μ_a values has been examined for a range of tissue optical properties and for different source-detector geometries. These results have been used to examine errors introduced by finite tissue volumes in the estimation of the concentration of an exogenous chromophore and in the measurement of haemoglobin oxygenation. The results provide some guidelines for applications of regular diffusion models for *in vivo* tissue spectroscopy.

2. Diffusion Theory Modelling

The transport of light within a highly scattering medium, such as tissue can accurately be described by radiative transport theory (Ishimaru 1989, Profio 1989). If the radiance within the medium is close to isotropic, then transport theory can be simplified to generate a diffusion equation for the fluence rate. Yoo *et al* (1990) showed that for tissue thicknesses greater than 10 mean free paths, diffusion theory provides an accurate prediction of the light fluence rate. The time-dependent diffusion equation is given by:

$$\frac{1}{c}\frac{\partial \Phi(r,t)}{\partial t} - D\nabla\Phi(r,t) + \mu_a\Phi(r,t) = S(r,t) \qquad (1)$$

Where $\Phi(\mathbf{r},t)$ is the fluence rate (in units of photons s^{-1} mm^{-2}) at any point $\mathbf{r}$, at time t, arising from the source function, $S(\mathbf{r},t)$ (units of photons s^{-1} mm^{-3}). Here μ_a is the

absorption coefficient (units of mm^{-1}) and D is the diffusion coefficient defined as $D = [3(\mu_a + \mu_s')]^{-1}$, where μ_s' is the reduced or transport scattering coefficient. This is defined as $\mu_s' = (1-g)\mu_s$ (mm^{-1}) where g is the average cosine of the scattering angle and μ_s is the anisotropic scattering coefficient. The fluence rate within a tissue volume depends non-linearly upon the optical coefficients of the volume, μ_a and μ_s', so the fluence rate is specified as $\Phi(r,t,\mu_a,\mu_s')$. A frequency-domain expression can be found, $\Phi(r,\omega,\mu_a,\mu_s')$, by Fourier transformation of the time domain solution or by solving the Fourier transformed diffusion equation. The expression for the fluence rate can be used to derive an expression for the photon current at the surface, $R(\rho,\omega,\mu_a,\mu_s')$ (in units of photons mm^{-2} s^{-1}), where :

$$R(\rho,\omega,\mu_a,\mu_s') = -D\ \nabla\Phi(r,\omega,\mu_a,\mu_s')|_{z=0} \qquad (2)$$

Reflectance corresponds to the observable measurement of photon current remitted from the surface of a scattering medium at a distance ρ from the source. For an infinite medium (Figure 1 f), the solution for the photon current radial from the source at r is:

$$R_\infty(r,\omega) = \frac{(1+kr)}{2(2\pi)^{3/2}r^2}\ e^{-kr-i\omega t} \qquad (3)$$

where k is a complex attenuation coefficient described by :

$$k = \left(\frac{\mu_a c + i\omega}{Dc}\right)^{1/2} \qquad (4)$$

Since the exact boundary conditions cannot be incorporated in diffusion theory (Lamarsh 1966), the effects of different boundary approximations have been examined in the literature (Patterson *et al* 1991b, Madsen 1992a). The simplest of these is to assume that the fluence drops to zero at the boundary, i.e. $\Phi(z=0) = 0$ for the semi-infinite case.

If the tissue is assumed to be semi-infinite with a totally absorbing boundary, the fluence rate must be zero at every point on the surface. This boundary condition was simulated with the method of images (Patterson *et al* 1991b), using a positive and negative source of photons below and above the surface, respectively. This approximation of two isotropic point sources simplifies the derivation of solutions for many boundary conditions. The isotropic sources of photons are located at a depth of $z_o = +/- 1/\mu_s'$, which is the transport mean free path for isotropic scattering. These assumptions lead to the photon current through a surface :

$$R_{\frac{\infty}{2}}(\rho_o, z_o, \omega) = \frac{z_o(1 + k\rho_o)}{(2\pi)^{3/2}\rho_o^3} e^{-k\rho_o - i\omega t} \qquad (5)$$

where $\rho_o = (\rho^2 + z_o^2)^{1/2}$. This fluence approximation, $\Phi(z=0) = 0$, is not physically accurate, yet it provides an adequate approximation for the reflectance for some situations. However, a more realistic estimate of the fluence can be made by assuming that the fluence is zero at an extrapolated boundary which is at a distance z_e beyond the physical boundary. In diffusion theory z_e is given by $z_e = 2D/\kappa$, where κ is a constant which depends on the refractive index mismatch, approximately equal to 0.4258 for a tissue-air interface (Moulton 1990, Keijizer *et al* 1988). In all the calculations in this paper, the extrapolated boundary condition has been used.

The expressions for semi-infinite and slab extrapolated boundary conditions can be written in terms of the photon current through a surface, equal to half of the zero fluence reflectance given above in equation 5. The semi-infinite reflectance is calculated from the contributions of a positive source located at a depth z_o, and a negative source located at $z_p = z_o + z_e$:

$$R_{\Sigma}(\rho,0,\omega) = \frac{1}{2}\left[R_{\Sigma}(\rho_n,z_n,\omega) + R_{\Sigma}(\rho_p,z_p,\omega) \right] \qquad (6)$$

where as above $\rho_n = (\rho^2 + z_n^2)^{1/2}$ and $\rho_p = (\rho^2 + z_p^2)^{1/2}$. Then the reflectance from the surface of a infinite slab, z=0, of thickness d, is :

$$R_{slab}(\rho,z=0,\omega) = R_{\Sigma}(\rho_n,z_n,\omega) + \frac{1}{2}\sum_{n=1}^{\infty}\left[\begin{array}{l} R_{\Sigma}(\rho_{+np},z_{+np},\omega) + R_{\Sigma}(\rho_{+np},z_{+np},\omega) \\ - R_{\Sigma}(\rho_{-np},z_{-np},\omega) - R_{\Sigma}(\rho_{-np},z_{-np},\omega) \end{array} \right] \qquad (7)$$

and the transmittance through the slab, at z=d, is given by :

$$T_{slab}(\rho,z=d,\omega) = \frac{1}{2}\sum_{n=1}^{\infty}\left[\begin{array}{l} R_{\Sigma}(\rho_{+np},z_{+np},\omega) + R_{\Sigma}(\rho_{+np},z_{+np},\omega) \\ - R_{\Sigma}(\rho_{-np},z_{-np},\omega) - R_{\Sigma}(\rho_{-np},z_{-np},\omega) \end{array} \right] \qquad (8)$$

where

$z_{+np} = nd + z_p$ $\qquad$ $\rho_{+np} = (\rho^2 + z_{+np}^2)^{1/2}$

$z_{-np} = nd - z_p$ $\qquad$ $\rho_{-np} = (\rho^2 + z_{-np}^2)^{1/2}$

It is interesting to note that the equations for the frequency-domain are often thought of as solutions describing photon density waves propagating through the medium [Fishkin et al. 1995]. From the equations above, k is a complex number equivalent to the effective attenuation coefficient of photon density waves in the medium. For steady state light (ω=0) the attenuation coefficient reduces to $k = (\mu_a/D)^{1/2} = (3\mu_a(\mu_s'+\mu_a))^{1/2}$.

The equations for spherical and cylindrical media are given in the frequency domain by Arridge et al. [1992] for the boundary condition of zero fluence at the surface, i.e. the extrapolated value is the radius. However, the extrapolated boundary calculations have been used here to better simulate a tissue air interface. Since extrapolated boundary

expressions are not available in the literature for the frequency domain, the time domain equations provided by Moulton were used to generate time series, which were Fourier transformed to give frequency domain data. The time domain expression for the reflectance from a sphere is:

$$R(r,\theta,t) = \frac{Dc\, e^{-\mu_a ct}}{2\pi r_s'^{2}(r_o r_s)^{1/2}} \sum_{m=0}^{\infty}\sum_{n=1}^{\infty} \left[\times \left(\left[\frac{\lambda_{nm}}{r_s'} - \frac{(2m+3)mr_s'}{\lambda_{nm} r_s^{2}} J_{m+3/2}\left(\lambda_{nm}\frac{r_s}{r_s'}\right)\right] + \frac{m}{r_s} J_{m+5/2}\left(\lambda_{nm}\frac{r_s}{r_s'}\right)\right)\right] \quad \textbf{(9)}$$

$$\times (2m+1)(\cos\theta)\, \exp\left(-\frac{\lambda_{nm}^2}{r_s'^{2}} Dct\right) \frac{J_{m+1/2}\left(\lambda_{nm}\frac{r_o}{r_s'}\right)}{\left[J_{m+3/2}(\lambda_{nm})\right]^2}$$

where r_s is the radius of the sphere, $r_o = r_s - 1/\mu_s'$, and $r_s' = r_s + r_e$. Here $P_m(x)$ are the Legendre polynomials and λ_{nm} are the positive roots of the cylindrical Bessel functions of the first kind, $J_{m+1/2}(x)$.

The time domain solution for reflectance from a finite cylinder is given by :

$$R(\rho_c,\theta,z,t) = \frac{Dc\Phi(z,t)}{\pi \rho_c'^{2}} \left[\times \left(\left[\frac{\lambda_{nm}}{\rho_c'} - \frac{2m(m+1)\rho_c'}{\lambda_{nm}\rho_c^{2}} \right] J_{m+1}\left(\lambda_{nm}\frac{\rho_c}{\rho_c'}\right) + \frac{m}{\rho_c} J_{m+2}\left(\lambda_{nm}\frac{\rho_c}{\rho_c'}\right)\right)\right] \quad \textbf{(10)}$$

$$\times \sum_{n=1}^{\infty}\sum_{m=0}^{\infty} (2-\delta_{m0})\cos(m\theta) \frac{J_m\left(\lambda_{nm}\frac{\rho_o}{\rho_c'}\right)}{\left[J_{m+1}(\lambda_{nm})\right]^2} \exp\left(-\frac{\lambda_{nm}}{\rho_c'} Dct\right)$$

where ρ_c is the radius of the cylinder, δ_{m0} is the standard Kronecker delta, $\rho_o = \rho_c - 1/\mu_s'$, and $\rho_c' = \rho_c + \rho_e$. Here $\Phi(z,t)$ is the one dimensional fluence distribution due to the ends of the cylinder, given by the expression :

$$\Phi(z,t) = \frac{c\, e^{-\mu_a ct}}{(4\pi Dct)^{1/2}} \sum_{n=-\infty}^{\infty} \left[\exp\left(-\frac{[z - z_o - 2nd']^2}{4Dct} \right) - \exp\left(-\frac{[z + z_p - 2nd']^2}{4Dct} \right) \right] \quad (9)$$

where d is the length of the cylinder and $d' = d + 2z_e$. The validity of these expressions has been checked with both Monte Carlo simulations and experimental measurements (Moulton 1990, Madsen 1992a, Madsen *et al* 1992b), from earlier studies. The change between the zero fluence boundary condition and the extrapolated condition was a few degrees in phase and perhaps a factor of 1% in modulation for most cases. The largest difference between the two models arises for small tissue volumes, and for small source-detector separations.

In frequency domain experiments there are three observables: steady state intensity, $I(\rho,\omega=0)$, phase shift, $\phi(\rho,\omega)$, and AC (or modulated) intensity, $I(\rho,\omega)$, where ρ is the distance between source and detector fibres, and ω is the modulation frequency. The most useful quantities are the phase shift relative to zero separation, $\phi(\rho,\omega) - \phi(0,\omega)$, and the modulation, $M(\rho,\omega)=I(\rho,\omega)/I(\rho,\omega=0)$, since they are both relative measurements taken at a single r value. Generally the goal is to determine μ_a and μ_s' from measurements of the phase and modulation, by solving the inverse of equations 6 - 8. This must be done in an iterative fashion by finding the values of μ_a and μ_s' which yield the phase and modulation equal to the experimental measurements. An exception to this is the infinite medium case, where simple analytic solutions are available for μ_a and μ_s'. For some of the more complicated models, such as the cylinder and sphere, it may be faster to use a pre-calculated look-up table or a trained neural network (Farrell *et al* 1992) rather than an iterative routine.

Some approximations have been made in the literature to generate analytic solutions for μ_a in terms of phase and modulation at low frequency, but these

approximations should be used with caution since they require $\mu_s c >> \omega$, which is only true for modulation frequencies, $f = \omega/2\pi$, much smaller than 500 MHz. In many cases, $\mu_s c$ is the same order of magnitude as ω, so that simplifications are not possible.

In this paper, theoretical data for phase and modulation have been generated for all of the different geometries using the extrapolated boundary conditions described by Moulton. The effects of finite volumes were examined with both experimental and theoretical data. Measurements can be made in either a reflectance geometry where source and detector are on the same surface of the object, or a transmittance geometry where they are on opposite surfaces. For reflectance measurements, the goal was to study the error introduced by using the simple semi-infinite expression, equation 6, in the analysis. To this end data were generated for slab, spherical and cylindrical objects, equations 7, 9 and 10 respectively, and analyzed with the semi-infinite model. Similarly in transmittance, data were generated for slab, spherical, and cylindrical geometries, equations 8, 9 and 10, and analyzed with the expressions for both an infinite medium and a slab. The benefit of using the infinite medium model in analyzing transmittance data will be more apparent upon examination of the results.

3. Methods

Diffusion theory solutions for the phase and modulation were compared to experimental measurements for sphere, slab, semi-infinite and infinite geometries, obtained with tissue simulating phantoms. All experiments were performed with a scattering medium composed of a lipid suspension with India ink added as an absorber. The lipid

suspension was a 1% mixture of Liposyn (Abbott Laboratories, Montreal) solids in distilled water, which has been shown to have a transport scattering coefficient similar to mammalian soft tissue (van Staveren *et al* 1991). The absorption of the suspension is essentially due to water for wavelengths between 600-850 nm (Wilson *et al* 1993, Hale *et al* 1973), so that ink was needed to provide a higher level of μ_a. The India ink absorption coefficient was measured by methods described in a previous paper, and did not significantly increase the scattering coefficient (Madsen *et al* 1992c). The infinite, semi-infinite and slab phantoms were contained in a 200x200x200 mm black lucite box, using movable walls for the slab and semi-infinite cases. This phantom was large enough that any boundary effects due to the walls could be neglected. The spherical phantoms were made with clear latex rubber balloons (rubber glove finger tips) inflated and filled with the scattering solution. The spherical phantoms were supported such that the difference in principal diameters was not more than 10-20% maximum. In most cases the optical properties were chosen to be $\mu_s' = 1.0$ mm^{-1} and $\mu_a = 0.01$ mm^{-1}, which are similar to typical values for human soft tissues (Cheong *et al* 1990). The maximum variation expected in muscle tissue oxygenation spectroscopy is μ_a=0.005 to μ_a=0.02 mm^{-1}, as calculated from the data of Wray *et al* (1988). The scattering coefficient for soft tissue can vary between μ_s'=0.6 and 2.5 mm^{-1} as a function of wavelength (Cope *et al* 1991), yet for a specific tissue type at a fixed wavelength the scattering coefficient does not change with tissue oxygenation (Wyatt *et al* 1990). The light source used was a 751 nm diode laser (Oriel Corp. Model#79401) directly modulated by a signal generator (Marconi 2202A) at f = 300 MHz. The light was delivered to and from the tissue phantom via fiber optic bundles of 3 mm diameter, and an additional fiber was used to deliver a reference signal (5% of the light). The detectors were IR sensitive

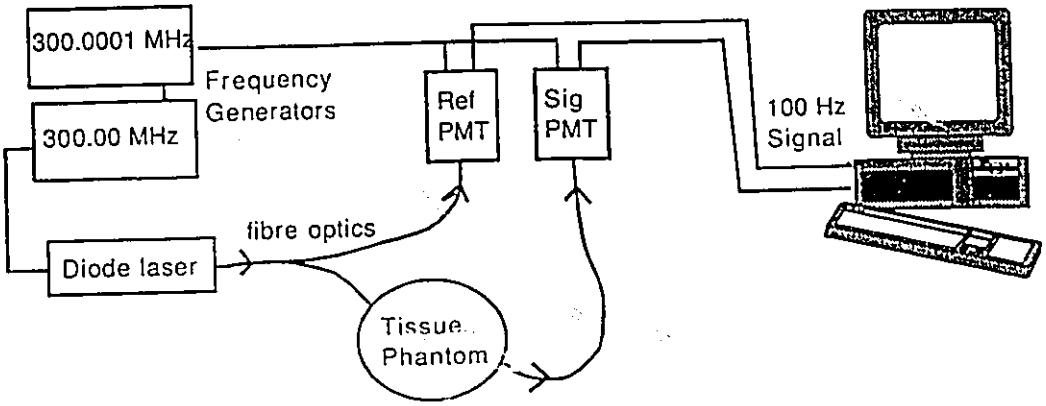

Figure 2 Schematic of frequency-domain system.

photomultiplier tubes (Hamamatsu Inc. Model# R928) which were gain modulated at 300.0001 MHz, to heterodyne the signal to a 100 Hz difference frequency (Gratton *et al* 1983). The signal could then be directly read by a A/D converter board in the lab computer, and relative intensity, phase shift and modulation were calculated. The apparatus is shown schematically in Figure 2.

Spectroscopic measurements were also made for phantoms containing methylene blue, as an example of an exogenous chromophore in tissue. The light source used for these spectral measurements was an arc lamp and monochromator system (ISS instruments), with the intensity modulated by a Pockel's cell and polarizer configuration. The maximum modulation frequency of this system, described in a previous paper, was 130 MHz (Patterson *et al* 1994). The fluorescence from the methylene blue was rejected by using a series of 10 nm bandpass filters matched to the excitation wavelength. The multiple filters were attached to the housings of the photomultiplier tubes with a scaled filter wheel. The absorption coefficient of the methylene blue in solution was independently measured in a spectrophotometer before addition of the scattering material. The details of the phantom measurements are discussed in the applications section.

4. Results

Figure 3 is a plot of phase shift and modulation for reflectance from both slabs of various thicknesses and spheres of various diameters, for a fixed source-detector separation of 30 mm. The points represent experimental measurements and the smooth lines represent the calculations from equations 7 and 9 for the optical properties, $\mu_a = 0.01$

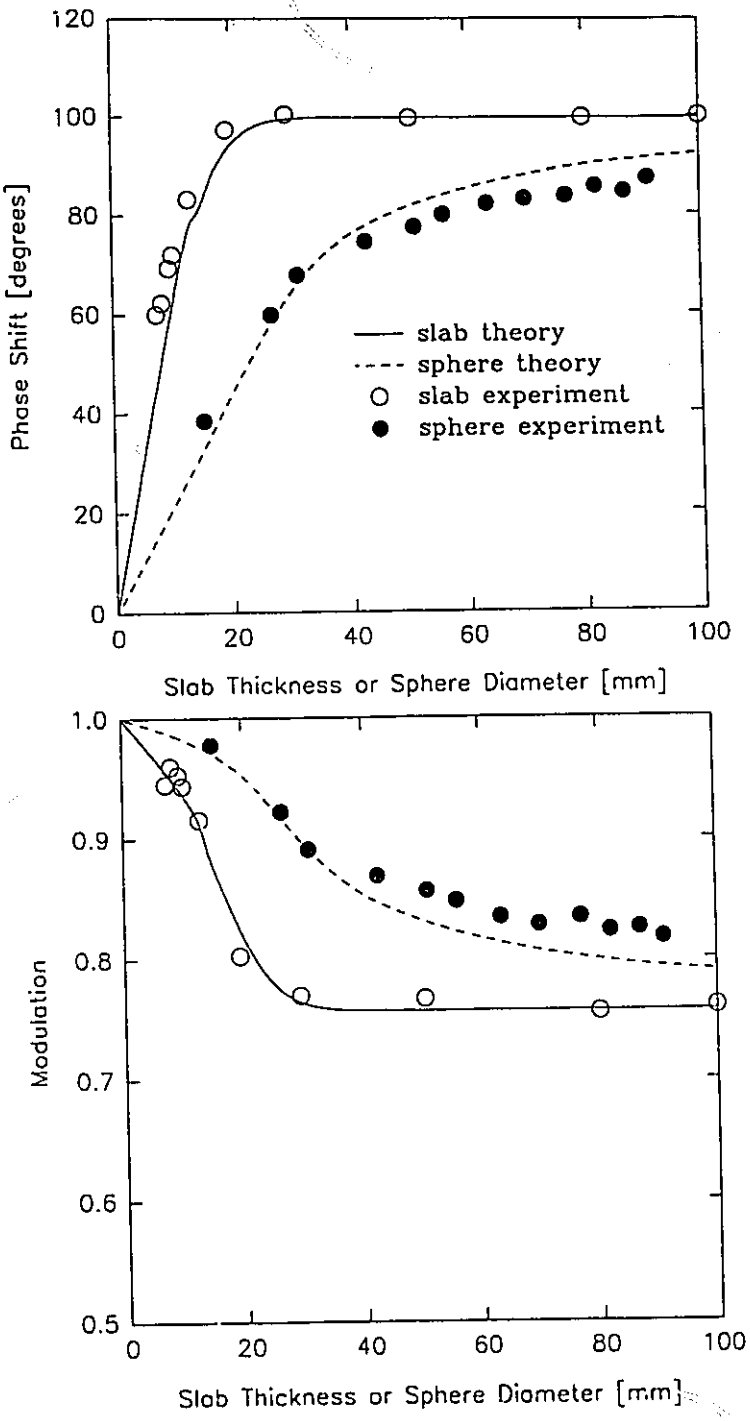

Figure 3 Reflectance measurements of phase and modulation for a source-detector separation of 30 mm, on tissue-simulating spheres and slabs of various thickness or diameter. (μ_s'=1.0 mm^{-1}, μ_a=0.01 mm^{-1}) The modulation frequency was f=300 MHz using 751 nm light. The smooth lines are plots of diffusion theory for the same optical

mm^{-1} and $\mu_s' = 1.0\ mm^{-1}$. Figure 4 is a similar plot, but for transmittance phase and modulation using an "infinite" phantom as well as slabs and spheres of various sizes. The source and detector were kept in the direct transmission geometry shown in Figure 1(f-i) (i.e. 180° transmission). The lines are calculations made with equations 3, 8 and 9. Figure 5 is the same as Figure 4, except no ink absorber was added to the phantoms, so that μ_a =0.0023 mm^{-1}, due to H_2O absorption only. The good agreement between experiments and diffusion theory solutions observed in (Figures 3, 4 and 5) provides the basis for using diffusion theory in subsequent calculations in this paper.

As described above, the phase and modulation measurements of Figure 3 were used to calculate μ_a and μ_s' of the medium assuming a semi-infinite geometry. The results of this analysis are plotted in Figure 6, for both experimental and theoretical data. Calculations from a true semi-infinite medium are shown as the horizontal lines at μ_s' = 1.0 mm^{-1} and μ_a = 0.01 mm^{-1}. The departure from the horizontal lines increases for smaller spheres and thinner slabs.

In Figure 7, the effects upon the μ_a estimate due to changing the source-detector distance have been examined for a thin slab. Phase and modulation were calculated for distances ρ=10 mm and ρ=50 mm, using μ_a = 0.005, 0.01, 0.02 mm^{-1} and a fixed μ_s'=1.0 mm^{-1}. The scattering and absorption coefficients were found by assuming the data to be from a semi-infinite geometry, and the departure from horizontal represents the error due to the slab's lower boundary.

The theoretical data for transmittance through a slab, sphere and cylinder has been used in Figures 8 and 9 to calculate observed errors in μ_a when either a slab or infinite model are assumed. Data was generated for the μ_a values of 0.005, 0.01 and 0.02 mm^{-1}, for a fixed μ_s' = 1.0 mm^{-1}. As above, the departure from the horizontal represents the

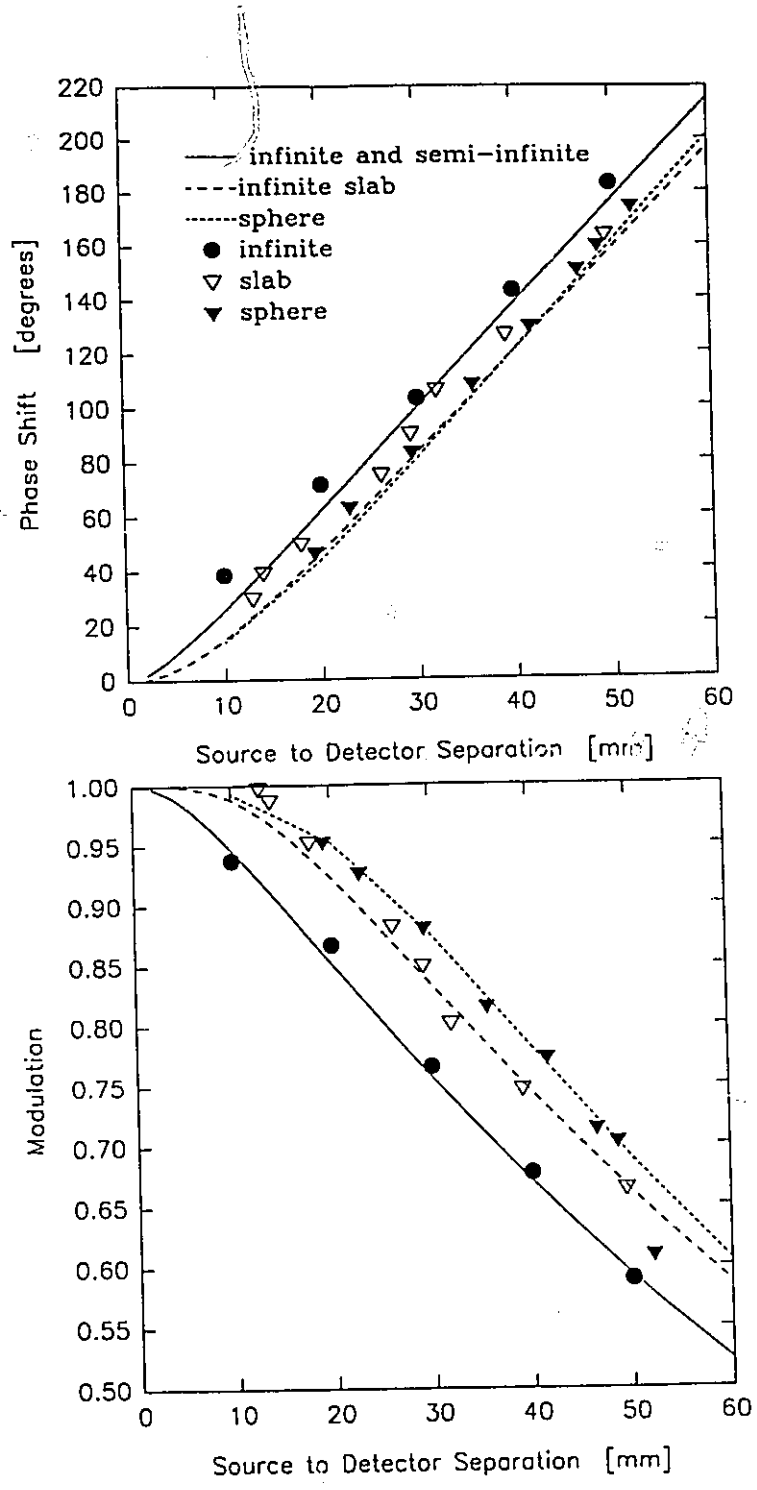

Figure 4 Transmittance measurements of phase and modulation for varying thicknesses of infinite, slab, and sphere tissue-simulating phantoms. (the same optical properties as Figure 3) The smooth lines are diffusion theory calculations.

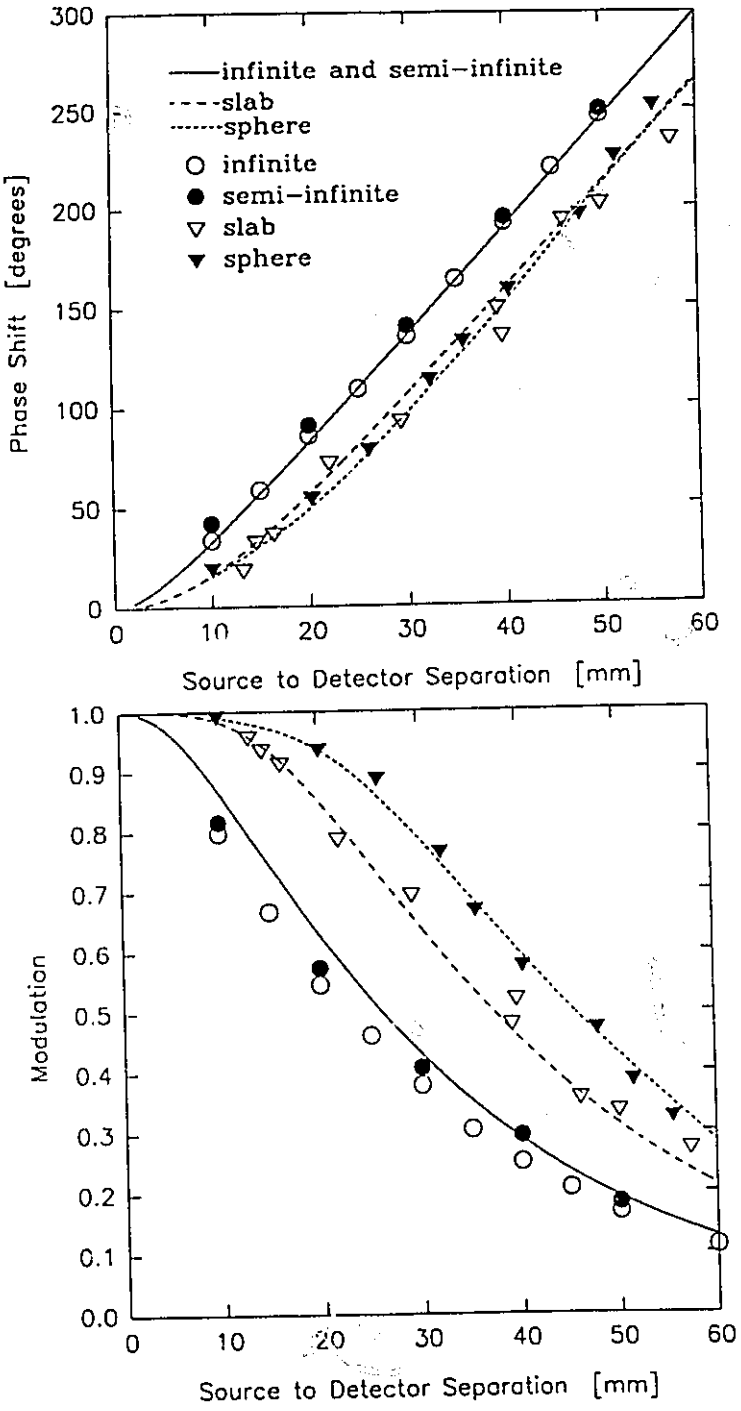

Figure 5 Transmittance measurements as in Figure 4 with optical properties $\mu_s' = 1.0\ mm^{-1}$, and $\mu_a = 0.0023\ mm^{-1}$.

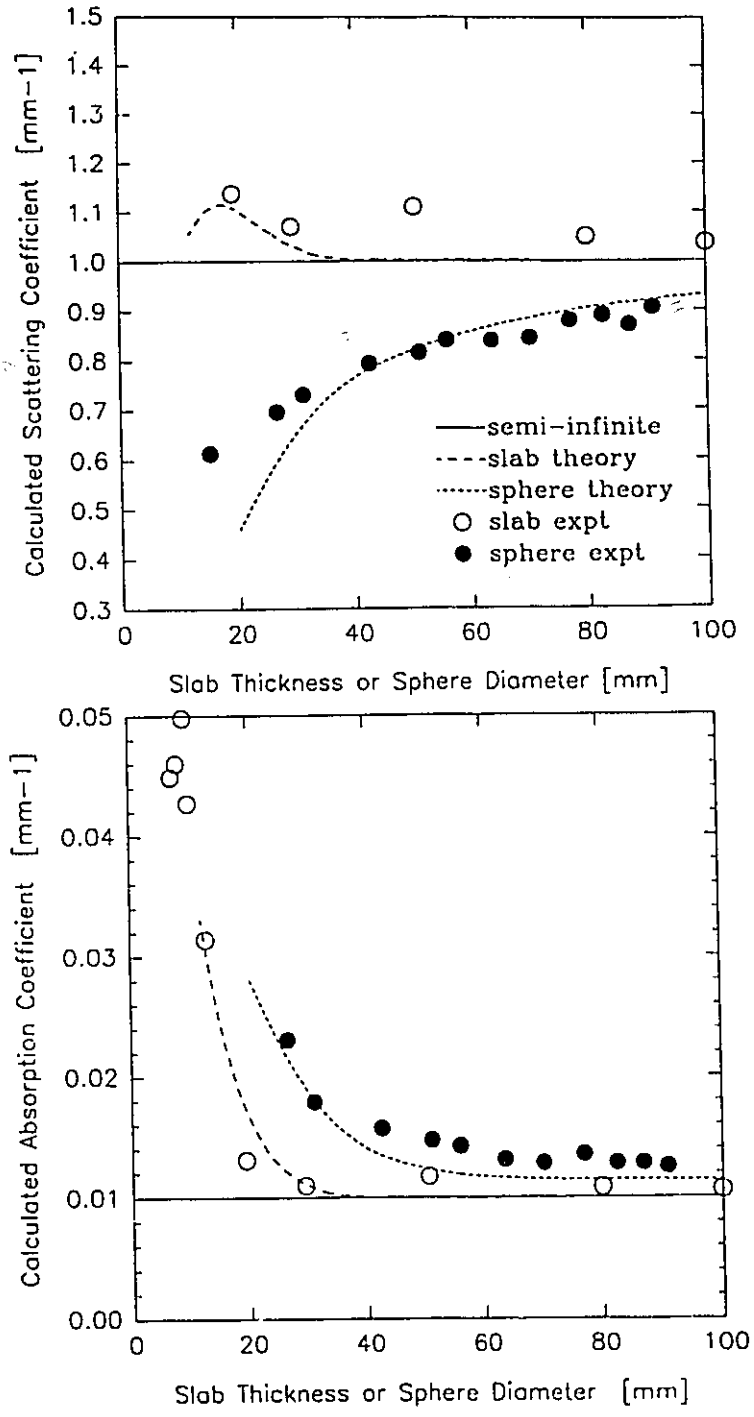

Figure 6 Derived absorption and scattering coefficients for the reflectance data of Figure 3, using the semi-infinite diffusion theory equations for phase and modulation for the analysis. The departure from the horizonal solid line represents error in the estimate.

error in the μ_a estimate.

5. Discussion and Applications

Thin Sample Reflectance

The distribution of paths that photons travel between a source and detector in a scattering medium can be greatly affected by changes in the boundaries or by the presence of inhomogeneities. The effects which would be created by an absorbing layer below the tissue surface are similar to those caused by reducing the thickness of the tissue sample (Figure 1 b). In both cases, long pathlength photons which would reach the detector are lost at the distal surface, so that a deep absorbing object or layer will cause the average photon pathlength to be reduced. Decreasing the average photon pathlength causes an overall decrease in the phase shift as seen in Figure 3 where phase reduces to zero for thinner slabs and spheres. Increasing the number of photons lost at the surface of the medium will also cause the modulation to tend to 1.0, as seen in Figure 3. These effects upon the phase and modulation, due to the boundaries, result in changes in the calculated μ_a and μ_s' values. For thick tissue slabs (here greater than 40mm) the calculated absorption and scattering coefficients are not significantly affected by the lower surface of the slab, as seen in Figure 6. However for thinner slabs, the lower surface causes a departure from the true absorption coefficient which increases with decreasing slab thickness, d. Diffusion theory and the experimental results agree to within 10-20%, however the consistency of the trend is perhaps more important here. Clearly the presence of an internal absorbing object or layer will result in an apparently increased absorption

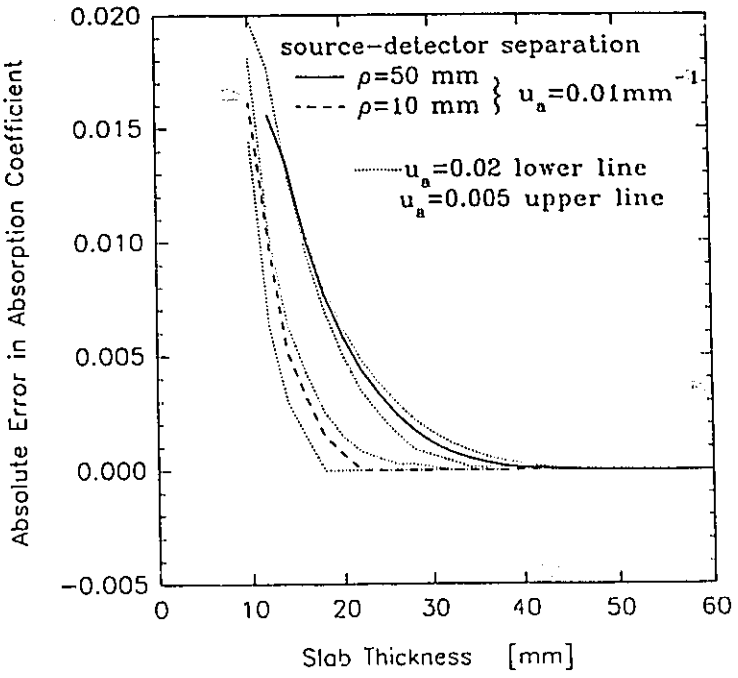

Figure 7 Error in the observed absorption coefficient is shown for a thin sample reflectance measurement, analyzed with the semi-infinite diffusion model. Two different source-detector separations were used, 10 and 50 mm. Three different absorption coefficients were examined. The values of μ_a were calculated for 3 mm increments in slab thickness.

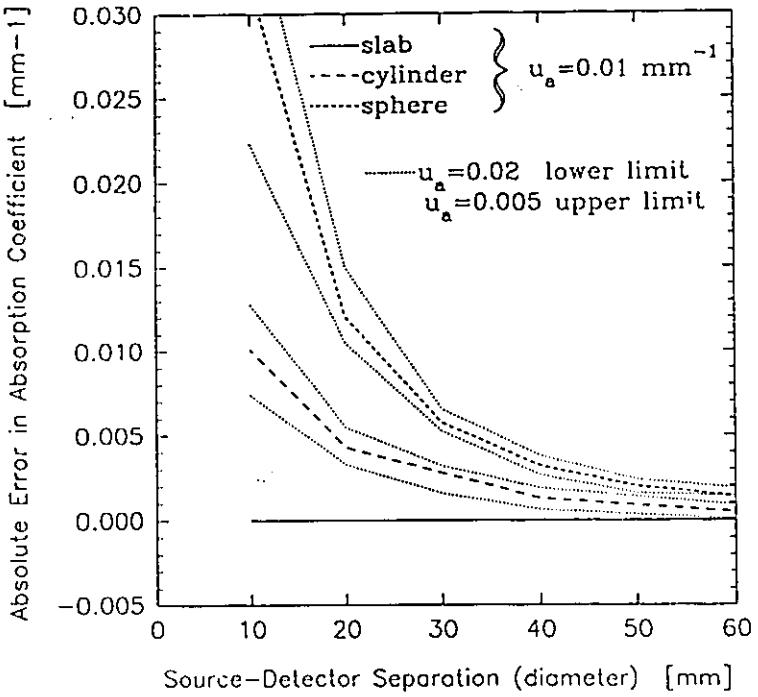

Figure 8 Error in the observed absorption coefficient due to interpreting transmittance data from tissue-simulating spheres and cylinders of various sizes with a slab diffusion model. In all cases μ_s'=1.0 mm^{-1} and the three μ_a values used were 0.02, 0.01, and 0.005 mm^{-1}. (f=300MHz) The values of μ_a are calculated for 10 mm increments in sphere and cylinder diameter

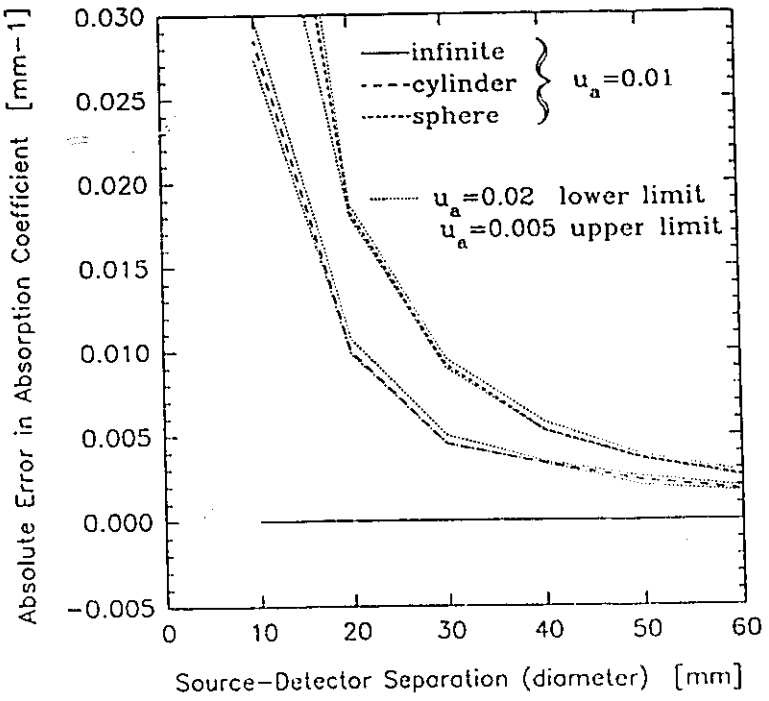

Figure 9 Error in the observed absorption coefficient due to interpreting transmittance data from tissue-simulating spheres and cylinders with the infinite medium diffusion model. Conditions were the same as in Figure 8.

coefficient and the depth of the object will significantly affect the magnitude of the change. There are many clinical situations where a measurement of the average μ_a and μ_s' values will be affected by layers of tissue such as skin, or by local inhomogeneities hidden within the tissue, such as blood vessels, and bones.

Several groups have noted that the separation of the source and detector fibers influences the average depth that the photons travel in sampling the tissue (Sevick *et al* 1992, Maier *et al* 1993). Therefore, the source-detector separation, ρ, will affect the μ_a value derived if the tissue is assumed to be semi-infinite but is not. From Figure 7, the effect of mistakenly treating a thin tissue as a semi-infinite volume can be seen. Examining the observed absorption coefficient for ρ=10 mm, significant (10%) departure from the true μ_a value occurs at d < 18-32 mm, whereas for ρ=50 mm, the overestimate in μ_a begins for slab thicknesses of d < 35-50 mm. The absorption coefficients were chosen to represent the typical values found in NIRS measurements. In summary, for typical tissue optical properties the minimum tissue thickness which could be analyzed with the semi-infinite reflectance technique is near 20 mm, when the source-detector separation is 10 mm.

The effect of a change in μ_s' was also examined, although the data have not been presented here. It was found that for a specific μ_a value, decreasing the μ_s' value of the sample would cause an increase in μ_a offset which would be proportional to $(\mu_s')^{1/2}$. This relation might be expected because the optical penetration depth of light scales with the optical properties of the tissues as $1/(3\mu_a\mu_s')^{1/2}$ for cw light, so that decreasing the μ_s' value of a sample allows more light to be lost at the tissue boundaries. Metabolic changes such as tissue oxygenation, do not alter the scattering value of a tissue sample nearly as much as μ_a. Therefore changes in μ_s' are not expected to be a large problem for tissue

oxygenation measurement.

The effect of modulation frequency upon the finite volume effects was also examined. Several researchers have mentioned that the depth of penetration of AC light intensity within tissue is a function of the modulation frequency (Sevick *et al* 1992, Maier *et al* 1993). The penetration depth for photon waves is given by 1/k where k is the real component of the attenuation coefficient

$$k = \left(\frac{\mu_a^2 + (\omega/c)^2}{D^2} \right)^{1/4} \cos\left[\frac{1}{2} \tan^{-1}\left(\frac{\omega}{\mu_a c} \right) \right] \qquad (12)$$

so that for higher frequencies the penetration depth will be reduced. The driving frequencies used in typical clinical situations would be below 500 MHz, although much higher frequencies can be obtained, with more expensive equipment. Measurement at higher frequencies reduces the average penetration depth of the photons and thus will decrease the error in μ_a due to lower boundaries. However, the strength of the frequency dependence is not enough to significantly reduce the boundary effects of the thin slab for typical tissue optical properties.

Curved Surface Reflectance

The effects of a curved boundary surface have been examined here by using phase and modulation data calculated from a spherical geometry (Figure 1 c) to calculate the μ_a and μ_s' values plotted in Figure 6. Similar to the thin slab case, the finite curved boundary results in an increase of the absorption coefficient, which is a direct result of photons being lost at the boundary and not accounted for in the semi-infinite equation. The observed value of μ_a tends to increase with decreasing radius of the object. The agreement between experiment and theory is not as good as anticipated, which could

possibly due to the phantoms taking more of an oblate spheroid shape causing more photons to be lost at the lateral boundaries. Perhaps more importantly, the expected trends in μ_a and μ_s' are observed. The value of absorption coefficient is always significantly different from the infinite medium case for the conditions examined here. However for the largest sphere (radius r = 50 mm), the overestimate in μ_a is only 10%, which is approaching a clinically acceptable error. The chord length was used in all of the calculations for μ_a and μ_s' as this gave a minimum error in μ_s', since the calculated μ_s' is more sensitive to the source-detector distance than the calulated μ_a.

The error in μ_a estimated from the reflectance measurement of a curved surface can be minimized by using a larger source-detector separation. Increasing the source-detector separation to the maximum possible (i.e. 180° transmission), minimizes the deviation of μ_a from the true value. This configuration allows the least interaction between the path of the photon waves and the exterior boundaries, thus minimizing the effects of the curved boundary. Note from Figure 5 that the differences in phase and modulation between the infinite and semi-infinite geometries are essentially insignificant, so that transmission through a distance z will give the same phase and modulation values as reflectance measurement across a surface at distance ρ.

The effects of the upper surface can also be minimized by using lower modulation frequencies. Lower frequencies have a higher penetration in tissue, so that the relative number of photon paths encountering the upper surface can be minimized with lower frequency photon waves.

Sample Transmittance

For an irregularly shaped tissue sample, it is often easy to perform transmittance

measurements across a section of the sample. The optical coefficients can be recovered by assuming that the transmittance is across an infinite slab of tissue, i.e. assuming that the lateral boundaries have no effect. The limits of this assumption have been examined here using spheres and cylinders as the objects. Data calculated from sphere and cylinder diffusion theory were used to solve for μ_a and μ_s' assuming a slab geometry and an infinite geometry, and the results are presented in Figures 8 and 9 respectively. One would expect the slab assumption to produce more accurate results, however there are certain advantages to using the infinite medium solution. In Figure 8, the slab model solution provided an offset in μ_a which was not constant for different real μ_a values. However when the same data were analyzed with the infinite medium model (as shown in Figure 9), the total error in μ_a is larger for a given object size, but the error in μ_a is not a strong function of the original value (i.e. the three μ_a values produce the same absolute error). This suggests that changes in μ_a with wavelength can reliably be measured with the infinite medium model since the boundaries will cause a nearly constant offset (i.e. μ_a(observed) = μ_a(real) + constant) for the range of μ_a values encountered in NIRS. The implications of this are examined in the applications section.

As in the case of a thin slab, the error in μ_a was found to change with μ_s' values of the scattering coefficient of the sample. The value of μ_a offset varied inversely with $(\mu_s')^{1/2}$. This variation should be expected since for lower scattering values more photons would reach the boundaries and leave the sample volume.

The frequency dependence was also examined for transmittance measurements. A change in the frequency had an even smaller effect in transmittance than in reflectance. To reduce the effect of lateral boundaries in transmittance, the highest frequency possible should be used, so that the AC light which reaches the detector has travelled the most

direct path. However, increasing the frequency from 300 MHz to 2 GHz, produced no significant improvement in the calculated μ_a. Using frequencies much lower than 300 MHz would cause an increase in the observed μ_a value, which would be more significant for smaller objects.

Transmittance measurements on large tissue volumes (i.e. diameter > 50 mm) such as a neonate head (Figure 1 b) can be used to recover the average μ_a and μ_s' values using the slab model solution from diffusion theory, with an error in μ_a on the order of 0.0001 to 0.001 mm^{-1}. The volume of a neonate head will exhibit the same boundary effects as the spheres and cylinders used in these simulations. An interesting result here has been that measurements across large tissue volumes, for example diameter > 100 mm, can be solved with any of the diffusion theory solutions with an error in μ_a of only 0.001 mm^{-1} from the real value. This result is very encouraging for oxygenation monitors, as well as possible near-infrared imaging applications, since it indicates an inherent insensitivity to boundary conditions for large source-detector separations. A NIRS computed tomography measurement could use the slab model to recover the μ_a values along the distribution of photon paths between source and detector, with a negligible error in μ_a, for large uniform tissue volumes. However, measurements on tissue volumes which are smaller than 100 mm in diameter must be handled with some judgement. There is no easy method of finding the appropriate boundary condition to use, so that each individual case must be examined. For example, approximation of an arm or leg by a cylindrical volume may be necessary for large source-detector separations.

One of the more surprising observations of this study is that phase and modulation data from transmittance across a small object can be solved with the infinite medium model, and the offset in μ_a due to the boundaries is not affected by the real μ_a value of the

tissue. This can only be true for a specific range of μ_a values, however for the range typically observed with *in-vivo* spectroscopy the offset is constant, as shown in Figure 9. This effect can be utilized to measure absolute changes in μ_a values due to changes in either chromophore concentration or wavelength, as further discussed below.

Spectroscopy and PDT dosimetry

The results shown in Figure 9, have important implications for spectroscopy of small tissue volumes when using a transmission geometry. It appears that changes in the absorption coefficient will not alter the constant offset in μ_a due to the boundaries, if an infinite geometry model is used to solve for the optical coefficients. This suggests that changes in μ_a can be accurately measured for arbitrarily small tissue volumes. As a result, changes in μ_a due to increasing levels of a photosensitizer could be measured, since the constant offset of μ_a due to the boundaries would not vary. Alternatively, the changes in μ_a with different wavelengths could be used to quantify the concentration of photosensitizer present in tissue. This hypothesis was tested in a tissue simulating phantom similar to that used in the previous experiments. Spectroscopic measurements were taken, in transmittance mode, of a spherical scattering phantom containing 1% Liposyn with 0.5 μg/ml methylene blue added to create a predictable spectral peak, shown as the dotted line in Figure 10. Before the blue absorber was added, measurements of phase and modulation were taken to recover the μ_a and μ_s' values of the solution, for the range of wavelengths used here, 560 to 760 nm. After the absorber was added, measurements of phase were used to calculate the μ_a value at each wavelength using the pre-measured value of μ_s'. The premeasured value of μ_s' had to be used here since modulation measurements become less useful for larger μ_a values. The ability to use the

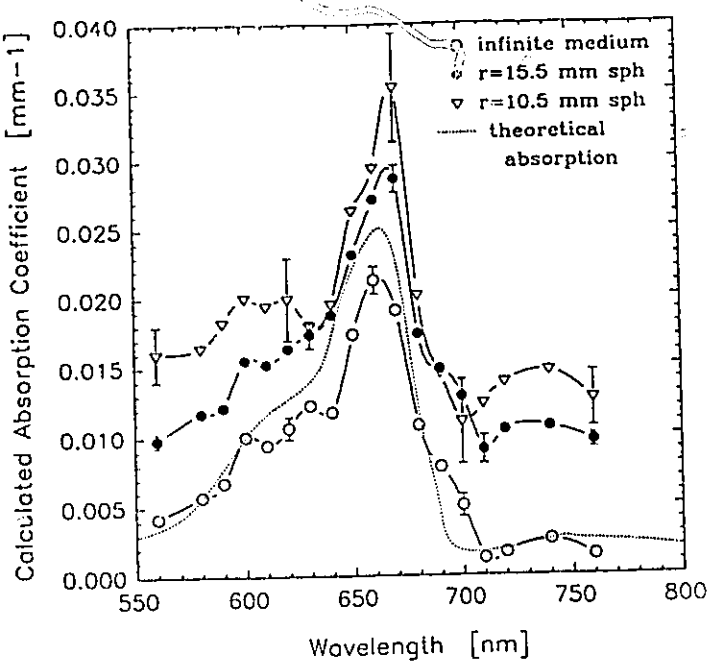

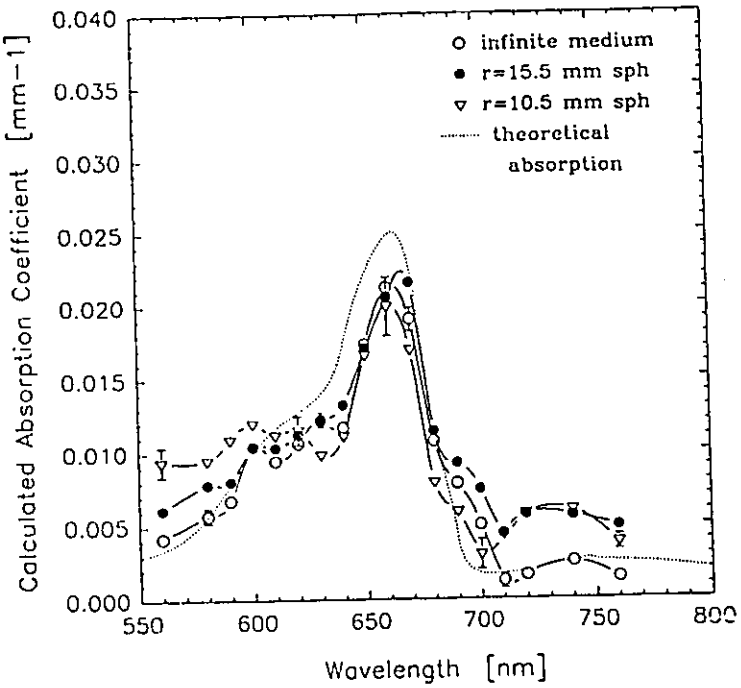

Figure 10 Measured absorption spectrum of 0.5 μg/ml Methylene Blue within a 1% Liposyn suspension in water. Spherical phantoms of diameter 31 mm and 21 mm were used along with a semi-infinite phantom. The dotted line represents the measurement of μ_s in a standard spectrometer before the addition of Liposyn. Phase measurements were taken in transmittance mode at a frequency of 130 Mhz.

(a) The data were used with an infinite medium diffusion model to solve for μ_s.

(b) The data were used with a slab diffusion model to solve for μ_s.

pre-measured value of μ_s' results in needing only one observable, phase, ϕ, to determine the absorption coefficient at any wavelength, i.e. $\mu_a(\phi,\lambda)$. The phase measurements were made at 10 nm increments, for two spherical tissue phantoms of radius 10.5 and 15.5 mm.

In Figure 10 a, the derived values of μ_a are shown for the two spherical phantoms as well as the "infinite" phantom. The methylene blue absorption peak measured with a spectrophotometer is shown on the same figure. As expected from the theoretical analysis shown in Figure 9, the increase in μ_a due to the boundaries of each object is constant, causing the whole μ_a curve to be offset from the real value. Within experimental error, the top of the absorption peak is offset by the same amount as the wings. Hence the methylene blue concentration could be accurately estimated regardless of object size by subtracting the background from the peak. In Figure 10(b), the analysis of $\mu_a(\Phi)$ was done with the slab model for the two spherical phantoms. All three μ_a values are much closer together on peak, however in the wings of the peak the three curves separate significantly. As expected from Figure 8, analyzing finite boundary data with the slab model yields an offset in the μ_a value which is not constant with changes in the real μ_a value. While using the slab model produces absolute measurements of μ_a which are closer to the true value, relative changes in μ_a are better analyzed by using the infinite medium model.

Further experiments have also been completed with scattering phantoms to directly measure the increase in μ_a due to adding aliquots of india ink. In each case the observed increase in μ_a was equal to the real increase in μ_a, within experimental error. The results of these studies imply that absolute changes in μ_a can be quantified for arbitrarily small tissue volumes using the transmittance phase measurement, and premeasured values of μ_a and μ_s'. For PDT dosimetry, injected levels of photosensitizers could be quantified in this

manner and further testing of this method during PDT studies with small animals is planned.

Blood Oxygenation Measurement

There has been considerable interest in using frequency domain measurements as a low cost method of monitoring blood oxygenation if the absorption coefficients due to oxygenated and deoxygenated haemoglobin (HbO_2 and Hb) can be measured *in-vivo*. Oxygen saturation, $Sa(O_2)$, of a tissue is defined as the percentage of Hb molecules oxygenated in the tissue :

$$Sa(O_2) = \frac{[HbO_2]}{[HbO_2] + [Hb]} \times 100\%$$

There are several chromophores which contribute to the absorption of near-infrared light in soft tissue, where the main changes in μ_a with oxygenation come from haemoglobin and cytochrome aa_3 (Wray *et al* 1988). The remaining absorption in soft tissue is mainly due to water (approximately 80% of soft tissue is water). Cope *et al* (1991) have developed sophisticated methods of recovering the concentration changes in Hb and HbO_2 by fitting multiple wavelength measurements of μ_a to a linear summation of measured absorption coefficients for all of the absorbers listed here. This method should produce a best estimate for the oxygen saturation, assuming all of the absolute absorptions coefficients of Hb and cytochrome aa_3 can be measured in purified form. Other attempts have suggested that the oxygenation saturation can be measured considering only the absorption due to haemoglobin and water (Sevick *et al* 1991, Wilson *et al* 1992). This calculation may be accurate if the absorption due to cytochrome aa_3 is insignificant, which is true if the concentration of cytochrome aa_3 is less than 10 to 20 μM in tissue, using the estimates

of μ_a from Wray *et al* (1988). Similarly the absorption due to water can be approximated by assuming a constant 80% concentration of water and tabulated values of $\mu_a(H_2O)$. The validity of these assumptions will be addressed later.

If the absorption is assumed to be due only to Hb, HbO_2 and water, then a measurement of $Sa(O_2)$ can be made with only two wavelengths. The two wavelengths chosen are often near the isobestic point for absorption by Hb and HbO_2 which occurs near 810 nm. Since the water contribution is known *a priori* (assuming 80% concentration), the calculation to find the concentrations of [Hb] and [HbO_2] is then a simple matter of solving a 2x2 matrix equation :

$$\mu_a(\lambda_1) = [Hb]\bullet\mu_a(Hb \text{ at } \lambda_1) + [HbO_2]\bullet\mu_a(HbO_2 \text{ at } \lambda_1)$$

$$\mu_a(\lambda_2) = [Hb]\bullet\mu_a(Hb \text{ at } \lambda_2) + [HbO_2]\bullet\mu_a(HbO_2 \text{ at } \lambda_2)$$

Since clinical monitors are presently being evaluated using this type of 2 wavelength system, it is important to examine the effects of a finite volume upon the measurement of tissue oxygen saturation. Small tissue volumes could significantly alter the accuracy of such a system as a decrease in signal due to photons lost at the boundaries would be interpreted as a higher μ_a value.

A two wavelength system was simulated here using data for λ_1 = 810 nm and λ_2 = 750 nm for typical tissue concentrations of water, Hb and HbO_2. Phase and modulation data were generated for spheres of different radii, assuming the absorption coefficients anticipated for 4 different oxygen saturation levels, $Sa(O_2)$= 90, 70, 50 , and 30%. These data were analyzed with the infinite medium model to calculate μ_a for the different objects. These μ_a values were then used to find [Hb] and [HbO_2] concentrations at each wavelength according to the equations above. In Figure 11 a, the data are plotted as $Sa(O_2)$ vs object size. If there was no finite volume effect on the derived absorption

coefficient, the lines of 90, 70, 50, and 30% would all be horizontal. However, it is observed that as the object size decreases, the calculated oxygen saturation departs from the true values. This departure comes directly from the tendency of the infinite model to overestimate μ_a for finite tissue volumes. In the limit of zero radius, the lines all converge to a single value, because both $\mu_a(\lambda_1)$ and $\mu_a(\lambda_2)$ will approach infinity due to the influence of boundaries. Clearly the value at zero radius does not have any physical meaning here, however the qualitative change in the observed $Sa(O_2)$ level indicates that 2 wavelength measurements cannot provide accurate measurement of $Sa(O_2)$ for small tissue samples (i.e. spheres of diameter < 100 mm). The implications of this for irregular tissue volumes is not as easily predicted, but there is a simple solution which eliminates the boundary errors.

Three measurement wavelengths can be used to remove the constant offset produced by the boundaries of the tissue sample. The problem becomes a 3x3 system of linear equations which is still relatively easy to solve :

$$\mu_a(\lambda_1) = [Hb]\cdot\mu_a(Hb \text{ at } \lambda_1) + [HbO_2]\cdot\mu_a(HbO_2 \text{ at } \lambda_1) + \mu_a(const)$$

$$\mu_a(\lambda_2) = [Hb]\cdot\mu_a(Hb \text{ at } \lambda_2) + [HbO_2]\cdot\mu_a(HbO_2 \text{ at } \lambda_2) + \mu_a(const)$$

$$\mu_a(\lambda_3) = [Hb]\cdot\mu_a(Hb \text{ at } \lambda_3) + [HbO_2]\cdot\mu_a(HbO_2 \text{ at } \lambda_3) + \mu_a(const)$$

The observed μ_a values derived in the example above were used with this 3x3 matrix to solve for the [Hb] and $[HbO_2]$ concentrations and the $Sa(O_2)$ values for different radii. In Figure 11 a, these values of $Sa(O_2)$ are plotted as the straight horizontal lines. This exercise demonstrates that finite volume effects can be removed from the measurements of $Sa(O_2)$ by assuming a constant absorption coefficient error is present due to the

boundaries and by using a 3 wavelength system to account for it. Here the wavelengths used were 750, 810, and 900 nm, which provide a stable solution since the values of $\mu_a(Hb)$ and $\mu_a(HbO_2)$ differ significantly across this range of wavelengths.

This has been a somewhat simple representation of tissue optical properties and some mention needs to be made of real tissues. As discussed above, the scattering coefficient was also found to affect the finite volume measurement of μ_a. Here the scattering coefficient, or the differential path-length, was assumed constant at all the wavelengths used for measurement. In Figure 11b the calculation of the oxygen saturation was repeated with data where the constant offset in μ_a has a gradient due to the change in μ_s' at the different wavelengths, which is proportional to $1/\lambda$. This calculation is presented for the same conditions as in Figure 11a. but here the values of μ_s' for the three wavelengths were 1.0, 0.93, 0.83 mm^{-1} for 750, 810, and 900 nm, respectively. This gradient in the μ_s' values produces a gradient in the μ_a offset. The effect of a changing μ_a offset with wavelength becomes a significant problem for objects of diameter less than 50 mm. The saturation levels drop to zero as the object gets smaller since the differences in μ_a offset between different wavelengths becomes greater and causes the system of equations to overestimate the value of [Hb]. This demonstrates that the finite volume effects cannot be exactly eliminated for arbitrarily small objects, however measurements will be approximately true for larger objects.

The current example is merely illustrative and is not proposed as a solution to solve all of the problems associated with measuring $\mu_a(\lambda)$, or $Sa(O_2)$ in small volumes. Some finite volume effects can be corrected for, yet this problem is perhaps overshadowed by the original preposition that a two wavelength measurement can actually measure oxygen saturation. The value of this simulation is to demonstrate that if the boundary

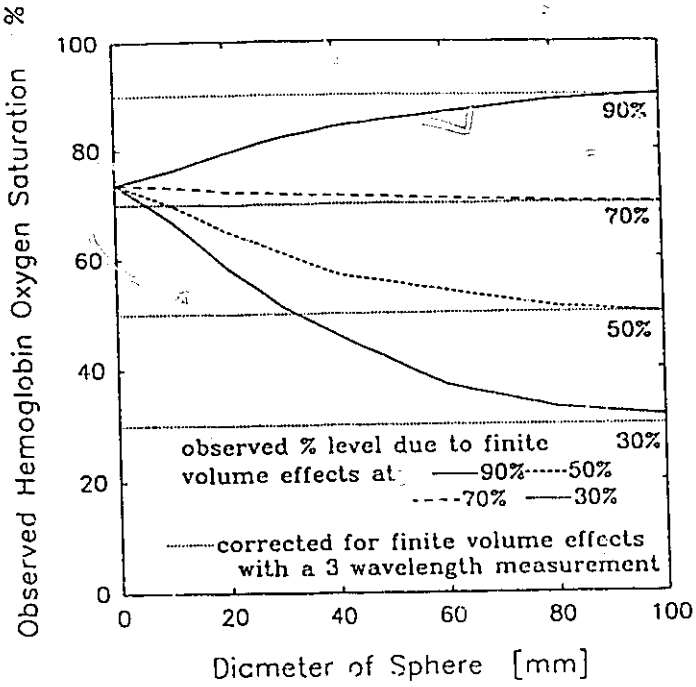

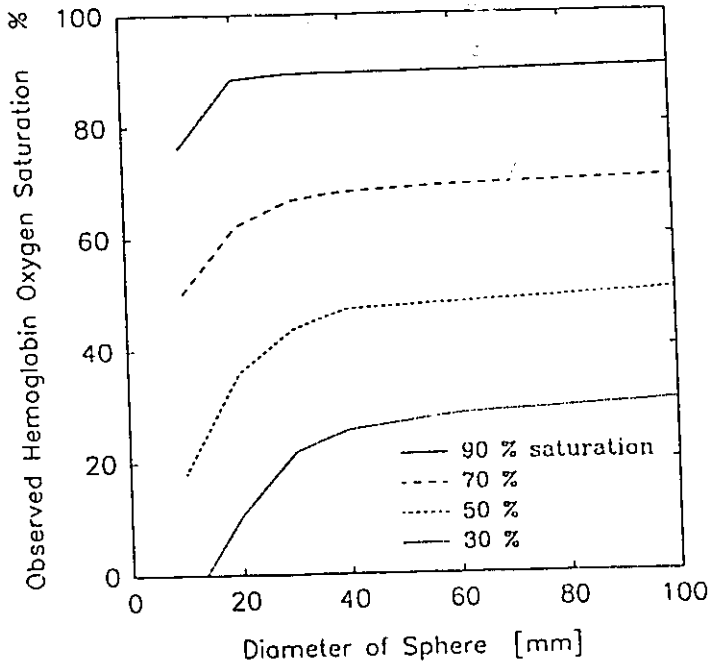

Figure 11 (a) Tissue oxygen saturation calculated for a simulated two wavelength measurement system as a function of the size of the tissue volume (here assumed to be spherical). Four oxygen saturation levels have been used 90, 70, 50, and 30%. Departure from the horizontal represents error in estimate due to the volume effects upon phase and modulation measurements. The horizontal dotted lines use a third wavelength to improve the estimate.

(b) Tissue oxygen saturation calculations including a change in the scattering coefficient with wavelength, demonstrating the complexity of trying to correct for all finite volume effects. At the smallest volumes (diameter < 40 mm) the three wavelength measurement system cannot compensate for small volume effects if the scattering coefficient is a function of wavelength.

effects are neglected in tissue oxygenation measurement, there can be serious errors in the estimate of $Sa(O_2)$. Care should be used in applying tissue oxygenation monitors to tissue volumes which are small or which contain inhomogeneities.

6. Conclusions

Clinical application of frequency domain NIRS must rely on the approximation of simple boundary conditions, since the actual tissue geometry is seldom accurately known, and since complex shapes cannot readily be incorporated in the analysis. The goal of this study has been to examine the nature of errors introduced in estimates of μ_a by the failure to include boundary effects in the modelling. The slab, sphere and cylinder geometries are used in this paper to represent data which exhibits finite volume effects similar to potential clinical situations. These data have been interpreted with simple diffusion models such as the semi-infinite and slab geometries in an effort to quantify possible errors incurred with clinical tissue spectroscopy. It has been assumed here that simple diffusion models must be used to recover μ_a and μ_s' values, since the complexity of modelling each individual tissue volume seems unrealistic in terms of the time required. Limits upon the size of finite tissue volumes which can be sampled by *in-vivo* frequency domain measurements have been suggested along with methods of reducing the boundary effects due to thin samples and curved surfaces. Ultimately, it appears that each different geometry must be evaluated separately in order to determine if boundary effects will be a problem, however there may be standard geometries used in clinical practice in which the boundary effects will always be negligible. In general, for large tissue volumes, radius

> 50 mm, the apparent increase in μ_a due to the boundary is on the order of 0.001 mm^{-1} which is probably an acceptable error. The error in μ_a will be significantly reduced if the object can be modelled accurately as a sphere or cylinder. However, diffusion calculations of sphere and cylinder geometries are time consuming, even on the fastest computers readily available. Recovery of μ_a and μ_s' values with sphere and cylinder models is probably best accomplished with a look-up table or with a trained neural network. Spectroscopy of small objects, radius < 50 mm, is probably limited to measuring relative changes in μ_a unless the boundary conditions can be simulated well by a regular geometry.

The errors in μ_a measured from a thin sample or a sample containing hidden inhomogeneities can be minimized by first decreasing the source-detector distance, and secondly using higher modulation frequencies. Alternatively, if the upper surface is a problem (such as a curved boundary) then larger source-detector separations will provide better measurements of the internal optical properties. Use of the lowest frequency which gives an acceptable signal to noise ratio, will allow the deepest sampling of the tissue volume.

There are also some practical limitations to experimental measurements of phase and modulation on very small objects which have not been discussed here. Measurement with small source-detector separations yields a modulation which is very close to unity. In this region the change in modulation is often smaller than the noise in the measurement. For distances smaller than 20 mm is has been recommended in a previous paper to use measurements of phase shift and relative intensity between two detector points on the tissue (Wilson *et al* 1993), to avoid the poor S/N ratio of demodulation at small distances.

Finally, the two applications discussed here serve mainly as illustrations of the effects produced by taking spectroscopic measurements on small objects. The measurement of photosensitizer in a small tissue volume is a problem which arises when making dosimetric measurements in PDT experiments on small animals, or on human extremities. The tissue oxygenation simulations serve more as a warning to using clinical instruments without examining the boundary effects of the tissue volume. Possible solutions to reducing the finite volume effects in oxygenation saturation measurement have been presented here.

Acknowledgements

This work was financially supported by the National Institutes of Health grant P01-CA43892. B Pogue would like to acknowledge the use of some diffusion theory programs written by J D Moulton.

References

Arridge S R, Cope M, Delpy, D T 1992 The theoretical basis for the determination of optical pathlengths in tissue: temporal and frequency analysis *Phys. Med. Biol.* **37** 1531-1560

Brazy J E, Lewis D V, Mitnick M H, Jobsis F F 1985 Noninvasive monitoring of cerebral oxygenation in preterm infants: preliminary observations *Pediatrics* **75** 217-225

Chance B, Nioka S, Kent J, McCully K, Fountain M, Greenfield R, Holtom G 1988 Time-resolved spectroscopy of haemoglobin in resting and ischemic muscle *Anal. Biochem.* **174** 698-707

Cheong W, Prahl S A, Welch A J 1990 A review of the optical properties of biological tissues *IEEE J. Quant. Elec.* **26** 2166-2185

Cope M, Delpy D T 1988 System for long-term measurement of cerebral blood and tissue oxygenation on newborn infants by near infra-red transillumination *Med. & Biol. Eng. & Comp.* **26** 289-294

Cope M, van der Zee P, Essenpreis M, Arridge S R, Delpy D T 1991 Data analysis for near infrared spectroscopy of tissue: problems in determining the relative cytochrome aa_3 concentration *Proc. SPIE* **1431** 251-262

Delpy D T, Cope M, van der Zee P, Arridge S, Wray S, Wyatt J S 1988 Estimation of optical pathlength through tissue by direct time of flight measurement *Phys. Med. Biol.* **33** 1433-1442

Farrell T, Wilson B C, Patterson M S 1992 The use of a neural network to determine optical properties from spatially resolved diffuse reflectance measurements *Phys. Med. Biol.* **37** 2281-2286

Ferrari M, Wei Q, Carraresi L, De Blasi R, Zaccanti G 1992 Time-resolved spectroscopy of the human forearm *J. Photochem. Photobiol. B: Biol.* **16** 141-153

Gratton E, Limkeman M 1983 A continuously variable frequency cross-correlation phase fluorometer with picosecond resolution *Biophys. J.* **44** 315-324

Hale G M, Querry M R 1973 Optical constants of water in the 200 nm to 200 μm wavelength region *Appl. Opt.* **12** 555-563

Jobsis F F 1977 Noninvasive, infrared monitoring of cerebral and myocardial oxygen sufficiency and circulatory parameters *Science* **198** 1264-1267

Ishimaru A 1989 Diffusion of light in turbid material *Appl. Opt.* **28** 2210-2215

Lamarsh J R 1966 *Introduction to Nuclear Reactor Theory* (Massachusetts: Addison-Wesley)

Keijzer M, Star W M, Storchi P 1988 Optical diffusion in layered media *Appl. Opt.* **27** 1820-1824

Maier J S, Gratton E 1993 Frequency-domain methods in optical tomography: detection of localized absorbers and a backscattering reconstruction scheme *Proc. SPIE* **1888** 440-451

Madsen S J 1992 Experimental studies of time-resolved light propagation in turbid media *Ph.D. Thesis* McMaster University

Madsen S J, Wilson B C, Patterson M S, Park Y D, Jacques S L, Hefez Y 1992 Experimental tests of a simple diffusion model for the estimation of scattering and absorption coefficients of turbid media from time-resolved diffuse reflectance measurements *Appl. Opt.* **31** 3509-3517

Madsen S J, Patterson M S, Wilson B C 1992 The use of india ink as an optical absorber in tissue-simulating phantoms *Phys. Med. Biol.* **37** 985-993

Moulton J D 1990 Diffusion modelling of picosecond laser pulse propagation in turbid media *M.Eng. Thesis* McMaster University

Patterson M S, Chance B, Wilson B C 1989 Time resolved reflectance and transmittance for the non-invasive measurement of tissue optical properties *Appl. Opt.* **28** 2331-2336

Patterson M S, Moulton J D, Wilson B C, Chance B 1990 Applications of time-resolved light scattering measurements to photodynamic therapy dosimetry *Proc. SPIE* **1203** 62-74

Patterson M S, Moulton J D, Wilson B C, Berndt K W, Lakowicz J R 1991 Frequency-domain reflectance for the determination of the scattering and absorption properties of tissue *Appl. Opt.* **30** 4474-4476

Patterson M S, Madsen S J, Moulton J D, Wilson B C 1991 Diffusion equation representation of photon migration in tissue *IEEE Microwave Theory and Techniques Symposium Digest* 905-908

Patterson M S, Pogue B W 1994 Mathematical model for time-resolved and frequency-domain fluorescence spectroscopy in biological tissues *Appl. Opt.* **32** in press

Profio A E 1989 Light transport in tissue *Appl. Opt.* **28** 2216-2222

Sevick E M, Chance B, Leigh J, Nioka S, Maris M 1991 Quantitation of time and frequency-resolved optical spectra for the determination of tissue oxygenation *Anal. Biochem.* **195** 330-351

Sevick E M, Lakowicz J R, Szmacinski H, Nowaczyk K, Johnson M L 1992 Frequency domain imaging of absorbers obscured by scattering *J. Photochem. Photobiol. B: Biol.* **16** 169-185

Tromberg B J, Svaasand L O, Tsay T T, Haskell R C 1993 Properties of photon density waves in multiple-scattering media *Appl. Opt.* **32** 607-616

Wilson B, Farrell T, Patterson M S 1990 An optical fiber-based diffuse reflectance spectrometer for non-invasive investigation of photodynamic sensitizers *in vivo* in *Future Directions and Applications in Photodynamic Therapy* (SPIE Inst. series) 219-232

Wilson B C, Sevick E, Patterson M S, Chance B 1992 Time-dependent optical spectroscopy and imaging for biomedical applications *Proc. IEEE* **80** 918-930

Wilson B C, Patterson M S, Pogue B W 1993 Instrumentation for *in vivo* tissue spectroscopy and imaging *Proc. SPIE* **1892** 132-147

Wray S, Cope M, Delpy T D, Wyatt J S, Reynolds E 1988 Characterization of the near infrared spectra of cytochrome aa_3 and haemoglobin for the non-invasive monitoring of cerebral oxygenation *Biochim Biophys Acta* **933** 184-192

Wyatt J, Cope M, Delpy D, van der Zee P, Arridge S, Edwards A, Reynolds E 1990 Measurement of optical path length for cerebral near-infrared spectroscopy in newborn infants *Dev. Neurosci.* **12** 140-144

van Staveren H J, Moes C J M, van Marle J, Prahl A, van Gemert M J C 1991 Light scattering in Intralipid-10% in the wavelength range of 400-1100 nm *Appl. Opt.* **30** 4507-4514

Yoo K M, Liu F, Alfano R R 1990 When does the diffusion approximation fail to describe photon transport in random media *Phys. Rev. Lett.* **64** 2647-2650

Introduction to Paper #2

This paper was an extension of chapter 2 and Paper #1 to examine the errors inherent in a frequency-domain tissue spectrometer. The errors which can be incurred are strongly dependent upon the geometry of the sources and detectors and which observables are used. After the preliminary analysis of chapter 2 it seemed likely that a multiple detector system was needed to provide stable and accurate spectroscopic measurements. This paper examined the two most popular configurations for source and detector and examined the magnitudes of the random, systematic and physiologic errors expected.

As in Paper #1, the calculations and experiments were done by myself under the supervision of Dr. Patterson. The assistance of Dr. J. Hayward was necessary in caring for and anaesthetizing the rabbits used in the physiologic measurements. The write up of the paper was done me and edited by Dr. Patterson.

Assessment of a wavelength tunable frequency domain system for noninvasive tissue spectroscopy

Brian W. Pogue and Michael S. Patterson*

Hamilton Regional Cancer Centre/McMaster University
699 Concession Street
Hamilton, Ontario, CANADA L8V 5C2

* Telephone (905) 387-9711, x 7005
FAX (905) 575-6330
Email mpatterson@octrf.on.ca

Abstract

A system is described and evaluated for noninvasive measurement of the scattering and absorption coefficients of tissue in the 600 - 850 nm range. An arc lamp/monochromator combination provides a tunable source which is intensity modulated at 135 MHz by a Pockel's cell and coupled by fiber optics to the tissue surface. Diffusely reflected light is collected at distances of 1 and 2 cm from the source and the intensity ratio and phase difference between these two signals are measured. These data are analyzed by means of a diffusion model of light to provide estimates of the scattering and absorption coefficients. The accuracy of these estimates is assessed by calculation of the influence of instrumental noise, tissue optical properties and modulation frequency. Because the model is based on the assumption of a semi-infinite tissue geometry, systematic errors caused by idealized finite volumes (slabs, cylinders and spheres) are also considered. The biomedical utility of the system is illustrated by noninvasive measurement of the uptake of an intravenously injected dye in rabbit leg muscle.

Key words: tissue optics, noninvasive spectroscopy, diffusion theory, frequency-domain.

1. Introduction

In the red and near infrared region of the optical spectrum (roughly 600 - 1200 nm) light can readily penetrate several centimeters of tissue due to low intrinsic absorption [1]. With appropriate illumination and detection geometries, relatively large tissue volumes can therefore be sampled and quantitative estimates of the tissue absorption coefficient may allow calculation of the concentration of endogenous or exogenous chromophores. The former include hemoglobin and cytochromes and the latter photosensitizers used in photodynamic therapy. Because of intense light scattering in tissue, quantitative determination of the absorption coefficient is a challenging problem which requires the application of physical models of light propagation.

In recent years a number of strategies have been proposed based on spatially resolved [2-6], time domain [7-10], or frequency domain [11-15] measurements of light which has been diffusely reflected from the tissue. Patterson [16] has recently reviewed the advantages of each approach and pointed out that the optimum method depends on the demands of the specific problem. The system described in this paper uses a light source which is intensity modulated at 135 MHz and coupled by fiber optics to the tissue surface. Light which is detected on the tissue surface some distance away is modulated at the same frequency, but reduced in intensity and delayed in time. A model of light propagation based on diffusion theory can be used to estimate the scattering and absorption coefficients of the tissue from the attenuation and time delay (phase shift). This approach offers the following specific advantages:

i) The use of an arc lamp / monochromator source allows selection of wavelength over a broad range. Complete absorption spectra can be acquired from wavelength scans.

ii) Measurements are made at only one or two points on the tissue surface.

iii) No absolute measurements are required.

iv) Frequency domain techniques can provide quantum noise limited performance at reasonable cost.

Except for the tunable source, the approach is similar in principle to that described previously by Fantini et al. [14] who used four sources and a single detector. The work described in this paper had three main goals:

i) Characterization of the instrument noise and calculation of its influence on the precision of estimates of the tissue absorption and scattering coefficients. As well, a comparison was made between calculations based on measurements at one and two detector locations.

ii) Determination of the influence of finite tissue volume on the estimates of the tissue optical properties. Data reduction is usually based on the assumption that the tissue is a semi-infinite medium and previously we studied the systematic errors introduced by this assumption for a one detector system [17]. Here that work is extended to a system where measurements are made at two detector locations.

iii) Application of the system to a real biological problem : noninvasive measurement of the average tissue concentration of a dye similar to those used for photodynamic therapy. We believe this to be the first time frequency domain methods have been used to acquire complete quantitative in vivo absorption spectra.

2. Theory

We assume that the biological tissue of interest is a macroscopically uniform turbid medium characterized by an optical absorption coefficient, μ_a, a transport (or effective isotropic) scattering coefficient, μ'_s, and an average speed of light c_n. In the wavelength region 600-1200 nm, $\mu'_s >> \mu_a$, and diffusion theory has been shown to provide an accurate description of light propagation [18]. The diffusion equation can be solved analytically for simple geometries and detailed results have been presented by Moulton [19] and Arridge et al. [20]. In this paper we are primarily interested in the simple geometry shown in Fig. 1 where light delivery and detection occur on the surface of an infinite tissue half-space. As shown in an earlier paper [17] the ac component of reflectance, $R(\rho, \omega, \mu_a, \mu'_s, c_n)$, which is the number of photons crossing the tissue boundary per unit time per unit area due to a unit source modulated at frequency $f = \omega/2\pi$ can be written as

$$R(\rho,\omega,\mu_a,\mu'_s,c_n) = \frac{1}{2(2\pi)^{1/2}}\left[\frac{z_o(1+k\rho_o)}{\rho_o^3}\,e^{-k\rho_o} + \frac{z_p(1+k\rho_p)}{\rho_p^3}\,e^{-k\rho_p}\right] \tag{1}$$

where $z_o = 1/\mu'_s$, $z_p = z_o + 2D/\kappa$, $D = [3(\mu_a + \mu'_s)]^{-1}$ and κ is a constant which depends on c_n and the speed of light in the nonscattering medium above the tissue. For a tissue-air boundary $\kappa \approx 0.43$ [3]. We also define $\rho_o^2 = \rho^2 + z_o^2$, $\rho_p^2 = \rho^2 + z_p^2$ and the complex attenuation coefficient

$$k = \left(\frac{\mu_a c_n + i\omega}{D c_n}\right)^{1/2} \tag{2}$$

Note that $R(\rho, \omega, \mu_a, \mu'_s, c_n)$ is complex, so that the phase of the ac reflectance signal relative to the source, θ, is given by

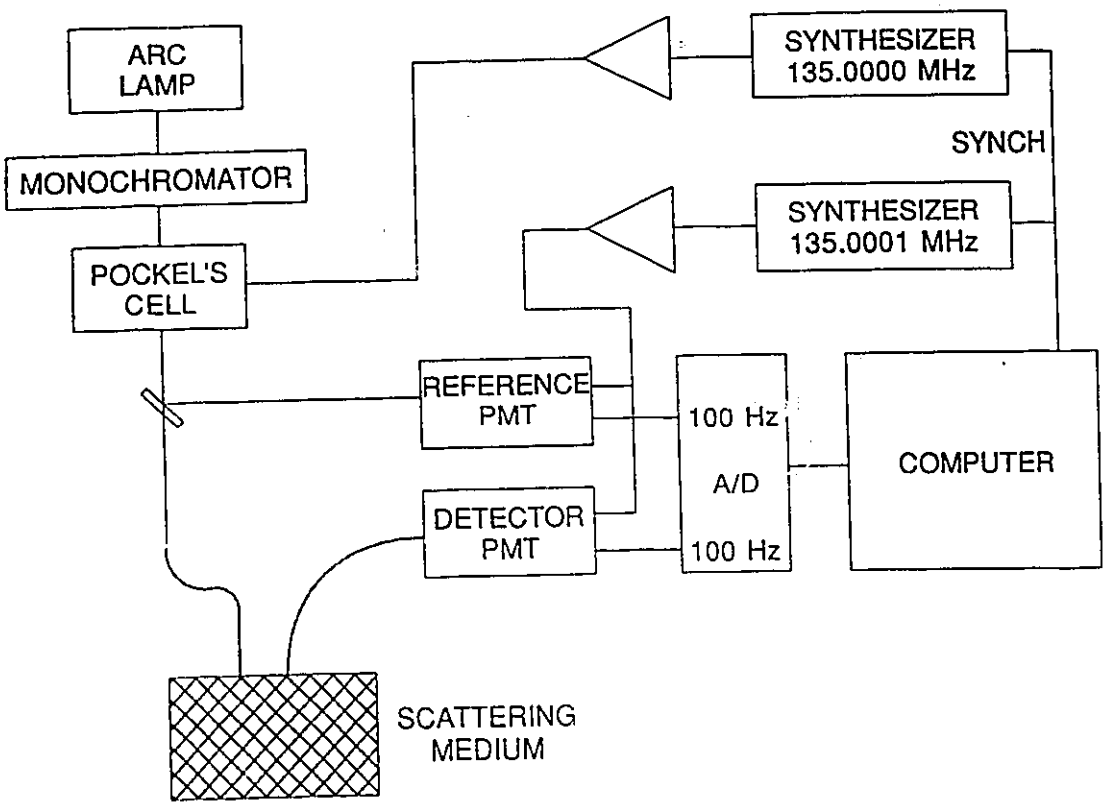

Figure 1 Schematic diagram of the experimental apparatus for frequency domain measurements.

$$\theta = \arctan \frac{Im[R]}{Re[R]} \tag{3}$$

and the amplitude, A, is

$$A = [Re^2(R) + Im^2(R)]^{1/2} \tag{4}$$

Of course it is not possible to have a source with negative intensity, so there is always a dc component present as well. This component is evaluated by setting $\omega = 0$ in Eq. (1). The modulation of the detected signal is defined as

$$M(\omega) = A(\omega)/A(0) \tag{5}$$

The goal of the measurements is to determine μ_a and μ'_s from R. (It is usual to assume that $c_n \equiv .214$ m ns^{-1} for soft tissue [21].) Two general strategies have been adopted. One is to position a single detector at distance ρ and to measure M and θ [11]. The two equations 3 and 5 can be solved numerically for μ_a and μ'_s once M and θ are measured. This approach requires an additional reference measurement at $\rho = 0$, which is usually accomplished by abutting the source and detector fiber bundles. An alternative method is to measure the phase and dc intensity at two distances ρ_1 and ρ_2 [22]. From Eq. (1) equations can be derived for $\theta(\rho_2) - \theta(\rho_1)$ and $A(\rho_2, 0)/A(\rho_1, 0)$ in terms of μ_a and μ'_s. These can be solved numerically for μ_a and μ'_s and no reference measurement for $\rho = 0$ is required. This approach can be extended to more than two detector positions (or, equivalently, one detector and multiple sources) in which case the estimation of μ_a and μ'_s becomes an optimization problem [14].

The equations described above were derived for the semi-infinite geometry. In an earlier paper [17] we assessed the influence of finite tissue size on estimates of μ_a and μ'_s made with a one detector phase and modulation system. In that study analytical

solutions of the diffusion equation for slab, cylinder and sphere geometries were used to generate data which were then used as input to the algorithm based on semi-infinite geometry. Here we extend that study to a two detector system where the observables are the phase difference $\theta(\rho_2) - \theta(\rho_1)$ and the intensity ratio $A(\rho_2, 0)/A(\rho_1, 0)$.

3. Apparatus and Methods

The apparatus used for the measurement of phase and intensity of multiply scattered light is illustrated schematically in Fig. 1. The instrumentation is essentially an adaptation of the frequency domain fluorometer described by Gratton and Limkeman [23]. The light source is a 300 W xenon arc lamp with an integral parabolic reflector which produces a collimated beam. This beam is focused on the entrance slit of a monochromator and the light which emerges from the exit slit is recollimated. The intensity of this beam is modulated by a Pockel's cell at 135 MHz, passes through a beam splitter (92° transmission, 8% reflection) and is then focused onto a 3 mm diameter optical fiber bundle. This bundle delivers the modulated light to the tissue surface. The DC intensity at the end of the fiber bundle is typically 10 μW in a bandpass of 10 nm, although there are much more intense peaks above 800 nm. The modulation attained with the Pockel's cell is only about 8%. Much higher modulation and intensity can be achieved with lasers or modulated LED's, but none of these sources offers the wide tuning range of the arc lamp/monochromator combination.

Another 3 mm bundle collects scattered light at the tissue surface and its output is coupled via a lens to the photocathode of a photomultiplier tube (R928 Hamamatsu). A filter wheel can be used to interpose a bandpass filter between the bundle and the PMT. This may be necessary to reject fluorescent light under some circumstances, e.g.

absorption spectroscopy of a fluorescent dye. A second PMT is also coupled via a fiber bundle to the light reflected from the beam splitter. This detector provides the reference for phase and intensity measurements. The photomultiplier tubes were always operated with 1000 V from anode to cathode.

Both PMT's are mounted in special housings (ISS, Champaign IL) which allow the PMT gain to be modulated at high frequency by injection of an RF signal at the last dynode. If the gain modulation is performed at a frequency slightly offset (in this case, 100 Hz) from the Pockel's cell modulation frequency, a 100 Hz heterodyne signal is generated which contains all the phase and amplitude information. This low frequency signal is sampled at 1 kHz and converted to a 12 bit digital value by a proprietary signal processing board (ISS, Champaign IL). The data are acquired over a variable sampling period and then a fast Fourier transform is performed. The transform yields the dc amplitude, and the ac amplitude and phase at the heterodyne frequency.

In vivo experiments were performed on three New Zealand white rabbits. Each rabbit was anaesthetized by injection into the ear vein of 5 mg/kg xylazine, 50 mg/kg ketamine and 1 mg/kg acepromazine maleate. The leg was shaved and a piece of black plexiglass 0.6 cm x 4 cm x 6 cm was clamped over the femoral biceps muscle. Sufficient pressure was applied to ensure close contact between plastic and tissue. Three holes were drilled in the plastic: one held the source fiber bundle, the second held the detector bundle at a centre-to-centre distance of 1 cm and the third positioned the detector at 2 cm from the source. This arrangement, which minimized motion of the fibers relative to the muscle, was essential for reliable measurements. Data were acquired sequentially at the two source detector distances by manually moving the detector fiber bundle as required.

Data were acquired at 13 wavelengths from 560 to 830 nm. The wavelength was

then fixed at 660 nm and aliquots of the dye nickel phthalocyanine tetrasulfonate ($NiPcS_4$, Alpha Pharmaceutical Inc, Utah) were injected via the ear vein. $NiPcS_4$ has a strong absorption peak at 660 nm, a weaker peak at 600 nm and no detectable fluorescence. Two solutions of $NiPcS_4$ were used: 10 mg/ml for the first two animals and 20 mg/ml for the third. After the injection of each 0.5 ml aliquot, the signal at 1 cm source-detector separation was recorded for 15 s. This was repeated three times to estimate the variance in the measurements, and then the detector fiber was moved to the second position. Four 15 s measurements were then performed at this distance. After injection of the last aliquot, measurements were again performed over the complete wavelength range.

4. Results

This section of the paper is divided into three parts. In the first we will examine how noise in the measurement of phase and intensity affects the precision of the estimates of μ_a and μ'_s made with one and two detector systems. The second part will deal with systematic errors in μ_a and μ'_s caused by finite tissue volumes for a two detector instrument. Finally we will present the results of *in vivo* measurements of μ_a and μ'_s made with our two detector system.

4.1 Errors Due to System Noise

To measure the typical variance in phase and amplitude, the source and detector fibers were fixed on the surface of a block of white linear polyethylene (10 cm x 10 cm x 5 cm). The detected signal was sampled for 30 consecutive 0.5 s time intervals. The dc amplitude, ac amplitude and phase were calculated for each interval, as were the mean and standard deviation in each quantity. The source intensity was then reduced using a

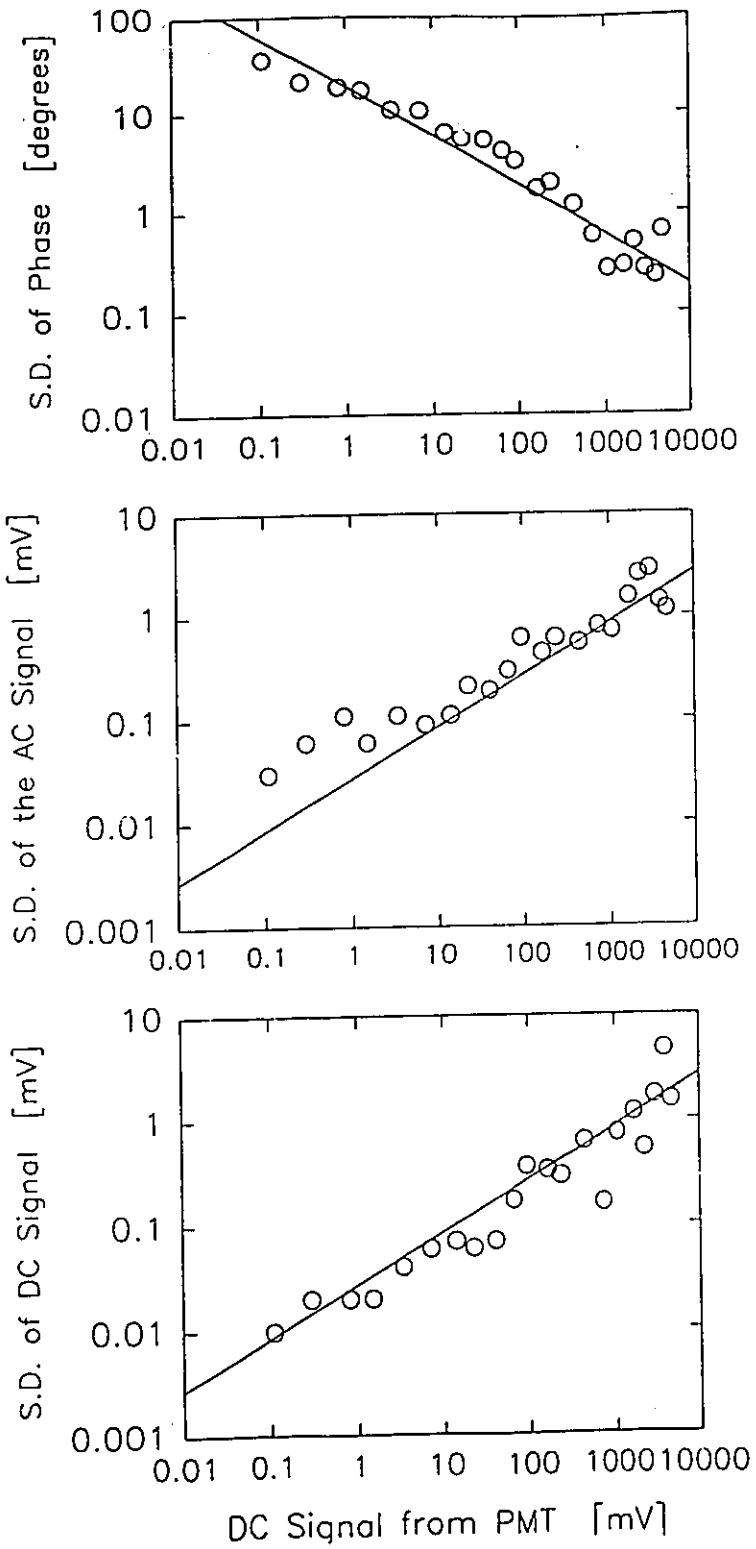

Figure 2 Standard deviation in phase, ac signal and dc signal as function of the dc signal level. The points are experimental results for 0.5 s data acquisition, and the straight lines are theoretical predictions based on measurements of the incident optical power on the photocathode and the manufacturer's data for photocathode quantum efficiency. The modulation was 8%.

continuously variable neutral density filter (Newport Corporation, Irvine CA) and the 30 measurements were repeated. In Fig. 2 the standard deviations in the phase, ac amplitude and dc amplitude are plotted as functions of the dc signal amplitude (in mV). Also shown on these plots are the expected values of the standard deviation if the only source of noise is quantum fluctuations in the number of electrons emitted from the photocathode. In order to make this theoretical estimate, the source wavelength was set to 630 nm and the total optical power at the PMT end of the detector fiber was measured using a calibrated meter (Model 840, Newport Corporation, Irvine CA). The PMT manufacturer states that the photocathode quantum efficiency at this wavelength is 0.07, so that the photocathode current can be calculated by assuming that all of the light emitted by the detector bundle reaches the photocathode. Using these data and assumptions, we calculated that a dc signal of 1 V at 630 nm corresponds to a photocathode current of 2.7×10^6 electrons s^{-1}. As explained in detail by Carlson [24], the standard deviation in the dc and ac signal amplitudes as well as the phase can then be calculated from knowledge of this average current and the sampling period. For example, in 0.5 s the total number of photoelectrons is, on average, 1.35×10^6 so the standard deviation would be the square root of this number, 1.16×10^3 , and the predicted standard deviation in the 1V dc signal would be 0.86 mV. The standard deviation in the dc and ac amplitude would vary with the square root of the dc signal amplitude, and the standard deviation in phase would vary inversely as the square root of the dc signal amplitude, assuming that the modulation is constant. Similarly, the standard deviation in all three observables would ideally scale inversely with the square root of the total sampling time.

Since Eq. (1) does not have an analytical solution for μ_a, μ'_s, it is necessary to perform a numerical simulation to assess the propagation of experimental uncertainties

into the estimates of the optical properties. We first considered a system with one detector located 2 cm from the source. Our practical experience with tissue *in vivo* has shown that this is the maximum distance at which useful signals can be obtained with the arc lamp source in the 600-850 nm spectral range. First, Eq. (1) was used to calculate the phase and modulation of the detected signal (assuming 8% source modulation) at 135 MHz for given values of μ_a and μ'_s. We assumed that enough light was available to produce a full scale dc signal (4 V), and values of the dc amplitude, ac amplitude and phase were sampled from normal distributions having standard deviations corresponding to the theoretical data in Fig. 2. (Since a one second integration time was assumed in this analysis, the data in Fig.2 were modified appropriately). An iterative Newton Raphson algorithm was then used to solve for μ_a and μ'_s given the observed phase and modulation. This was repeated 200 times so that the standard deviation in μ_a and μ'_s could be calculated. This process was repeated for 384 sets of optical properties where μ_a was varied from 0.0025 to 0.06 mm^{-1} and μ'_s from 0.25 to 4.0 mm^{-1}. The results are presented as lines of constant relative uncertainty as functions of μ_a and μ'_s; the uncertainty in μ_a is shown in Fig. 3a and the uncertainty in μ'_s in Fig. 3b. A value of, for example, 10, means that the standard deviation in the estimate of the interaction coefficient is equal to 10% of its true value.

We next considered a system with two detectors at distances of 1 and 2 cm. In this case the reflectance at the near detector will be greater than at the far detector. We assumed that sufficient light was available so that a full-scale signal was measured on the near detector. Equation (1) was then used to calculate the phase difference and intensity ratio, and standard deviations were assigned from the theoretical data in Fig. 2. As described above, a Monte Carlo simulation was performed to determine the uncertainties

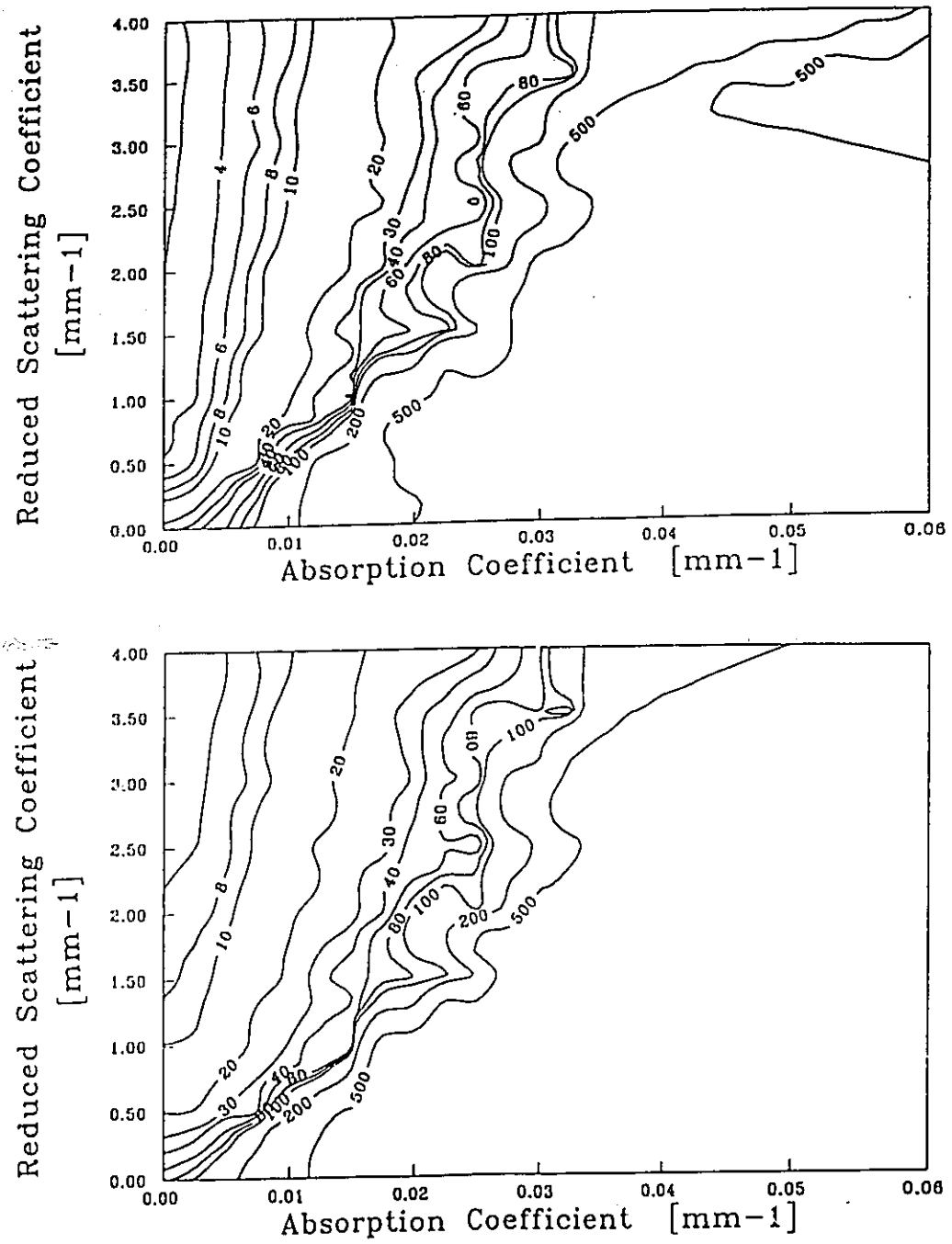

Figure 3 Calculated percent relative uncertainty (standard deviation/value *100) in the absorption (a) and reduced scattering (b) coefficients as functions of the tissue optical properties for a system based on measurements of phase and modulation at a source-detector distance of 2 cm and 135 MHz operation. Calculations were based on a one second data acquisition, theoretical shot-noise such as shown in Fig. 2 and numerical solution of Eq. (1).

in μ_a and μ'_s obtained by numerical solution of the equations derived from Eq. (1). The relative uncertainties in μ_a and μ'_s are plotted for a range of tissue optical properties in Figs. 4a and 4b respectively. In this case the lower signal at the far detector is the dominant source of error, and better performance could be obtained if light reaching the near detector were attenuated by a well-calibrated filter. To simulate this approach we assumed that an attenuator was selected which resulted in equal signals at both detectors when $\mu'_s = 1.0\ mm^{-1}$ and $\mu_a = 0.01\ mm^{-1}$. (The optical density of this filter would be 1.42 according to Eq. (1)). Clearly the signals could be equalized at any predetermined values of μ_a and μ'_s, but these were chosen as representative of tissues in the red and near infrared [1]. The uncertainty in μ_a which can be achieved with this equalized system is shown in Fig. 5. The uncertainties in μ'_s (not shown) were comparable to those in μ_a.

We also examined the effects of increasing the modulation depth and frequency. While it is not practical to do this with our arc lamp system, diode lasers can readily be modulated at higher frequencies with modulation approaching 100%. Greater modulation is desirable because the rms phase noise is inversely proportional to the amplitude of the ac signal. Increasing the modulation frequency is useful because the relative error in the phase is inversely proportional to frequency. The effect of changing modulation frequency from 135 Mhz to 500 MHz on the uncertainty in μ_a can be assessed by comparison of Fig. 6 with Fig. 5. The effect of increasing the modulation from 8% to 100% is shown by comparison of Fig. 7 with Fig. 5.

4.2 Errors Due to Finite Tissue Volume

In this section we will demonstrate the errors which occur when data obtained from a finite scattering medium are analyzed with the equation derived for an infinite half

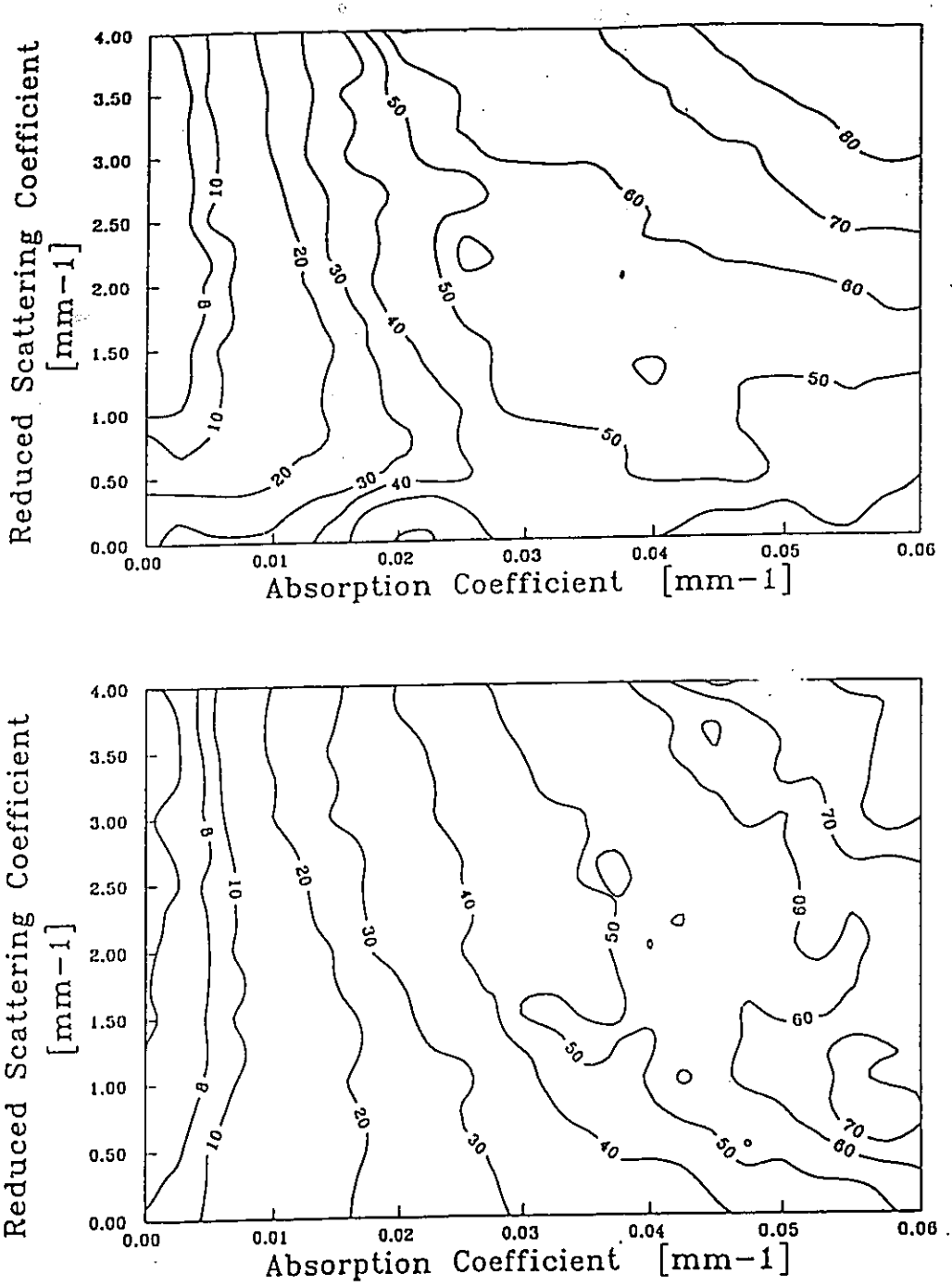

Figure 4 Calculated percent relative uncertainty in absorption (a) and reduced scattering (b) coefficients for a system based on measurements of phase difference and intensity ratio between source-detector distances of 1 and 2 cm. It was assumed that a full-scale signal was measured by the near detector and the signal at the far detector, calculated by Eq. (1), was smaller.

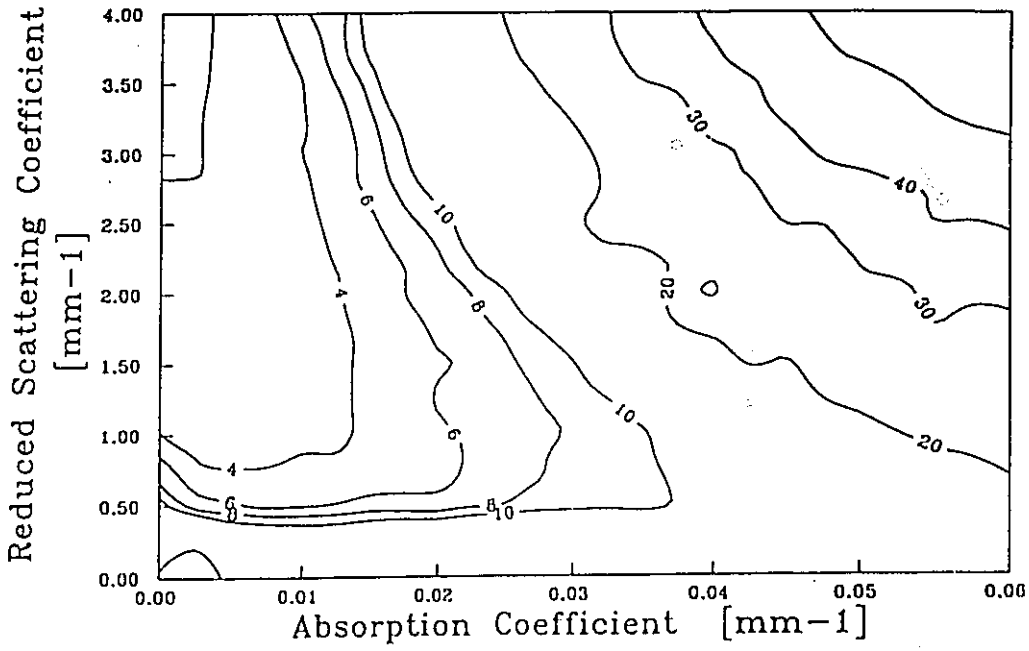

Figure 5 Calculated percent relative uncertainty in the absorption coefficient for the same conditions as Fig. 4a, except that an attenuator has been added to the detector at 1 cm distance so that the signal is equal to that measured at 2 cm for $\mu_a = 0.01$ mm^{-1} and $\mu'_s = 1.0$ mm^{-1}.

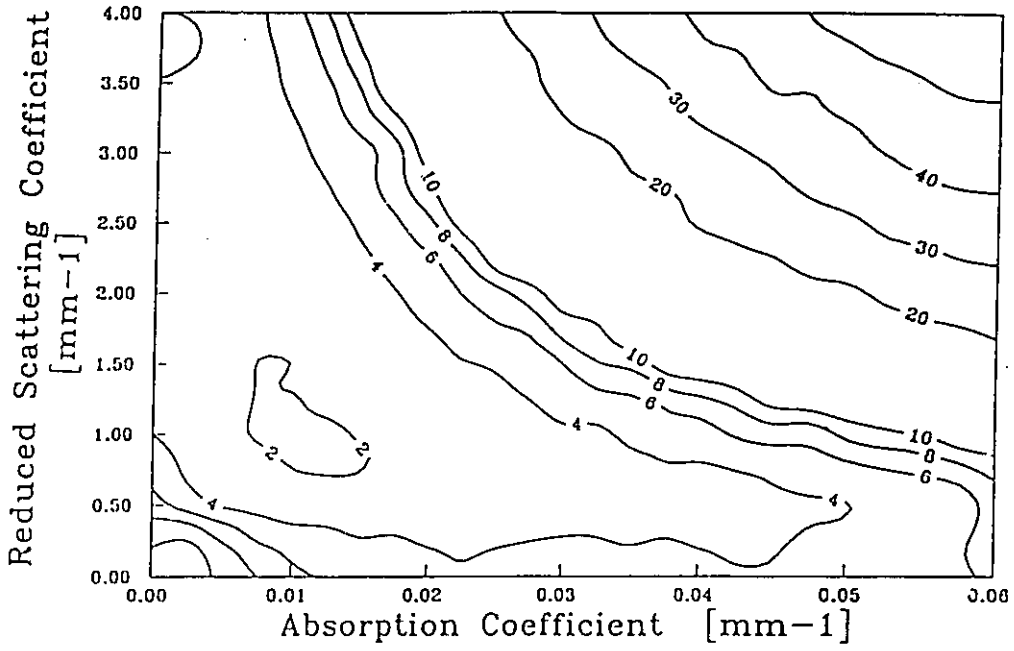

Figure 6 Calculated percent relative uncertainty in the absorption coefficient under the same conditions as Fig. 5, except that the modulation frequency has been increased to 500 MHz.

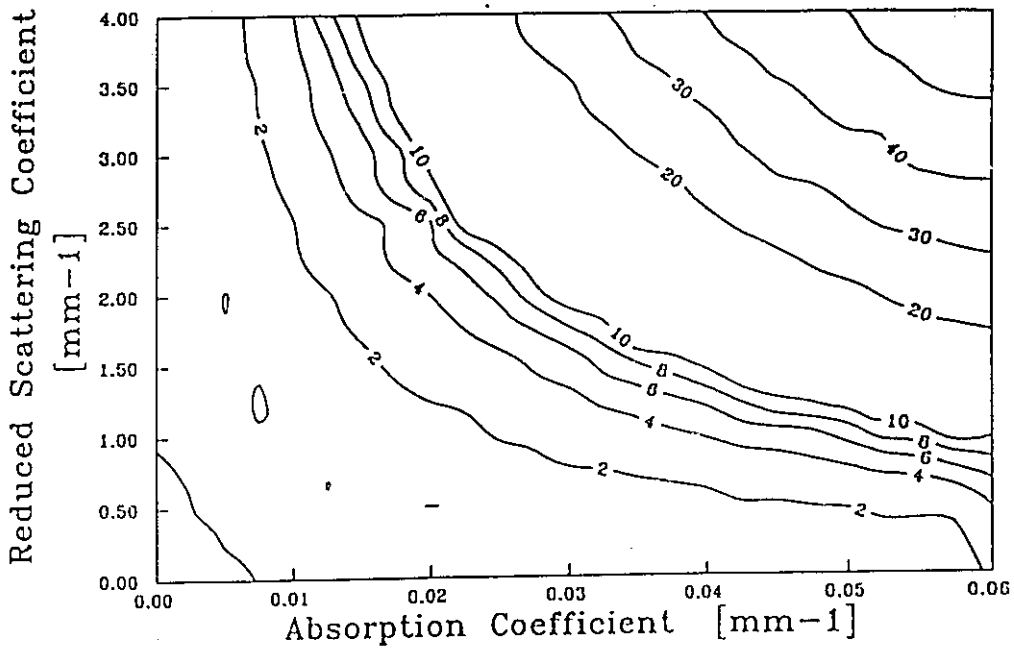

Figure 7 Calculated percent relative uncertainty in the absorption coefficient under the same conditions as Fig. 5, except that the source modulation has been increased from 8% to 100%.

space, i.e. Eq. (1). We restricted our study to a two detector system based on phase and dc intensity measurements at 1 cm and 2 cm, as the performance of a one detector system has been assessed in a previous paper [17]. The modulation frequency was 135 MHz. First we considered the case where the source and both detectors were located on the surface of an infinite slab of variable thickness. The analytical solution for the slab [17] was used to calculate the reflectance at each detector and hence the phase difference and dc intensity ratio. These data were then used as the input to the iterative algorithm based on Eq. (1). No noise was added to the data in this case. Fig. 8 shows the absolute error in the scattering and absorption coefficients as functions of slab thickness for slabs with μ'_s = 1.0 mm^{-1} and μ_a = 0.005, 0.01, 0.02 mm^{-1}. Similar results are shown in Fig. 9 where μ_a = 0.01 mm^{-1} and μ'_s = 0.5, 1.0, 2.0 mm^{-1}.

We also examined the influence of a curved surface by considering cylindrical and spherical tissue volumes. The analytical solutions of Moulton [19] for an infinite cylinder and a sphere were used to calculate the reflectance at distances of 1 and 2 cm along the surface of the object, and these results were used to compute phase difference and intensity ratios. As described above, these data were then used as input to the algorithm based on Eq. (1) and the errors in μ_a and μ'_s were calculated. These are plotted as a function of cylinder diameter in Fig. 10 for μ'_s = 1.0 mm^{-1} and μ_a = 0.005, 0.01, 0.02 mm^{-1}. Results for the spherical case are shown in Fig. 11.

4.3 Results of *In Vivo* Measurements

In Figure 12 we show the absorption and scattering spectra for two of the rabbits measured before the injection of any $NiPcS_4$ and after injection of the last aliquot (total doses of $NiPcS_4$ 7.6 mg/kg and 20.3 mg/kg). The representative error bars show the

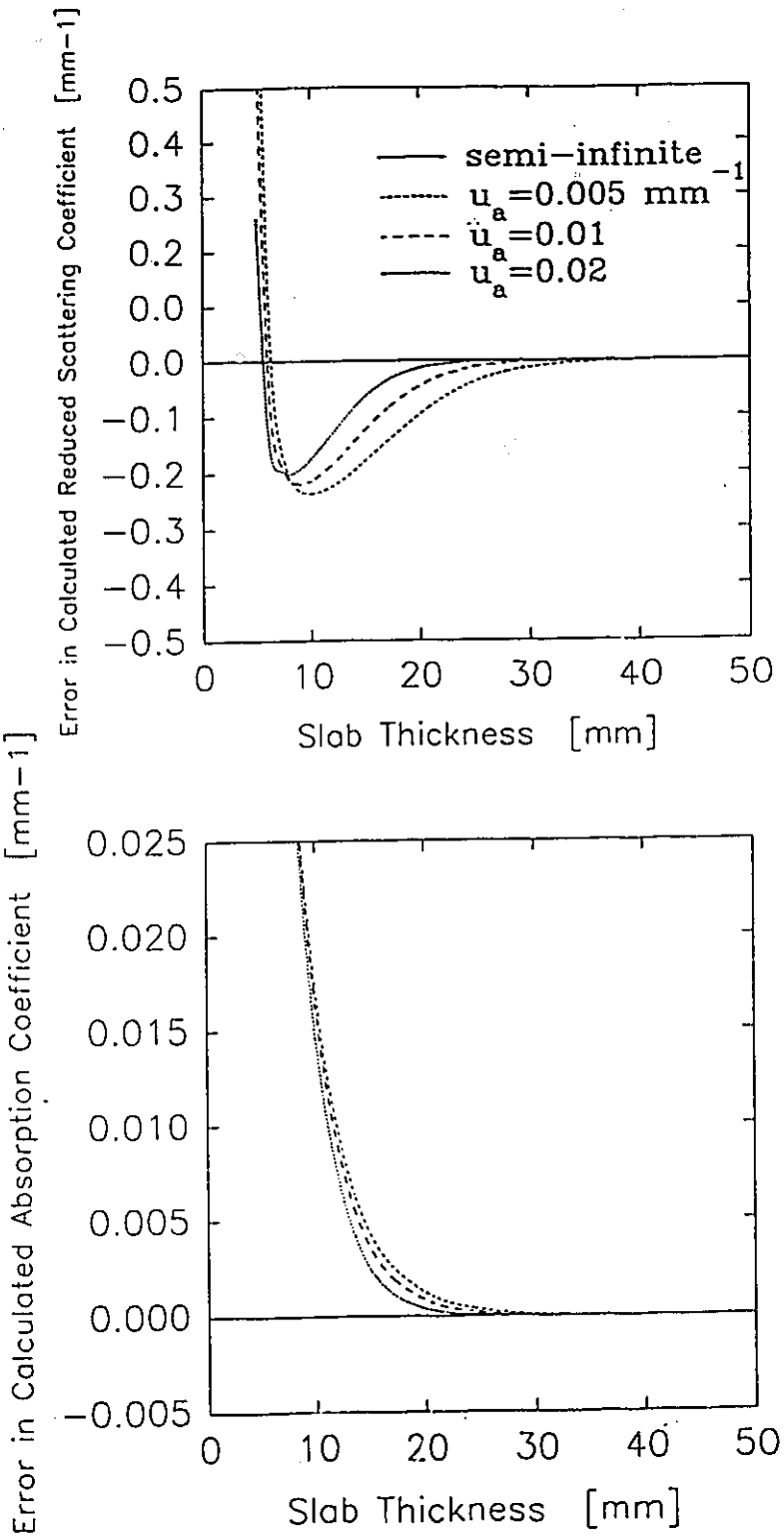

Figure 8 Calculated absolute errors in the absorption and reduced scattering coefficients as functions of slab thickness for μ'_s = 1.0 mm^{-1} and μ_a = 0.005, 0.010, 0.020 mm^{-1}. Calculations are for a two detector system (1 cm and 2 cm) based on phase difference and intensity ratio operated at 135 MHz. The systematic error shown here is caused by the assumption of semi-infinite geometry.

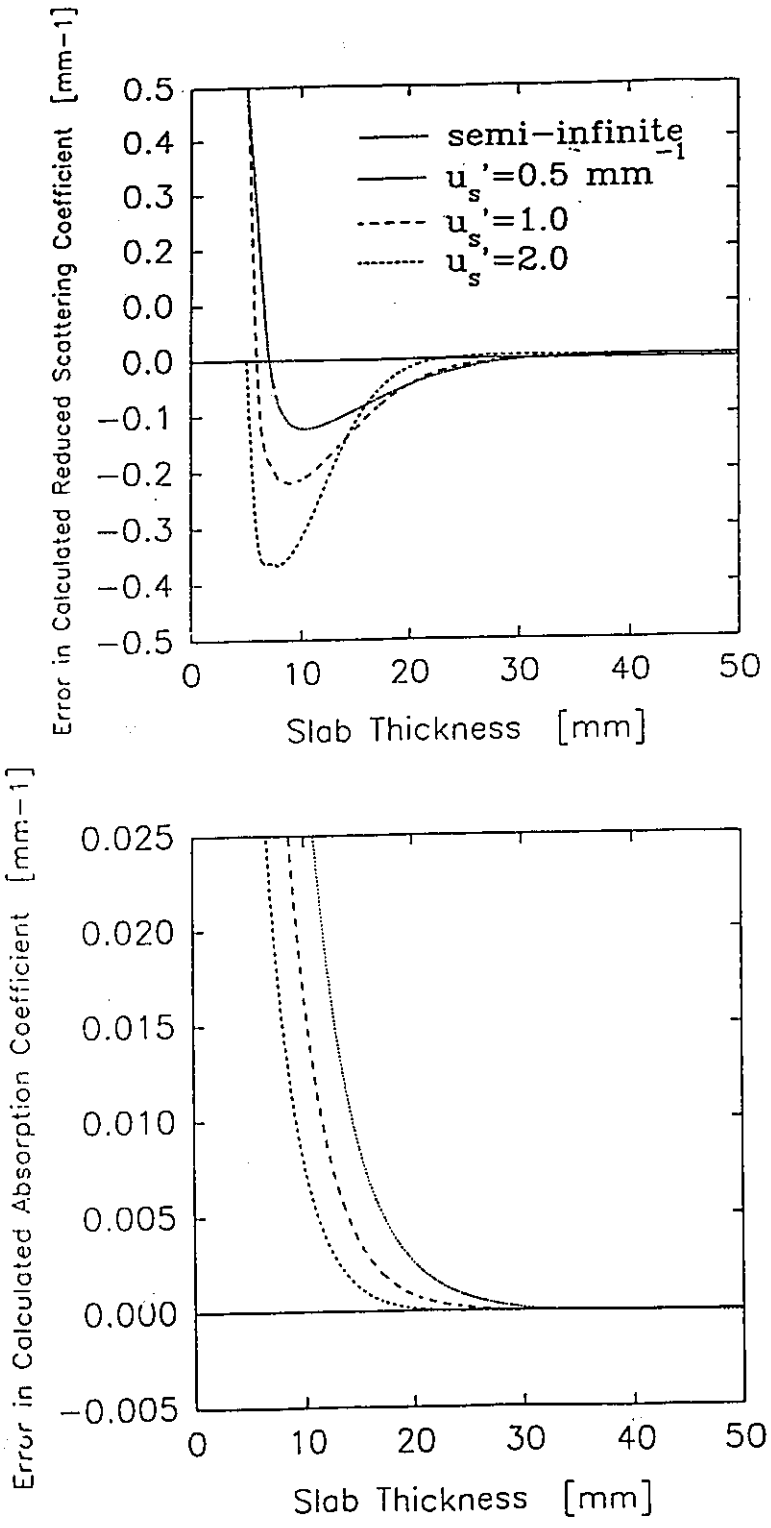

Fig. 9 Similar to Fig. 8 for the case of $\mu_a = 0.01$ mm^{-1} and $\mu'_s = 0.5, 1.0, 2.0$

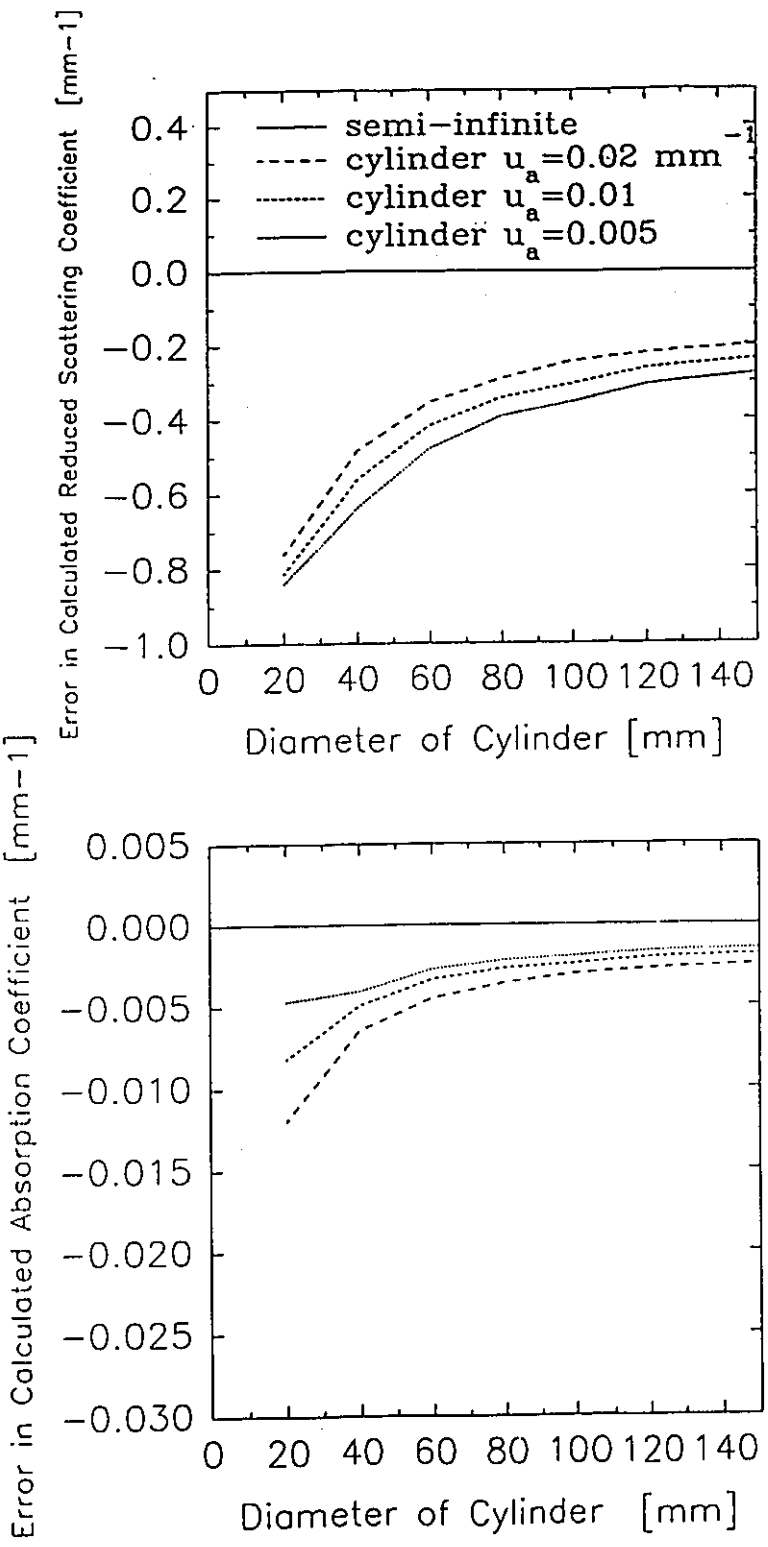

Fig. 10 Calculated systematic errors in μ_a for cylindrical tissue volumes with $\mu'_s = 1.0$ mm^{-1} and $\mu_a = 0.005, 0.010, 0.020$ mm^{-1}.

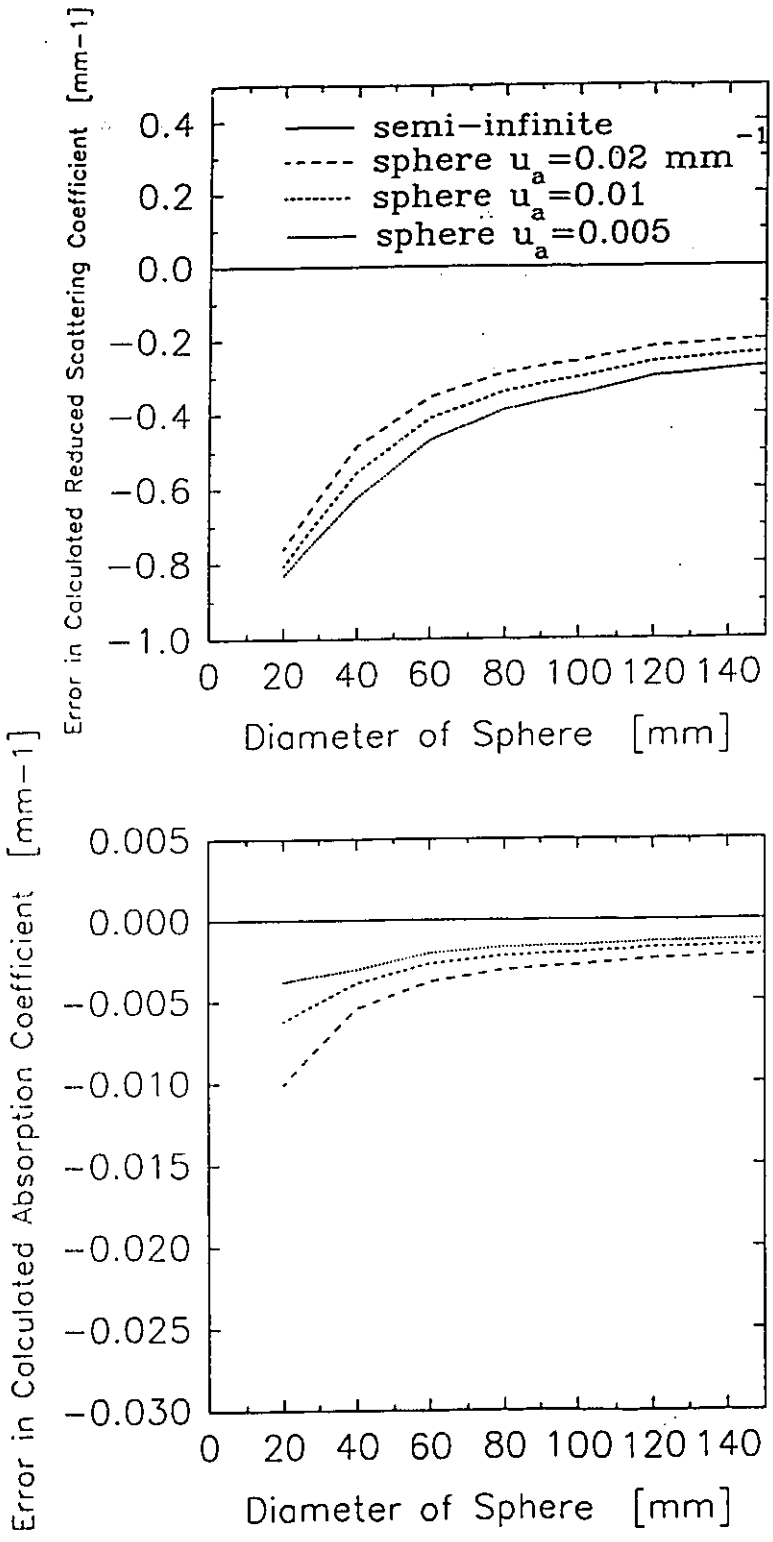

Fig. 11 Calculated systematic errors in μ_a and μ'_s for spherical tissue volumes with $\mu'_s = 1.0$ mm^{-1} and $\mu_a = 0.005, 0.010, 0.020$ mm^{-1}.

standard deviations in μ_a and μ_s' based on the four measurements of phase and intensity at each source-detector distance. The absorption and scattering coefficients at 660 nm are plotted as functions of the total injected dose of $NiPcS_4$ for all three rabbits in Fig. 13.

5. Discussion and Conclusions

While other sources of noise may affect a tissue spectroscopy system, quantum fluctuations in the detected light impose an ultimate limit on performance. As shown in Fig. 2 the system described here operates close to that theoretical limit under typical conditions. The propagation of these experimental uncertainties into the estimates of the tissue optical properties depends strongly on the optical properties themselves and the strategy used to deduce them. The data in Fig. 3 illustrate that a system based on phase and modulation measurements at a single detector position gives acceptable results (say <10% uncertainty in μ_a) only when the absorption coefficient is less than 0.005 mm^{-1} and the scattering coefficient is greater than 1.0 mm^{-1}. Performance degrades rapidly outside this regime, especially when μ_a increases, mainly because there is little demodulation and the uncertainty in this quantity dominates. This could be improved by operating at a higher frequency or higher modulation but, as mentioned above, this was not practical with our arc lamp system. As illustrated in Fig. 4, a more useful strategy is to use two (or more) detector locations. Comparison of Fig. 4a to 3a shows that the regime over which 10% precision in μ_a is achieved is comparable for the two approaches but that the two detector method does not fail catastrophically as μ_a increases. Even better performance can be attained by attenuating the light reaching the near detector so that all the available source power can be used to maximize the signal at the far detector. These measurements would require the use of set of well calibrated neutral density filters or a

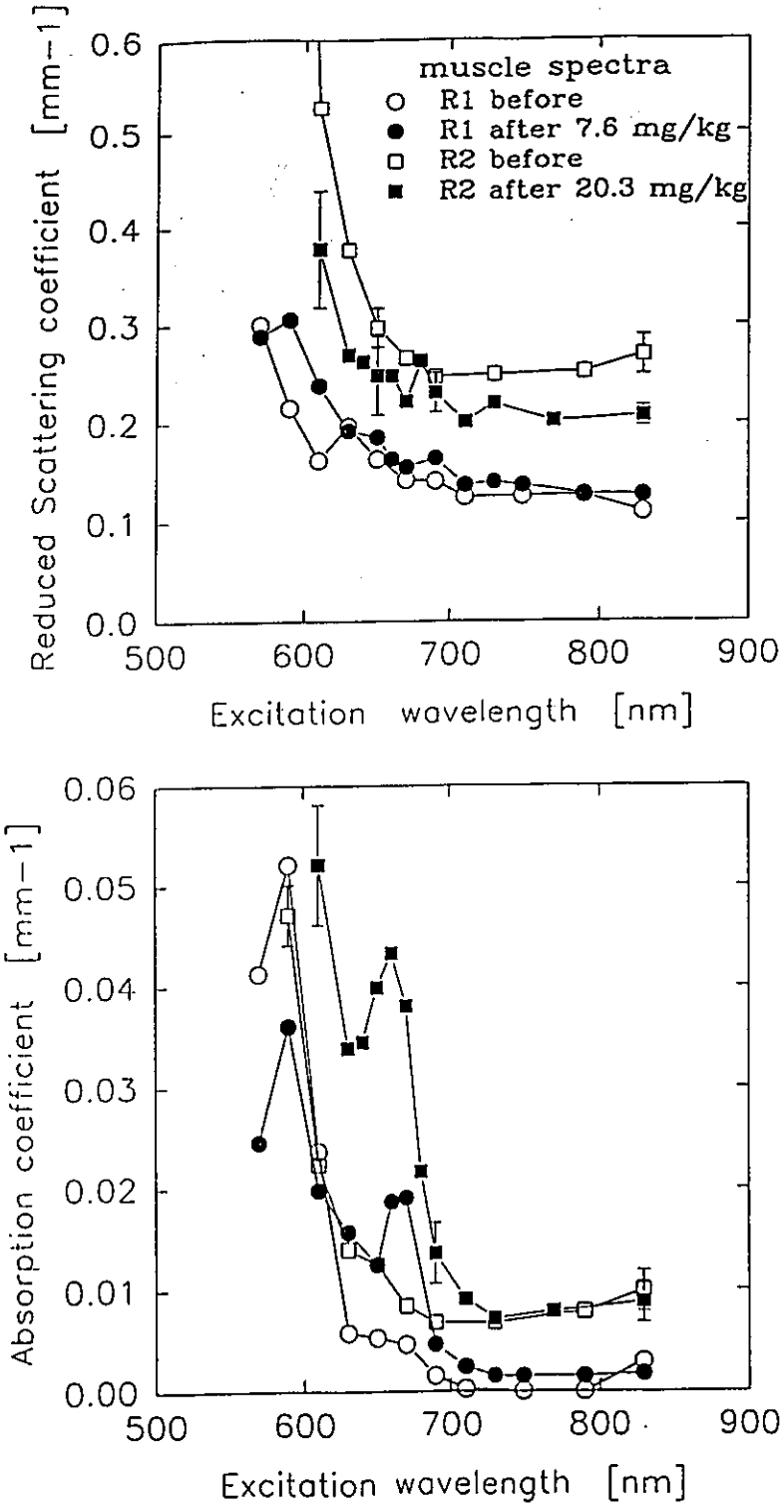

Fig. 12 Reduced scattering and absorption spectra measured on the femoral biceps muscle of two rabbits before (hollow symbols) and after (solid symbols) the injection of $NiPcS_4$. Rabbit #1 (circles) was injected with a total dose of 7.6 mg kg^{-1} and rabbit #2 (squares) received a total dose of 20.3 mg kg^{-1}.

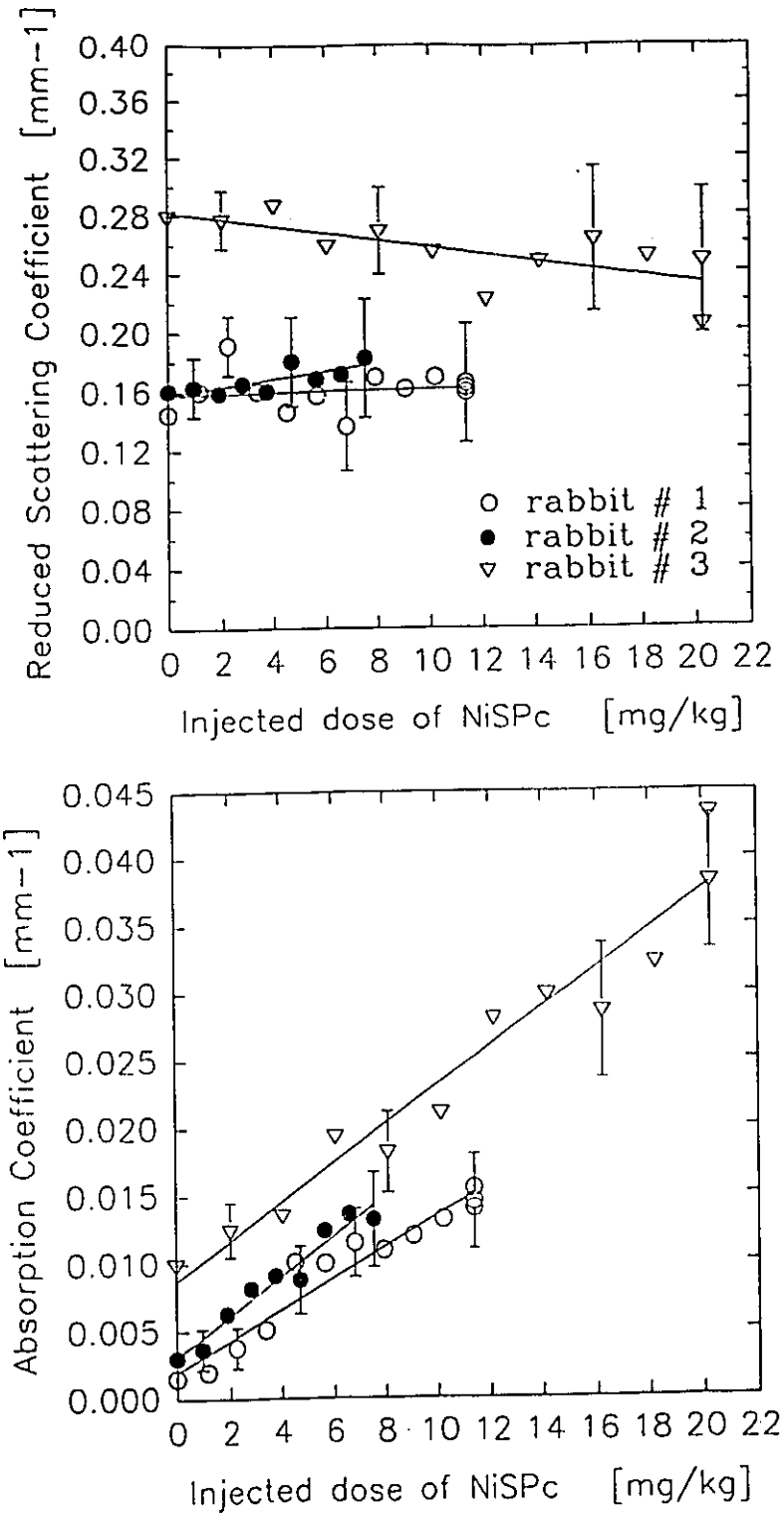

Fig. 13 Reduced scattering and absorption coefficients at 660 nm measured for three rabbits as functions of increasing total injected dose of $NiPcS_4$.

variable attenuator which could be used to keep the signal constant at each photomultiplier tube. This would minimize the errors in the measurement by measuring the attenuation level rather than lowering the amount of light reaching the PMT. We did not do this on our experimental system, but the numerical simulation results presented in Fig. 5 show 10% precision in μ_a can be achieved over a much wider range of tissue optical properties ($\mu'_s > 0.5$ mm^{-1}, $\mu_a < 0.02$ mm^{-1}).

The precision in μ_a at $\mu_a = 0.01$ mm^{-1}, $\mu'_s = 1.0$ mm^{-1}, where the signals at both detectors were equalized, is about 4%. It should be stressed that this is not an absolute limit and that it applies only to a system with the source characteristics described above. In principle, better performance can be achieved by use of a more intense source, a higher modulation frequency, greater modulation depth, or a longer measurement period. For example, as shown in Fig. 6, operation of the system at 500 MHz could yield, at best, 2% precision in μ_a. Increasing the modulation depth to 100% could reduce the uncertainly to 1% (see Fig. 7) while maintaining operation at 135 MHz. This is comparable to the performance reported by Fantini et al. [14] for their fixed wavelength system which employs LED's modulated at 120 MHz. At $\mu'_s = 0.8$ mm^{-1} and $\mu_a = 0.008$ mm^{-1} they estimate the uncertainty in both μ'_s and μ_a to be 1.4%.

Regardless of random experimental uncertainties, systematic errors due to oversimplification of the physical model may be much larger. In this paper we considered only the influence of finite tissue volume on the estimates of μ_a and μ'_s but other factors such as macroscopic tissue heterogeneity could be equally important. For the simplest case, where the tissue volume was considered to be an infinite slab, the effect of using the semi-infinite model in the analysis is an overestimation of μ_a. The reduced scattering coefficient is underestimated, except for very thin slabs. As shown in Fig. 8, the absolute

error in μ_a is only weakly dependent on μ_s. As we showed in a previous paper, this suggests that changes in μ_a can be accurately measured even if the tissue geometry is not well known and not accounted for. For the arrangement considered here (i.e. detectors at 1 and 2 cm) errors in μ_a exceed 10% only when the slab thickness is less than 23 mm for $\mu'_s = 1.0\ mm^{-1}$. For lower values of μ'_s (see Fig. 9) this occurs at a somewhat greater thickness, but a practical "rule-of-thumb" would be to use the semi-infinite model with caution if the tissue thickness is less than the maximum source-detector separation.

The results for cylindrical and spherical tissue volumes are shown in Figs. 10 and 11 respectively. In each case both μ_a and μ'_s are underestimated for objects with diameters between 20 and 150 mm. This is in contrast to our previous results for a one detector (i.e. phase and modulation based) system where μ'_s was underestimated and μ_a was overestimated. The magnitude of the errors is comparable with either approach, although the two detector system is somewhat inferior overall. The finite volume studies were disappointing as we had initially hoped that a two detector system would be less prone to these sorts of errors. This is not the case, however, and the semi-infinite model must be applied with caution, especially if the goal is to recover the absolute absorption and/or scattering coefficient. Of course more complex models can be applied if sufficient information is available about the tissue geometry but this is often not the case in biomedical applications.

In Figs. 12 and 13 we showed how the frequency domain system can be used to address a biological problem: measurement of the uptake kinetics of a dye in a specific organ. While there was considerable variation in the absolute values of μ_a and μ'_s for the muscle itself, the increase in μ_a for a given injected dose of $NiPcS_4$ was similar for all three animals. The increase also depended linearly on total injected dose, which would

be expected since the dye remains in circulation. From measurements of the extinction coefficient of $NiPcS_4$ in a conventional spectrometer we calculated the average concentration of the dye in the muscle and the specific uptake ratio (i.e. ratio of muscle concentration to injected dose). This was 0.104, 0.134 and 0.135 for rabbits 1, 2, 3 respectively. Assuming the total body blood volume to be 60 ml/kg [25] and the average concentration of blood in the muscle to be 1%, the expected uptake ratio would be 0.167, so the results are quite reasonable. No significant change was seen in μ'_s in any of the animals, demonstrating the ability of this approach to measure changes in absorption in the presence of multiple scattering.

The values of μ'_s and μ_a are both low compared to literature values for skeletal muscle but it should be noted that there are few *in vivo* measurements for muscle at all, and none that we are aware of for the rabbit. As discussed above, these absolute values could be subject to significant systematic error caused by the finite tissue volume. Because we pressed a plate onto the surface of the muscle, the measurement geometry more closely resembled a slab rather than a sphere or cylinder. Under these conditions we would expect the scattering coefficient to be underestimated (see Figs. 8, 9) and the absorption coefficient to be overestimated. However, it is unlikely that μ_a could actually be lower than the measured value, because if the blood content is 1% and the hemoglobin oxygenation is 75%, μ_a should be about 0.008 mm^{-1} at 660 nm due to the presence of blood alone [26]. As discussed above, changes in μ_a can be determined more accurately and we believe the uptake measurements to be reliable.

From the *in vivo* data presented in Figs. 12 and 13, the standard deviation in μ_a and μ'_s is typically 20% for a 15 s measurement time. Referring to Fig. 4, the expected errors due to shot noise for $\mu'_s = 0.2$, $\mu_a = 0.01$ would be 30% in μ_a and 15% in μ_s for

a one second data acquisition. Hence the shot-noise contribution to the noise for a 15 s measurement should be only about 8% in μ_a and 4% in μ'_s. This suggests that other sources of variation such as movement or changes in tissue blood content or oxygenation with time were more important than the inherent instrument noise in determining the precision of the μ_a and μ'_s estimates.

6. Acknowledgements

This work was financially supported by the National Institutes of Health Grant PO1-CA 43892. The authors are grateful to Joe Hayward for his assistance with the animal experiments and to Donna Laking for her preparation of the manuscript.

7. References

1. W.F. Cheong, S.A. Prahl and A.J. Welch, "A review of the optical properties of biological tissues", *IEEE J. Quantum Elect.* 26, 2166-2185 (1990).

2. R.A.J. Groenhuis, H.A. Ferwerda and J.J. ten Bosch, "Scattering and absorption of turbid materials determined from reflection measurements. 1: Theory", *Appl. Opt.* 22, 2456-2462 (1983).

3. T.J. Farrell, M.S. Patterson and B.C. Wilson, A diffusion theory model of spatially resolved, steady-state diffuse reflectance for the noninvasive determination of tissue optical properties *in vivo*", *Med. Phys.* 19, 879-888 (1992).

4. S.L. Jacques, A. Gutsche, J. Schwartz, L. Wang and F.K. Tittel, "Video reflectometry to extract optical properties of tissue *in vivo*", in *Medical Optical Tomography: Functional Imaging and Monitoring*, G. Muller ed. pp. 211-226, SPIE Optical Engineering Press, Bellingham (1993).

5. R. Splinter, G.A. Nanney, L. Littman, C.H. Chuang, R.H. Svenson, J.R. Tuntelder and G. P. Tatsis, "Monitoring tissue optical characteristics *in situ* using a CCD camera", *Lasers in the Life Sciences* 6, 15-25 (1994).

6. R.A. Bolt and J.J. ten Bosch, "On the determination of optical parameters for turbid materials", *Waves in Random Media* 4, 233-242 (1994).

7. D.T. Delpy, M. Cope, P. van der Zee, S. Arridge, S. Wray and J. Wyatt, "Estimation of optical pathlength through tissue from direct time-of-flight measurements", *Phys. Med. Biol.* 33, 1433-1442 (1988).

8. M.S. Patterson, B. Chance and B.C. Wilson, "Time-resolved reflectance and transmittance for the noninvasive measurement of tissue optical properties", *Appl. Opt.* 28, 2331-2336 (1989).

9. M. Ferrari, Q. Wei, L. Carraresi, R.A. deBlasi and G. Zacuanti, "Time-resolved spectroscopy of the human forearm", *J. Photochem. Photobiol. B: Biol.* 16, 141-153 (1992).

10. H. Liu, M. Miwa, B. Beauvoit, N.G. Wang and B. Chance, "Characterization of absorption and scattering properties of small-volume biological samples using time-resolved spectroscopy". *Anal. Biochem.* 213, 378-385 (1993).

11. M.S. Patterson, J.D. Moulton, B.C. Wilson, K.W. Berndt and J.R. Lakowicz, "Frequency-domain reflectance for the determination of the scattering and absorption properties of tissue", *Appl. Opt.* 30, 4474-4476 (1991).

12. S.J. Madsen, P. Wyss, L.O. Svaasand, R.C. Haskell, Y. Tadir and B.J. Tromberg, "Determination of the optical properties of the human uterus using frequency-domain photon migration and steady state techniques", *Phys. Med. Biol.* 39, 1191-1202 (1994).

13. S.J. Madsen, E.R. Anderson, R.C. Haskell and B.J. Tromberg, "Portable high-bandwidth frequency-domain photon migration instrument for tissue spectroscopy", *Optics Lett.* 19, 1934-1936 (1994).

14. S. Fantini, M.A. Franceschini-Fantini, J.S. Maier, S.A. Walker, B. Barbieri and E. Gratton, "Frequency-domain multichannel optical detector for noninvasive tissue spectroscopy and oximetry", *Opt. Eng.* 34, 32-42 (1995).

15. E.M. Sevick, B. Chance, J. Leigh, S. Nioka and M. Maris, "Quantitation of time- and frequency-resolved optical spectra for the determination of tissue oxygenation", *Anal. Biochem.* 195, 330-351 (1991).

16. M.S. Patterson, "Noninvasive measurement of tissue optical properties: current status and future prospects", *Comments Mol. Cell Biophys.*, in press.

17. B.W. Pogue and M.S. Patterson, "Frequency-domain optical absorption spectroscopy of finite tissue volumes using diffusion theory", *Phys. Med. Biol.* 39, 1157-1180 (1994).

18. M.S. Patterson, B.C. Wilson and D.R. Wyman, "The propagation of optical radiation in tissue I. Models of radiation transport and their application", *Lasers Med. Sci.* 6, 155-168 (1991).

19. J.D. Moulton, *Diffusion Modelling of Picosecond Laser Pulse Propagation in Turbid Media*, M. Eng. Thesis, McMaster University, Hamilton, Canada, 1990.

20. S.R. Arridge, M. Cope and D.T. Delpy, "The theoretical basis for the determination of optical pathlengths in tissue: temporal and frequency analysis", *Phys. Med. Biol.* 37, 1531-1560 (1992).

21. F.P. Bolin, L.E. Preuss, R.C. Taylor and R.J. Ference, "Refractive index of some mammalian tissues using a fiber optic cladding method", *Appl. Opt.* 28, 2297-2303 (1989).

22. S. Fantini, M.A. Franceschini, J.B. Fishkin, B. Barbieri and E. Gratton, "Quantitative determination of the absorption spectra of chromophores in strongly scattering media: a light-emitting-diode based technique", *Appl. Opt.* 33, 5204-5213 (1994).

23. E. Gratton and M. Linkeman, "A continuously variable frequency cross-correlation phase fluorometer with picosecond resolution", *Biophys. J.* 44, 315-324 (1983).

24. A.B. Carlson, *Communication Systems: An Introduction to Signals and Noise in Electrical Communication*, McGraw Hill, New York, 19865.

25. E.D. Olfert, B.M. Cross and R.A. McWilliam (eds.), *Guide to the Care and Use of Experimental Animals Vol. 1*, Canadian Council on Animal Care, Bradda, Ottawa, Canada, 1993.

26. M. Cope and D.T. Delpy, "System for long-term measurement of cerebral blood and tissue oxygenation on newborn infants by near infra-red transillumination", *Med. Biol. Eng. Comput.* 26, 289-294 (1988).

Introduction to Paper #3

The following paper was stimulated by experiments where the fluorescence of a photosensitizer caused a large disagreement between theory and experiment. The fluorescence quantum yield of some PDT photosensitizers can be quite high, such as the drug used in this study. It was realized that the elimination of fluorescence by filters would be difficult for the case of a small Stokes shift. These preliminary experiments launched the theoretical investigation into modeling diffuse fluorescence signals within tissue. The theoretical expressions were tested by comparison with data measured from tissue phantoms with well known interaction coefficients.

The derivation of the theory was done by jointly Dr. Patterson and myself. The experiments and calculations were done by myself under the supervision of Dr. Patterson. Dr. Patterson wrote the manuscript of the paper.

A MATHEMATICAL MODEL FOR TIME-RESOLVED AND FREQUENCY-DOMAIN FLUORESCENCE SPECTROSCOPY IN BIOLOGICAL TISSUES

Michael S. Patterson[1,2] and Brian W. Pogue[1]

[1] **Hamilton Regional Cancer Centre and McMaster University,**
699 Concession Street,
Hamilton, Ontario, L8V 5C2, CANADA

[2] **Ontario Laser and Lightwave Research Centre,**
Toronto, Ontario, CANADA

Abstract: In general it is not possible to write an analytic expression for the fluorescence signal generated by a fluorophore distributed in a scattering medium such as tissue. However, by assuming the scattering properties of the tissue are the same at the excitation and emission wavelengths, we have derived a simple relationship between the fluorescence and scatter signals. Along with diffusion theory, this was used to write expressions for the fluorescence signal detected at the tissue surface in both the time and frequency domains. Experiments using the fluorophore aluminum chlorosulphonated phthalocyanine in tissue-simulating materials confirmed the accuracy of the model. Applications to *in vivo* spectroscopy are discussed.

Key words: fluorescence spectroscopy, tissue optics, diffusion theory, multiple scattering

I. INTRODUCTION

Fluorescence spectroscopy is a powerful analytic technique which is finding increasing application in medicine (1). Its use has been reported in the diagnosis of the early stages of cancer as well as the differentiation of atherosclerotic plaque from normal vessel endothelium. Fluorescence spectroscopy has also been used *in vivo* to measure the concentration of various exogenous agents such as the photosensitizers used in photodynamic therapy. Most applications have relied on measurement of the steady state emission spectrum with subsequent analysis of the spectrum for the relative concentration of potential fluorophores. A few investigators, however, have explored the use of fluorescence lifetime as a diagnostic tool. It has long been recognized that quantitative measurements of the emission spectrum or (to a lesser extent) the lifetime can be perturbed by multiple scattering of both the excitation and emission light in the host tissue. A typical situation is illustrated in Fig.1 where excitation light of wavelength λ_x is delivered to the tissue at one point (usually by an optical fiber), and emission light is collected at another point at position, $\underline{r}$. Let us describe the photon fluence rate distribution of the excitation light in the tissue by $H(\underline{r}',\mu_{ax}, \mu_{sx}, g_x, n_x, t)$ indicating that it is a function of position $\underline{r}'$, the absorption coefficient μ_a, the scattering coefficient μ_s, the scattering anisotropy parameter g, the index of refraction n and, in the case of non-cw illumination, time t. The subscript on each of the tissue dependent properties indicates that these quantities are functions of wavelength, in this case λ_x. If a fluorophore is distributed throughout the tissue at concentration C, and its extinction coefficient at λ_x is ε_x, the additional absorption coefficient attributable to it is

$$\mu_{fx} = C\varepsilon_x \tag{1}$$

In an infinitesimal time interval dt' at time t', the total number of fluorescence photons

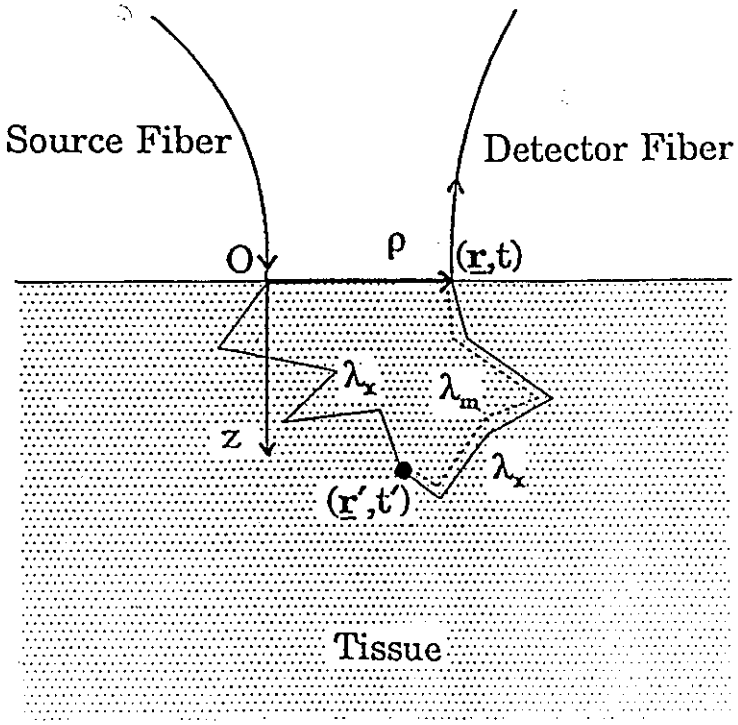

Fig. 1 Schematic illustration of fluorescence spectroscopy in a turbid medium such as biological tissue. Excitation photons (wavelength λ_x) are delivered to the tissue by an optical fiber at the origin, and a fraction of these reach the detector at distance ρ by many different multiple scattering paths. Fluorescence photons (wavelength λ_m) are generated throughout the tissue, and some also reach the detector. If the optical properties of the tissue are identical at λ_x and λ_m, a fluorescence photon generated at location $\underline{r}'$ at time t' has the same probability of being at location $\underline{r}$ at time t as an excitation photon which is also at $\underline{r}'$ at t'.

generated in wavelength interval $d\lambda_m$ in a volume element d^3r' at $\underline{r}'$ is

$$H(\underline{r}', \mu_{ax}+\mu_{fx}, \mu_{sx}, g_x, n_x, t')\ \mu_{fx}\Phi(\lambda_x, \lambda_m)\, d^3r' d\lambda_m$$

where $\Phi(\lambda_x, \lambda_m)$ is the quantum efficiency per unit wavelength for emission at λ_m, given excitation at λ_x. If we now wish to calculate the number of these fluorescence photons which reach the surface at time t and position $\underline{r}$, we must evaluate the escape function $E(\underline{r}-\underline{r}', \mu_{am}+\mu_{fm}, \mu_{sm}, g_m, n_m, t-t')$ which is the probability (per unit time and area) that a photon will reach the surface at $(\underline{r},t)$ if it is emitted at $(\underline{r}',t')$. Note that the escape function depends on the optical properties of the tissue and fluorophore at the emission wavelength. Assuming for the moment that all the fluorescence photons are promptly emitted, we can write the total fluorescence signal per unit time and area, $F_{xm}(\underline{r},t)$ as

$$F_{xm}(\underline{r}, t) = \mu_{fx}\Phi_{xm}\int_{t'}\int_{\underline{r}'} H_x(\underline{r}', t')\, E_m(\underline{r}-\underline{r}', t-t')\, d^3r' dt' \qquad (2)$$

where the explicit dependence of F, H, E and Φ on wavelength is represented by the appropriate subscripts and $\Phi_{xm} = \Phi(\lambda_x, \lambda_m)\, d\lambda_m$. The actual fluorescence decay can be incorporated by convolving $F_{xm}(\underline{r},t)$ with the decay impulse response. Suppose, for example, that the decay can be represented by a single lifetime τ. Then the detected signal can be written as the convolution integral

$$F_{xm}(\underline{r}, t) * \frac{1}{\tau} e^{-t/\tau} \qquad (3)$$

More complicated multi-exponential decays could also be incorporated in a straightforward manner but will not be discussed further in this paper.

It is also possible for observations of fluorescence to be made in the frequency domain rather than the time domain. In this case, the excitation light is amplitude modulated at a frequency f (typically 100 MHz) and the measured quantities are the phase and modulation of the detected fluorescence. Expressions for phase and

modulation can be derived by Fourier transformation of Eqs. (2) and (3) and this will be demonstrated in the next section.

In general, analytic solutions of Eqs. (2) and (3) are not possible. Most models reported to date have considered only the steady-state version of Eq. (2), and a one-dimensional geometry to simplify the volume integral (2-5). It has also been assumed either that both the fluence and escape function decrease exponentially with depth with empirical attenuation coefficients (4,5) or that approximate models of light propagation such as diffusion theory or the Kubelka Munk equation can be used to describe the propagation of light in the tissue (2,3,6). Of course direct solutions can be produced by Monte Carlo simulation (7) but this can be very time-consuming and provides little physical insight into the problem.

In this paper we develop a different approach for the case where the scattering properties of the tissue can be assumed to be the same at λ_x and λ_m but the absorption coefficient is different. It is known that in the visible and near infrared portion of the spectrum μ_s and g are slowly varying functions of wavelength (8) so that this assumption is justified if $\lambda_m - \lambda_x \leq 100$ nm. We will show that under these circumstances, a simple relationship exists between the fluorescence and excitation photon fluences which eliminates the need to evaluate the volume integral in Eq.(2). This has also recently been shown by Wu et al(9), although their derivation is somewhat different as noted below. We will use this general relationship plus the diffusion approximation to develop expressions for the fluorescence signal detected under the conditions of Fig.1 in the time and frequency domains.

Experimental measurements of phase and modulation of both excitation and emission light were made in tissue-simulating phantoms. These measurements

showed that the model provided accurate predictions for these parameters as functions of modulation frequency and source-detector separation. We expect the model to be most useful in situations where λ_x, $\lambda_m > 600$ nm as diffusion theory is most accurate in this regime. Immediate applications of the model include i) correction of emission spectra for scattering and absorption in the host tissue, ii) correction of fluorescence lifetime measurements for the influence of light propagation in the tissue and (iii) correction of time-resolved light scattering measurements for the effect of fluorescence.

II. THEORY

Our first task is to derive a relationship between the density of excitation photons (i.e. number of photons per unit volume) and the density of fluorescence photons in a multiple scattering medium such as tissue, for the case of an impulse source of excitation at t = 0. The emission of a fluorescence photon is in reality a discrete event which may occur after absorption of an excitation photon. If we are dealing with an ensemble of many photons, however, we can regard fluorescence emission as a continuous process. Hence, for every excitation photon which is in the medium during the time interval dt', $(\mu_{fx}\, \Phi_{xm}\, c\, dt')$ fluorescence photons are generated in the detection bandpass $d\lambda_m$.

Consider first the case where the optical properties of the medium are identical at the excitation and emission wavelengths and where fluorescence emission is prompt. Once a fluorescent photon is generated, it will propagate (on average) through the medium exactly as the excitation photon from which it arose as illustrated in Fig. 1. Thus, for every excitation photon which is in the medium during the time interval $(t', t' + dt')$ and which is subsequently found in a volume element d^3r about $\underline{r}$ at time t, the

number of fluorescence photons found in d^3r about $\underline{r}$ at time t will be ($\mu_{fx}\ \Phi_{xm}\ c\ dt'$). In the case of non re-entrant boundaries, any excitation photon which is in d^3r about $\underline{r}$ at t must have been in the medium at all times in the interval (0, t). Calculation of the fluorescence photon density therefore simply requires integration of the contributions arising from all possible time intervals dt'. Representing the excitation photon density by $N_x(\underline{r},t)$ and the fluorescence photon density by $N_f(\underline{r}, t)$ we can write

$$\frac{N_f(\underline{r}, t)}{N_x(\underline{r}, t)} = \mu_{fx}\Phi_{xm}c\int_0^t dt' \qquad (4)$$

$$= \mu_{fx}\Phi_{xm}c\,t \qquad (5)$$

In deriving this relationship we have ignored the fact that fluorescence photons are emitted isotropically whereas the angular flux (or radiance)of excitation photons may be anisotropic. Strictly speaking, this would mean that excitation and emission photons do not have equal probability of reaching $\underline{r}$ at time t even if they are both at r' at time t'. We will return to this point in Section 5, but note here that we do not expect this difference to be significant if the photons undergo many scattering events before detection.

Now let us consider the case where we allow the absorption coefficient of the medium to be wavelength dependent, but assume that the scattering properties are independent of wavelength. A fluorescence photon which is generated at time t' and is subsequently detected at time t will have travelled a distance c(t-t') in the medium. Its probability of survival without absorption is exp [- (μ_{am} + μ_{fm}) c (t-t')] whereas the corresponding probability for an excitation photon is exp [- (μ_{ax} + μ_{fx}) c (t-t')]. Therefore, for every excitation photon in d^3r about $\underline{r}$ at t, there are exp [(β_x - β_m) (t-t')] $\mu_{fx}\ \Phi_{xm}$ c

dt' fluorescence photons which were created during dt' where

$$\beta_x = c(\mu_{ax} + \mu_{fx}) \tag{6}$$

$$\beta_m = c(\mu_{am} + \mu_{fm}) \tag{7}$$

The ratio of total fluorescence photon density to excitation photon density is given by the integral

$$\frac{N_f(\underline{r}, t)}{N_x(\underline{r}, t)} = \mu_{fx}\Phi_{xm}c\int_0^t e^{(\beta_x-\beta_m)(t-t')}dt' \tag{8}$$

$$= \frac{\mu_{fx}\Phi_{xm}c}{\beta_x-\beta_m}\left[e^{(\beta_x-\beta_m)t}-1\right] \tag{9}$$

Eq.(9) can be expressed in an alternate form by noting that

$$N_x(\underline{r}, t) = N_o(\underline{r}, t)\, e^{-\beta_x t} \tag{10}$$

where N_o ($\underline{r}$, t) is the photon density that would be observed in a conservative (i.e. nonabsorbing) medium. Substitution of Eq. (10) into Eq. (9) leads to

$$N_f(\underline{r}, t) = \frac{\mu_{fx}\Phi_{xm}c}{\beta_x-\beta_m} N_o(\underline{r}, t)\left(e^{-\beta_m t}-e^{-\beta_x t}\right) \tag{11}$$

$$= \frac{\mu_{fx}\Phi_{xm}c}{\beta_x-\beta_m}\left[N_m(\underline{r}, t) - N_x(\underline{r}, t)\right] \tag{12}$$

where N_m ($\underline{r}$, t) is the excitation photon density that would be observed if the excitation wavelength were changed to λ_m. Eq.(12) is very similar to the expression derived by Wu et al.(9) except that their independent variable was the number of photon interactions in the medium rather than the continuous variable of elapsed time. The two approaches can be shown to be equivalent in cases where photons undergo a large number of interactions before detection. Equation (9) applies for an impulse excitation source, but since a source extended in time or space can be regarded as a superposition of such impulses, it has a

wider utility. A case of particular interest is cw excitation for which Eq.(12) reduces to

$$N_f(\mathcal{L}) = \frac{\mu_{fx}\Phi_{xm}C}{\beta_x-\beta_m}\left[N_m(\mathcal{L}) - N_x(\mathcal{L})\right] \tag{13}$$

where suppression of the time dependence implies that each term in Eq.(12) has been integrated over time from 0 to ∞.

We also note that Eq.(9) can be modified to include delayed fluorescence as stated explicitly in Eq.(3).

The development so far has been general, in the sense that no approximate model of radiation transport has been used in the derivation. In the remainder of this section, we will derive explicit equations for the fluorescence signal by using the diffusion approximation to first generate an analytic expression for the excitation photon fluence rate. We will restrict our attention to the geometry of Fig.1, i.e. we assume that a spatial and temporal impulse of excitation light is incident on the surface of a semi-infinite tissue block which has spatially invariant optical properties and which contains a fluorophore uniformly distributed at a concentration C. We will calculate the fluorescence signal (number of photons per unit area per unit time) reaching the tissue surface at a distance ρ from the source. For simplicity we will assume that the photon fluence rate at the surface is zero. More exact boundary conditions can be incorporated by establishing an extrapolated boundary at which the fluence rate is zero (10) but the additional complication does not significantly change the results presented here.

As discussed by Patterson et al. (11), an expression for the excitation photon fluence rate in the tissue under these conditions, H_x (ρ, z, t), can be derived by the method of images. The number of excitation photons reaching the surface per unit area per unit time, R_x (ρ, t), can then be calculated by Fick's law (12) as

$$R_x(\rho, t) = -D\frac{\partial}{\partial z}H_x(\rho, z, t)\Big|_{z=0} \tag{14}$$

and has been given by Patterson et al. (11) for a unit impulse source as

$$R_x(\rho, t) = \frac{z_o}{(4\pi Dc)^{3/2}}\, t^{-5/2}\exp\left(-\frac{\rho^2+z_o^2}{4Dct}\right)e^{-\beta_x t} \tag{15}$$

$$z_o = \frac{1}{\mu_s(1-g)} \tag{16}$$

where

$$D \cong \frac{1}{3\mu_s(1-g)} \tag{17}$$

To calculate the number of fluorescence photons reaching the surface per unit area per unit time we use Eq.(9) to calculate the fluorescence photon fluence rate and then Eq.(14) to yield

$$F_{xm}(\rho, t) = \frac{\mu_{fx}\Phi_{xm}cz_o}{(4\pi Dc)^{3/2}(\beta_x-\beta_m)}\, t^{-5/2}\exp\left(-\frac{\rho^2+z_o^2}{4Dct}\right)\left(e^{-\beta_m t}-e^{-\beta_x t}\right) \tag{18}$$

Note that Eq.9 applies to the photon fluence rate as well as the photon density (12), since H = cN. Delayed fluorescence could be included in this equation by an appropriate convolution but this does not lead to a closed form for F_{xm} (ρ, t). In the frequency domain, however, this convolution is reduced to a multiplication and analytic forms can be derived. In the next section such equations will be derived which can be tested by direct measurement.

In the frequency domain, where the source is modulated at a frequency f, the observable quantities are i) the phase delay between the signal and the excitation source θ(f) and ii) the modulation of the signal relative to the modulation of the source, M(f). More specifically

$$M(f) = \frac{Sig(f)}{Sig(0)}\cdot\left(\frac{Src(f)}{Src(0)}\right)^{-1} \tag{19}$$

where Sig(f) is the AC component of the signal at frequency f, Sig (0) is the DC component of the signal, Src (f) is the AC component of the source at frequency f and Src (0) is the DC component of the source. The modulation and phase of the excitation light, M_x (ρ, f) and θ_x (ρ, f) can be found by Fourier transformation of Eq.(15) and the corresponding quantities M_f (ρ, f) and θ_f (ρ, f) for the fluorescent light by a similar treatment of Eq.(18). Using the notation of an earlier paper by Patterson et al. (13), the Fourier transform of R_x (ρ, t) which we will denote by R_x (ρ, f) can be written as

$$\widetilde{R}_x(\rho, f) = \frac{z_o e^{-\psi_i}(1+\psi_o^2+2\psi_i)^{1/2}}{2\pi(\rho^2+z_o^2)^{3/2}} \left(\begin{array}{l} \cos\left[\psi_r - \tan^{-1}\left(\frac{\psi_r}{1+\psi_i}\right)\right] \\ + i\sin\left[\psi_r - \tan^{-1}\left(\frac{\psi_r}{1+\psi_i}\right)\right] \end{array} \right) \quad (20)$$

where

$$\psi_o = \left[\frac{(\rho^2+z_o^2)\sqrt{\beta_x^2+(2\pi f)^2}}{Dc}\right]^{1/2} \quad (21)$$

$$\psi_i = \psi_o \cos\left[\frac{1}{2}\tan^{-1}\left(\frac{2\pi f}{\beta_x}\right)\right] \quad (22)$$

$$\psi_r = -\psi_o \sin\left[\frac{1}{2}\tan^{-1}\left(\frac{2\pi f}{\beta_x}\right)\right] \quad (23)$$

The phase and modulation are calculated from the real and imaginary parts of the Fourier transform as

$$\theta_x(\rho, f) = \tan^{-1}\frac{\mathbb{I}m[\widetilde{R}_x(\rho, f)]}{\mathbb{R}e[\widetilde{R}_x(\rho, f)]} \quad (24)$$

and $$M_x(\rho, f) = \left(\frac{\mathbb{R}e^2[\widetilde{R}_x(\rho, r)] + \mathbb{I}m^2[\widetilde{R}_x(\rho, f)]}{\mathbb{R}e^2[\widetilde{R}_x(\rho, 0)] + \mathbb{I}m^2[\widetilde{R}_x(\rho, 0)]}\right)^{1/2} \quad (25)$$

By comparing Eqs.(18) and (12) it can be seen that the Fourier transform of F_{xm} (ρ, t) can be written as

$$\tilde{F}_{xm}(\rho, f) = \frac{\mu_{fx}\Phi_{xm}C}{\beta_x - \beta_m}\left[\tilde{R}_m(\rho, f) - \tilde{R}_x(\rho, f)\right] \tag{26}$$

where R_m (ρ, f) has the form of Eq. (20) except that all absorption dependent quantities are evaluated at λ_m. Incorporation of fluorescence decay with a single lifetime τ can be included by multiplying the expression in Eq.(26) by the Fourier transform of $\tau^{-1}\exp(-t/\tau)$ so we have

$$\tilde{F}_{xm}(\rho, f) = \frac{\mu_{fx}\Phi_{xm}C}{\beta_x - \beta_m}\left[\tilde{R}_m(\rho, f) - \tilde{R}_x(\rho, f)\right]\cdot\left[\frac{1 - i2\pi f\tau}{1 + (2\pi f\tau)^2}\right] \tag{27}$$

The phase and modulation can be straightforwardly evaluated from the real and imaginary parts as shown in Eqs. (24) and (25). Finally, we note that under some experimental conditions described below, the detector receives both the excitation signal R_x (ρ, f) and the fluorescence signal F_{xm} (ρ, f). In this case the Fourier transform of the total signal, denoted by T_{xm} (ρ, f) is given by

$$\tilde{T}_{xm}(\rho, f) = \tilde{R}_x(\rho, f) + \frac{\mu_{fx}\Phi_{xm}C}{\beta_x - \beta_m}\left[\tilde{R}_m(\rho, f) - \tilde{R}_x(\rho, f)\right]\cdot\left[\frac{1 - i2\pi f\tau}{1 + (2\pi f\tau)^2}\right] \tag{28}$$

3. EXPERIMENTAL METHODS

The purpose of the experiments was to test the predictions of Eqs.(20), (27) and (28) by making measurements of phase and modulation in the

geometry of Fig.1 using a tissue-simulating phantom. We first describe the methods used to determine the quantities required in the model (μ_{ax}, μ_{am}, μ_{fx}, μ_{fm}, D, Φ_{xm}, τ, n) and then the apparatus used to measure phase and modulation.

3.1 Optical properties of Tissue-Simulating Medium and Fluorophores

The fluorophore used in the experiments was aluminum chlorosulphonated phthalocyanine (AlSPC) (Porphyrin Products, UT) with an average sulphonation per phthalocyanine molecule of 3.5. This material is under active investigation by a number of groups as a photosensitizer for photodynamic therapy (14). The absorption spectrum and fluorescence emission spectrum (for excitation at 650 nm) were measured by standard spectrometric techniques using 0.25 μg ml^{-1} AlSPC in 0.9% phosphate buffered saline (PBS) and are illustrated in Fig.2. The fluorescence quantum yield was not measured but the value of 0.58 reported by Brannon and Magde (15) for AlSPC in 1-chloronaphthalene was used in the calculations. The absorption coefficient of the fluorophore at the emission wavelength (μ_{fm}) is also required. If the detection bandpass is small, an appropriate value can be determined from Fig.2. In some experiments described below, however, no wavelength discrimination was used on the detector. Under these conditions, we could calculate the fluorescence signal in discrete emission wavelength intervals, and take the complex sum of these components to get the total fluorescence signal. For simplicity, however, we considered the emission to be effectively monochromatic and used an average value of μ_{fx} which was

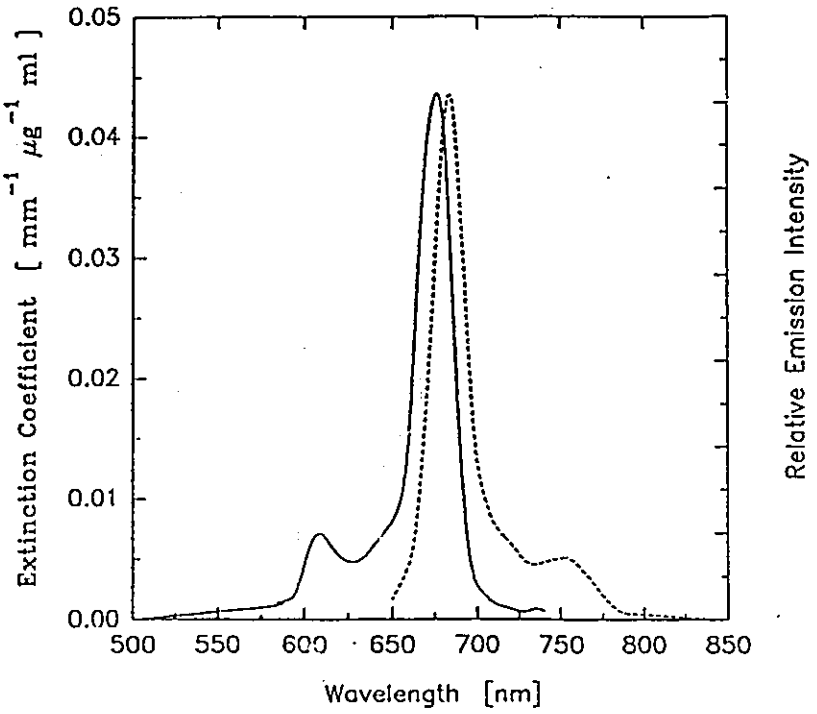

Fig. 2 Extinction coefficient (solid line) and fluorescence emission spectrum (excitation wavelength 650 nm) for aluminum chlorosulphonated phthalocyanine (AlSPC) in saline. The emission spectrum has not been corrected for the wavelength dependent response of the detector. Since the same detector is used for all experiments, however, this correction is not required in the calculations described in the text.

determined by weighting the measured absorption coefficient by the emission spectrum, $I_m(\lambda)$, in Fig. 2. Explicitly

$$\langle \mu_{fx} \rangle = \frac{\int \mu_{fm}(\lambda)\, I_m(\lambda)\, d\lambda}{\int I_m(\lambda)\, d\lambda} = 0.0228 mm^{-1} \mu g^{-1} ml \qquad (29)$$

We also need τ, the lifetime of the AlSPC fluorescence. This was determined from measurements of phase and modulation (see below) made on a 1 cm cuvette containing 0.25 μg ml^{-1} AlSPC in 0.9% PBS, a standard method described by Lakowicz et al. (16). The value of 6.8 $\pm$ 0.3 ns obtained by us is in good agreement with the result τ = 6.8 $\pm$ 0.6 ns reported by Brannon and Magde (15) in 1-chloronaphthalene and suggests that the quantum yield is also similar in the two solvents.

The tissue-simulating material consisted of an aqueous suspension of phospholipids to which variable amounts of India ink were added to control the absorption coefficient. The phospholipid suspension consisted of 1% Intralipid (Kabivitrum, CA) in de-ionized water. The scattering properties of this material have recently been studied by van Staveren et al. (17) and we used their polynomial expression to generate values of D. The absorption coefficient of the tissue-simulating material is the sum of that due to the added ink and a small contribution from the Intralipid suspension. The absorption coefficient of ink was measured using the techniques of Madsen et al. (18). While the details will not be repeated here, it should be noted that measurements of transmission in a spectrophotometer are not sufficient, because the ink particles also scatter light.

The absorption coefficient of Intralipid itself is very low and Driver et al. (19) have determined that, at 630 nm, it is not significantly different from that of water. We assumed, therefore, that the absorption of the Intralipid emulsion was equal to the values tabulated by Hale and Querry (20) for pure water.

3.2 Measurement of Phase and Modulation

A schematic diagram of the experimental system is shown in Fig.3. The light source was either a HeNe laser (632.8 nm) or an arc lamp / monochromator combination (ISS, Urbana IL). The collimated light was modulated by a Pockel's cell, passed through a 92%/8% beam splitter and then focused onto a 1.6 mm diameter optical fiber bundle. This bundle transmitted light to the surface of the tissue-simulating phantom, which consisted of a black plexiglass tank 20 x 20 x 12 cm filled with the Intralipid/ink/AlSPC suspension described above. An identical fiber bundle was positioned on the phantom surface at a variable separation and the distal end of this bundle was coupled to a photomultiplier tube (PMT) (R928, Hamamatsu). An identical PMT was used to generate a reference signal from the other arm of the source beam. As shown in Fig. 3 it was possible to insert a bandpass filter in front of the detector PMT to reject either fluorescent or excitation light.

The modulation frequency of the Pockel's cell could be varied up to 140 MHz. The gain of the PMT's was modulated at a frequency offset 100 Hz from the Pockel's cell frequency by altering the voltage across two of the dynodes.

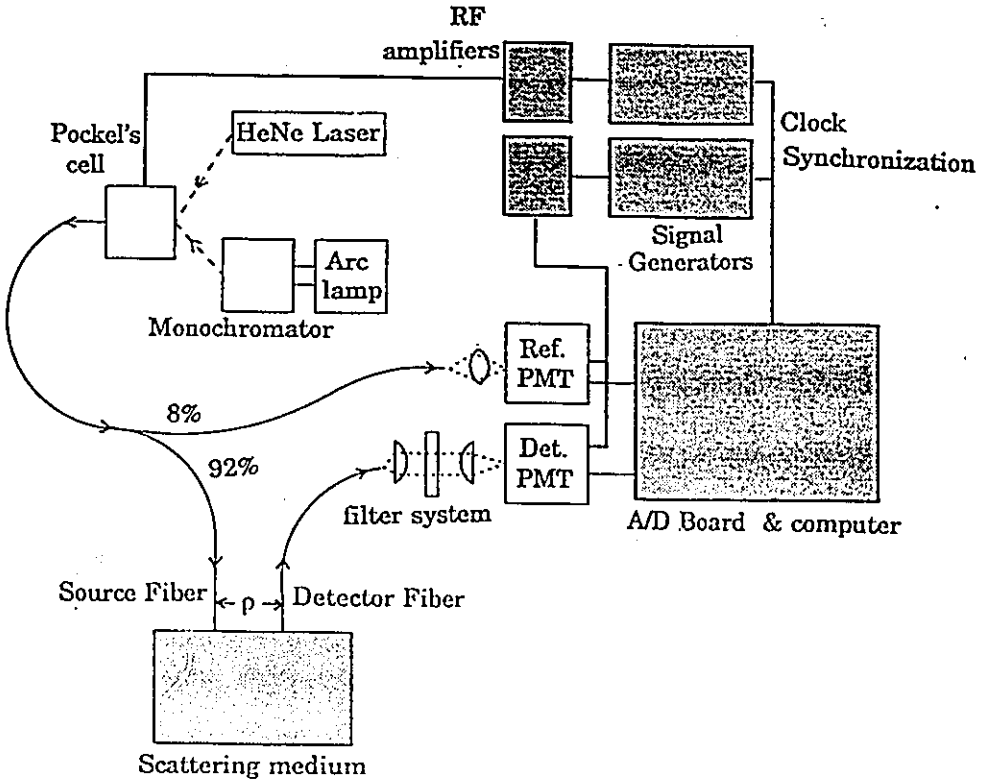

Fig. 3 Schematic diagram of the frequency-domain system. Selection of the filter in front of the detector PMT permits the measurement of scattered light alone, fluorescent light alone, or the sum of these two components.

As explained by Gratton et al. (21), phase and modulation information is retained in the two 100 Hz heterodyne signals and these signals are amplified, sampled and digitized by a commercial board (ISS, Urbana) installed in a personal computer. Proprietary software (ISS, Urbana) was used to process the signals and extract phase and modulation data. The principles of the signal processing have been described by Federsen et al. (22).

4. RESULTS

We first present measurements of modulation and phase of the scattered excitation light, the fluorescent light and the scattered plus fluorescent light as functions of the source-detector separation. The phantom for this experiment consisted of 1% Intralipid plus 0.5 μg ml^{-1} AlSPC. No ink was added to this mixture so that the signals could be measured over as large a distance range as possible. The minimum source-detector separation was determined by the outer diameter of the optical fiber bundles. The light source was a HeNe laser (632.8 nm) and modulation frequencies of 60 and 140 MHz were used. In order to measure only scattered light, a 630 nm, 10 nm bandpass interference filter was placed in front of the detector PMT as shown in Fig.3. To measure a pure fluorescence signal, this filter was replaced by a 680 nm, 10 nm bandpass filter. Measurements of the total (i.e. scatter plus fluorescence) signal were made by removing all filters. Calculations of the modulation and phase of the scattered light versus distance were made with Eq.(20) using D = 0.258 mm (the value of

van Staveren et al. (17) at 630 nm), μ_{fx} = 0.0025 mm^{-1} (the AlSPC absorption coefficient according to Fig. 2), and c = 225 mm ns^{-1} (the speed of light in water). The modulation and phase of the fluorescence signal were predicted using Eq. (27), with D = 0.269 nm (the mean of van Staveren's values for 630 and 680 nm) and c = 225 mm ns^{-1} as above, μ_{fm} = 0.021 mm^{-1} at 680 nm, and τ = 6.8 ns. The expression in Eq. (28) was used to calculate modulation and phase of the total signal using the parameters above except that μ_{fm} = 0.0114 mm^{-1} as in Eq. (29), since no wavelength discrimination was used at the detector. The quantum yield is also required in this calculation and, as discussed above, Φ_{xm} = 0.58 was used. Experimental results are compared with theoretical predictions in Fig. 4a (for 60 MHz modulation) and Fig. 4b (for modulation at 140 MHz). The following observations can be made from these data:

i) Predictions of the model for all three types of signal (scatter, fluorescence, total) are within the experimental uncertainties, and the performance of the model is quite good overall. Note that the experimental uncertainties increase with ρ because the magnitude of all signals decreases as the detector - source separation is increased.

ii) As described by Patterson et al. (13), the phase of the scatter signal increases with ρ due to the propagation delay, and the modulation decreases due to the greater attenuation of the AC component compared to the DC component. This attenuation increases with modulation frequency so the effect is more pronounced at 140 MHz than 60 MHz.

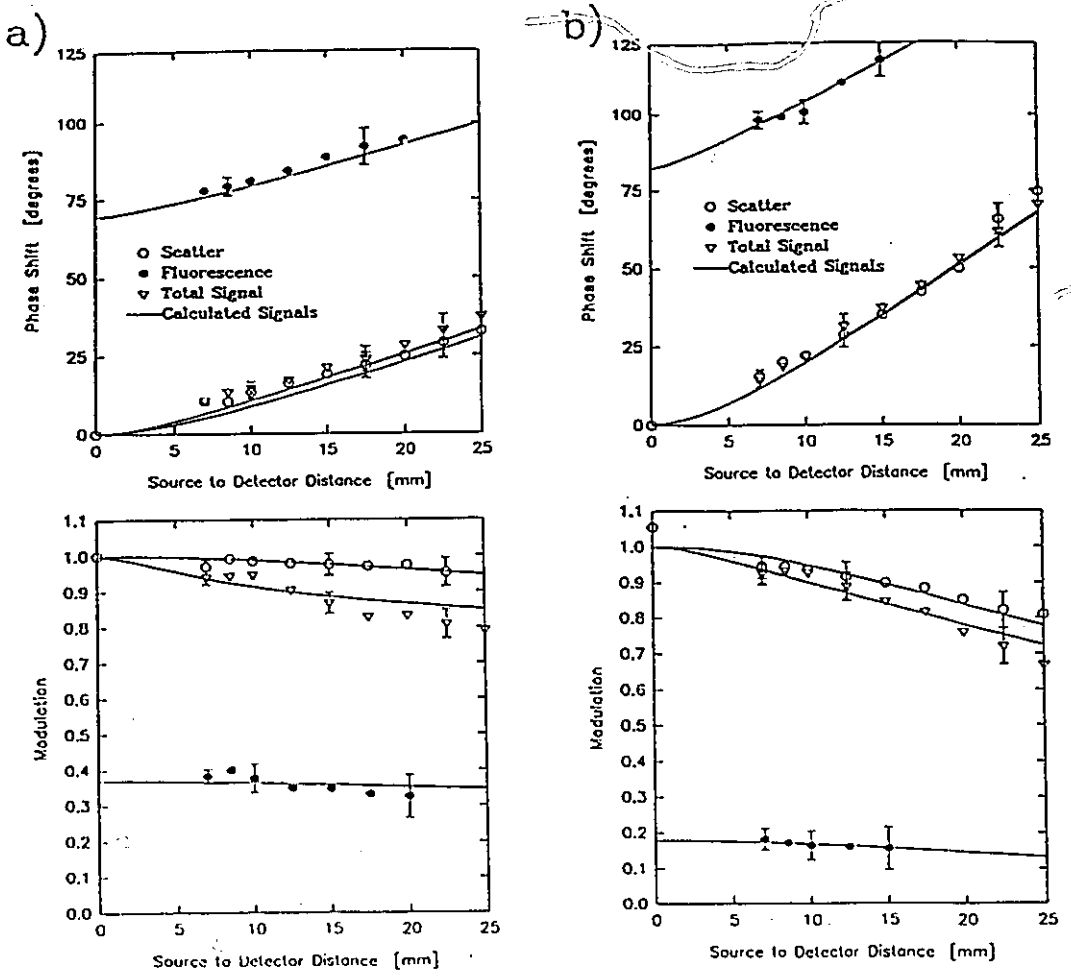

Fig. 4 Measurements of the phase and modulation of scattered light, fluorescent light and scatter plus fluorescence as functions of source-detector distance. The smooth lines are the result of calculations described in the text. Measurements were performed at a) 60 MHz and b) 140 MHz. The phantom consisted of 1% Intralipid plus 0.5 μg ml^{-1} AlSPC. The excitation wavelength was 633 nm and the fluorescence component was detected at 680 nm. For the measurement of scatter plus fluorescence, no wavelength discrimination was employed.

iii) The phase and modulation of the fluorescence signal at $\rho = 0$ is due almost entirely to the finite lifetime of AlSPC fluorescence as little propagation in the turbid medium is involved. As ρ increases, the phase increases almost in parallel with that of the scatter signal. This is not generally true (see below), but in this case the absorption of fluorescent light at 680 nm is more likely than the absorption of scattered light at 630 nm (see Fig. 2). Hence most of the fluorescent light "seen" by the detector is generated relatively close to the detector and its propagation delay is characteristic of the excitation light. If the relative magnitudes of absorption coefficients at λ_x and λ_m were interchanged, the phase shift of the fluorescence signal would be considerably larger. The relative change in modulation with ρ is also about the same for the fluorescence and scatter signals.

iv) The total signal plotted in Figs. 4a and 4b consists of the complex sum of the scatter signal and the fluorescence signal at all wavelengths. Because the absorption of fluorescence light is more likely than that of scattered light in this case, the fluorescence component is relatively small and the modulation and phase of the total signal is not very different from that of the scatter signal. Note, however, that the modulation appears to be more sensitive to the presence of this small component than the phase. The situation is quite different when the absorption coefficient at λ_m is comparable to, or lower than, that at λ_x. In Fig. 5 we show the behavior

of the total signal for the same phantom when excitation is performed at 670 nm, close to the peak of the AlSPC absorption coefficient. (In this case, separation of the fluorescence and scatter signals is not possible because of the overlap shown in Fig. 2.) Here the modulation and phase diverge rapidly from the prediction for the scatter signal alone because of the greater magnitude of the fluorescence component. In this case, there is also a systematic disagreement between the experimental results and the predictions based on Eq.(28). This can be attributed to the simple assumption that the fluorescence is effectively monochromatic and that we can use the single absorption coefficient in Eq.(29) to describe its propagation. If instead we divide the fluorescence emission into 10 nm bands, assign an absorption coefficient to each band from Fig.2, and calculate the fluorescence as the complex sum of the contribution from each band, the predictions of modulation and phase are in very good agreement with experiment. This complication is necessary in this case because absorption in the phantom is due almost solely to AlSPC, and therefore varies strongly with wavelength.

A more realistic phantom was prepared by adding sufficient ink to increase the absorption coefficient (without AlSPC) to 0.015 mm^{-1}, a value typical of soft tissues at these wavelengths (8). Measurements of phase and modulation, shown in Fig.6, were made before and after the addition of 0.5 $\mu g\ ml^{-1}$ AlSPC, the

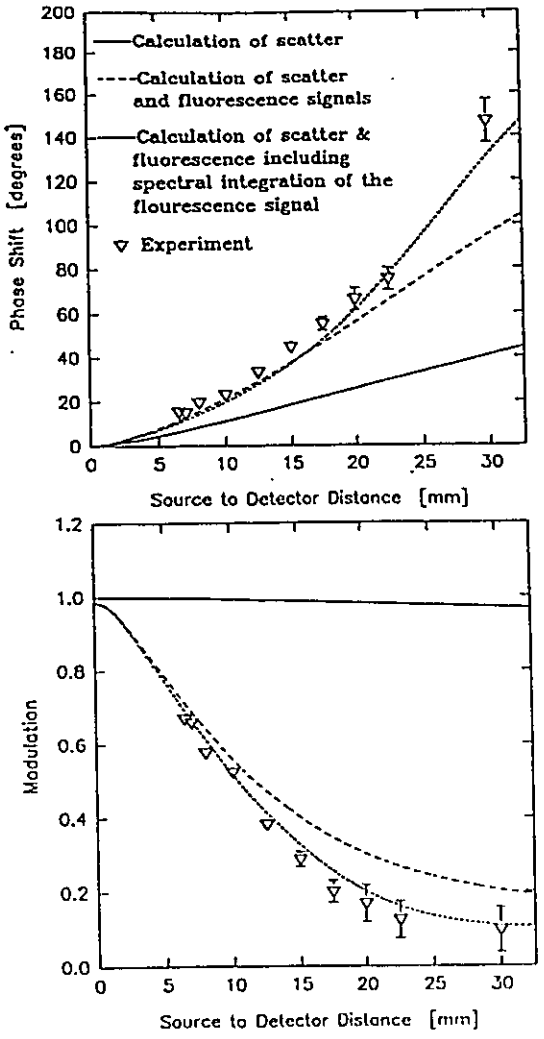

Fig. 5 Measurements of phase and modulation of the total (i.e. scatter plus fluorescence) signal under the same conditions as Fig.4 except that the excitation wavelength was 670 nm. In this case, good agreement with experimental results was achieved when the model was used to calculate the components of fluorescence in 10 nm wavelength intervals. These components were then summed at each source-detector distance to estimate the total signal.

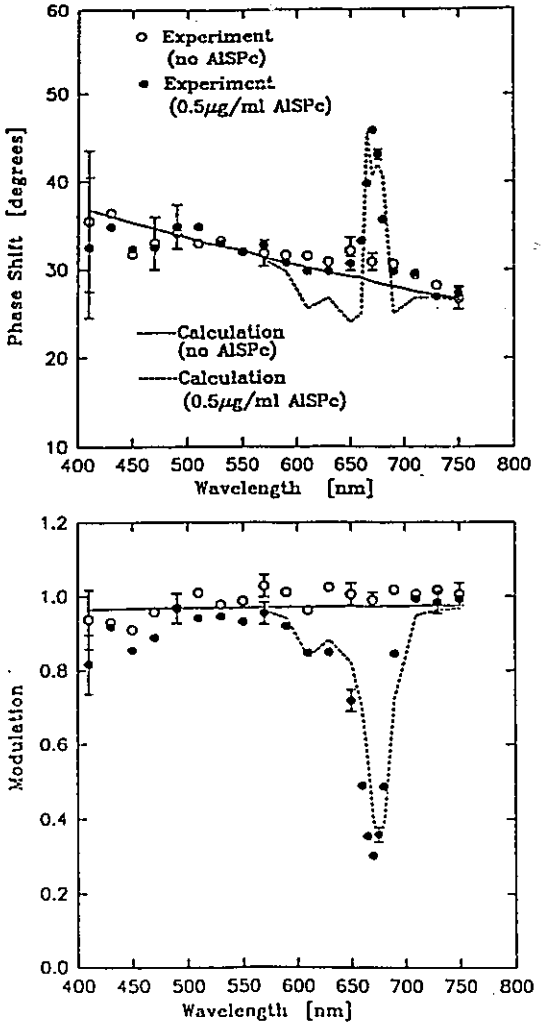

Fig. 6 Measurements of phase and modulation of fluorescence plus scatter as functions of the excitation wavelength. The phantom consisted of 1% Intralipid plus sufficient India ink to increase the absorption coefficient to 0.015 mm^{-1}. Measurements were performed before and after the addition of 0.5 μg ml^{-1} AlSPC. The source-detector separation was 20 mm.

source-detector separation was fixed at 20 mm and the excitation wavelength was scanned from 400 to 750 nm. Calculations of modulation and phase before the addition of AlSPC were made at each excitation wavelength by assuming that μ_{ax} = 0.015 mm^{-1} (the ink absorption coefficient varies little with wavelength over this range) and that D was given by the expression of van Staveren et al. (17). Agreement between experiment and theory is good over the entire wavelength range. It is interesting to note that the phase decreases with wavelength because of the increase of *D*, but that the modulation is almost completely insensitive to this change in the scattering properties. Calculation of the modulation and phase after the addition of AlSPC was performed as described above. The value of *D* used at each wavelength was the mean of those reported by van Staveren et al. for λ_x and 680 nm, the wavelength of maximum fluorescence emission. The agreement with experiment is quite good except for the phase in the 600 - 650 nm band. Some of this disagreement could be attributed to the fairly large bandpass of the source (14 nm) which would tend to smooth features predicted by the theoretical expression.

As a final test of the model in Fig. 7, we plot the relative ratio of the *DC* component of fluorescence to the *DC* component of the scatter for the same experimental conditions which applied to Figs. 4a and 4b, i.e. excitation at 630 nm and detection at either 630 (scatter signal) or 680 (fluorescence signal). Both experimental data and theoretical predictions have been normalized to the ratio at ρ = 35 mm, the largest source - detector distance. (We did not attempt

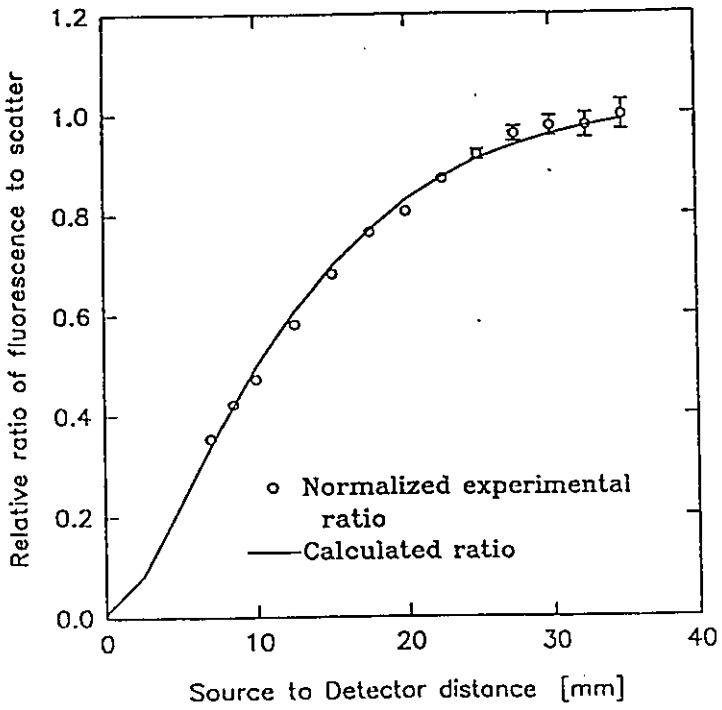

Fig. 7 Ratio of steady state fluorescence (at 680 nm) to steady state scatter (633 nm) versus source-detector separation. Experimental conditions were the same as for Fig.4. Both the experimental data and the model predictions have been normalized to their respective values at ρ = 35 nm.

to measure the absolute fluorescence/scatter ratios because our experimental set-up made it difficult to change filters quickly and reproducibly.) The model accurately predicts the relative increase of the fluorescence signal with distance - an effect that would be even more pronounced if we had $\beta_x > \beta_m$ rather than *vice versa*.

5. DISCUSSION AND CONCLUSIONS

Before discussing possible applications of the model proposed here, we should review the assumptions made in its derivation. The general expression in Eq.(12) is valid in any homogeneous non re-entrant geometry as long as the scattering properties are identical at λ_x and λ_m, and the radiance (or angular flux) of the excitation light in the tissue is close to isotropic. Since the scattering properties of tissue are weakly dependent on wavelength (8), the first condition is equivalent to setting a limit on $(\lambda_m - \lambda_x)$. Not enough is known about the optical properties of all tissues to put limits on this difference with absolute confidence, but a reasonably safe requirement would be $\lambda_m - \lambda_x < 100$ nm. The second requirement of isotropic radiance should not be confused with a requirement for isotropic scattering. Even though the scattering in tissue is highly forward peaked, the radiance will be nearly isotropic as long as $\mu_a << (1\text{-}g)\ \mu_s$ and the point of interest is not too close to a highly directional photon source (23). The condition of approximately isotropic radiance is the same condition required for the diffusion equation to be a reasonable description of light transport in tissue. It is generally agreed that use of diffusion theory is justified for wavelengths greater than 600 nm

and less than 1300 nm in soft tissues (24). The other equations for the fluorescence signal (Eq.(18) for the time domain and Eq.(27) for the frequency domain) were derived for a specific geometry using the diffusion approximation. In addition to the restrictions noted above, there is a lower limit on the source-detector separation for which Eq.(15), necessary in the derivation, is valid. In a separate study (25) we found this limit to be about $[(1-g)\,\mu_s]^{-1}$, which is typically one millimetre in most soft tissues.

From this discussion it is evident that the model will be most accurate for describing fluorescence in tissue when $\lambda_x > 600$ nm and $(\lambda_m - \lambda_x) < 100$ nm. These are the conditions under which fluorescence and absorption spectroscopy of photosensitizers in tissue have been attempted. We will now consider the use of the model to address some specific problems in quantitative *in vivo* spectroscopy.

5.1 Measurement of Fluorophore Concentration

Steady state fluorescence spectroscopy has been suggested by several groups as a means of noninvasively measuring the concentration of a photosensitizer in tissue. For example, Potter and Mang (6) used 630 nm excitation and 690 nm emission to estimate the uptake of Photofrin II in various tissues. (A long wavelength excitation is advantageous as a larger volume of the tissue is sampled than with UV excitation.) The assumption is usually made that the fluorescence signal is proportional to fluorophore concentration. Inspection of

Eq.(13) shows that this is the case only if μ_{fx}, $\mu_{fm} << \mu_{ax}$, μ_{am} so that the presence of the fluorophore does not perturb the absorption coefficient of the tissue. While this is a reasonable assumption for Photofrin, it is not valid for second generation sensitizers with large extinction coefficients, such as AlSPC. As a concrete example, suppose that we measured the fluorescence signal for AlSPC in tissue using the geometry of Fig.1 with λ_x = 610 nm and λ_m = 680 nm. In Fig.8 we show the dependence of the signal on AlSPC concentration for two source detector separations as calculated with Eq.(27). We have assumed that (1-g) μ_s = 1.0 mm^{-1} for the tissue and that $\mu_{am} = \mu_{ax}$ and ranges from 0.01 to 0.1 mm^{-1} depending on the tissue type. For ρ = 1 mm, the response is linear to within 20% and fairly independent of tissue type. If we increase ρ to 7 mm (which would be useful in sampling a greater depth of tissue), the response becomes nonlinear and, in fact, the signal actually decreases for concentrations of AlSPC greater than 3 $\mu g\ g^{-1}$. The amplitude of the signal for a given concentration of AlSPC also depends strongly on the absorption coefficient of the tissue itself.

In all our calculations, we have assumed that once fluorescence photons are absorbed they do not contribute to the detected signal. In fact, if they are absorbed by the fluorophore they can give rise to a second fluorescence source. Such a source can be incorporated into the model through Eq. (5), and in Fig. 8 the effect of including this term is shown by the dashed lines. Experimental results were also obtained under the conditions μ_s' = 1.0 mm^{-1} and $\mu_{ax} = \mu_{am}$ = 0.01 mm^{-1}. These results have also been plotted in Fig.8b with the maximum signal

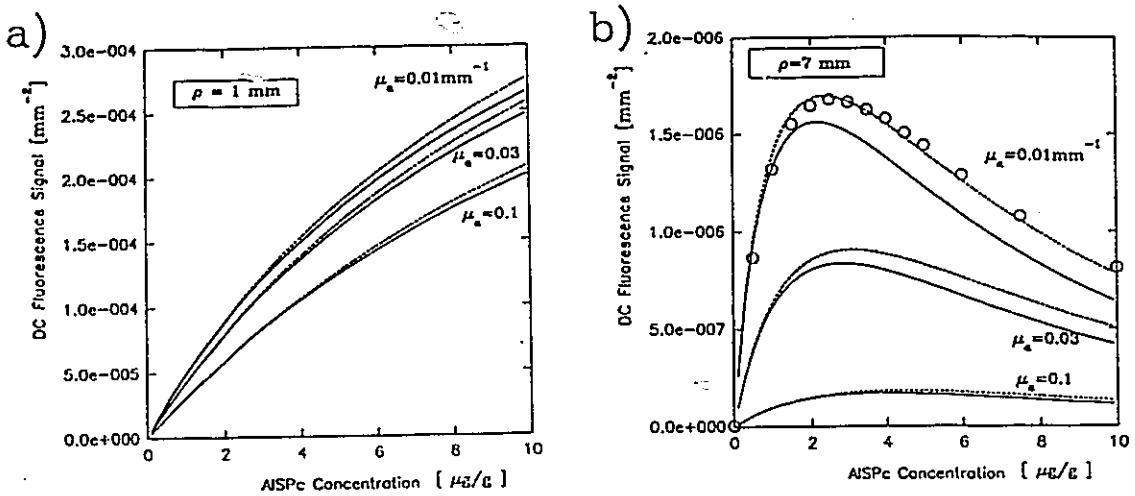

Fig. 8 Calculated steady state fluorescence (photons per square millimetre at the surface for each excitation photon) as a function of AlSPC concentration for the geometry illustrated in Fig. 1. For the host tissue we have assumed that (l-g) μ_s = 1.0 mm^{-1} and the absorption coefficient is 0.01, 0.03 or 0.10 mm^{-1}. We have also assumed that fluorescence excitation occurs at 610 nm and that detection is performed through a 680 nm, 10 nm bandpass filter (50% transmission at peak). In Fig. 8a, ρ = 1 mm, the fluorescence signal increases almost linearly with AlSPC concentration and depends little on the tissue absorption coefficient. When ρ is increased to 7 mm (Fig. 8b), the dependence of fluorescence signal on AlSPC concentration is nonlinear, and the signal amplitude is also much more sensitive to the optical properties of the host tissue. The dashed lines are the model predictions including secondary fluorescence as explained in the text. Experiments were performed under these conditions for ρ = 7 mm, and the relative fluorescence signal is shown by the open circles. These data have been normalized to match the maximum signal to the model prediction.

normalized to the model predictions. Very good agreement is observed between the two. The striking observation that identical fluorescence signals can be observed for fluorophore concentrations differing by an order of magnitude emphasizes the importance of light propagation in the interpretation of such measurements.

5.2 Measurement of Quantum Yield

The quantum yield of a fluorophore can be a sensitive indicator of its chemical environment. Often the relative dependence of Φ_{xm} on emission wavelength contains the desired information (e.g. shifts in emission peaks), but the absolute value of Φ_{xm} can also be important. Any attempt to determine Φ_{xm} from fluorescence measurements is subject to the same sorts of errors discussed above, i.e. the dependence of the signal on tissue optical properties at λ_x, λ_m as well as a possible perturbation of those properties by the fluorophore itself. A number of groups have suggested techniques by which the absorption and scattering properties of the tissue can be derived from noninvasive diffuse reflectance measurements. Wu et al. (9) have used measurements of reflectance made in the same geometry as the fluorescence measurements to correct emission spectra for propagation effects and to recover the true form of Φ_{xm}. Their strategy was based on the same approach embodied in Eq.(12), so that reflectance measurements are required at both the excitation and emission wavelengths. If measurements are not made in the same geometry, then a model which accurately incorporates the

irradiation and detection geometries must be used. The model developed here is suitable provided the restrictions discussed above are met.

5.3 Measurements of Fluorescence Lifetime

Since the fluorescence lifetime and fluorescence quantum yield are intimately related (27), measurements of lifetime can also be useful indicators of fluorophore environment. Measurement of fluorescence lifetimes in tissue is complicated because, as discussed in Section 2, the temporal or frequency domain behavior of a fluorescence signal is dependent not only on the lifetime but also the propagation of excitation and emission light within the tissue. Examination of Eq.(18) confirms that propagation effects are most important when:

(i) the fluorescence lifetime is short

(ii) the excitation source and fluorescence detector are far apart

(iii) the host tissue is strongly scattering and weakly absorbing.

An illustration of potential distortion is given in Fig.4. In the frequency domain, the phase of the fluorescence signal increases with source-detector separation and can exceed 90° - the largest phase shift due to lifetime alone. As the phase shift due to true lifetime effects approaches 90°, the additional delay due to propagation effects becomes more important, as a small change in phase near 90° corresponds to a large change in lifetime. The model presented here could be particularly useful in the choice of optimum frequencies for measurements of fluorescence lifetime. As explained in Section 4, the data

shown in Fig. 4 were obtained for a case where most of the observed fluorescence is generated "locally". In this case, fluorescence phase measurements could be corrected by simply subtracting the phase of the excitation light measured at the same point. It should be emphasized that this is not generally true. If the fluorescent light is less likely to be absorbed in the tissue than the excitation light, then the phase difference between the two will depend strongly on source-detector distance. This is shown explicitly in Fig. 5 where the total (fluorescence plus scatter) signal rapidly diverges from the expected behaviour of the excitation signal. In such cases a quantitative model of propagation effects, such as proposed here, is required to estimate the true lifetime.

5.4 Correction of Absorption Measurements

The original impetus for the work presented here was not fluorescence spectroscopy but absorption spectroscopy. As reported in earlier papers (13,26) we intended to use measurements of modulation and phase in tissue along with Eq.(20) to make quantitative estimates of the absorption spectrum. The goal was to identify and quantify specific chromophores such as AlSPC. Our initial measurements, which employed no wavelength discrimination at the detector, were similar to those shown in Fig.6. Instead of an expected decrease in phase and increase in modulation at 675 nm due to absorption effects, these quantities displayed exactly the opposite behavior. As we have shown in this paper, this effect can be accurately predicted by considering the fluorescence of

AlSPC. It is not possible to remove all of the fluorescence contribution with filters, due to the close overlap of emission and absorption spectra as shown in Fig.2. Under these conditions, even quantitative absorption spectroscopy must rely on a model of fluorescence such as that developed in this paper.

6. ACKNOWLEDGEMENTS

This work was supported by the Ontario Laser and Lightwave Research Centre. The authors are grateful to Jun Wu and colleagues at MIT for making Reference 9 available to us prior to its publication. We also thank Ruth Alexander for her careful preparation of the manuscript.

7. REFERENCES

1. S. Andersson-Engels and B.C. Wilson, "*In vivo* fluorescence in clinical oncology: fundamental and practical issues", J. Cell. Pharmacol. 3 66-79 (1992).

2. A.E. Profio and J. Sarnaik, "Fluorescence of HpD for tumor detection and dosimetry in photoradiation therapy", in Porphyrin Localization and Treatment of Tumors (D.R. Doiron and C.J. Gomer, eds.) Alan R. Liss, New York, 1984, pp. 163-175.

3. W.J.M. van der Putten and M.J.C. van Gemert, "A modelling approach to the detection of subcutaneous tumours by haematoporphyrin-derivative fluorescence", Phys. Med. Biol. 28 639-645 (1983).

4. A.F. Gmitro, F.W. Cutruzzola, M.S. Stetz and L.I. Deckelbaum, "Measurement depth of laser-induced tissue fluorescence with application to laser angioplasty", Appl. Opt. 27 1844-1849 (1988).

5. R. Richards-Kortum, R.P. Rava, M. Fitzmaurice, L.L. Tong, N.B. Ratliff, J.R. Kramer, and M.S. Feld, "A one-layer model of laser-induced fluorescence for diagnosis of disease in human tissue: applications to atherosclerosis", IEEE Trans. Biomed. Eng. 36 1222-1232 (1989).

6. W.R. Potter and T.S. Mang, "Photofrin II levels by *in vivo* fluorescence photometry", in Porphyrin Localization and Treatment of Tumors (D.R. Doiron and C.J. Gomer, eds.) Alan R. Liss, New York, 1984, pp. 177-186.

7. M. Keijzer, R.R. Richards-Kortum, S.L. Jacques, and M.S. Feld, "Fluorescence spectroscopy of turbid media: autofluorescence of the human aorta", Appl. Opt. 28 4286-4292 (1989).

8. W.F. Cheong, S.A. Prahl, and A.J. Welch, "A review of the optical properties of biological tissues:, IEEE J. Quantum Electron. 26 2166-2185 (1990).

9. J. Wu, M.S. Feld, and R.P. Rava, "An analytical model for extracting intrinsic fluorescence in a turbid media", Appl. Opt. (in press).

10. M.S. Patterson, S.J. Madsen, J.D. Moulton, and B.C. Wilson, "Diffusion equation representation of photon migration in tissue", 1991 IEEE MTT-S Digest, pp. 905-908.

11. M.S. Patterson, B. Chance, and B.C. Wilson, "Time resolved reflectance

and transmittance for the non-invasive measurement of tissue optical properties", Appl. Opt. 28 2331-2336 (1989).

12. J.J. Duderstadt and L.J. Hamilton, Nuclear Reactor Analysis, John Wiley and Sons, New York, 1976.

13. M.S. Patterson, J.D. Moulton, B.C. Wilson, K.W. Berndt, and J.R. Lakowicz, "Frequency-domain reflectance for the determination of the scattering and absorption properties of tissue", Appl. Opt. 30 4474-4476 (1991).

14. B.W. Henderson and T.J. Dougherty (eds.), Photodynamic Therapy: Basic Principles and Clinical Applications, Marcel Dekker, New York, 1992.

15. J.H. Brannon and D. Magde, "Picosecond laser photophysics. Group 3A phthalocyamines", J. Am. Chem. Soc. 102 62-65 (1980).

16. J.R. Lakowicz, Principles of Fluorescence Spectroscopy, Plenum, New York, 1983.

17. H.J. van Staveren, C.J.M. Moes, J. van Marle, S.A. Prahl, and M.J.C. van Gemert, "Light scattering in Intralipid-10% in the wavelength range of 400-1100 nm", Appl. Opt. 30 4507-4514 (1991).

18. S.J. Madsen, M.S. Patterson, and B.C. Wilson, "The use of India ink as an optical absorber in tissue-simulating phantoms", Phys. Med. Biol. 37 985-993 (1992).

19. I. Driver, J.W. Feather, P.R. King, and J.B. Dawson, "The optical properties of aqueous suspensions of Intralipid, a fat emulsion", Phys. Med. Biol. 34 1927-1930 (1989).

20. G.M. Hale and M.R. Querry, "Optical constants of water in the 200 nm to 200 μm wavelength region", Appl. Opt. 12 555-563 (1973).

21. E. Gratton and M. Limkeman, "A continuously variable frequency cross-correlation phase fluorometer with picosecond resolution", Biophys. J. 44 315-324 (1983).

22. B.M. Feddersen, D.W. Piston, and E. Gratton, "Digital parallel acquisition in frequency domain fluorometry", Rev. Sci. Instrum. 60 2929-2936 (1989).

23. H.C. van de Hulst, Multiple Light Scattering, Academic Press, New York,

1980 pp. 331-339.

24. M.S. Patterson, B.C. Wilson, and D.R. Wyman, "The propagation of optical radiation in tissue. II: Optical properties of tissues and resulting fluence distributions", Lasers Med. Sci. 6 379-390 (1991).

25. T.J. Farrell, M.S. Patterson, and B.C. Wilson, "A diffusion theory model of spatially resolved, steady-state diffuse reflectance for the noninvasive determination of tissue optical properties *in vivo*", Med. Phys. 19 879-888 (1992).

26. M.S. Patterson, J.D. Moulton, B.C. Wilson, and B. Chance, "Applications of time-resolved light scattering measurements to photodynamic therapy dosimetry", SPIE Vol. 1203 Photodynamic Therapy: Mechanisms II (T.J. Dougherty, ed.) SPIE, Bellingham, 1990, pp. 62-75.

27. N.J. Turro, "Modern Molecular Photochemistry", The Benjamin/Cummings Publishing Co., Menlo Park, p. 109, 1978.

Introduction to Paper #4

The following paper was stimulated by the access to a multigrid finite difference algorithm which could be used to solve numerically the discretized diffusion equation. A major limitation to the inverse imaging problem for diffuse tomography has been the computational time required to turn experimental measurements into images of scattering and absorption coefficients. The following paper was an attempt to test the algorithm proposed by Arridge *et al* (1993) with a fast forward calculation of diffusion theory. Most of the results were preliminary and so the paper was submitted to the SPIE conference rather than a refereed journal. However the analysis was very useful for understanding the limitations of a diffuse optical tomography system and its potential applications.

The finite difference algorithm was developed by John Adams at the National Centre for Atmospheric Research in Boulder, Colorado. The application and testing of this code towards optical tomography was done by myself. The Monte Carlo algorithm used to generate test data was supplied by Dr. Tom Farrell at the Hamilton Regional Cancer Centre, and altered to our boundary conditions by myself and Dr. Farrell. The text of the article was written by me and edited by Dr. Patterson.

Forward and Inverse Calculations for 3-D Frequency-Domain Diffuse Optical Tomography

Brian W. Pogue[1], Michael S. Patterson[1,2] and Tom J. Farrell[1]

[1]Hamilton Regional Cancer Centre and McMaster University

699 Concession Street, Hamilton, ON, Canada L8V 5C2

[2] Ontario Laser and Lightwave Research Centre,

University of Toronto, Toronto, ON, Canada

ABSTRACT

A fast iterative imaging algorithm has been developed to examine the potential of Diffuse Optical Tomography (DOT) for clinical imaging. Forward calculations using diffusion theory were used to generate light fluence distributions within highly scattering media such as tissue. A 3-D multigrid finite difference algorithm has been employed to solve the complex diffusion equation in the frequency-domain for irregular objects with spatially varying absorption and scattering coefficients. An iterative inversion scheme has been used to solve for the distribution of interaction coefficients from tomographic measurements of the phase and amplitude of the AC photon density at the surface of the object. The time required to calculate images can be minimized using the multigrid finite difference forward solution along with a Newton-Raphson steepest descent inversion

algorithm. The potential of DOT was evaluated using theoretical 3-D test objects with various absorption and scattering inhomogeneities from which the phase and amplitude data were calculated from both finite difference and Monte Carlo simulations. Estimates of the resolution and contrast were calculated in order to assess the detectability of biological targets, such as tumours, blood volume changes, or blood oxygenation changes. The three dimensional nature of these calculations should be beneficial for optimized iterative reconstruction.

1. INTRODUCTION

One of the most promising methods of optical imaging uses intensity-modulated light transmitted through tissue to estimate the interaction coefficients of the tissue. Using a model for light propagation in tissue the exact values of the absorption and transport elastic scattering coefficients can be calculated from measurements of phase and AC photon density made in the frequency domain. Light propagation within a highly scattering medium such as tissue can be modelled accurately with the diffusion equation, for large propagation distances[1,2,3,4]. Numerical simulations using diffusion theory can be used to predict the potential of this technique in clinical imaging situations. The goal of the present research is to theoretically evaluate frequency-domain Diffuse Optical Tomography (DOT) as a useful clinical tool.

In this paper, a 3-dimensional multigrid finite-difference solver (MUDPACK[5]) has been used to solve the forward imaging problem, where the spatial distribution of absorption (μ_a) and scattering (μ_s') coefficients are known and the light fluence distribution due to a source must be calculated. The geometry chosen for this study has been a

cylindrical tissue-simulating object, which approximates applications such as mammographic examinations or neonatal cerebral oxygenation tomographic imaging (see Figure 1). The forward calculations have been used to estimate the resolution and contrast expected with frequency-domain DOT imaging for values of μ_a and μ_s' typical of human tissue.

In an effort to examine the accuracy of these calculations, other forward methods have been used as a comparison. For homogeneous objects, forward solutions can also be found analytically from Green's theory solutions to the frequency-domain diffusion equation[3,4]. The analytic calculations cannot be used easily for large inhomogeneities, however the 1st order perturbation calculations of Barbour *et al*[6] and Kaltenbach *et al*[7] have been used to compare the expected resolution for a point inhomogeneity within a tissue-like medium. For large inhomogeneous objects, Monte Carlo forward calculations[8] have been used to compare with the finite difference calculations.

The inverse imaging algorithm is based on the method used in electrical impedance tomography applications[9], and outlined by Arridge[10] for applications in time-resolved optical imaging. The central problem is to recover the distribution of μ_a and μ_s' within a tissue volume from measurements of phase and AC intensity on the exterior of the object. The inverse algorithm uses an initial 'guess' at the interaction coefficients, and then calculates the correction to these values which would reduce the error between the observed measurements and the calculated measurements, based upon that guess. The optimization routine is the Newton-Ralpson steepest descent algorithm with a Levenberg-Marquardt regularization cycle[11], which provides a robust solution to the inverse problem. The accuracy of the algorithm was tested for two different grid sizes, and for multiple inhomogeneities.

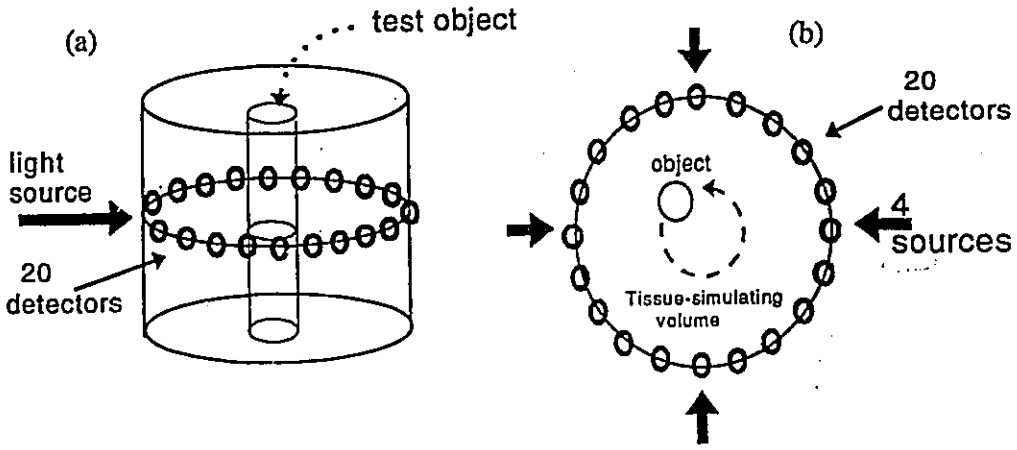

Figure 1 Simulation geometry. Cylinder 100 mm diameter, 100 mm length with the image plane at the mid point. Optical properties used were $\mu_a = 0.01$ mm^{-1} and $\mu_s' = 1.0$ mm^{-1} for most. Both the 3 dimensional perspective, and the 2 dimensional imaging plane are shown. The number of objects and positions within the cylinder can vary.

After the reconstruction algorithm was optimized and tested with the Monte Carlo data, it was used to examine some of the anticipated problems associated with DOT imaging. One of the main problems anticipated was the response of the algorithm to changes in source-detector geometry, due either to blood flow pulsations or to patient movement. To minimize errors due to baseline offsets or to these distance fluctuations, the algorithm created here uses differences in phase and AC intensity data. This assumes that data can be measured under two conditions, one where the inhomogeneities are not present and one where they are, and the two sets of data are then processed to yield the effect of the inhomogeneities alone. This type of data could be produced by shifting the wavelength of the light, or by measuring before and after the administration of a contrast agent. This difference imaging could provide the most practical solution for eliminating physiologic noise or positioning errors.

The clinical use of near-infrared imaging depends upon being able to detect and image realistic biological targets. The effects of typical blood flow and oxygenation changes have been estimated in an effort to predict how successful the imaging system would be. Blood volume changes near 10 % should be detectable with a resolution of perhaps 1 cm, however images of blood oxygenation changes will have a much lower spatial resolution. The effects of tumours could be detected from their corresponding increase in blood volume due to increased vascularization. These estimates have been discussed in connection with the imaging algorithm used here.

2. FORWARD PROBLEM

2.1 Diffusion Theory

The transport of near-infrared light in tissue can be modelled accurately with diffusion theory [6]. Here we use the frequency domain diffusion equation for the fluence rate $\Phi(\mathbf{r},\omega)$ within a scattering medium :

$$-\nabla^2\Phi(\boldsymbol{r},\omega) + k^2\,\Phi(\boldsymbol{r},\omega) = S(\boldsymbol{r},\omega) \qquad (1)$$

at any point r within the tissue, for a source $S(r,\omega)$ modulated at frequency $\omega=2\pi f$. Here k is the complex attenuation coefficient, $k=[(\mu_a + i\omega/c_t)/D]^{1/2}$, where $c_t = c/n$ is the velocity of light in tissue for index of refraction n. D is the diffusion coefficient given by $D = [3(\mu_a+\mu_s')]^{-1}$ for absorption and reduced scattering coefficients μ_a and μ_s', respectively. Analytic solutions of this equation given by Arridge[4] and Moulton[3] for several regular geometries can be used to predict the light signal at any point in a homogeneous tissue volume. The measured light signal at the surface is given by the exiting photon current, $\mathbf{R}(\mathbf{r},\omega)$, however for the finite difference calculations the signal measured is the photon density at pixels on the surface, $N(r,\omega)$. The DC intensity any point is given by the current with the frequency set to zero, $I_{DC} = N(r,0)$. The amplitude of the AC signal at any point is given by the magnitude of the complex current, $I_{AC} = [N(\mathbf{r},\omega)N^*(\mathbf{r},\omega)]^{1/2}$, and the phase shift relative to the source is given by $\phi = \tan^{-1}[\mathbb{I}m\{N(\rho,\omega)\} / \mathbb{R}e\{N(\rho,\omega)\}]$. The solution to the complex frequency domain diffusion equation provides a method of calculating these three observables at all points on the surface of a tissue phantom. The analytic solutions of the diffusion equation have been used to calculate phase and intensity at various points around the surface of a cylinder due to a point source at angle 0°, with

μ_s'=1.0 mm^{-1}, μ_a=0.01 mm^{-1}, f = 300 MHz, for a radius of 50 mm as shown in figure 2. These calculations are used to determine the accuracy of the numerical calculations presented in the next section.

2.2 Homogeneous Simulation: Analytic vs. Finite Difference

Equation (1) is essentially the complex Helmholtz equation which can be solved numerically as a boundary value problem, with $\Phi(r_{surf},\omega) = 0$ on the surface, s, and $\Phi(r_o,\omega)=S(r_o,\omega)$ at the source location, r_o. More accurate boundary conditions could be used, however for these initial calculations, the simplest boundary condition is used. The volume of tissue can be approximated by a discrete lattice of points, and the discretized version of equation 1 can be solved:

$$\frac{\Phi_{i+1jk} + \Phi_{i-1jk}}{\Delta L_i^2} + \frac{\Phi_{ij+1k} + \Phi_{ij-1k}}{\Delta L_j^2} + \frac{\Phi_{ijk+1} + \Phi_{ijk-1}}{\Delta L_k^2} - \left[\frac{2}{\Delta L_i^2} + \frac{2}{\Delta L_j^2} + \frac{2}{\Delta L_k^2} + k^2\right]\Phi_{ijk} = \frac{S_{000}}{D} \qquad (2)$$

where i, j, and k are the 3 direction axes x, y, and z respectively, and ΔL is the step size in each of the directions indicated by a subscript, and S_{000} is the source at location i=0, j=0, k=0 (Press *et al*[12]).

The numerical solution of this equation can be accomplished by any of a number of standard finite differencing techniques. The fastest of these methods is the multigrid solution, where the equation is solved on several grids of varying mesh size in an effort in improve the speed of convergence. A good review of multigrid solutions for elliptic problems is provided by Fulton *et al*[13]. The theory behind the use of multigrids can be stated in simple terms. The accuracy in the solution of the equation for finite difference calculations depends upon the mesh size, i.e. the size of ΔL. Very coarse mesh grids (

large ΔL) are good for solving problems quickly, however they yield large errors due to the coarse step size. Fine mesh grids produce smooth and accurate solutions but they require a large numbers of iterations to achieve a solution, requiring a long time. Multigrid routines are used to solve the problem on several sized grids simultaneously, using the coarse grids to provide quick steps toward the solution, and using the finer grids to smooth the solution for better accuracy. The process of interpolation between grids and smoothing with finer resolution is quite detailed and is well documented in the literature and a precise description of the MUDPACK routine used here is given in Adams[5]. Multigrid solutions have not been used in many applications, mainly due to the complexity of coding the algorithm, but in this application the speed of the solution is most important.

A cylinder with a radius of 50 mm and length of 100 mm was modelled (see Figure 1) using 20 detector locations on the perimeter and homogeneous optical properties. In the tests of optical reconstruction, the 4 source locations shown were used, while for the preliminary testing of the influence of grid size only one source was used. This geometry was chosen to approximate a first generation optical CT imaging system. Numerical simulations for this size cylinder were carried out with three different sized grids: 17 x 17 x 17, 33 x 33 x 33, and 65 x 65 x 65. The observed phase, modulation and LOG(DC intensity) are graphed in figure 2 for 20 detector locations on the surface of the homogeneous cylinder at equal angle spacings from the source. The agreement between the analytic values and those calculated on the finest grid provides the basis for using the numerical solution in further studies. All future forward simulations of inhomogeneous phantoms in this paper were calculated on the fine grid. A typical calculation time for this size grid was 50 seconds on a SUN SPARC 10 workstation.

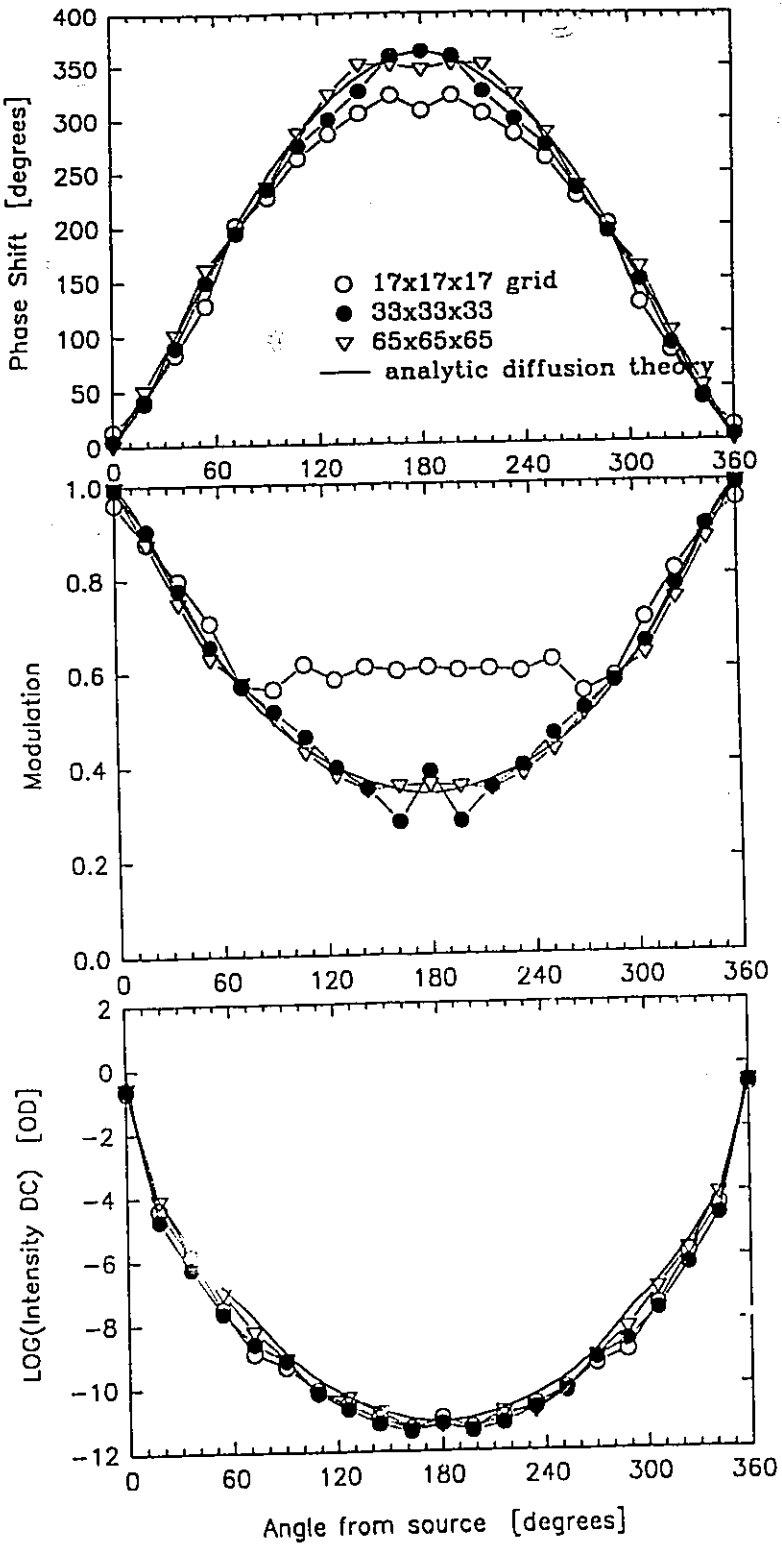

Figure 2 Homogenous cylinder calculations for a 100 mm diameter, with $\mu_a = 0.01$ mm^{-1} and $\mu_s' = 1.0$ mm^{-1}. Three finite difference calculations on different grid sizes, and analytic diffusion theory calculations. (f=300 MHz)

These simulations are used to estimate the resolution and contrast available for imaging through a 100 mm volume as described in sections 2.4 and 2.5.

2.3 Inhomogeneous Simulation: Monte Carlo vs. Finite Difference

A previous paper[14] confirmed that there is qualitative agreement between inhomogeneous diffusion calculations and experimental measurements on tissue-simulating phantoms. However some discrepancies still remained between the finite difference calculations and the experimental measurements. To examine this problem further, a Monte Carlo model was used to calculate the phase and AC intensity at the surface of a cylinder due to a point source. The Monte Carlo model is described in papers Flock *et al*[15] and Farrell *et al*[6] using isotropic scattering with a randomly distributed scattering length. Angular bins of $\pi/100$ were used to score the photons at points on the surface of the cylinder recording the time into bins of approximately 4 picoseconds. The time series for each detector was then fourier transformed to yield phase and amplitude data.

The radius of the cylinder was reduced to 25 mm in order to decrease the time needed to run the Monte Carlo program. The same optical properties were used as in figure 2, $\mu_s' = 1.0\ mm^{-1}$, and $\mu_a = 0.01\ mm^{-1}$. It was determined that 100 million incident photon histories were needed to get good statistics at the 180° detector. The phase as calculated by the Monte Carlo simulations was in good agreement with the finite difference values, but unexplained differences in the absolute intensity remain.

In figures 3 and 4, the results from two inhomogeneous cylinders are shown, where the phase shift and $LOG(I_{AC})$ are plotted as difference data (i.e. the phase shift is subtracted from the homogenous case, and the same for the log intensity data). In Figure 3, the data plotted results from a simulation with a cylindrical absorbing inhomogeneity

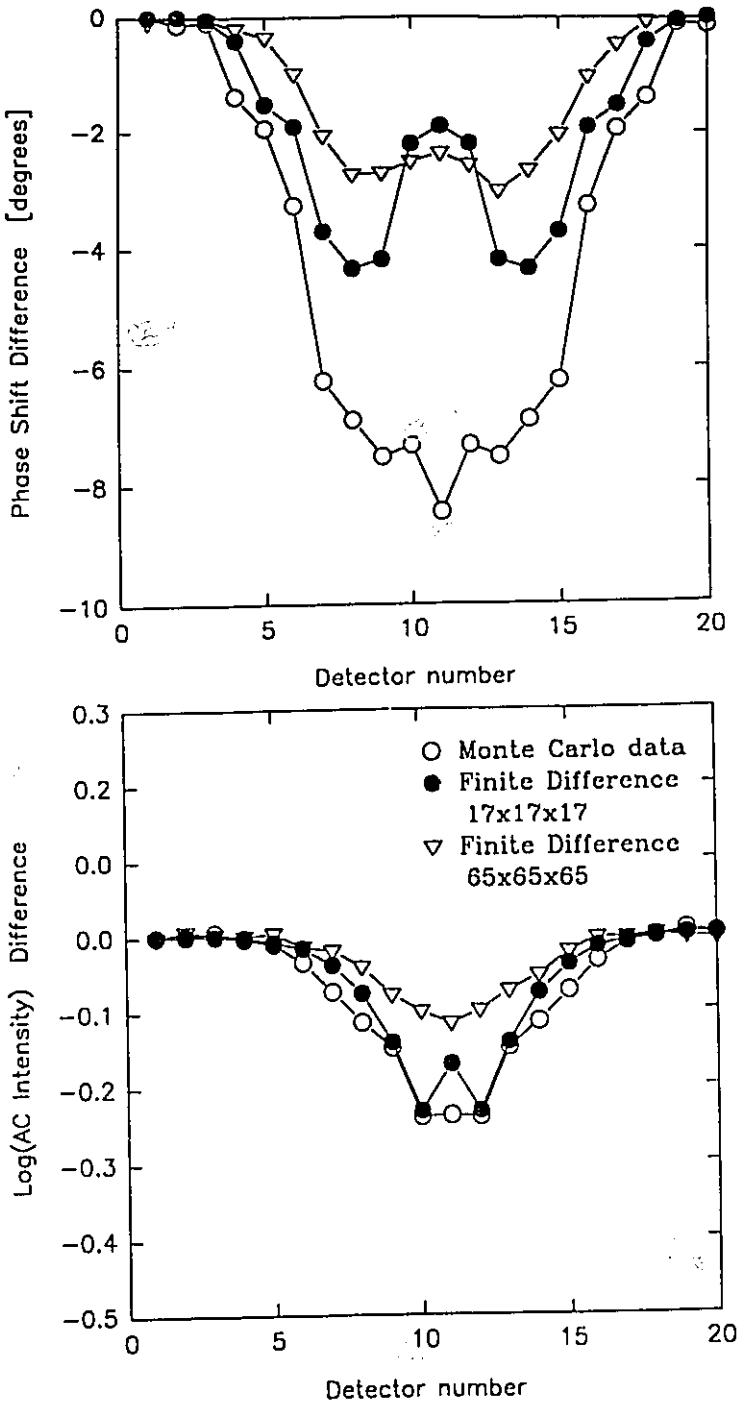

Figure 3 Inhomogeneous cylinder calculations for a 50 mm diameter cylinder. (same optical properties as Figure 1) An absorbing object at the centre with 10 mm diameter, $\mu_{ao} = 0.02$ mm^{-1}, $\mu_s' = 1.0$ mm^{-1}. The data graphed is subtracted from the homogeneous cylinder to yield difference data. (f=274 MHz)

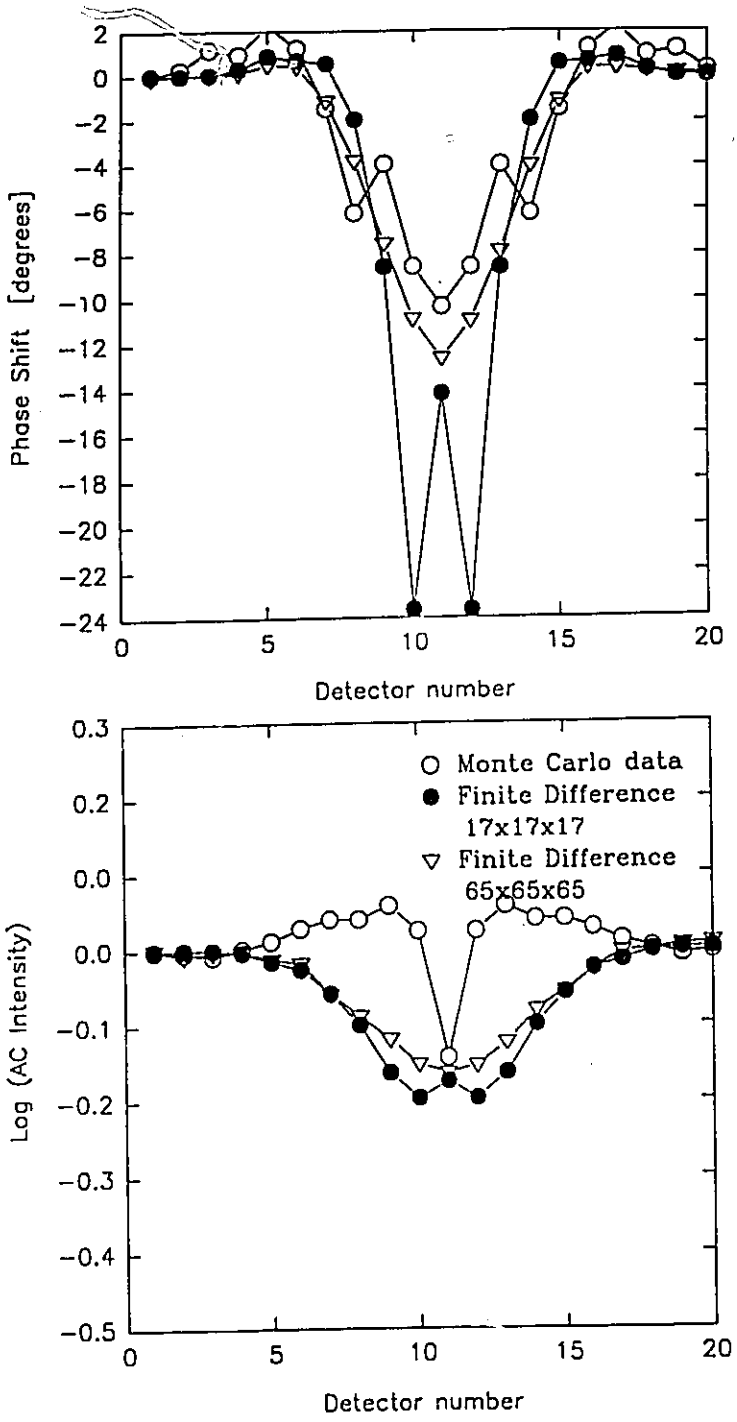

Figure 4 Inhomogeneous cylinder calculations as in figure 3, except for a scattering object at the centre. The object is 10 mm diameter, $\mu_a = 0.01$ mm^{-1}, $\mu_s' = 2.0$ mm^{-1}.

at the centre with μ_a=0.02 mm^{-1}, μ_s'=1.0 mm^{-1}, and a diameter of 10 mm. In Figure 4, the data plotted is from a simulation with a scattering inhomogeneity at the centre with μ_s'=2.0 mm^{-1}, μ_a = 0.01 mm^{-1} and a diameter of 10 mm. The differences between the Monte Carlo and finite difference data were fairly large, which is a concern which still needs to be addressed, however the overall trend of the data was correct for both simulations. These data were also used in the inverse problem section to test the reconstruction algorithm.

2.4 Forward Calculations of Resolution

Images of a point object obtained by the finite difference calculations were used to predict the resolution for thick tissue volumes. In figure 5, the FWHM of the transmittance change due to a point absorbing object translated laterally between a source-detector pair is plotted versus depth of the object. The tissue thickness used was 100 mm with optical properties μ_a=0.01 mm^{-1} and μ_s'=1.0 mm^{-1}. A depth of zero corresponds to the location of the object at the tissue surface, whereas a depth of 50 mm corresponds to location of the object in the midplane. The volume of the point object was 3.8 mm^3 and with absorption coefficient μ_{ao}=0.1 mm^{-1}. The error in the estimate of FWHM arises from pixel to pixel variations in the simulation. The 100 mm cubic volume was discretized into 64x64x64 voxels, so that the precision of the resolution estimate cannot be better than the pixel size, 1.5625 mm. This type of transmittance measurement is representative of imaging a tissue volume using a scanned pair of source-detector fibres. The same situation was also treated analytically by assuming the object to be a point absorbing perturbation. The details of this method have been described by others[6,7]. The smooth lines of figure 5 are the analytic calculations of the FWHM, for three different

frequencies: 0, 300 Mhz and 1 Ghz. It was observed that increasing the modulation frequency to 1 Ghz decreases the FWHM by at most a few mm for objects in the centre of the tissue. For these frequencies, the lateral resolution through 100 mm of tissue would be limited to near 20 mm FWHM.

2.5 Forward Calculations of Contrast

Detection of a small absorbing volume within a larger tissue volume has been a concern for the development of transillumination systems. Finite difference calculations for a 1 cm diameter spherical object within a 10 cm diameter spherical phantom were used to estimate the improvement in contrast possible with the use of higher frequencies. In figure 6, the percentage change in the transmittance signal is graphed as a function of the absorption coefficient of the object. The transmittance is shown for steady state (i.e. f=0), and for modulated light at f = 300 MHz and f= 1 GHz. For steady state, the change in the transmittance reaches a maximum of 11% near μ_a = 0.03 mm^{-1}, while the contrast at higher frequencies continues to increase with increasing absorption coefficient. While higher frequencies provide greater changes in the transmittance, it should be noted that these frequencies also yield less total intensity. The intensity changes for transmittance through the 100 mm homogeneous sphere of optical properties μ_a = 0.01 and μ_s' = 1.0 mm^{-1}, are -10.9 OD, -11.3 OD, and -12.9 OD for frequencies f=0, 300 MHz, and 1 GHz, respectively. This calculation suggests that the contrast of small objects imbedded within a 100 mm tissue volume could be greatly aided by the use of high frequency measurements, assuming that the intensity is still high enough for measurement.

Both the optical properties of the object as well as its size can affect the transmitted intensity observed across a tissue volume. The effects of larger objects with

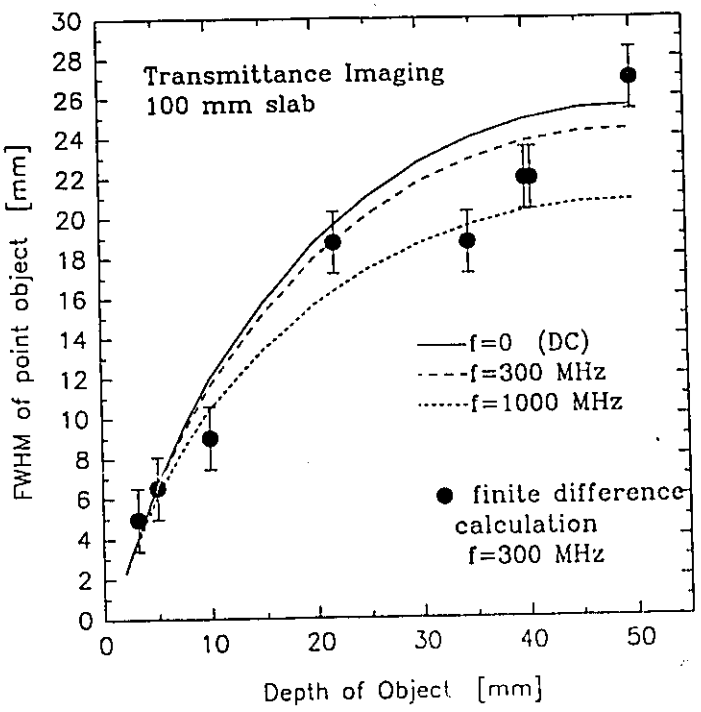

Figure 5 Analytic Calculations of Full Width at Half Maximum (FWHM) for a point absorbing perturbation within a 100 mm diameter cylinder, with the source and detector separated by 180°. The points are finite difference calculations. (Same optical properties as figure 1).

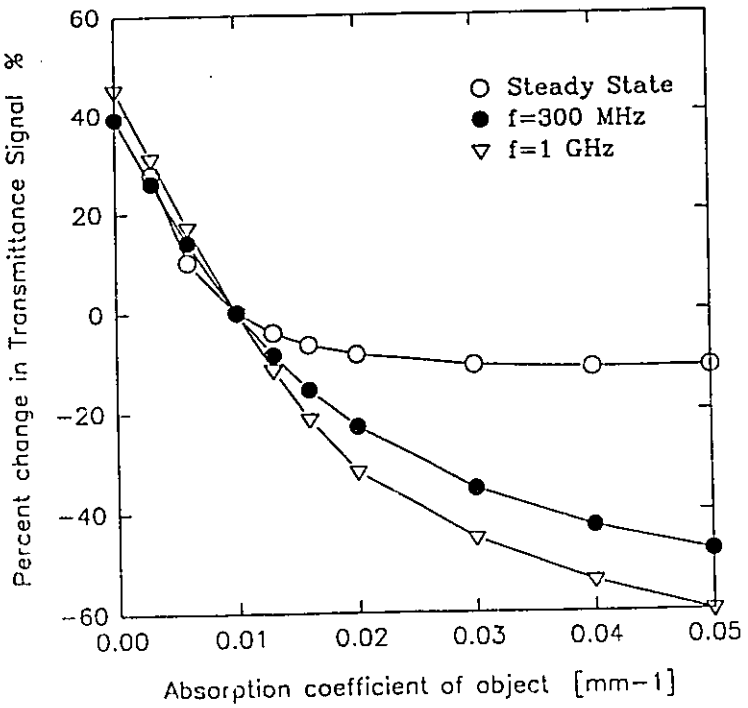

Figure 6 Finite difference calculations of the percent transmittance change for the same arrangement as figure 5, for a 10 mm spherical object at the centre of the cylinder. The object has the same scattering as the background, while the absorption coefficient is varied.

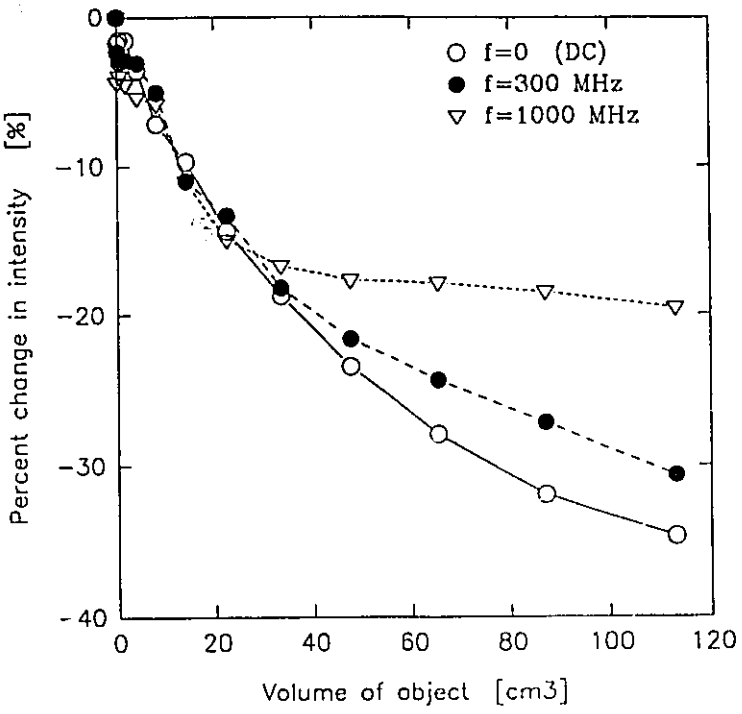

Figure 7 Calculations as in Figure 6, but with the object absorption coefficient fixed at $\mu_{ao} = 0.011$ mm^{-1}, and the size of the object is varied.

lower changes in μ_a were modelled for the same geometry as in figure 6. In figure 7, the absorption coefficient used was 10% higher than the background (i.e. μ_{a0}=0.011 mm^{-1}) for spheres of diameter between 0 and 60 mm located at the centre of the larger sphere. The decrease in intensity is more complicated than in figure 6, since there are several effects occurring as the size of the object changes. For small objects the intensity decrease is larger for higher frequency, which is similar to figure 6 where the photon path distribution at higher frequencies is narrower, so that more of the light is attenuated by the object. However for larger objects, the lower frequency signal shows a larger attenuation. The broader photon path distribution at low frequencies must permit more interaction with the larger objects, decreasing the overall transmission through the region. This calculation suggests that while imaging of small objects is aided by the use of high frequencies, larger regions are better sampled by low frequency or CW light.

3. INVERSE PROBLEM

3.1 The Inverse Algorithm

Reconstructing optical images of the tissue from measurements at the surface, as illustrated in figure 1, is not as simple as straight line backprojection methods used in x-ray CT, because the photon paths are diffuse and multiply scattered. The distributions of photon paths can be calculated with diffusion theory, but recovering the original interaction coefficient distribution is a fairly complex inverse problem. In this paper, the finite difference forward calculation is used to generate a Jacobian matrix, J, which is the derivative of photon density at each detector with respect to the interaction coefficients (μ_a and μ_s') of each pixel in the image. Here the absorption coefficient is used to illustrate

the algorithm (i.e. each element of J is given by $j_{i,j} = \partial\Phi_i/\partial\mu_{aj}$). This matrix is a calculation of the sensitivity of each detector to changes in μ_a at each of the image pixels. Using this matrix and a 1st order Taylor's expansion, a Newton-Raphson iterative algorithm for calculating the μ_a vector can be found from solving the matrix equation[9] :

$$(\underline{\Delta\mu}_a^k)\,(\boldsymbol{J}^k) \;=\; (\underline{\Phi}^k_{calc} - \underline{\Phi}_{obs}) \qquad (3)$$

where $\underline{\Delta\mu}_a^k$ is the k th iteration for the update of the $\underline{\mu}_a$ vector, $\underline{\Phi}_{obs}$ is the vector of observed fluences, and $\underline{\Phi}^n_{calc}$ is the vector of calculated photon densities at the k th iteration. The $\underline{\mu}_a$ vector has n x n components corresponding to the values in the plane of the detector array, where n is the number of pixels in each side. The inverse of the Jacobian matrix times the observed change in photon density at each detector, yields the change in absorption coefficient at each pixel. However the inversion of the J matrix requires multiplication by the transpose on each side, $\mathbf{J}^t$, to generate a square matrix, and then regularization by adding a factor, λ^k, times the identity matrix, **I**, yielding :

$$\Delta\mu_a^k = (J^k)^t\,(\underline{\Phi}^k_{calc} - \underline{\Phi}_{obs})\,\left[\,(J^k)^t(J^k) + \lambda^k I\,\right]^{-1} \qquad (4)$$

More detailed derivations of these equations are available in many treatments of inverse problems.

To this point the derivation was limited to the absorption coefficient, μ_a and the photon fluence, Φ, however the real observed quantities are phase and intensity, ϕ and I, and the interaction is described by both absorption and scattering coefficients. Thus the real calculation is a 2 x 2 matrix equation where the four derivative matrices are $\partial\phi/\partial\mu_a$, $\partial\phi/\partial\mu_s'$, $\partial I/\partial\mu_a$, $\partial I/\partial\mu_s'$, and the inversion equation is :

$$\begin{bmatrix}\Delta\mu_a\\ \Delta\mu_s'\end{bmatrix} = \begin{bmatrix}J^T(I,\mu_a) & J^T(\Phi,\mu_a)\\ J^T(I,\mu_s') & J^T(\Phi,\mu_s')\end{bmatrix}\begin{bmatrix}(I_{calc} - I_{obs})\\ (\Phi^n_{calc} - \Phi_{obs})\end{bmatrix} \cdot \left[\begin{pmatrix}J(I,\mu_a)J^T(I,\mu_a)+J(\Phi,\mu_a)J^T(\Phi,\mu_a) & J(I,\mu_s')J^T(I,\mu_a)+J(\Phi,\mu_s')J^T(\Phi,\mu_a)\\ J(I,\mu_a)J^T(I,\mu_s')+J(\Phi,\mu_s')J^T(\Phi,\mu_a) & J(I,\mu_s')J^T(I,\mu_s')+J(\Phi,\mu_a)J^T(\Phi,\mu_a)\end{pmatrix} + \begin{pmatrix}\lambda_1 I & 0\\ 0 & \lambda_2 I\end{pmatrix}\right]^{-1} \quad (5)$$

Images of the absorption and scattering coefficients at each pixel are created by starting with the homogenous solution as the first guess of $\mu_a(i,j,k)$ and $\mu_s'(i,j,k)$ at all points and iterating to find the corrected values. In principle the light measurements could be done in 3 dimensions with a fully 3 dimensional reconstruction, but this is too computationally intensive for the average workstation. Therefore we have restricted the measurements and reconstruction to one transverse plane midway between the ends of the cylinder (see figure 1). Note however that the propagation of light is handled as a fully three dimensional phenomenon.

Another problem in diffuse tomography is the choice of the number of sources and detectors. While it is customary in electrical impedance tomography to choose 16 sources and 16 detectors, it should be noted that many of these data may be redundant for small geometries. The photons which sample the object scatter out in all directions from the source, so that one source can yield many detected measurements at the periphery of the sample. In this work the number of sources has been chosen to be 4, which we estimate to be the minimum number needed to provide reliable reconstruction. The observed photon density vectors in equation 5, Φ_{obs} and I_{obs}, are arrays of 80 phase measurements and 80 AC intensity measurements, respectively, corresponding to 20 detectors for each of the 4 source locations. The optimum number of sources needed is clearly dependent upon the resolution required and the time available for reconstruction.

One of the major problems with optical imaging is the extreme sensitivity to changes in source-detector distances or changes in the boundary conditions. One of the

ways to minimize the effects of these problems is to use difference imaging. This would be possible if two wavelengths could be used, one at a wavelength where the tissue sample is relatively homogeneous, and one wavelength where the inhomogeneities are maximized. One example of this could be in blood oxygenation imaging, where at 800 nm the absorption coefficients of oxygenated and deoxygenated hemoglobin are the same, so that this wavelength would provide a relatively homogeneous image. Then the difference image could be made by subtracting the phase and intensity measured at another wavelength were the contrast is high between the two blood types (e.g. at 760 nm). In the inverse imaging tested in this paper, all of the data used was difference data, similar to figures 3 and 4.

3.2 Monte Carlo Reconstruction Tests

As a test, the values of phase change and intensity change plotted in figures 3 and 4 were used to reconstruct images of the test objects. The resulting tomographic images of μ_a and μ_s' are plotted in figures 8 and 9. Figure 8 corresponds to the absorbing object at the centre with $\mu_a = 0.02$ mm^{-1} and scattering the same as the background. Figure 9 corresponds to the scattering inhomogeneity with $\mu_{s0}' = 2.0$ mm^{-1} and absorption the same as the background. The images here have been reconstructed on a 15x15 grid and then smoothed and dithered to provide a continuous grey scale image. Therefore the resolution of the image is limited to 1/15 of the image size, which here corresponds to 3 mm.

3.3 Finite Difference Reconstruction tests

The reconstruction based on the Monte Carlo data was qualitatively accurate, lending some confidence to the inverse solution. However it is not practical to generate data by

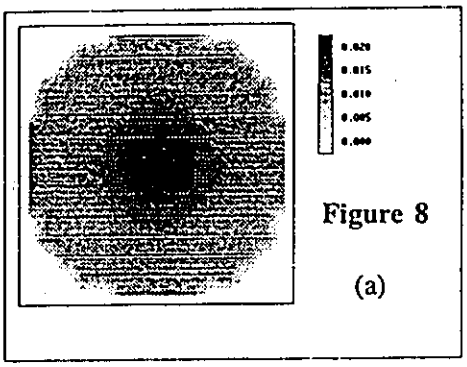

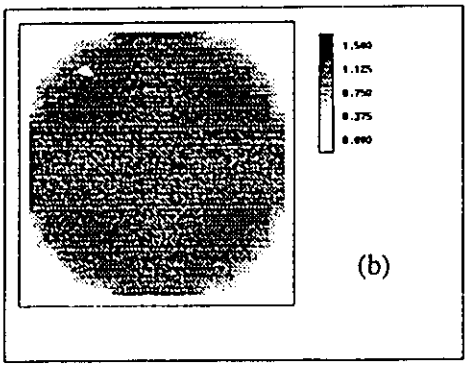

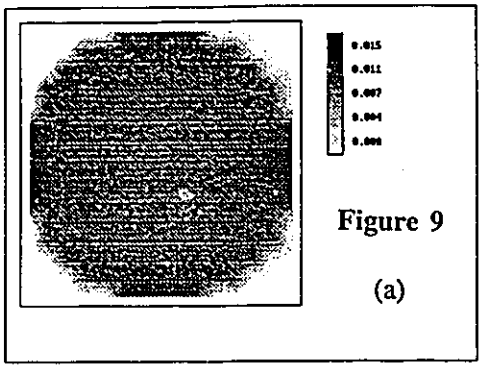

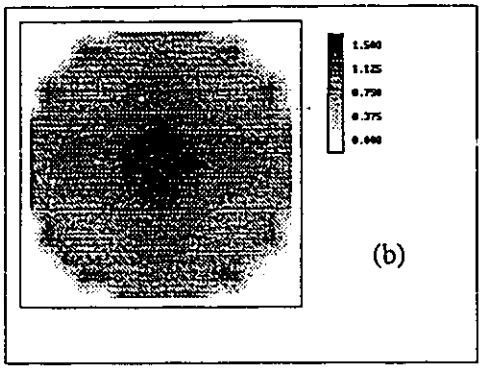

Figure 8 Reconstruction of Monte Carlo data of an absorbing object within a 50 mm cylinder. Original object was 10 mm in diameter with μ_a=0.02, and μ_s'=1.0mm^{-1}. Background was μ_a=0.01 and μ_s'=1.0mm^{-1}.
(a) Absorption coefficient map
(b) Scattering coefficient map.

Figure 9 Reconstruction of Monte Carlo data of a scattering object within a 50 mm cylinder, with background as in Figure 8. Original object was 10 mm in diameter with μ_a=0.01 and μ_s'=2.0 mm^{-1}.
(a) Absorption coefficient map
(b) Scattering coefficient map.

the Monte Carlo method when the object is not axially symmetric. Further studies were performed using a high resolution finite difference calculation of provide the "experimental" data. A test image with both a scattering and an absorbing object present was used to examine the ability of the algorithm to image multiple objects. The test image is shown in Figure 10(a), with the absorbing object shown in black and the scattering object shown in white, each were 2 times the value of the background coefficients. The reconstructed maps of μ_a and μ_s' are shown in Figures 10(b) and 10(c) respectively. Again the initial forward data was calculated on a 65x65x65 grid, and the reconstruction was done on a 17x17x17 grid, using only 5 iterations. Both the absorption and scattering maps are reconstructed with reasonable accuracy and there is little "crosstalk" between them.

The main advantage of using a 3-dimensional forward calculation for iterative imaging is the ability to accurately model the light transport within the tissue, and better predict the quantitative values of phase and intensity changes. To demonstrate the three dimensional nature of the algorithm, six test images were generated where the inhomogeneity within the cylinder was translated in the z direction through the imaging plane. Figures 11(a)-(f) show reconstructed images with a spherical absorbing object, radius equal to 10 mm and $\mu_a = 0.02$ mm^{-1}, located at distances of 30, 20, 15, 10, 5 and 0 mm, between the centre of the object and the image plane. As the object approaches the image plane the DOT image clearly shows the image increasing in contrast.

The effects of noise were also examined by adding typical experimental noise to the data before reconstruction. The noise added to the data was normally distributed about the mean with a standard deviation of ± 1% for the absolute intensity and ±0.5° for the phase. The reconstructions did not show any significant alterations due to this noise level.

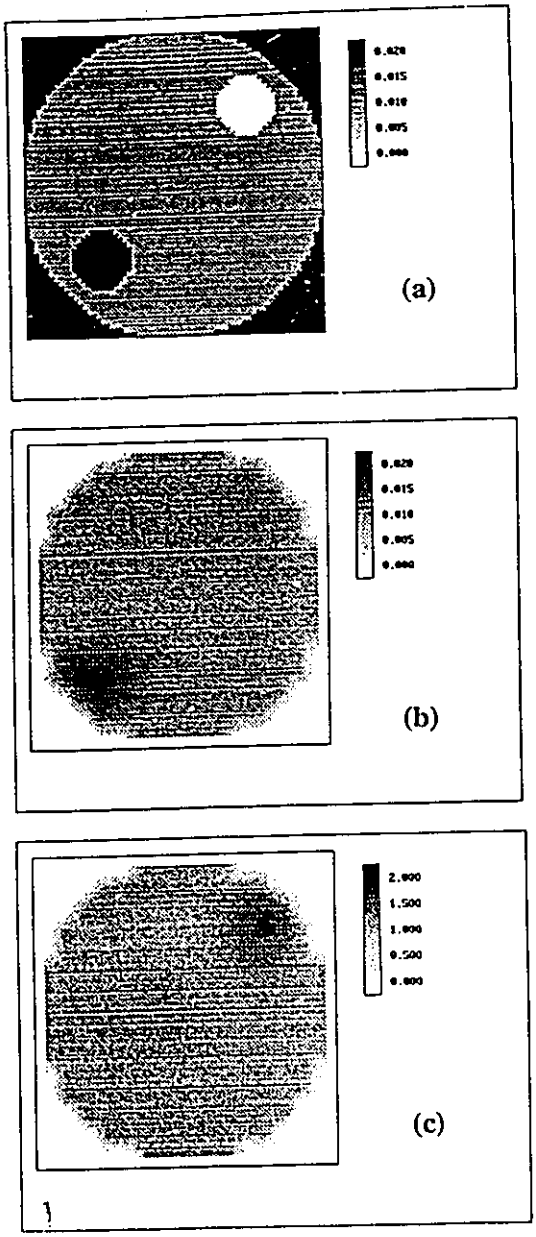

Figure 10 Reconstruction of a test image from phase and AC intensity data generated on a 65x65x65 finite difference grid. Image reconstruction is done on a 17x17x17 grid. The test image is shown in part (a) with background μ_a=0.01, μ_s'=1.0 mm^{-1} and diameter 100 mm. The black test object has μ_a=0.02, μ_s'=1.0 mm^{-1} and the white test object has μ_a=0.01, μ_s'=2.0 mm^{-1}. Part (b) is the absorption coefficient image, and part (c) is the scattering coefficient image.

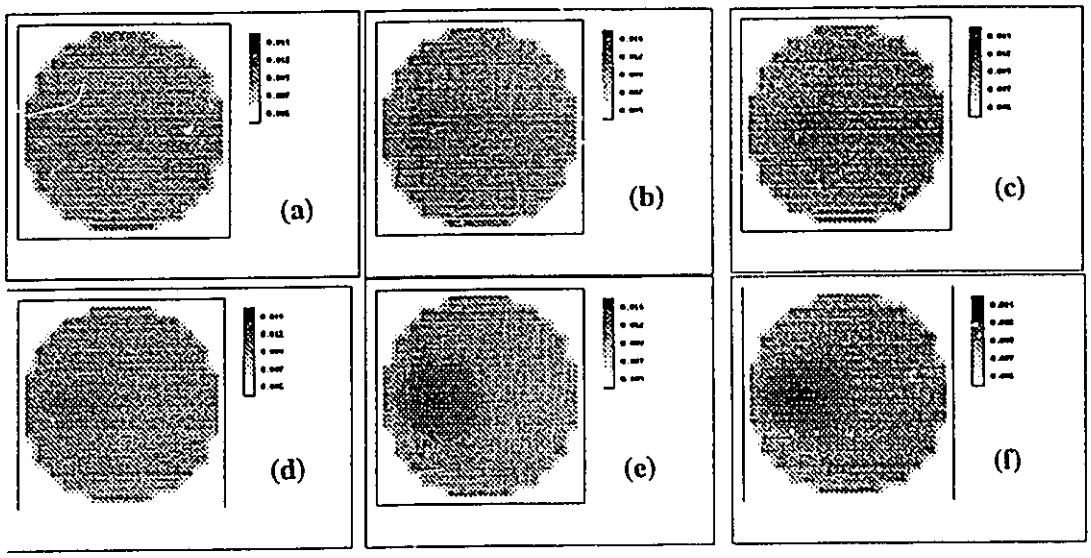

Figure 11 Six absorption coefficient images reconstructed from finite difference test data. An absorbing object is positioned as different distances from the image plane, (a) 30 mm, (b) 20 mm, (c) 15 mm, (d) 10 mm, (e) 5 mm, (f) 0 mm. Imaging different slices of the test cylinder with an absorbing spherical object, μ_{ao}=0.02 and 10 mm radius.

This indicates that the typical noise level in our system should not significantly hinder the reconstruction of optical images.

The reconstruction algorithm can be used with different resolutions. Naturally the finer the grid resolution, the better the reconstruction will be, but this is at the expense of a greatly increased calculation time. The time for reconstruction is roughly proportional to the square of number of pixels in the image. Different methods can be used to improve the speed of inversion of the jacobian matrix, but this calculation is still time consuming. The problem has been minimized here by reconstructing on a 17x17 image plane, however it is important to understand the loss of resolution which will be observed with this coarse pixel size. Reconstructions on 17x17 and 33x33 sized grids have been used with the longest reconstruction times taking up to 12 hours for 33 x 33, while the shortest reconstructions can take as little as 10 minutes with the 17x17 grid. In Figure 12, a test image with three absorbing objects was used to demonstrate the benefit of iterative imaging. The first iteration reconstruction of the image is shown in Figure 12(b) and the improvement after 5 iterations is shown in figure 12(c). In figure 12(b) the three objects are not resolved, and the absorption coefficient of the objects is not representative of their true values. In Figure 12 (c) the three objects are resolved, and the absorption coefficient levels of the objects are more representative of their real values.

4. DISCUSSIONS AND APPLICATIONS

4.1 Image reconstruction accuracy

Recently many researchers have demonstrated imaging methods for use in DOT using 2 dimensional numerical or analytic calculations. The major limitation with the

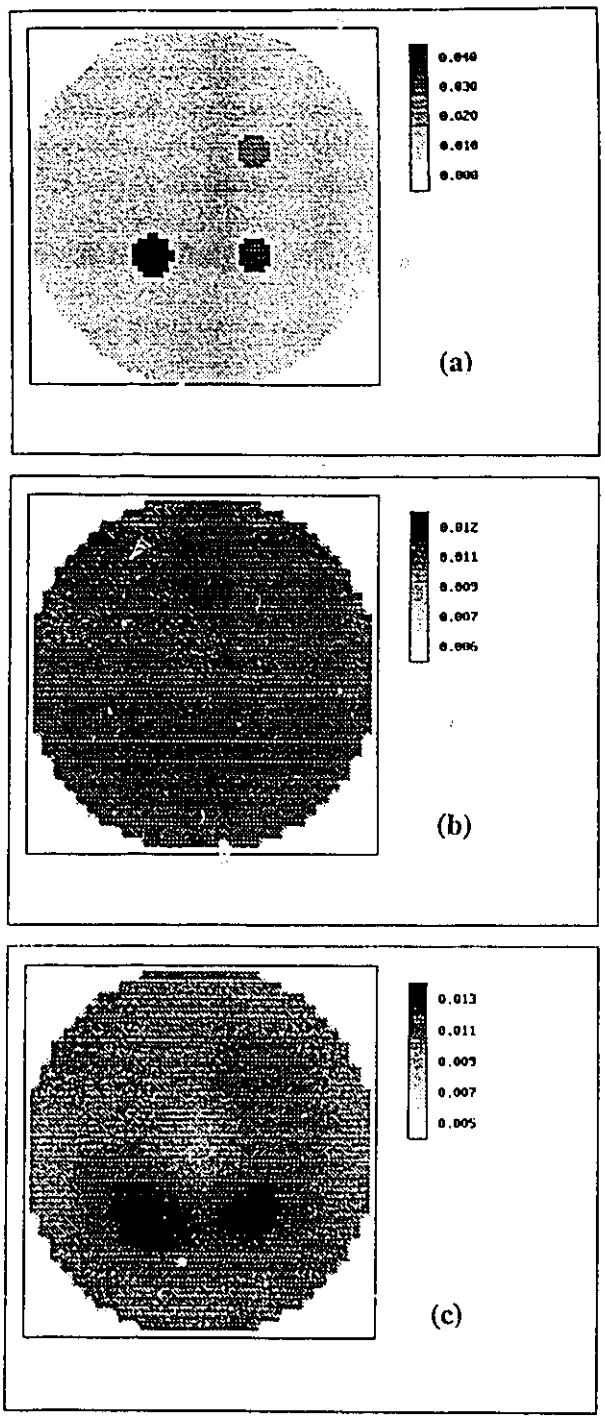

Figure 12 Reconstruction of a test cylinder containing three absorbing objects. Part (a) shows the test image, with background as before and three objects with μ_a=0.04, 0.03 and 0.02, shown respectively by increasing black levels. Part (b) shows the reconstruction on a 33x33x33 sized grid for one iteration. Part (c) shows the same reconstruction after 5 iterations.

iterative reconstruction methods is the long time required to obtain the solution, especially when extended to 3 dimensions. A faster 3 dimensional reconstruction algorithm has been developed by Barbour *et al*[6] based on analytic diffusion theory and a perturbation approach. The application of these calculations are limited to conditions which are within the perturbation assumptions. Other researchers have suggested simpler methods for image recovery such as backprojection with curved statistical paths[16,17]. Backprojection of the imaging data should be equivalent to the first iteration of the calculations used here since it is a first order calculation of the image from precalculated weighting functions. Backprojection yields a fast solution for the imaging problem, and may be the most appropriate clinical solution, however iterative reconstruction should provide improved imaging quality if it can be accomplished on a fast time scale. From the images in figure 12, there is an obvious improvement in both the resolution and contrast from iterative reconstruction. In the future, with improved computational speed and with parallel processor workstations, iterative imaging algorithms should be a viable solution for clinical imaging.

This paper demonstrates some of the simple features required of an imaging system. The arrangement of 4 sources and 20 detectors has provided adequate sampling for the reconstructions examined. The minimization of the number of sources needed is necessary to decrease the acquisition time for real clinical applications. The location of the 4 sources in this simulation creates an increased sensitivity along the two axes of the sources, which can sometimes appear as a reconstruction artifact (see figures 8 and 9). However this is never large enough to dominate the image. Also, the reconstruction of objects near the periphery of the object, such as in figure 10, are limited by the relatively coarse grid. Further testing of the algorithm is ongoing with both simulated and real data.

The comparison between Monte Carlo difference data and finite difference data showed some serious discrepancies, although the data produced images which were representative of the original objects. Real experimental data will be used to test the algorithm in the near future. Experimental noise in the measurements does not appear to be a large problem here since reconstruction of images with typical detector noise added to them did not show a significant change from images with no noise added. The overall blurring of the image seems to dominate the reconstruction process much more that the noise does, assuming the noise level does not exceed 10% of the signal. A more serious problem not modelled may be the lack of information of the source-detector geometry.

4.2 Assessment of *In Vivo* Applications

Some simple diffusion theory calculations can demonstrate that optical imaging will be restricted to relatively thin tissue volumes (i.e. thickness < 100 mm)[18]. The input near-infrared light intensity is limited by A.N.S.I. standards for medical diagnostic applications to between 0.2 to 1 Watt/cm^2. A lower limit of 10^{-15} Watts is approximately the minimum detectable level using current photomultiplier tube technology. Based upon the typical absorption and scattering coefficients observed in tissue spectroscopy, a reduction in transmitted intensity of 10^{-15} will be observed for tissues between 70 mm and 100 mm, at best. Some of the most likely applications identified presently for these tissue thicknesses are mammographic imaging or neonatal oxygenation monitoring. The calculations in this paper have focused on imaging through a 100 mm diameter cylinder and sphere since these geometries are typical of the maximum thickness for clinical applications.

In order to evaluate specific imaging geometries, typical values of the interaction

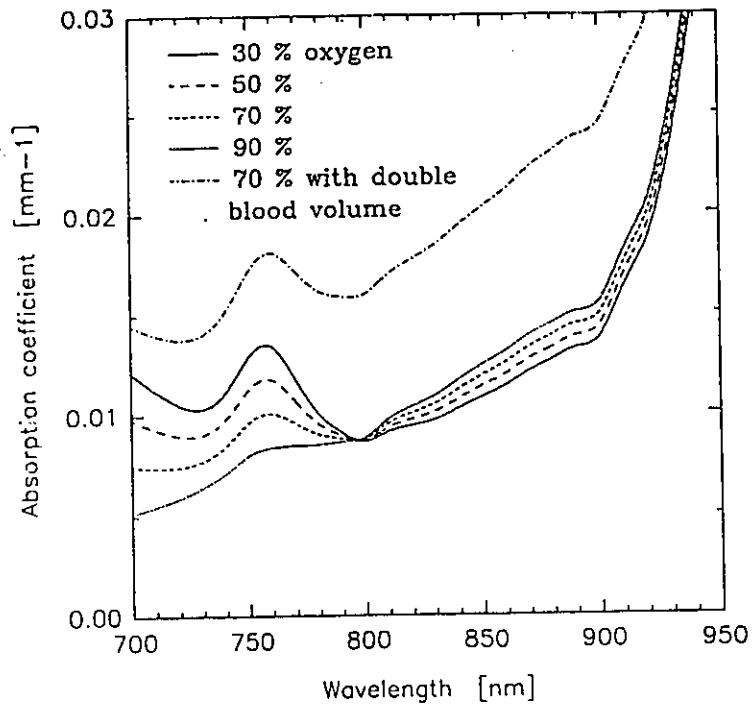

Figure 13 Theoretical calculation of the absorption spectrum of tissue based upon the typical values of hemoglobin and water present in tissue from Wray *et al*[19]. Using 80% water in tissue, and 0.084 mM hemoglobin, and varying levels of oxygenation. One calculation is based upon 0.168 mM hemoglobin.

coefficients must be found from the literature. In figure 13 the spectra of Hb and HbO_2 as given by Wray *et al*[19] are used to plot the absorption coefficient of typical tissue at different concentrations of Hb:HbO_2. The assumptions used in this calculation were that the concentration of Hb in tissue was 0.084 mM, and that the cytochrome concentration does not greatly affect the spectrum. Also the tissue was assumed to be composed of 80% water, and the absorption coefficients of water were calculated from the data of Hale and Querry[20]. It was assumed that no other chromophores contribute to the absorption coefficient. Figure 13 can be used to illustrate the changes in μ_a expected due to blood volume changes versus blood oxygenation changes. The maximum useful change in μ_a due to blood oxygenation is near λ = 755 nm since wavelengths shorter than 700 will be too highly attenuated by tissue. Blood volume changes would produce a shift in the whole spectrum as shown by the top line of Figure 13 for factor of 2 increase.

4.3 Breast Cancer Imaging

In terms of NIR breast cancer detection, Peters *et al*[21] reported only minor changes in the optical properties of excised normal and malignant breast tissues, and suggested that the majority of contrast in optical detection would come from increased vascularity. Profio *et al*[22] evaluated the basis of contrast in transillumination for breast cancer detection and found that the major source was an increase in blood vessel number and size in the tissue surrounding a cancerous lesion. They reported a 4 fold increase in RBC concentration in the outer areas of the tumour as compared to both the normal tissue and the tumour core. In the spectral region of 700-900 nm this increase in blood volume within tissue would lead to approximately a 4 fold increase in the absorption coefficient, as seen in figure 13. Assuming that the imaging of breast tumours is based on an increase

in blood volume due to increased vascularization, imaging with frequency domain systems should provide an increased contrast by a factor of 4 or 5 above cw light, for small lesions. This estimate is based upon the simulations plotted in figure 4, and assuming a change in μ_a from 0.01 to 0.04 for a 10 mm diameter lesion. However, the data in figure 5 suggest that the lateral resolution would not be significantly improved.

4.4 Tissue Oxygenation Imaging

For applications in neonatal tissue oxygen monitoring, the contrast produced from different oxygen concentrations within the blood is provided by the ratio of Hb to HbO_2. From Figure 13, the maximum change in μ_a is a factor of 2 from regions of high to low oxygen saturation. Imaging would require the ability to discriminate perhaps a 10 % change in μ_a, such as in Figure 7. The calculations in Figure 7 suggest that the diameter of such a region must be greater than 20 mm in order to produce a measurable change. Also the effect of frequency is not significant at these object sizes, and for larger regions the intensity decrease is actually greater for lower frequencies. Thus the calculations here would suggest that tissue oxygenation monitoring would best be accomplished with low frequency light modulation, and is probably limited to relatively large regions (i.e. regions > 20 mm at the centre of a 100 mm tissue volume). The resolution should be better for regions nearer the sources and detectors, at the periphery of the tissue volume. However calculations similar to those in Figure 7 for objects at the edge of the tissue volume show better contrast for lower frequencies as well.

Acknowledgements

We gratefully acknowledge the use of John Adams' MUDPACK multigrid routines and would also like to thank Dr. Tom Chow for use of his graphics program. The Ontario Laser and Lightwave Research Centre provided financial support for this work.

References

1 M. S. Patterson, B. Chance, B. C. Wilson, "Time resolved transmittance and reflectance for the non-invasive measurement of tissue optical properties," Appl. Opt. **28** 2331-6 (1989)

2 M. S. Patterson, J. D. Moulton, B. C. Wilson, K. Berndt, J. R. Lakowicz, "Frequency-domain reflectance for the determination of the scattering and absorption properties of tissue," Appl. Opt. **30**, 4474-6 (1991)

3 J. D. Moulton, Diffusion modelling of picosecond laser pulse propagation in turbid media *M.Eng. Thesis*, McMaster University (1990)

4 S. R. Arridge, M. Cope, D. T. Delpy, "The theoretical basis for the determination of optical pathlengths in tissue: temporal and frequency analysis," Phys. Med. Biol. **37** 1531-1560 (1992)

5 J. C. Adams, "MUDPACK: Multigrid portable Fortran software for the efficient solution of linear elliptic partial differential equations," Appl. Math. Comp. **34** 113-146 (1989)

6 R. L. Barbour, H. L. Graber, Y. Wang, J. H. Chang, R. Aronson, "A perturbation approach for optical diffusion tomography using continuous-wave and time resolved data," Medical Optical Tomography: Functional Imaging and Monitoring ed. G Muller (SPIE Press, Bellingham) (1993)

7 J. M. Kaltenbach, M. Kaschke, "Frequency- and time-domain modelling of light transport in random media," Medical Optical Tomography: Functional Imaging and Monitoring ed. G Muller (SPIE Press, Bellingham) pp 65-86

8 T. J. Farrell, M. S. Patterson, B. C. Wilson, "A diffusion theory model of spatially resolved, steady-state diffuse reflectance for the noninvasive determination of tissue optical properties *in vivo*," Phys. Med. Biol. **19**, 879-888 (1992)

9 T. J. Yorkey, J. G. Webster, W. J. Tompkins, "Comparing reconstruction algorithms for electrical impedance tomography," IEEE Trans. Biomed. Eng **34**, 11, 843-852 (1987)

10 S. R. Arridge, "The forward and inverse problems in time resolved infra-red imaging," Medical Optical Tomography: Functional Imaging and Monitoring ed. G. Muller, (SPIE Press, Bellingham) (1993)

11 R. Fletcher, Practical Methods of Optimization Vol I, (John Wiley & Sons, Toronto) (1980)

12 W.H. Press, S.A. Teukolsky, W.T. Vetterling, B.P. Fannery, Numerical Recipes in Fortran 2nd Ed. (Cambridge U. Press, New York) pp 816-862 (1992)

13 S. R. Fulton, C. E. Ciesielski, W. H. Schubert, "Multigrid methods for elliptic problems: A Review" Monthly Weather Review **114**, 943-959 (1986)

14 M. S. Patterson, B. W. Pogue, B. C. Wilson, "Computer simulation and experimental studies of optical imaging with photon density waves," Medical Optical Tomography: Functional Imaging and Monitoring ed. G. Muller (SPIE Press: Bellingham) (1993)

15 S. T. Flock, M. S. Patterson, B. C. Wilson, D. R. Wyman, "Monte Carlo modelling of light propagation in highly scattering tissues - I: Model predictions and comparison with diffusion theory," IEEE trans. Biomed. Eng. **36**, 1162-1168 (1989)

16 J. S. Maier, E. Gratton, "Frequency-domain methods in optical tomography: detection of localized absorbers and a backscattering reconstruction scheme" SPIE proc. **1888** 440-451 (1993)

17 D. A. Benaron, "Optical Biopsy and Imaging in Medicine: Imaging of brain haemorrhage and fluid accumulation using 2-D time-resolved optical tomographic scanning," Advances in Optical Imaging and Photon Migration (OSA : Washington) pp33-36 (1994)

18 B. C. Wilson, M. S. Patterson, B. W. Pogue, "Instrumentation for *in vivo* tissue spectroscopy and imaging," Proc. SPIE **1892** 132-147 (1993)

19 S. Wray, M. Cope, D. T. Delpy, J. S. Wyatt, E. Reynolds, "Characterization of the near infrared spectra of cytochrome aa_3 and haemoglobin for the non-invasive monitoring of cerebral oxygenation," Biochim Biophys Acta **933** 184-192 (1988)

20 G. M. Hale, M. R. Querry, "Optical constants of water in the 200 nm to 200 μm wavelength region," Appl. Opt. **12** 555-563 (1973)

21 V. G. Peters, D. R. Wyman, M. S. Patterson, G. L. Frank, "Optical properties of

normal and diseased human breast tissue in the visible and near infrared," Phys. Med. Biol. 35 1317-1334 (1990)

22 A. E. Profio, G. A. Navarro, O. W. Sartorius, "Scientific basis of breast diaphanography," Med. Phys. 16 60-65 (1989)

Introduction to Paper #5

The following paper was a continuation of the work done in the previous paper. The imaging algorithm seemed to perform well enough to be tested with experimental data. The following article analyses the effects of noise, systematic errors, number of iterations and agreement with experimental data.

The experiments were done at the Hamilton Regional Cancer centre with the same apparatus used throughout this thesis. The measurements were taken by Huabei Jiang, a visiting graduate student from Dartmouth College. The reconstructions and analysis were performed by me. The article was written by Dr Patterson and I with some suggestions from the group at Dartmouth.

Initial Assessment of A Simple System for Frequency Domain Diffuse Optical Tomography

B. W. Pogue[1], M. S. Patterson[1,2], H. Jiang[3], K. D. Paulsen[3]
[1]Hamilton Regional Cancer Centre and McMaster University
699 Concession Street, Hamilton, ON, Canada L8V 5C2
[2] Ontario Laser and Lightwave Research Centre
University of Toronto, Toronto, ON, Canada
[3] Thayer School of Engineering, Dartmouth College, New Hampshire

Abstract

Diffuse optical tomography is an imaging technique whereby spatial maps of absorption and scattering coefficients are derived from the characteristics of multiply scattered light transmitted through the object. The system described here used four intensity modulated light sources and measurements of the intensity and phase (relative to each source) at 16 or 20 detectors on the surface of a 10 cm diameter cylinder. An iterative Newton-Raphson algorithm was used to estimate the absorption and scattering coefficients at each pixel in a 17 x 17 array by minimizing the difference between measured and calculated values of the intensity and phase at the measurement sites. Forward calculations of the intensity and phase were based on a multigrid finite difference solution of the frequency domain diffusion equation. Numerical simulations were used to examine the resolution, contrast and accuracy of the reconstructions as well as the effects of measurement noise, systematic uncertainties in source-detector location, and accuracy of the initial estimates for the optical properties. Experimental tests also confirmed that the system could identify and locate both scattering and absorbing inhomogeneities in a tissue-simulating phantom.

1. Introduction

In recent years the application of near-infrared light for diagnostic medical imaging has been under intense investigation. While transillumination for breast cancer detection has been used for decades with limited success, recent improvements in light generation and detection techniques have stimulated new interest in optical imaging of scattering media such as tissue (Alfano 1994, Chance and Alfano 1994, Chance and Alfano 1995). Some investigators have attempted to use short light pulses with time-gated detection to reduce image degradation caused by multiply scattered light, while others have used all of the diffuse light for imaging measurements. Several researchers have demonstrated the detection of absorbing and scattering objects within a highly scattering medium using frequency domain light signals (Berndt *et al* 1991, Sevick *et al* 1992, Maier *et al* 1993, Fishkin *et al* 1993, Patterson *et al* 1993). The method employed in this paper uses intensity modulated light propagating through up to 10 cm of a cylindrical scattering object with non-invasive surface detection of the light signal's phase shift and intensity. These data are then used to reconstruct the spatial maps of the absorption and scattering coefficients of the objects. The goal of this work has been to develop a practical system and associated algorithm which could be used for optical imaging of tissue.

Jobsis (1977) first demonstrated that changes in the absorbance of tissue could be related to tissue oxygenation changes, and Cope *et al* (1988) have used this type of measurement for continuous neonate oxygenation monitoring *in vivo*. While these early methods could quantify absorption changes, the effects of light scattering were assumed to be constant throughout the measurement. More recently, several groups have developed models of light transport which can be used to decouple the effects of scattering and

absorption in order to quantify these coefficients (Bonner *et al* 1987, Star *et al* 1988, Patterson *et al* 1991c). All of these methods are based on the diffusion approximation to radiative transport theory (Lamarsh 1966, Ishimaru 1989). The recovery of both coefficients requires the measurement of additional features of the light signal besides the intensity, such as time-to-peak-intensity for a time resolved system (Patterson *et al* 1989) or the phase shift for a frequency-domain system (Patterson *et al* 1991). Frequency-domain measurements are especially useful for tissue spectroscopy applications due to the simplicity of the apparatus, and the high signal to noise ratio which can be achieved (Fantini *et al* 1995, Gratton *et al* 1983).

Arridge *et al* (1985) outlined the calculations necessary for optical imaging based upon relative absorption changes and, more recently, the steps required to decouple the absolute absorption and scattering coefficients from time domain measurements (Arridge *et al* 1993). Since photon paths in the medium are diffuse, a crucial step in reconstruction is the calculation of the effect that each voxel of the image has on each measurement. Various methods have been used to estimate these "weighting functions" or "sensitivity matrices", including Monte Carlo simulation (Barbour *et al* 1993), analytic perturbation theory (Maier *et al* 1993), and analytic solutions for a spherical inhomogeneity (O'Leary *et al* 1994). It is often assumed that the weighting function for a homogeneous medium can be used, but Arridge (1991) has stressed the importance of an iterative approach whereby the function is recalculated during the reconstruction process.

In this paper, a similar approach was used to generate an iterative imaging algorithm with an emphasis on speed and practicality. A small number of light sources (4) and detectors (16 or 20) were used. This algorithm has been tested on both simulated data and real experimental data measured on a tissue-simulating phantom. Reconstruction

was performed on a relatively coarse grid with spatial resolution of about 6 mm. All forward calculations were performed using a multigrid algorithm to solve the finite difference approximation to the diffusion equation for light propagation. We also assumed that all measurements on the object to be imaged could be made relative to a set of measurements on a homogeneous object. This is an easier problem to solve, since measurements and calculations must agree only in changes in quantities like the intensity, rather than their absolute values. It is not unrealistic, however, as reference measurements might be provided from a reference tissue-phantom or from measurements made on the same object at a different wavelength. For example, if the goal were to image hemoglobin oxygenation, data acquired at a wavelength of 805 nm, where hemoglobin and oxyhemoglobin have the same absorption coefficient, might serve as a reference.

The light sources were intensity modulated and measurements of phase and AC intensity were made on the surface of the phantom. The algorithm used to solve the inverse problem was a Newton-Raphson calculation similar to one used in some electrical impedance tomography applications (Yorkey *et al* 1987). An iterative process was used to find the values of absorption and scattering at each pixel of the image which minimize the differences between the experimental data and the calculations of the finite difference forward model. Numerical experiments were performed to test the accuracy of the reconstruction and the improvements provided by iteration. The effects of experimental noise, the accuracy of the initial guess, and systematic errors in source-detector separation were also explored. Experiments were performed with inhomogeneities representing realistic changes in the absorption and scattering coefficients as well as a "cyst-like" object filled with water. In all cases our system, despite its simplicity, was able to detect, localize and characterize the imbedded objects, suggesting that diffuse optical tomography

may have potential in some clinical problems.

2. Theory and Calculations

2.1 *The Inhomogeneous Diffusion Equation*

Since the transport of near-infrared light in tissue can be modelled accurately with diffusion theory (Patterson *et al* 1991), the frequency domain diffusion equation can be used to predict the photon fluence rate $\Phi(\mathbf{r},\omega)$, at any location, $\mathbf{r}$, within the tissue :

$$\nabla \cdot D(r) \nabla \Phi(r,\omega) - (\mu_a(r) + i\omega/c_n)\ \Phi(r,\omega) = S(r,\omega) \qquad (1)$$

for a source $S(\mathbf{r},\omega)$ which is sinusoidally modulated at frequency $\omega=2\pi f$, where f is typically in the MHz range. Here $D(\mathbf{r})$ is the diffusion coefficient, given by $D(\mathbf{r}) = (3[\mu_a(\mathbf{r})+\mu_s'(\mathbf{r})])^{-1}$ for absorption and reduced scattering coefficients $\mu_a(\mathbf{r})$ and $\mu_s'(\mathbf{r})$, respectively. The velocity of light in tissue for average index of refraction n, is $c_n = c/n$. When the diffusion coefficient is uniform throughout the volume, the first term in equation (1) becomes $D\nabla^2\Phi(\mathbf{r},\omega)$, so that equation (1) reduces to the Helmholtz equation with the complex wavenumber given by :

$$k = \left(\frac{\mu_a + i\omega/c_n}{D} \right)^{1/2} \qquad (2)$$

Analytic solutions of this equation for homogeneous optical coefficients are given in detail by Moulton (1990) and Arridge (1992) for several regular geometries. However for imaging, spatial variation of the optical coefficients must be taken into consideration to yield the following equation :

$$\nabla^2\Phi(r,\omega) + \frac{\nabla D(r)}{D(r)}\cdot\nabla\Phi(r,\omega) - \left(\frac{\mu_a(r)+i\omega/c_n}{D(r)}\right)\Phi(r,\omega) = \frac{S(r,\omega)}{D(r)} \quad (3)$$

The light signal, which is measured at the surface by a detector, is proportional to the photon current across the boundary. This current is proportional to the gradient of the fluence at the boundary and is given by Fick's Law :

$$J(\rho,\omega) = -D\nabla\Phi(r,\omega) \quad (4)$$

Solution of equation (3) also requires information about $\Phi(r,\omega)$ and/or its gradient at the boundary of the volume of interest. The boundary condition we used is discussed below.

2.2 *Forward Calculations: Solution of the Diffusion Equation*

Equation (3) is a complex elliptic equation which can be solved numerically for $\Phi(r,\omega)$ as a boundary value problem. The tissue volume can be approximated by a discrete lattice of points, and the discretized version of equation (3) can be written as a finite difference expression:

$$\frac{\Phi_{i+1jk}+\Phi_{i-1jk}}{\Delta L_i^2} + \frac{\Phi_{ij+1k}+\Phi_{ij-1k}}{\Delta L_j^2} + \frac{\Phi_{ijk+1}+\Phi_{ijk-1}}{\Delta L_k^2} + \left(\frac{D_{i+1jk}}{D_{ijk}}-1\right)\frac{\Phi_{i+1jk}-\Phi_{ijk}}{\Delta L_i^2} + \left(\frac{D_{ij+1k}}{D_{ijk}}-1\right)$$
$$+\left(\frac{D_{ijk+1}}{D_{ijk}}-1\right)\frac{\Phi_{ijk+1}-\Phi_{ijk}}{\Delta L_k^2} - \left[\frac{2}{\Delta L_i^2}+\frac{2}{\Delta L_j^2}+\frac{2}{\Delta L_k^2}+\left(\frac{\mu_{a,ijk}+i\omega/c_n}{D_{ijk}}\right)\right]\Phi_{ijk} = S_{ij} \quad (5)$$

where i, j, and k are the 3 direction axes x, y, and z respectively. ΔL is the step size in each of the directions indicated by a subscript, and S_{ijk} is the source. If the spatially varying values of D_{ijk}, $\mu_{a,ijk}$ and S_{ijk} are known, then the fluence at any point, $\Phi_{i,j,k}$ can be found through pointwise Guass-Seidel relaxation of the grid fluence values (Adams 1989, Press *et al* 1992).

The numerical solution of this equation can be accomplished by a number of standard finite differencing techniques (Press *et al* 1992). One of the fastest methods is the multigrid solution and Fulton *et al* (1986) have reviewed the application of this method to elliptic problems. The theory behind the use of multigrids can be stated in simple terms. The accuracy in the solution of the equation for finite difference calculations depends upon the mesh size, i.e. ΔL. Very coarse mesh grids (large ΔL) are good for solving problems quickly, however they yield large errors due to the coarse step size. Fine mesh grids (small ΔL) produce smooth and accurate solutions but they require a large numbers of iterations to achieve a solution. Multigrid routines solve the problem on several sized grids simultaneously, using the coarse grids to provide quick steps toward the solution, and the finer grids to smooth the solution for better accuracy. The process of interpolation between grids and smoothing with finer resolution is quite detailed and a precise description of the MUDPACK routine used here is given in Adams (1989). Multigrid solutions have not been used in many applications, mainly due to the complexity of coding the algorithm, but in this application the speed of the solution is very important because of the need to perform many forward calculations.

For the forward calculations it was assumed that $\Phi(\mathbf{r},\omega) = 0$ on the tissue surface. This is the simplest boundary condition to implement and is justified for two reasons. First, as discussed in the *Introduction*, we are concerned with changes in phase and intensity relative to a homogeneous object, rather than the absolute values of phase and intensity. As shown in a previous study (Pogue *et al* 1995), these relative values are insensitive to the detailed nature of the boundary condition. Second, the experiments described below were performed with an index-matched absorbing boundary which comes closest to providing the zero-fluence boundary condition. Another simplification was

made in calculating the detector signals: instead of finding the gradient specified in equation (4), the value of the photon fluence rate at the grid point closest to the line between the detector and the centre of the cylinder was used. This is justified because the fluence rate at the detector is forced to zero, so that the normal component of the gradient will be proportional to the fluence rate just inside the surface.

Solution of equation (3) yields a complex number for the photon fluence rate at each grid point. The AC intensity is given by the magnitude of this number, and the phase relative to the source is equal to the arctangent of the ratio of the imaginary part to the real part. Data sets for reconstruction consisted of the phase differences and log of the AC intensity ratios between the test object and a homogeneous object of the same dimensions.

For numerical experiments, a cylinder with a diameter of 100 mm and length of 100 mm was modelled (see Figure 1) using up to 20 detector locations on the perimeter. In the tests of optical reconstruction the 4 source locations shown were used, resulting in 80 measurements of phase and AC intensity in total. This geometry was chosen as a practical optical CT imaging system. Numerical simulations for this size cylinder were carried out with three different sized grids: 17x17x17, 33x33x33, and 65x65x65. Using these square grids, a cylinder was simulated by simply setting the absorption coefficient to very high values, $\mu_a = 1000\ mm^{-1}$, outside the radius of the cylinder. In this way the fluence values would be approximately zero outside the cylinder radius, and inside the cylinder the fluence would be determined by the μ_a and μ_s' values, and the source position. In a previous study (Pogue *et al* 1995), it was shown that there was excellent agreement between the analytic diffusion theory solution for a homogeneous cylinder and the finite difference calculations at all three grid sizes. In this paper, all forward simulations used

to generate 'test data' for inhomogeneous objects were calculated on the finest grid (65x65x65). Reconstructions were performed on either the 17x17x17 or the 33x33x33 grids, providing grid resolutons of 6.25 mm and 3.13 mm, respectively. However it should be noted that the resolution of the image is also limited by the diffuse spread of the light (see Discussions). Typical forward calculation times on a SUN SPARC 10 workstation were 50 seconds for the finest grid, and less than a second for the coarsest grid.

2.3 *Inverse Calculations: Newton-Raphson Iteration*

Reconstructing optical images of the tissue from measurements at the surface, as illustrated in figure 1, is not as simple as the straight line backprojection methods used in x-ray CT because the photon paths are diffuse and multiply-scattered. The distributions of photon paths can be calculated with diffusion theory, but recovering the interaction coefficient distribution is a fairly complex inverse problem. In this paper, the finite difference forward calculation is used to generate a Jacobian matrix, **J**, which is the derivative of the log of AC light intensity (I_{AC}) or phase (ϕ) at each detector, for each source, with respect to the interaction coefficients (μ_a and μ_s') of each pixel in the image. The forward solution is calculated twice for each Jacobian value with and without an increase in the pixel value of μ_a or μ_s', and the finite difference of the detected phase or log intensity are used. In the following equation, the absorption coefficient is used to illustrate the algorithm (i.e. each element of the matrix $\mathbf{J}(I_{AC},\mu_a)$ is given by $j_{i,j} = \partial I_{AC,i}/\partial \mu_{a,j}$ where i is the source-detector pair and j is the image pixel). This matrix represents the sensitivity of each source-detector pair to changes in μ_a at each of the image pixels. Using this matrix and a 1st order Taylor's expansion, a Newton-Raphson iterative

algorithm can be used to calculate the μ_a vector from the equation (Yorkey *et al* 1987):

$$J^k(I_{AC},\mu_a)\ (\underline{\Delta\mu_a^k}) \;=\; (\underline{I_{AC}}^k_{calc} - \underline{I_{AC}}_{obs}) \qquad (6)$$

where $\underline{\Delta\mu_a}^k$ is the update of the $\underline{\mu_a}$ image vector at iteration number k, $\underline{I_{AC}}_{obs}$ is the vector of observed AC intensities, and $\underline{I_{AC}}^k_{calc}$ is the vector of calculated AC intensities at iteration number k. Note that the Jacobian matrix itself is recalculated at every iteration. The $\underline{\mu_a}$ image vector has n x n components, where n is the number of pixels on each side of the square image. The inverse of the Jacobian matrix times the observed change in AC intensity at each detector yields the change in absorption coefficient at each pixel. However the inversion of the J matrix requires multiplication by the transpose on each side, J^t, to generate a square matrix, and then Tikhonov regularization by adding a factor, λ^k, times the identity matrix, I (not to be confused with I_{AC}), yielding :

$$\Delta\underline{\mu_a}^k = (J^k)^t\ (\underline{I_{AC}}^k_{calc} - \underline{I_{AC}}_{obs})\ \left[\ (J^k)^t(J^k) + \lambda^k I\ \right]^{-1} \qquad (7)$$

More detailed derivations of these equations are available in many treatments of inverse problems (Fletcher 1980, Colton *et al* 1992). It should be noted that the purpose of the regularization of equation 6 is to compensate for the ill-conditioned nature of the Jacobian matrix, which results from the low sensitivity to changes in μ_a in regions of the image which are distant from both the source and the detector. It should also be mentioned that small variations in the Jacobian were observed between neighbouring pixels, and these high frequency spatial variations appear to be a result of the relaxation method used in the finite differencing. These fluctuations were smoothed by simply averaging the nearest 9 pixels at all points in the Jacobian. The effect of this smoothing is a minor loss in resolution, while the accuracy of the inversion process is improved.

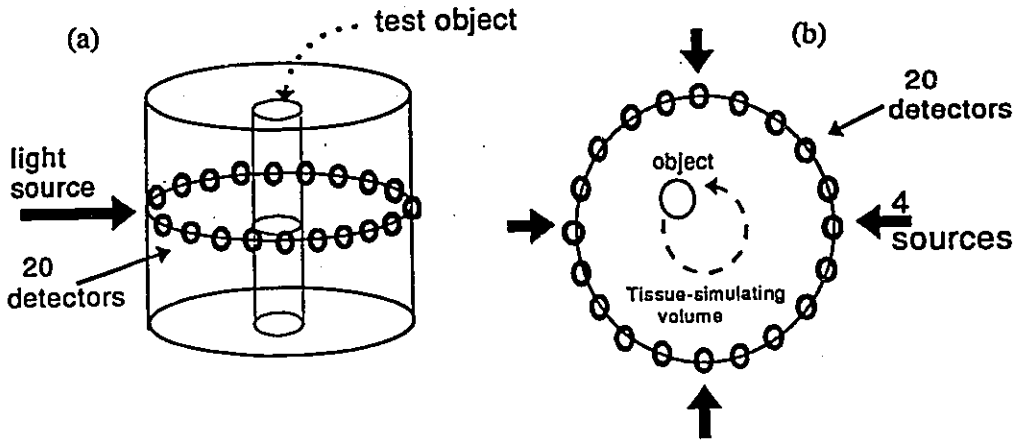

Figure 1 The geometry used for tomography simulations, with 4 source locations and 20 detector locations surrounding a 100 mm cylinder at the midplane. The object position and optical properties can be varied to test the imaging algorithm. Both the 3-D perspective view and the 2-D imaging plane are shown. Reconstructions are all constrained to the 2-D imaging plane. (b) demonstrates the rotation of the object about the centre of the phantom which was used in the experiments instead of changing the source position.

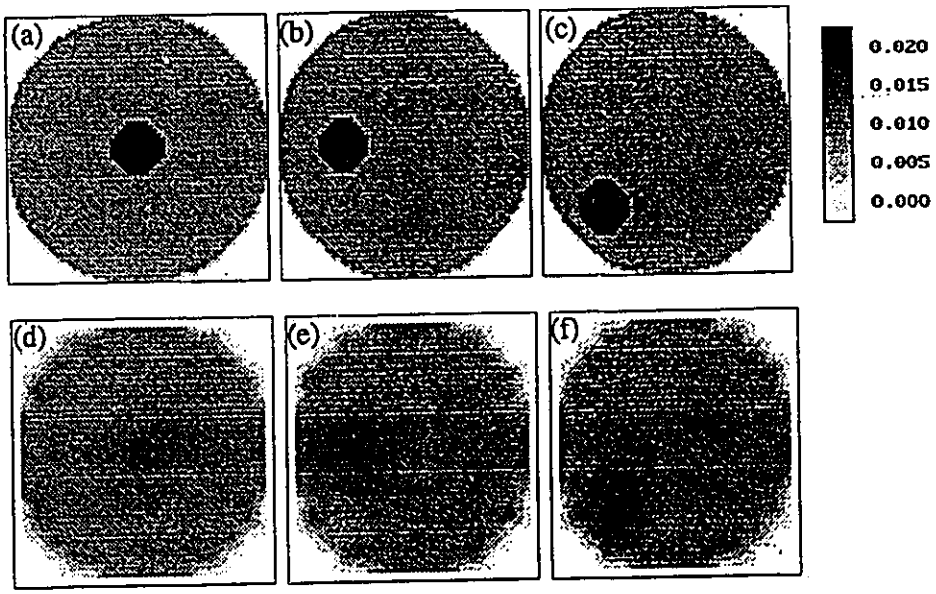

Figure 2 The three test images used to assess reconstruction resolution, contrast, and accuracy in different areas of the imaging plane. For each of the images the total diameter was 100 mm, and the inhomogeneities were 20 mm in diameter. All three tests had (grey) background optical properties of $\mu_a = 0.01$ mm^{-1} and $\mu_s' = 1.0$ mm^{-1}. The (black) inhomogeneity in the images had twice the absorption, $\mu_a = 0.02$ mm^{-1}, with the same scattering value. The grey scale in the corner shows the absorption coefficient. These images were reconstructed from a 65x65x65 grid finite difference forward calculation.

To this point the derivation has been limited to the absorption coefficient, μ_a, and the log AC intensity, but the observed quantities are both phase and log AC intensity, ϕ and I_{AC}, and the interaction is described by both absorption and scattering coefficients. The complete calculation therefore incorporates four derivative matrices $\partial\phi/\partial\mu_a$, $\partial\phi/\partial\mu_s'$, $\partial I_{AC}/\partial\mu_a$, $\partial I_{AC}/\partial\mu_s'$, and is a 2 x 2 matrix equation :

$$\begin{bmatrix}\Delta\mu_a\\ \Delta\mu_s'\end{bmatrix} = \begin{bmatrix}J^t(I_{AC},\mu_a) & J^t(\phi,\mu_a)\\ J^t(I_{AC},\mu_s') & J^t(\phi,\mu_s')\end{bmatrix}\begin{bmatrix}(I_{AC_{meas}} - I_{AC_{calc}})\\ (\phi^n_{calc} - \phi_{obs})\end{bmatrix}$$
$$\cdot\left[\begin{pmatrix}J(I_{AC},\mu_a)J^t(I_{AC},\mu_a)+J(\phi,\mu_a)J^t(\phi,\mu_a) & J(I_{AC},\mu_s')J^t(I_{AC},\mu_a)+J(\phi,\mu_s')J^t(\phi,\mu_a)\\ J(I_{AC},\mu_a)J^t(I_{AC},\mu_s')+J(\phi,\mu_s')J^t(\phi,\mu_a) & J(I_{AC},\mu_s')J^t(I_{AC},\mu_s')+J(\phi,\mu_a)J^t(\phi,\mu_a)\end{pmatrix} + \begin{pmatrix}\lambda_1 I & 0\\ 0 & \lambda_2 I\end{pmatrix}\right]^{-1} \quad (8)$$

At each iteration, the reconstruction error χ^2 was minimized by using a Levenberg-Marquardt loop to find the optimum regularization values λ_1 and λ_2. The reconstruction error χ^2 was defined as:

$$\chi^2 = \frac{1}{2N}\sum_{i=1}^{N}\left(\frac{I_{AC_{i\,calc}} - I_{AC_{i\,obs}}}{\sigma(I_{AC})}\right)^2 + \left(\frac{\phi_{i\,calc} - \phi_{i\,obs}}{\sigma(\phi)}\right)^2 \quad (9)$$

where N is the number of source-detector pairs. The values of $\sigma(I_{AC})$ and $\sigma(\phi)$ were the standard deviations of the noise in a typical measurement.

Images of the absorption and scattering coefficients were created by starting with a homogenous solution as the first guess of $\mu_{a,ijk}$ and $\mu_{s,ijk}'$ at all points and iterating to find the corrected values. In principle the light measurements could be done in 3 dimensions with a fully 3 dimensional reconstruction of the tissue volume, but this is too computationally intensive at the present time for a typical workstation. Therefore we have restricted the measurements and reconstruction to one transverse plane midway between the ends of the cylinder. Figure 1 (a) shows the imaging plane from the 3-dimensional perspective, while figure 1 (b) shows the 2-D imaging plane as a slice removed from the cylinder. All forward calculations of the light propagation are performed in 3 dimensions,

but because only the central plane was reconstructed, it was necessary to assume a "thickness" for this plane. Separate calculations (Pogue *et al* 1995) showed that the resolution is about 20 mm on the central axis of the phantom, and this was the value assumed for the slice thickness in the reconstruction. Since no measurements are taken out of the imaging plane, it is not possible to reliably estimate the optical coefficients outside this plane.

While it is customary in electrical impedance tomography to use 16 sources and 16 detectors for imaging, the optimum number of sources and detectors is not known for optical tomography. A larger number of sources and detectors yields a larger data set, which in turn may improve the accuracy and resolution of the reconstructed image. However the image quality will also depend on several other factors, such as the noise level and the complexity of the object. An important factor in iterative imaging is to lower the computational time required for the reconstruction, and this can be done by reducing the number of Jacobian values which need to be calculated. The number of Jacobian values depends directly on the number of sources and detectors. The multigrid algorithm used in this study allowed placement of sources only on the boundary of the rectangular grid, so only 4 sources were used. The photons which sample the object scatter out in all directions from the source, so that one source can yield useful data at all detector locations. The observable vectors in equation 8, ϕ_{obs} and $I_{AC,obs}$, are arrays of 80 phase measurements and 80 AC intensity measurements, respectively, corresponding to 20 detectors for each of the 4 source locations. For the experiments only 16 detectors were used with the same 4 source locations. The optimum number of sources needed is probably dependent upon the resolution required and the time available for reconstruction.

Most of the images shown here have been reconstructed on a 17x17 grid and then

smoothed and "dithered" to provide a continuous grey scale image. Therefore the pixel resolution of the image is limited to 1/16 of the image size, which here corresponds to 6.25 mm for the finite difference images (since they are of 100 mm phantoms) and 5.3 mm for the experimental data (since they were 86 mm phantoms). This size of grid was chosen from preliminary calculations which indicated that the real FWHM resolution would be limited to 20 mm at the centre, for a 100 mm diameter object (Pogue *et al* 1995). Therefore the pixel size of 6.25 mm should be more than adequate except, perhaps, near the surface. This choice of reconstruction grid also greatly reduces the computation time for the Jacobians. The computation time for the total Jacobian matrix of μ_a and μ_s' is less than 5 minutes on a SUN SPARC 10 station with one processor. For complicated objects the pixel size may not be adequate, so that the algorithm was set up to reconstruct images on a 33x33 sized grid as well.

3. Experiments

The experiments used to test the tomography reconstruction algorithm were performed on tissue simulating liquids in cylindrical containers. The main phantom was manufactured from black ABS plastic and was 86 mm in inner diameter and 300 mm in length. Source and detector fibre bundles were inserted through holes drilled in the side of the cylinder midway along its length. The holes were sealed with pieces of clear mylar (50 μm thickness) glued to the inside surface of the cylinder. Inhomogeneities were included in the phantom as cylinders, of 250 mm length and 25 mm diameter, made of clear thin mylar and filled with liquid of various optical properties. The 16 detector locations were equally spaced around the circumference, and a single source hole was

located midway between two of the detector holes. The source was a diode laser (wavelength 751 nm, and power 4.5 mW) and 3 mm diameter fibre bundles were used to deliver the light to the phantom and detectors. The diode laser output was modulated by about 40% at 150 MHz. The detection system has been described in detail by Gratton *et al* (1983) and employed two infrared sensitive photomultiplier tubes (Hamamatsu model R928) which were gain modulated at a frequency of 150.0001 MHz to heterodyne the signal down to the beat frequency of 100 Hz. For a typical measurement the phase noise was 0.2° and the AC intensity noise was 1.0%.

The tissue-simulating liquids consisted of distilled water, Intralipid and India Ink mixed in the appropriate proportions (van Staveren *et al* 1991, Madsen *et al* 1992). These phantom materials have been used in several studies, and the optical properties were well characterized. The optical coefficients of the material used to fill the phantom were $\mu_s' = 0.47 \pm 0.03$ mm^{-1} and $\mu_a = 0.0047 \pm 0.0003$ mm^{-1}. These values were measured with the frequency-domain spectroscopy system described in a previous study (Pogue *et al*, 1995). The inhomogenities used in the phantoms were filled with the same type of fluid but with various scattering and absorption coefficients. Measurements were taken for three different conditions: no object present, mylar cylinder filled with the same liquid as main phantom, and mylar cylinder filled with a different liquid. As in previous studies (Madsen *et al* 1993, Patterson *et al* 1993), we found that the perturbations due to the mylar cylinder alone were significant. Hence these measurements were used as the reference in difference imaging, rather than the data from the truly homogeneous phantom. It is important to note that the presence of the mylar was simply subtracted from the measured data of phase and log(intensity), and that this approximation of the mylar effects is probably valid to first order. It is difficult to avoid the phase shift and intensity

changes introduced by this boundary between two different scattering solutions in an experiment. Alternative experimental arrangements could be used, as discussed later.

4. Results

4.1 *Resolution, Contrast and Accuracy*

Initial studies were performed using a high resolution finite difference calculation (grid size of 65x65x65) to provide the simulated "experimental" test data. Forward calculations were performed with a single absorbing object of diameter 20 mm in three different locations as shown in figures 2 (a), (b), (c). Normally distributed random errors with standard deviations of 0.2° in phase and 1% in the AC intensity were added to the data. The background optical properties were $\mu_s' = 1.0$ mm^{-1}, $\mu_a = 0.01$ mm^{-1}, the absorbing object had the same μ_s' value but $\mu_a = 0.02$ mm^{-1}, and the modulation frequency was 300 MHz. The images, reconstructed on a 17x17 grid after 10 iterations, are shown in figures 2 (e), (f), (g). In figure 3 the reduced χ^2 value of the reconstruction is plotted as a function of the iteration number for the three images. After five or six iterations, little change is seen in χ^2 for any of the reconstructions. In figure 4 the absolute value of the absorption coefficient at the centre pixel of the inhomogeneity is plotted as a function of the iteration number. Again, this value stabilizes after 6 iterations. In figure 5 the full width at one tenth of the maximum reconstructed μ_a (FWTM) is plotted as a function of the iteration number. As the iterations progress, the width of the object decreases and reaches a minimum. Even though the object in the centre can be reconstructed with the lowest χ^2 error in the phase and AC amplitude, this image has the poorest resolution and contrast.

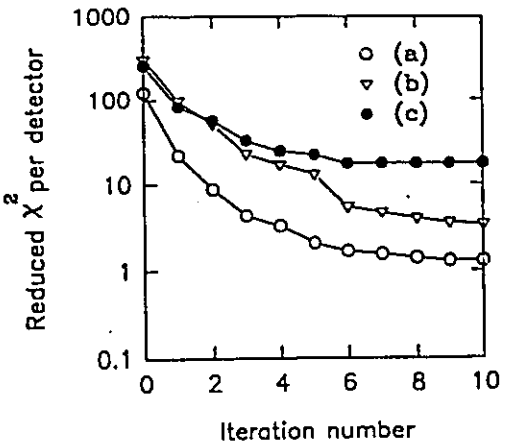

Figure 3 The reduced χ^2 reconstruction error for the test images shown in Figure 2 as a function of the iteration number. The standard deviations of noise added to the measurements were 0.2° in phase and 1% in AC intensity.

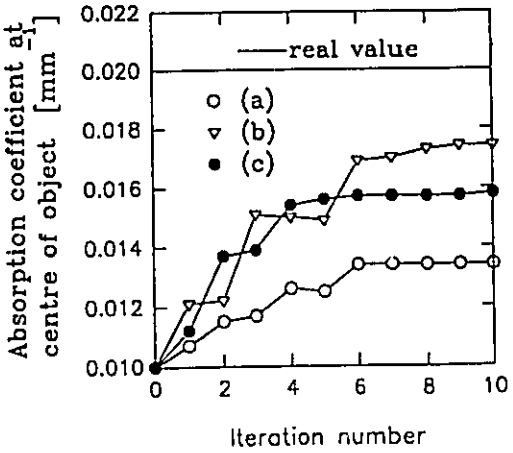

Figure 4 The value of the absorption coefficient at the centre of the reconstructed image of the inhomogeneity in each of the test images of Figure 2. The actual value for each was 0.02 mm^{-1}.

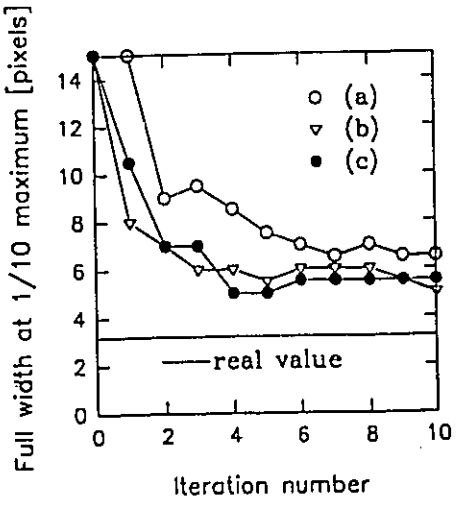

Figure 5 The full width at 1/10 maximum (FWTM) of the inhomogeneity is shown for the three test object reconstructions from figure 2. The real full width of the inhomogeneities was between 3 and 4 pixels.

In Figure 6(a), a test object with three different absorbing inhomogeneities was used to demonstrate the benefit of iterative reconstruction. This reconstruction has been done on a 33x33 grid to improve the quality of the image. The result of the first iteration is shown in Figure 6(b) and the improvement after 5 iterations is shown in figure 6(f). The first iteration, which fails to resolve the three objects is equivalent to a simple weighted backprojection (Maier *et al* 1993) since the sensitivity matrix (or Jacobian) is calculated for a homogeneous cylinder. Successive iterations show a definite improvement in the contrast and resolution although a low μ_a artifact is evident at the centre of the cylinder. The absorption coefficient of each of the three objects was seriously underestimated by the reconstruction algorithm, but the relative order of the three was correct.

4.2 *Random Errors: Experimental Noise*

A simple object, with one absorbing and one scattering inhomogeneity each 10 mm in diameter, was used to test the effects of random experimental errors on the reconstruction. Figures 7(a) and 7(b) show the absorption and scattering maps of the test object used to generate the forward data. In figures 7(c) and 7(d), the absorption and scattering reconstructions are shown for the same noise level as used before, 0.2° in phase and 1% in AC intensity. The reconstructions do not show any significant artifacts and the scattering and absorbing objects are clearly identified with little "cross-talk" between the images. In figures 7(e) and 7(f), the reconstructions are shown for noise levels of 1.0° in phase and 1% in AC intensity. Then, in figures 7(g) and 7(h) the noise level was increased to 5.0° in phase and 1% in AC intensity. The increased noise in the phase degrades the quality of the scattering image more significantly than the absorption image,

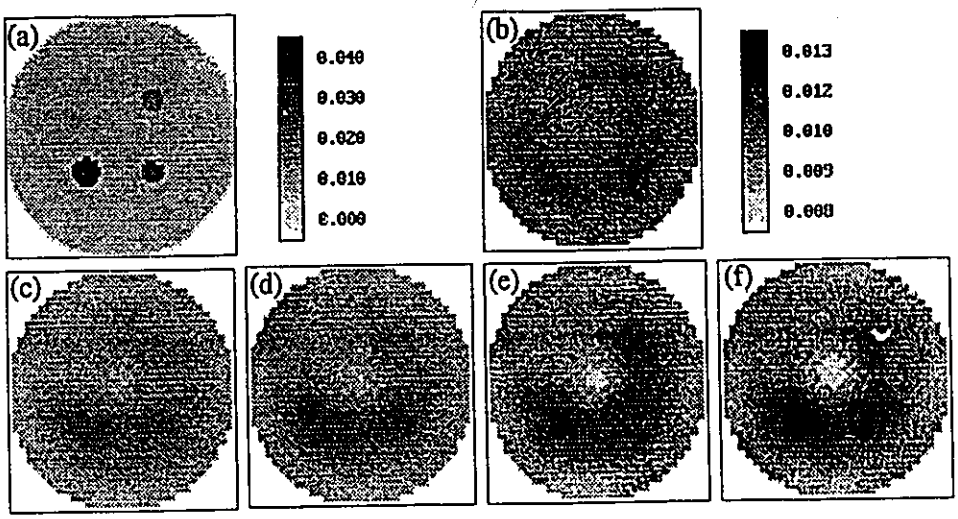

Figure 6 A test object is shown in figure (a) with three inhomogeneities. The (grey) background optical properties were $\mu_a = 0.01$ and $\mu_s' = 1.0$ mm^{-1}, and the three (darker) objects all had the same scattering with absorption coefficients of 0.02, 0.03, and 0.04 mm^{-1}. The diameter of the objects was 10 mm. The images in (b) to (f) shown the reconstructions after 1 to 5 iterations, respectively.

suggesting that the scattering coefficient reconstruction is more highly correlated with phase signal changes. Next the effect of increasing the AC intensity noise was examined. In figure 7(i) and 7(j), the noise level used was 5% AC intensity and 0.2° in phase, and in figures 7(k) and 7(l), 25% in AC intensity and 0.2° in phase. The absorption image is seriously degraded at the highest noise level and some minor artifacts are present in the scattering image. This would suggest that the absorption reconstruction is more highly correlated with the intensity signal.

4.3 *Systematic Errors*

One anticipated problem in medical optical imaging is the irregular geometry of specific tissue volumes which may be imaged, such as the breast or the neonate head. Small changes or uncertainties in the shape or size, which could significantly affect the reconstructed image, are quite possible throughout the course of a single measurement. In order to simulate changes in the tissue shape, data were generated from different elliptical shapes and reconstructed using the algorithm based on cylindrical geometry. Clearly the reconstruction grid could be altered to an ellipse as well, however this analysis allows a qualitative examination of systematic unknown distance errors in the reconstruction. In figure 8, the images are all absorption reconstructions of the test object, shown in figure 2(a). The data were generated for a circular inhomogeneity inside an ellipse with a fixed vertical dimension of 100 mm. In figure 8, the reconstruction circle is shown as (ii) and a compressed ellipse is shown as (i), and a stretched ellipse is shown as (iii). In each case the size of the inhomogeneity was kept the same but the horizontal dimension of the ellipse was varied. For figures 8(a), 8(b) and 8(c) the horizontal dimension was 80 mm, 90 mm and 95 mm, respectively. The horizontal dimension was

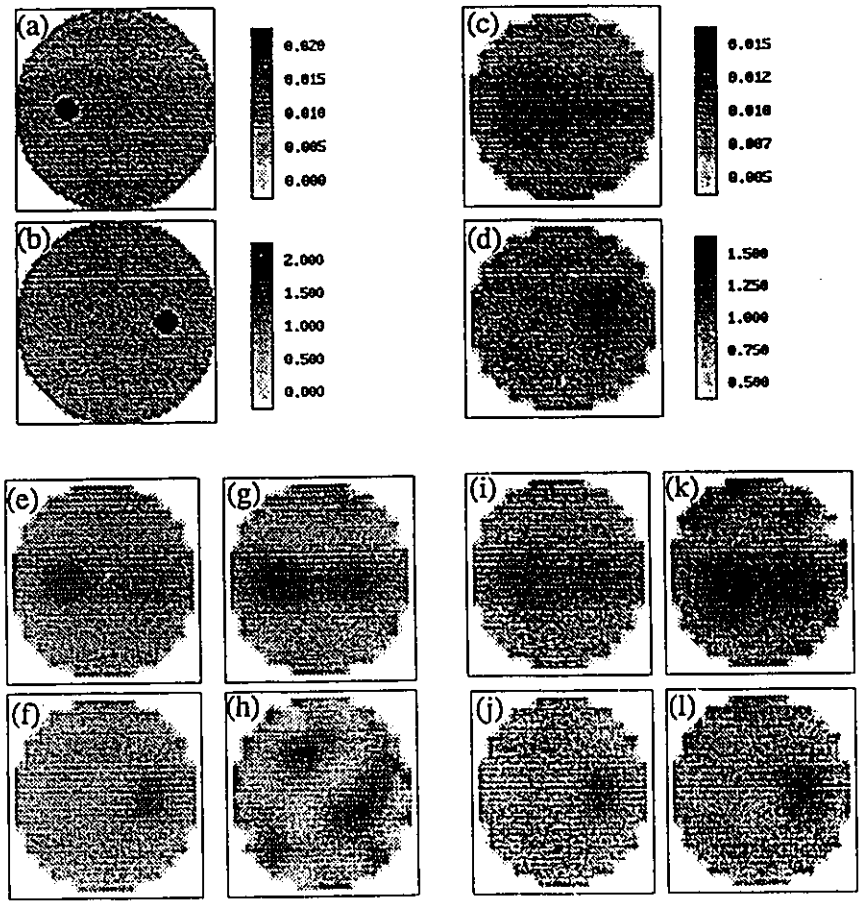

Figure 7 Absorption and scattering maps of a test object are shown in (a) and (b) respectively. The background optical properties were the same as in the previous images with the two objects, one absorbing $\mu_a = 0.02$ mm^{-1}, and the other scattering $\mu_s' = 2.0$ mm^{-1}, each of diameter 10 mm. Figures (c) and (d) show the reconstructions with random noise added to the data of 0.2° in phase and 1% in AC intensity. Figures (e) and (f) show the reconstruction for noise levels of 1% in AC intensity and 1.0 ° in phase. Figures (g) and (h) show the reconstruction for noise levels of 1% in AC intensity and 5.0° in phase. Figures (i) and (j) show the image for noise levels of 0.2° in phase and 5% in AC intensity. Figures (k) and (l) show the reconstructions for noise of 0.2° in phase and 25% in intensity.

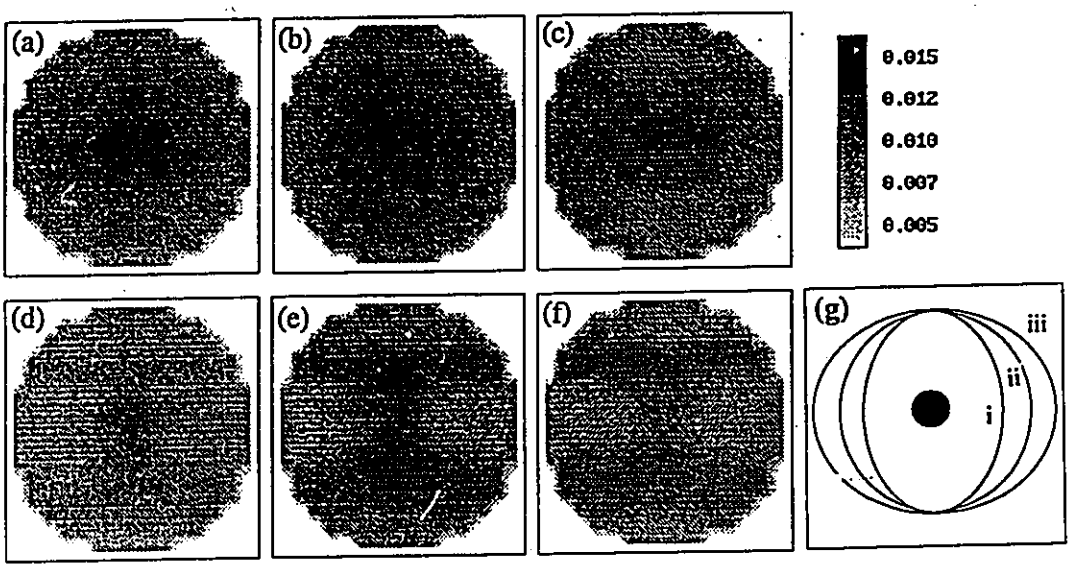

Figure 8 Reconstructions of a test object similar to that shown in figure 1(a) except that the horizontal dimension was changed to produce an ellipse. Reconstructions were performed assuming the large object was cylindrical, i.e. with systematic errors in source detector locations. Figures (a) to (c) are from 'squeezed' ellipses with horizontal axes of 80 mm, 90 mm and 95 mm, respectively. Figures (d) to (f) are taken from 'stretched' ellipses with horizontal axes of 105 mm, 110 m and 120 mm, respectively. A diagramatic representation of the ellipses are shown in figure (g), where the reconstruction circle is (ii) and the compressed ellipse is (i) and the stretched ellipse is (iii).

105 mm, 110 mm and 120 mm respectively for the ellipses used for figures 8(d), 8(e) and 8(f). The reconstructions of the compressed ellipses, figures 8(a)-(c), all demonstrate the same artifact; the circular object in the centre is stretched in the horizontal direction when reconstructed on the circular grid (i.e. without exact knowledge of the tissue dimensions). The reconstructions of the stretched ellipses, figures 8(d)-(f), show more serious reconstruction artifacts. For the 105 mm diameter ellipse, reconstructed in figure 8(d), the inhomogeneity is stretched in the vertical direction, however for the other two images, figures 8(e) and 8(f), the inhomogeneity appears as two separate objects. This analysis would suggest that small errors in the object size will not be a major problem, but that uncertainties larger that 5 mm may cause serious artifacts.

Another potential systematic error is the initial homogeneous estimate of μ_a and μ_s'. In figure 9, images of the test object shown in figure 2(b) were reconstructed with different initial estimates of the absorption coefficient. The correct value, $\mu_a = 0.01$ mm^{-1} was used to obtain figure 9(a), and values of 0.012, 0.015 and 0.020 mm^{-1} were used for the reconstructions shown in figures 9(b), 9(c) and 9(d), respectively. It is interesting to note that even for a 50% error in the initial guess, the image can still be reconstructed accurately, although some artifacts appear in the peripheral pixels. Figure 9(d) demonstrates that when the initial guess is 100% wrong, the algorithm is not able to converge to the global minimum χ^2 solution.

4.2 *Experimental Data Reconstruction Tests*

The first experiments used an object in the centre of the phantom, and measurements were taken at only 8 detectors for one source position. Because of symmetry it was assumed that the measurements would be the same at the opposite 8

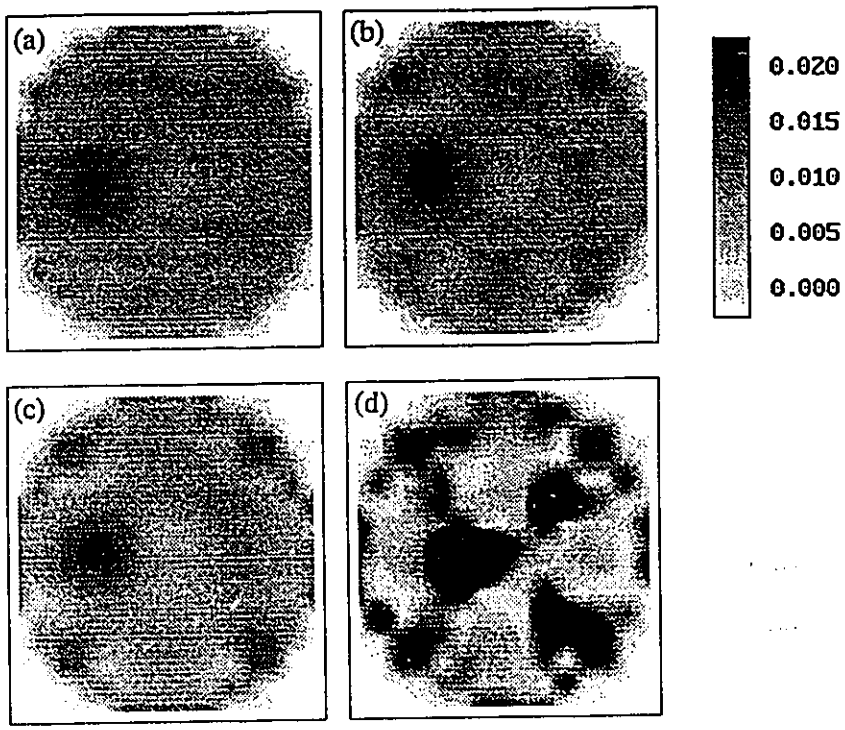

Figure 9 The reconstructions are of the test object in figure 1 (b). In figure (a) the initial guess of the homogenous absorption coefficient was accurate at 0.01 mm^{-1}, while in figures (b) to (d) the initial guess of μ_a was 0.012, 0.015 and 0.020 mm^{-1}, respectively. The image degradation in (d) shows the inability of the inverse algorithm to recover from grossly incorrect initial estimates.

detectors and that this data set could be used for all 4 source locations. Preliminary measurements confirmed symmetry in the relative phase and AC intensity.

The phantom used was 86 mm in diameter and 300 mm in length, with interior optical properties fixed from solution concentrations at $\mu_a = 0.0047$ mm^{-1} and $\mu_s' = 0.47$ mm^{-1}. The inhomogeneity used for all experiments was 25 mm in diameter, so the ratio of total diameter to inhomogeneity diameter was 3.4. The first phantom, reconstructed in figure 10, contained an object with $\mu_a = 0.0075 \pm 0.0005$ mm^{1}, and scattering equal to the background. The next, reconstructed in figure 11, had a higher scattering object, μ_s' $= 0.94 \pm 0.1$ mm^{-1}, with the absorption equal to the background. The object reconstructed in figure 12 had increases in both μ_a and μ_s' together (i.e. $\mu_a = 0.0075$ mm, $\mu_s' = 1.94$ mm^{-1}).

Figure 13 is an image of the same object used in figure 12, displaced from the centre by 10 mm. The data for this image were not as simple to collect as for the centred objects as the symmetry of source locations was lost. Therefore data were obtained at all detector locations for all 4 source positions. This was actually done by revolving the inhomogeneity about the centre of the large cylinder, as shown in figure 1(b). The reconstruction of the object is representative of the 'real' location, since the objects in figures 12 and 13 are offset by approximately 10 mm. The final data set examined here was collected from the same phantom with a water filled object located at the centre. The scattering coefficient of the water was not known but was presumably very small, and the absorption coefficient of water should be $\mu_a = 0.0026$ mm^{-1} (Hale and Querry). In the reconstruction, both μ_a and μ_s' (which are constrained to be positive) are essentially zero at the centre. Reconstructed images without this positive constraint yield images with negative values of the coefficients. There are some serious reconstruction

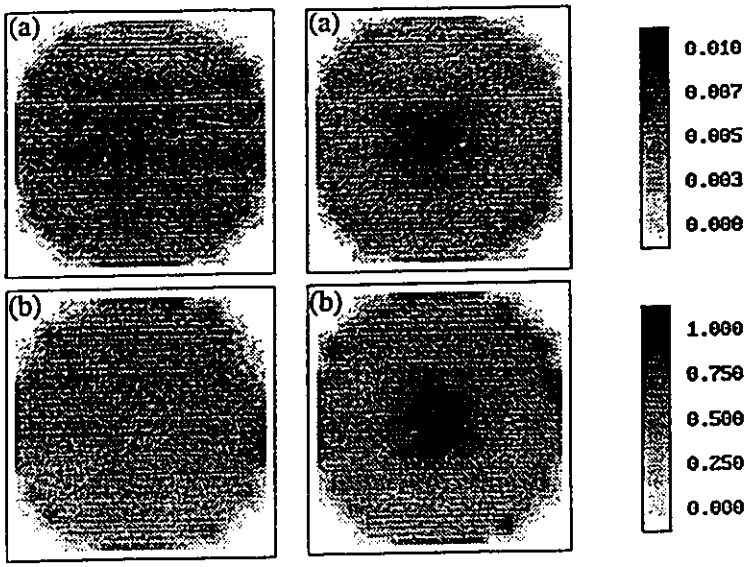

Figure 10 Reconstructions based on the experimental measurements of an absorbing object within a tissue-simulating scattering medium of diameter 86 mm. The (grey) background absorption was $\mu_a = 0.0047 \pm 0.0003$ mm^{-1}, and scattering was $\mu_s' = 0.47 \pm 0.03$ mm^{-1}. The inhomogeneity, located at the centre, had the same scattering coefficient, $\mu_a = 0.0075 \pm 0.0005$, and a diameter of 25 mm. The reconstructed absorption image is shown in (a) and the scattering in (b).

Figure 11 Reconstructions of the absorption coefficient (a) and the scattering coefficient (b) based on experimental measurements of a scattering inhomogeneity within a tissue-simulating phantom. Conditions were as in Figure 10, with the object in the centre having the same absorption coefficient as the background, with $\mu_s' = 0.94 \pm 0.06$ mm^{-1}.

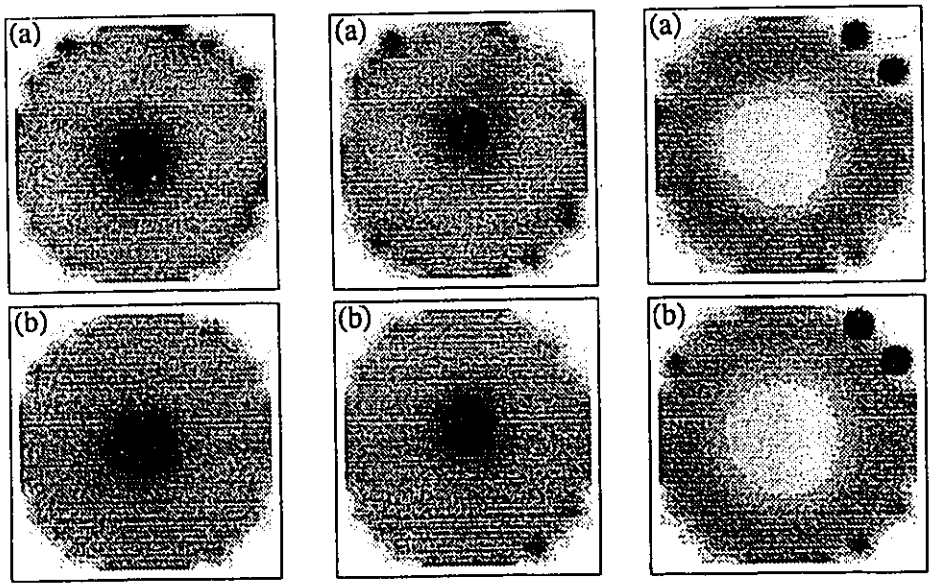

Figure 12 Reconstructions based on the experimental measurements of an absorbing and scattering object in the centre of the phantom used in Figures 10 and 11. The object had the same increase in μ_a as Figure 10 and the same increase in μ_s' as Figure 11.

Figure 13 Reconstructions from experimental measurements of the object described in Figure 12, but located 1 cm off centre.

Figure 14 Reconstructions based on experimental measurements of a pure water object located in the centre of the tissue-simulating phantom.

artifacts near the edges of the image, but it is possible to identify the non-scattering and low-absorption nature of the object, although its size is overestimated. This test is important for future imaging of brain regions containing optically clear cerebral-spinal fluid, and for imaging cysts in the breast.

5. Discussion

The purpose of this paper was not to perform an exhaustive examination of diffuse optical tomography, but rather to offer an initial assessment of the potential of a relatively simple algorithm based on a limited number of measurements. In an effort to maximize the speed of the reconstruction, only 80 measurements of phase and 80 measurements of intensity were made, and all forward calculations were performed on a coarse (17x17) grid using a finite difference method and simple boundary conditions. Despite these limitations and the fact that the system is underdetermined, useful images were recovered and the overall performance of the system was promising, as discussed in detail below.

In figures 2 - 5, it was demonstrated that an absorbing inhomogeneity could be reconstructed whether it was located at the centre or at the periphery of the imaging plane. Better accuracy was achieved when the inhomogeneity lay closer to the surface, which might be expected because the phase and (particularly) the intensity changes are greater. Interestingly, the achievable χ^2 error in the reconstruction was lowest when the inhomogeneity was at the centre, but this may reflect the contribution of the coarse discretization to the error when the object is closer to the surface. It is likely that a mesh of variable size is optimum, but this is more readily implemented in a finite element algorithm. It appeared in these tests (and others not shown here) that little improvement

in the images was achieved after more than 5 or 6 iterations. The ultimate spatial resolution of the imaging system has not been explicitly tested here, since this appears to be dependent upon many parameters such as the number of sources and detectors, and the signal to noise ratio of the measurements. The resolution of the imaging system will also be a function of position within the object, as earlier studies have demonstrated that the spread of photon paths is much wider at the centre than near the edges (Pogue *et al* 1995). The focus of this paper has been to examine the detectability of clinically relevant changes in the local optical properties rather than the resolution of high contrast targets.

In figure 6 it was shown that a relatively complex object can be reconstructed and 1 cm objects separated by about 2 cm can be clearly resolved. While the relative values of the recovered optical coefficients were correct in this case, the absolute values were considerably in error. It is difficult to explain the reason for the offset from the true values due to the non-linear response of the algorithm, especially when there are multiple inhomogeneities. Also an artificially low value of the absorption coefficient was found for the centre, perhaps because it was shielded by the absorbing objects around it.

The algorithm was shown to be surprisingly resistant to random measurements errors. Random phase errors, which mainly affect the reconstructed scattering coefficient image, were not detrimental until they exceeded 1°. Intensity errors have a more direct effect on the absorption image and are well tolerated to a level of 5% of the intensity. Since these random errors exceed those usually measured in experimental systems, noise may not be a critical problem in clinical systems, but this will depend on the size and optical properties of the tissue involved, as well as the source intensity and modulation.

Two possible systematic errors were also examined. In figure 8 it was shown that errors in source or detector position can lead to substantial reconstruction artifacts even

when relative phase and intensity are measured. It will probably be necessary to eliminate this artifact in a clinical system by providing auxiliary information about the optode location, or as may be practical in some sites, using a fixed source-detector array. Errors in the initial estimates of μ_a and μ_s' may prevent the algorithm from finding a good solution, although figure 9 suggests that these errors have to be relatively large to be fatal. More information about actual clinical subjects will be necessary before the limitations due to this variation can be assessed.

The experimental tests of this simple system were also encouraging. An object with only 50% contrast in absorption was located and reconstructed with reasonable accuracy. An object with only scattering changes was also easily recovered although here the separation between absorption and scattering images was not completely successful. On closer examination we found that the experimental data for phase change were not in agreement with forward calculations, even when the exact values of the optical properties were used. The maximum phase change for the scattering object was 15° while the forward diffusion calculation yielded only 10°. This may be due to limitations in diffusion theory or our simplistic corrections for the mylar cylinder (i.e. additive correction in phase and log intensity) may be in error. Further exploration of this question using Monte Carlo simulation could be useful, or use of solid phantoms such as those reported by Firbank *et al* (1994) would avoid some of these experimental problems.

The object which was both absorbing and scattering was well visualized, and its displacement by 1 cm was accurately recovered. Experiments with such asymmetric objects are extremely tedious with one detector and one source as all measurements must be taken sequentially. The development of diffuse optical tomography would be accelerated by the construction of a "parallel" system, but this will require a significant

capital investment. We also found that we were able to identify a non-scattering, low-absorbing object representing a fluid filled cyst or a sinus, although the size of this object was overestimated. Considering that diffusion theory is completely invalid inside such an object, the performance of the algorithm was surprisingly good. Some of the experimental images show significant artifacts near the surface of the phantom, presumably due to the high sensitivity of these pixels to noise or systematic errors. It might be best to empirically "damp" the Jacobian at these locations in future developments. As in similar inverse problems it may be possible to use prior knowledge of the object to aid in the reconstruction and to constrain the search for an optimum solution. This will have to be explored in the context of specific clinical applications where such information may be provided by other imaging modalities.

A complete reconstruction of one plane currently takes one to two hours on a common workstation. If it can be assumed that one of the interaction coefficients is spatially homogeneous, such as μ_s', reconstruction of the other can be accomplished in only 5 minutes. All forward calculations were made in three dimensions to provide realistic data for the numerical simulations but it may be acceptable to rely on 2 dimensional calculations for the clinical imaging applications. There is clearly a compromise between the number of voxels in the reconstruction, the number of iterations, and the number of sources and detectors. Considerable work remains to establish the optimum for different problems, but we believe the results achieved here for a "minimal" system are encouraging.

6. Acknowledgements

The financial support of this research by the Ontario Laser and Lightwave

Research Centre is gratefully acknowledged. The authors would also wish to thank John Adams of the National Centre for Atmospheric Research, Boulder CO, for providing his MUDPACK multigrid algorithm.

References

Adams J C, 1989 MUDPACK: Multigrid portable Fortran software for the efficient solution of linear elliptic partial differential equations *Appl. Math. Comp.* **34** 113-146

Alfano R, ed. 1994 *Advances in Optical Imaging and Photon Migration* Proceedings of the Topical Meeting, OSA Vol. 21

Arridge S. R., Cope M., van der Zee P., Hillson P.J., Delpy D.T., Visualization of the oxygenation state of brain and muscle in newborn infants by near infrared transillumination *In: Information Processing in Medical Imaging* Ed. S.L. Bacharach pp155-176, (Martinus Nijhoff, Holland, 1985)

Arridge S R, van der Zee P, Cope M, Delpy D T, 1991 Reconstruction methods for infrared absorption imaging, *Proceedings of SPIE* **1431** 204-215

Arridge S R, Cope M, Delpy, D T 1992 The theoretical basis for the determination of optical pathlengths in tissue: temporal and frequency analysis *Phys. Med. Biol.* **37** 1531-1560

Arridge S R, 1993 The forward and inverse problems in time resolved infra-red imaging, *Medical Optical Tomography: Functional Imaging and Monitoring* ed. G. Muller, (SPIE Press, Bellingham)

Barbour R L, Graber H L, Wang Y, Chang J H, Aronson R, 1993 A perturbation approach for optical diffusion tomography using continuous-wave and time resolved data, *Medical Optical Tomography: Functional Imaging and Monitoring* ed. G Muller (SPIE Press, Bellingham) 87-120

Berndt K W, Lakowicz J R, 1991 Detection and localization of absorbers in scattering media using frequency-domain principles *Proceed SPIE* **1431** 149-160

Bonner R F, Nossal R, Havlin S, Weiss G H, Model for photon migration in turbid biological media *J. Opt. Soc. Am. A* **4** 423-432

Chance B, Alfano R, ed. 1994 *Photon Migration and Imaging in Random Media and Tissues* Proceedings of SPIE Vol. 1888

Chance B, Alfano R, ed. 1995 *Optical Tomography, Photon Migration, and Spectroscopy of Tissue and Model Media: Theory, Human Studies, and Instrumentation* Proceedings of

SPIE vol. 2389

Colton D, Kress R, 1992 *Inverse acoustic and electromagnetic scattering theory* (Springer-Verlag, New York)

Cope M, Delpy D, 1988 System for long-term measurement of cerebral blood and tissue oxygenation on newborn infants by near infra-red transillumination *Medical and Biological Engineering and Computing*, May 1988, 289-294

Firbank M, Delpy D T 1994 A design for a stable and reproducible phantom for use in near infra-red imaging and spectroscopy *Phys. Med. Biol.* **38** 847-853

Fishkin J, Gratton E, 1993 Propagation of photon-density waves in strongly scattering media containing an absorbing semi-infinite plane bounded by a straight edge, *J. Opt. Soc. Am. A* **10** 127-140

Fletcher R, 1980 *Practical Methods of Optimization Vol I* (John Wiley & Sons, Toronto)

Fulton S R, Ciesielski C E, Schubert W H, 1986 Multigrid methods for elliptic problems: A Review *Monthly Weather Review* **114**, 943-959

Graber H L, Chang J, Aronson R, Barbour R L, 1993 Perturbation model for imaging in dense scattering media: derivation and evaluation of imaging operators *Medical Optical Tomography: Functional Imaging and Monitoring* ed. G Muller (SPIE Press, Bellingham) 121-143

Gratton E, Limkeman M 1983 A continuously variable frequency cross-correlation phase fluorometer with picosecond resolution *Biophys. J.* **44** 315-324

Jobsis F F, 1977 Non-invasive, infrared monitoring of cerebral and myocardial oxygen sufficiency and circulatory parameters *Science* **198** 1264-1267

Hale G M, Querry M R 1973 Optical constants of water in the 200 nm to 200 μm wavelength region *Appl. Opt.* **12** 555-563

Ishimaru A 1989 Diffusion of light in turbid material *Appl. Opt.* **28** 2210-2215

Kyriacou G A, Koukourlis C S, Sahalos J N 1993 A Reconstruction algorithm of electrical impedance tomography with optimal configuration of the driven electrodes *IEEE Trans. Med. Imag.* **12** 430-438

Lamarsh J R 1966 *Introduction to Nuclear Reactor Theory* (Massacheusetts: Addison-Wesley)

Madsen S J, Patterson M S, Wilson B C 1992 The use of india ink as an optical absorber in tissue-simulating phantoms *Phys. Med. Biol.* **37** 985-993

Madsen S J, Patterson M S, Wilson B C 1993 Numerical modelling and experimental studies of light pulse propagation in inhomogeneous random media *Proc. SPIE* **1888** 90-102

Maier J S, Gratton E 1993 Frequency-domain methods in optical tomography: detection of localized absorbers and a backscattering reconstruction scheme *Proc. SPIE* **1888** 440-451

Moulton J D 1990 Diffusion modelling of picosecond laser pulse propagation in turbid media *M.Eng. Thesis* McMaster University

O'Leary M A, Boas D A, Chance B, Yodh A G, 1994 Images of inhomogeneous turbid media using diffuse photon density waves, *Advances in Optical Imaging and Photon Migration* ed. Alfano R., OSA Procc. of the topical meeting, **21** 106-115

Patterson M S, Chance B, Wilson B C 1989 Time resolved reflectance and transmittance for the non-invasive measurement of tissue optical properties *Appl. Opt.* **28** 2331-2336

Patterson M S, Moulton J D, Wilson B C, Chance B 1990 Applications of time-resolved light scattering measurements to photodynamic therapy dosimetry *Proc. SPIE* **1203** 62-74

Patterson M S, Madsen S J, Moulton J D, Wilson B C 1991a Diffusion equation representation of photon migration in tissue *IEEE Microwave Theory and Techniques Symposium Digest* 905-908

Patterson M S, Moulton J D, Wilson B C, Berndt K W, Lakowicz J R 1991b Frequency-domain reflectance for the determination of the scattering and absorption properties of tissue *Appl. Opt.* **30** 4474-4476

Patterson M S, Wilson B C, Wyman D R, 1991c The propagation of optical radiation in tissue I. Models of radiation transport and their application *Lasers in Medical Science* **6** 155-168

Patterson M S, Pogue B W, Wilson B C, 1993 Computer simulation and experimental studies of optical imaging with photon density waves, *Medical Optical Tomography: Functional Imaging and Monitoring* ed. G. Muller (SPIE Press: Bellingham)

Press W H, Teukolsky S A, Vetterling W T, Fannery B P, 1992 *Numerical Recipes in Fortran* 2nd Ed. (Cambridge U. Press, New York) pp 816-862

Pogue B W, Patterson M S, 1995 Forward and inverse calculations for 3-d frequency-domain diffuse optical tomography *Proc. SPIE* 2389 (in press)

Pogue B W, Patterson M S, 1995 Frequency-domain tissue spectroscopy: testing and error assessment (manuscript being submitted)

Sevick E M, Lakowicz J R, Szmacinski H, Nowaczyk K, Johnson M L 1992 Frequency

domain imaging of absorbers obscured by scattering *J. Photochem. Photobiol. B: Biol.* **16** 169-185

Star W M, Marijnissen J P A, van Gemert J C, 1988 Light dosimetry in optical phantoms and in tissues: I. Multiple flux and transport theory *Phys. Med. Biol.* **33** 437-545

Wilson B C, Patterson M S, Pogue B W, 1993 Instrumentation for *in vivo* tissue spectroscopy and imaging," *Proc. SPIE* **1892** 132-147

van Staveren H J, Moes C J M, van Marle J, Prahl A, van Gemert M J C 1991 Light scattering in Intralipid-10% in the wavelength range of 400-1100 nm *Appl. Opt.* **30** 4507-4514

Yorkey T J, Webster J G, Tompkins W J, 1987 Comparing reconstruction algorithms for electrical impedance tomography, *IEEE Trans. Biomed. Eng* **34** 843-852

Appendix for Paper #5

A-1 Forward calculations versus experiments

The preceding paper discussed reconstruction for optical imaging using the multigrid finite difference forward calculation and Newton-Raphson inverse method. Emphasis was placed on the reconstruction accuracy of the algorithm, with no detailed examination of the forward calculations of phase and $\log(I_{AC})$. In this appendix, some of the forward data from the experiments is compared to the forward finite difference calculation. There are small differences between the forward calculations and the experiment which need to be examined in order to understand the accuracy of the inverse algorithm.

The original calculations of paper #4, based on the diffusion equation did not take into account the gradient of the diffusion coefficient, in the first term of equation 1. In all the calculations in paper #5, this was included. In figures A1 to A8, both types of calculations have been included to show the difference that this change makes. Figures A1 to A8 show the experimental measurements of phase shift, $\Delta\phi$, and logarithm of AC intensity ratio, $\log(I_{AC2}/I_{AC1})$, for one source and 16 detectors. If no inhomogeneity was present in the image, then both signals would be zero. The deviation from zero was due to the presence of the objects, or noise in the measurements. The data were all obtained from the same phantom as described in the paper, with $\mu_a = 0.0047 \pm 0.0003$ mm^{-1} and $\mu_s' = 0.47 \pm 0.03$ mm^{-1}. All objects were located in the centre of the phantom for these 8 data sets, and the optical properties are given in the following chart

Figure	μ_a [mm^{-1}]	μ_s' [mm^{-1}]
A1	0.0047 ± 0.0003	0.94 ± 0.03
A2	0.0071 ± 0.0006	0.47 ± 0.02
A3	0.0071 ± 0.0006	0.94 ± 0.03
A4	0.029 ± 0.003	4.7 ± 0.3
A5	0.0047 ± 0.0003	0.24 ± 0.02
A6	0.0035 ± 0.0002	0.47 ± 0.02
A7	0.0026*	≈ 0*
A8	0.0035 ± 0.0002	0.24 ± 0.02

* Phantom object was pure water, absorption value given by Hale and Querry, 1973.

The gradient in the diffusion coefficient appears to affect only those calculations in which there is a localized change in the scattering coefficient, as expected. For example the calculations in figures A2 and A6 show exactly the same results with and without the gradient in the diffusion coefficient, since the inhomogeneity was only shifted in the absorption coefficient for these two examples. On the whole there is good qualitative agreement between experiment and theory for all of the data sets, with the notable exception of figure A6. With the exception of this figure, the small discrepancies between experiment and theory can be attributed to slight errors in the exact values of μ_a and μ_s', or to slight distance errors. For example the distance from the inhomogeneity to the outside wall was 30 mm, but the exact positioning of the inhomogeneity was probably subject to 3 mm error. This means that the positioning was subject to perhaps 10% error. Similarly the errors in the calculated optical properties is in the range of 3% to 10%. These errors could easily account for the differences between the calculated and observed data sets,

except perhaps figure A2. In figure A2, there were likely some systematic errors involved in the measurements at detectors 12 to 16, possible due to human error.

Figure A7 shows the data collected for a water object with optical properties which violate the assumptions of diffusion theory. Yet the forward simulated data for this object are quite similar to the experimental values. In this figure the gradient in the diffusion coefficient appears to be quite important. For the calculated data, μ_s' in the object region cannot be set to zero, or the attenuation coefficient in the diffusion equation will be infinite. (i.e. $k = [(\mu_a + i\omega/c)/D]^{1/2}$). Therefore the forward calculations here used $\mu_s' = 0.1$ mm^{-1} and $\mu_a = 0.0026$ mm^{-1}. This value of μ_s' may be too high, however it is difficult to estimate this coefficient since a transport scattering coefficient is not really appropriate here.

A-2 Reconstruction Accuracy

Paper #5 also did not explicitly show the forward calculated values of phase shift and $\log(I_{AC})$ ratio after each iteration, and their convergence to the measured data. After each iteration, the reconstruction algorithm uses the new 'guess' at the images of μ_a and μ_s' to re-calculate the phase shift and intensity ratio at each detector. These values are compared to the observed data in the calculation of reduced chi squared. After each iteration the new image has a lower reduced chi squared value, which reflects the fact that the calculated signals are closer to the observed data. It is interesting to examine these calculated values to see how they change as a function of iteration number.

Figures A9 to A12 show the experimental data and calculated values for the first 5 iterations for 4 of the previous objects. Figure A9 is the data from the scattering object shown in figure A1, figure A10 is the data from the absorbing object shown in figure A2. Figure A11 is the data from the water object,

shown in figure A7, and figure A12 is the data from the scattering and absorbing object, shown in figure A3.

In figures A9, A10 and A12 the calculated data matches the experimental data quite well after 5 iterations. The systematic error in phase of figure A10 at detectors 13 and 14 is not matched, since the effects of these values are damped out by the other 3 source projections (Note: the data shown here is only for one source projection, the other 3 are the same data rotated for the each source position). The fit to the water data of figure A11 is not as good. The imaging algorithm has been constricted to positive values of μ_a and μ_s' only. For this data set the improvement between the second and fifth iterations is negligible. The main reason for this is that the reconstructed object size is too large, as seen in the original paper. Further iterations 'try' to impose negative μ_a and μ_s' values, but the algorithm will not allow this. This conflict essentially stops the image from being improved. The reconstruction of the water object is qualitatively correct, since low values of μ_s' and μ_a are assigned to the inhomogeneity. The major artifacts are that the size of the object is overestimated, and that μ_a is significantly lower than the real value. Perhaps a smaller step in the reconstruction of μ_a and μ_s' would allow a more accurate reconstruction in this case, so that the object size does not grow faster than the absolute value of the inhomogeneity.

While these data were not pertinent to the published paper, they are presented here in order to observe the iterative process and understand the effects which limit reconstructions. This type of comparison should be carried out with multiple inhomogeneity images to examine the performance of the algorithm.

Figure 1

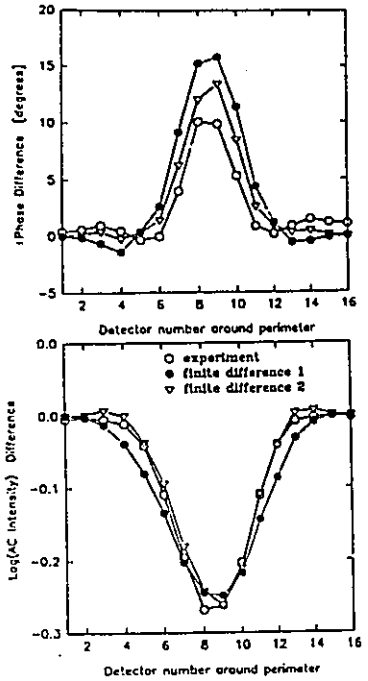

Figure 2

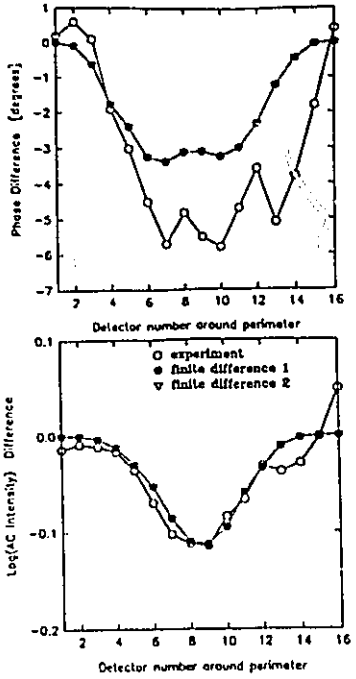

Figure 3

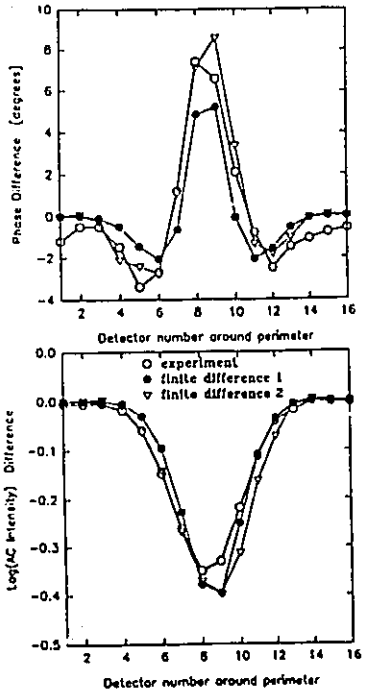

Figure 4

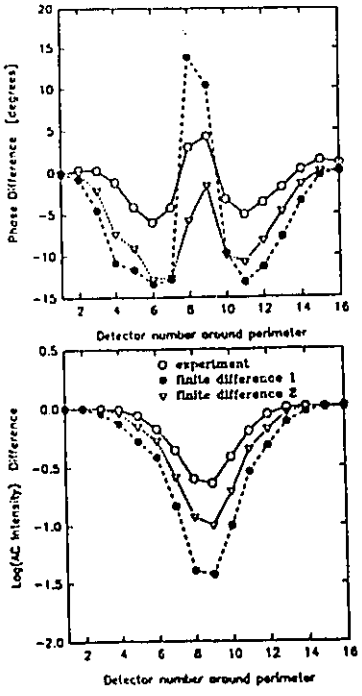

Figure 5

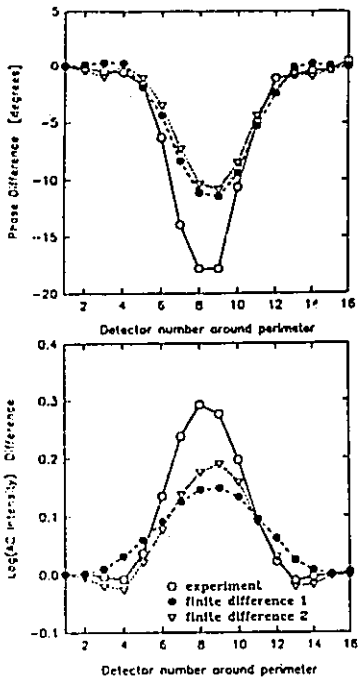

Figure 6

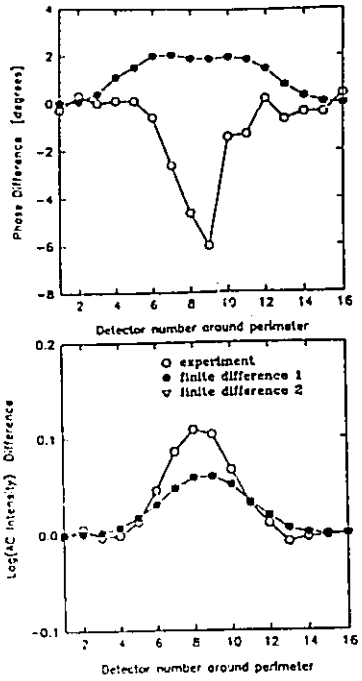

Figure 7

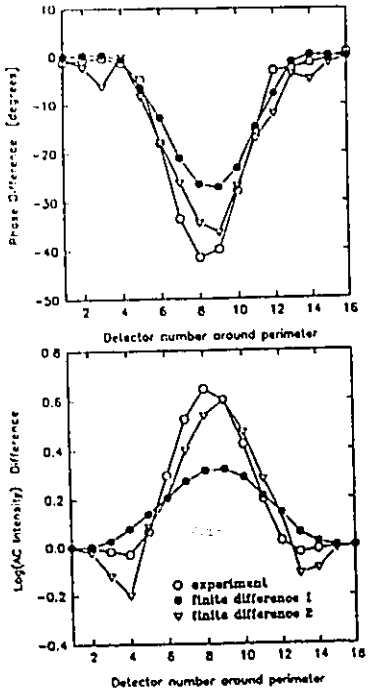

Figure 8

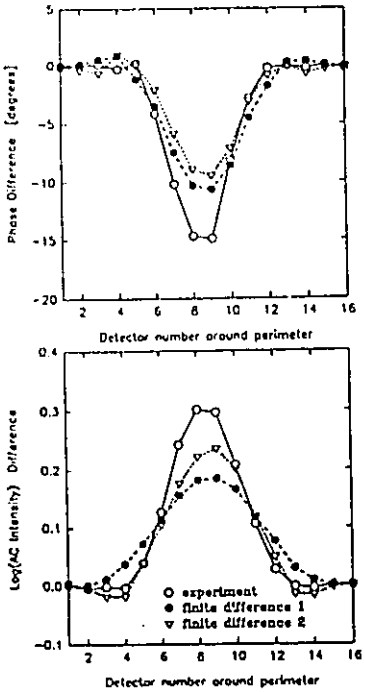

Figure 9

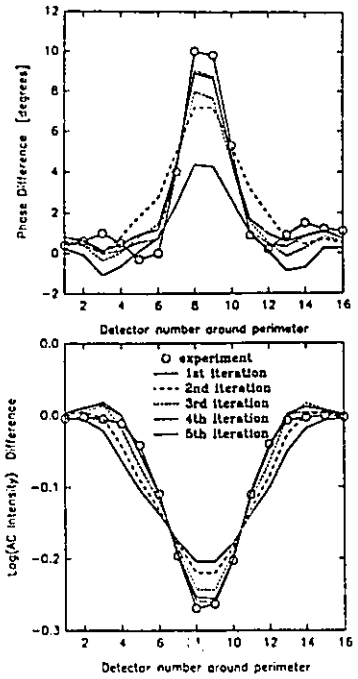

Figure 10

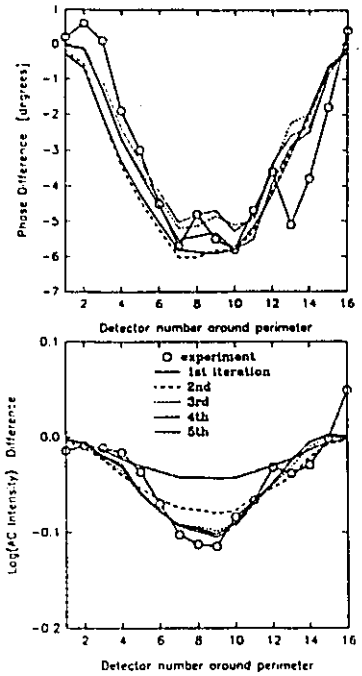

Figure 11

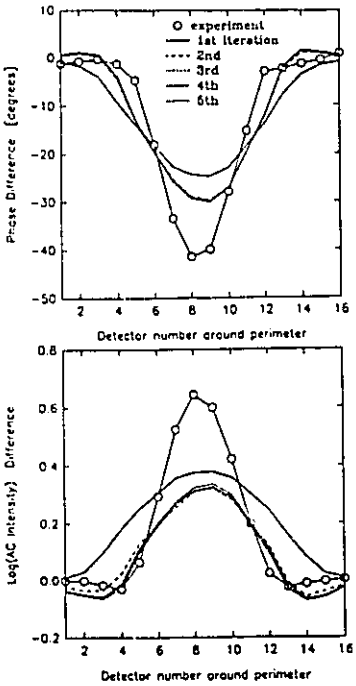

Figure 12

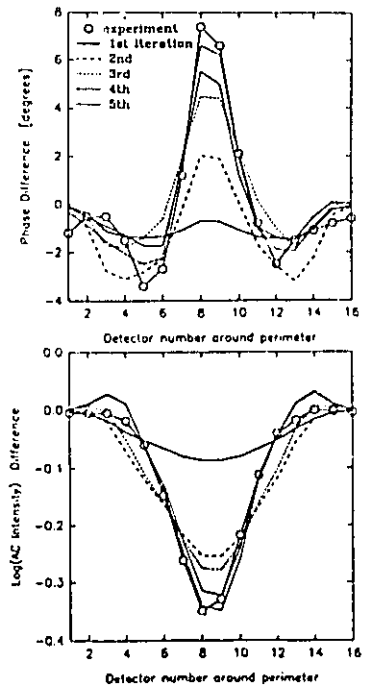

Chapter 5

Discussions and Conclusions

5.1 Tissue Spectroscopy

5.1.1 Accuracy and error estimation

In general frequency-domain measurements should be a relatively inexpensive and robust method of measuring tissue optical properties. However the estimation of the accuracy of any measurement is not a simple task. The calculations and measurements from paper #2 demonstrate that the precision of any frequency-domain spectroscopic measurement is dependent upon many parameters. The two major elements examined were the random or statistical errors associated with the detection of light and the systematic errors associated with assumptions about diffusion theory. In order to minimize the random errors from the detectors each particular system must be optimized to give a maximum signal. In general the most important elements, in order of importance, are:

(i) have a high fraction of the input light modulated,

(ii) have a high light intensity at each detector,

(iii) use as high a frequency as possible, and

(iv) use the largest separation between source(s) and detector(s) possible.

In cases where the tissue volume is small it may be better to use several frequencies rather

than several distances. Madsen *et al* (1994b) have demonstrated such a system which uses a network analyzer to sweep through a range of frequencies to provide fast accurate measurements. When measuring intensity ratios, it may also be useful to have a well calibrated set of attenuation filters to adjust the intensities rather than to allow the incident DC light intensity to be low at one of the detectors. This would permit use of the maximum light intensity at each detector, and the difference in intensities can be determined from the transmission of the pre-calibrated filter. This assumes that the filter can be characterized to better precision than the uncertainty in the DC intensity due to quantum statistics.

The applicability of diffusion theory has been explicitly tested by several investigations with Monte Carlo simulations (Hielscher *et al* 1993, Fishkin *et al* 1994, Bayes 1995), and with experimental results (Patterson *et al* 1991a, Tromberg *et al* 1992, Fishkin *et al* 1994, Haskell *et al* 1994, Madsen *et al* 1994a). Most researchers agree that using diffusion theory solutions for regular geometric shaped objects does not induce any systematic errors in deriving the values of μ_a and μ_s' from reflectance measurements. However measurements on real tissue are rarely, if ever, in regular geometries such as semi-infinite or slab. Papers 1 and 2 assessed the limitations of different geometries for analytic diffusion theory solutions. The three main questions which needed to be addressed were: what is the thickness of a homogeneous tissue needed to apply the semi-infinite solution?, what effects do other boundaries cause?, and what effects do curved surfaces cause? A general rule of thumb which can be used for homogeneous tissue spectroscopy is that the sample should be at least as thick as the largest source-detector separation. This is not an absolute truth but a useful guideline for routine clinical applications.

In general, boundaries which have been ignored but which make the objects size smaller, will cause an increase in the observed absorption coefficient. Convex curved boundaries, which have been assumed to be straight, will cause an increase in the signal reaching the detector, and cause an underestimate of μ_a. These offsets in the observed μ_a due to finite volumes are, in some instances, almost constant with respect to the real μ_a value. This constant offset in μ_a can be exploited for observing absolute changes in μ_a with wavelength or as a dynamic process. The constant offset can be subtracted out from two successive measurements to yield the net change in μ_a. For practical tissue spectroscopy some assumptions about the tissue boundaries have to be made since tissues are never in rigid geometrical shapes. It is also possible to use a numerical solution of the diffusion equation for irregular shapes but it is simpler to use analytic solutions where they are approximately true.

5.1.2 Diffuse fluorescence

The fundamental interactions of fluorescent light have been modelled in an attempt to understand and predict such measurements from tissue. The agreement between experiments in a scattering medium and the theoretical solution suggests that it may be possible to use this theory to interpret diffuse fluorescence signals from tissue samples. Two major limitations of the model derived in this paper are that the scattering coefficient was assumed to be the same at both the excitation and emission wavelengths, and that the fluorophore was assumed to be homogeneously distributed in the scattering volume. The first assumption is approximately true in tissue if the Stoke shift of the fluorophore is less than 100 nm. Most of the next generation photosensitizers being examined for PDT applications have absorption bands in the 600 to 700 nm range, and with fluorescence

emission less than 100 nm Stoke shifted from this. So this theory may be useful in interpreting diffuse fluorescence from these dyes within tissue.

While this study was encouraging, it only pertains to homogeneous tissue volumes with a uniformly distributed fluorophore. Experiments with AlSPc injected into rats were used to try and predict the relative fluorescent signal remitted from the leg muscle, without success. There was a large difference between the measured and calculated fluorescence as a function of distance (data not shown). Measurements of phase shift and intensity ratio were taken and used to calculate absorption and scattering coefficients, with poor results. In each case the scattering coefficient was lower than seemed reasonable, and the absorption coefficient did not increase with increasing concentrations of dye. In these experiments the rat muscle was approximately 1 centimetre in thickness. It appears that larger volumes of tissue are needed to test the theoretical expression developed here. Further testing of the analytic solutions in paper #3 both *in vitro* and *in vivo* is required.

Further computational studies have been reported by Sevick *et al* (1994) who examined the spatially resolved diffuse fluorescence signal from a homogeneously distributed fluorophore. The thrust of these studies was to examine the potential of diagnosis or imaging based on the fluorescent light signal. A 2-dimensional finite element code representation of the diffusion equation was used with an extra term to include the lifetime decay of the photosensitizer. In general there appeared to be good agreement between this calculation and the analytic solution developed here.

Some applications of homogenous tissue fluorescence could be in metabolic monitoring with a molecule whose lifetime is sensitive to the local environment. It has also been suggested that imaging based upon fluorescence lifetime changes would provide a means of contrast to differentiate between normal and cancerous regions (Wagnieres *et*

al 1995). Lifetime based imaging in a non-scattering environment has been demonstrated with a gain-modulated image intensifier with CCD detection for monitoring NADH function (Lakowicz *et al* 1992). The main advantage here is that cellular function or chemical environment are being directly imaged rather than simply the remitted intensity which depends on the absorption and scattering coefficients. It is well known that changes in pH or changes in the concentration of specific chemicals can affect the fluorescence lifetime of some molecules. There are several commercial fluorophores which have been developed to detect changes in O_2, CO_2, glucose, and calcium (Thompson *et al* 1993, Wilson D F *et al* 1989).

5.1.2 Potential and Future Directions

The near-future studies of frequency-domain spectroscopy will need to focus on specific applications. One of the main applications will be in developing a smaller detector probe than studied here. Using a smaller source-detector fibre distance will allow the optical biopsy of many more tissue sites. However the development of this type of detector will rely on the ability to have high frequency modulation and high fraction of the excitation intensity modulated. This can really only be achieved with diode lasers. Also the applicability of diffusion theory will be more questionable here. However the studies of Farrell *et al* (1991) suggest distances larger than a few scattering lengths are sufficient to yield photon diffusion. The studies of Fishkin (1994) and Haskell *et al* (1995) suggest that at modulation frequencies near 1 GHz, the full P_1 approximation must be used rather than diffusion theory. The P_1 solution may be applied just as easily as diffusion theory. The use of other models such as the Monte Carlo simulation may be practical since short distances are involved, and so the time for calculation would be

reduced.

The potential of frequency-domain spectroscopy has already been demonstrated by other researchers in the field. Franceschini *et al* (1993) and Duncan *et al* (1993) have described frequency-domain tissue spectrometers which were used to measure hemoglobin oxygenation saturation in a 'semi-infinite' tissue geometry. Measurements at multiple wavelengths were used to estimate the relative concentrations of Hb and HbO_2 within the tissue. These diagnostic measurements will benefit from the use of frequency-domain measurements due to their stability, depth of penetration and relatively low cost. The calculations of paper #2 of this thesis suggest that oxygen saturation measurements would be more stable and accurate with a three wavelength detection system since finite volume systematic errors can be minimized. It is also important to note that while statistical and systematic errors in the system can be minimized, there can be large fluctuations in measurements from *in vivo* tissue due to physiologic fluctuations. Pulse oximeters typically have to average a measurement over several seconds (2 to 15 seconds) (Poets *et al* 1994) in order to achieve a stable signal. Mengelkoch *et al* (1994) have also documented many factors which can produce erroneous artifacts in pulse oximeter measurements such as diode variability, skin pigment, poor peripheral perfusion and motion artifacts. Ultimately, the major limitation to the use of these systems will probably depend upon physiologic fluctuations during a measurement. Gratton *et al* (1995) have looked at using very fast measurements, in the range of milliseconds to specifically detect oxygenation fluctuations, rather than try to average them out of the measurement. This type of ultra fast measurement system may yield the most diagnostic information.

Diagnostic uses of frequency-domain spectroscopy are also being exploited in therapeutic areas. Madsen *et al* (1994a) have demonstrated the use of a frequency-domain

spectroscopy system to measure the optical properties of freshly excised uteri in order to have good estimates of the optical properties. These measurements will allow accurate light delivery in photodynamic therapy of the uterus. In paper #2 of this thesis, measurements of the uptake of a photosensitizer have been demonstrated for applications relating to PDT dosimetry. The routine use of a tissue spectroscopy system for fast point measurements is desirable. Tissue spectroscopy systems based upon CW, time resolved, and frequency-domain principles are being examined at various laboratories, but it is still an open question as to which type of system is preferable and probably depends strongly upon the application and the economics.

5.2 Tissue Imaging

5.2.1 Diffuse imaging potential

For applications in optical imaging, frequency-domain measurements may be a good solution for a difficult problem. Since frequency-domain measurements are quite noise resistant and relatively fast and possibly inexpensive, they can provide a robust measurement system for tissue thicknesses up to 90 mm. The major benefit of these measurements is that dynamic changes in the absolute values of μ_a and μ_s' can be observed simultaneously. The only other type of measurement system which could provide the same information presently is a time-resolved single photon counting system, but they are slower and more expensive. The data collection hardware for a optical tomography system will have to be rugged and reliable. A frequency-domain system using a diode laser source and photomultiplier for detection could provide rapid measurements at multiple points on the tissue surface. A multiplexing method could be used where several fibres feed into the source and/or detector, and each position (fibre)

is read out sequentially. This system would avoid the higher cost associated with multiple sources and detectors working in parallel. Such a system is being examined by Benaron (1995).

The inverse algorithm tested here seems to be quite stable and accurate for diffuse imaging. This algorithm is only one of several different types outlined in the literature. The major limitation to this reconstruction algorithm is the long time required to calculate the images. Faster reconstruction methods based upon backprojection or perturbation theory can be used, but it seems unlikely that they will provide as accurate a reconstruction as iterative methods. In an application such as diffuse imaging the resolution of the images will always be much lower than methods such as x-ray tomography simply because of the diffuse light paths. In order for this type of imaging to be clinically useful, it will be important to derive different information from the measurements as well as to exploit the potential for continuous or prolonged monitoring. Iterative imaging allows the algorithm to produce an accurate representation of the contrast and the positions of the objects. Future developments in computer architecture which increase the speed of workstations or allow highly parallel computation may be very beneficial in allowing interative reconstruction algorithms to work in near real time. Hardware developments could make computationally intensive algorithms such as the one presented here more attractive.

5.2.2 Future directions in diffuse optical tomography

Future development of the imaging algorithm should be in two directions. First the accuracy of the algorithm should be further examined with more experimental data, and secondly the speed of the calculation should be improved. The major problems with

the accuracy are associated with the reconstruction artifacts which appear in the experimental data at the perimeter of the images (see paper #5, figures 9 to 12). This is probably due to the coarse grid used for the reconstructions. A finer grid can be used to reconstruct these images at the cost of a greatly increased computation time. Faster methods to calculate the Jacobian matrix would be beneficial since this is the slowest part of the iterative calculation.

Another problem is associated with the MUDPACK multigrid algorithm used in these studies, in that sources must be located on the perimeter of a square grid. This was one of the contributing factors in limiting the number of sources used to 4, one on each side of the square. The algorithm which is needed for future work should ideally be on a cylindrical grid which better approximates the geometry of the tissue being examined. At present multigrid finite difference solvers are not common on circular grids.

For applications in real time monitoring, it may be possible to update only certain parts of the Jacobian matrix. Recent studies in electrical impedance tomography have investigated using only the source-detector pairs which yield the highest signal in the update of the Jacobian (Kyriacou *et al* 1993). In this way only selected parts of the image region would be updated with successive iterations. This allows faster calculation of the Jacobian at each iteration step and could be a possible use for real-time imaging.

A final application which may have some use in medical diagnosis is diffuse fluorescence imaging. Sevick *et al* (1994) have examined the time-resolved light signals remitted from a diffuse medium and postulated the ability to image the lifetime distribution of a fluorophore with tissue. It should be possible to use an optical imaging system to detect both excitation and fluorescence light from a tissue volume. The excitation light can be used to image the concentration of absorber within a scattering

medium, and to deconvolve the multiple-scattering effect out of the fluorescent signal. Using an iterative algorithm it should be possible to spatially resolve properties such as fluorescence lifetime. This is currently being examined with the imaging algorithm presented here (Paithankar and Sevick, private communication 1995).

5.3 Conclusions

Recently there has been considerable interest in optical spectroscopy of tissue. The studies in this thesis have concentrated on the use of frequency-domain light signals for non-invasive probe of tissue in the wavelength range of 400 to 850 nm. The studies presented in this thesis are a collection of experiments and calculations devoted to studying the general principles of this type of tissue spectroscopy. Real clinical applications will require much more work, however this work should be specific to the specific system designed. Hopefully, this study will serve as a starting point for understanding the benefits and limitations of frequency-domain tissue spectroscopy.

The most basic observations from this study are that there is reasonably good agreement between experimental measurements of scattering media, and the calculated values based upon diffusion theory. The analytic solutions presented in chapter 2, and in papers 1 and 2, are very useful in calculating the absorption and scattering coefficients of tissue using a iterative fitting routine, assuming that measurements of phase and relative intensity are possible. The precision and accuracy of any frequency-domain tissue spectroscopy instrument will depend upon the fibre delivery and detection geometry and the characteristics of the source(s) and detector(s). These parameters have been examined and the optimal design for one particular system was outlined in paper 2. The most important factors for the phase-intensity detection system were a high modulation, high

DC signal, high driving frequency, and large source-detector separations. Measurements of phase and modulation are probably quite useful for large source-detector separations, as mentioned in paper 1, however they are not useful for systems with a small source-detector separation, or for low frequency measurements. Finally, using analytic diffusion theory solutions should be possible for irregular geometries, under the specific limitations outlined in papers 1 and 2.

Fluorescence measurements in tissue are becoming one of the most popular diagnostic uses of light in medicine, because of the ability to detect micromolar quantities of fluorophores without the need for biopsy. While the specific applications are still in very early stages of development, the ability to predict fluorescent light propagation in tissue is essential in order to yield quantitative measurements from diffuse light measurements. The theory developed and tested in paper 3 of this thesis is one step towards developing a deconvolution algorithm. There was good agreement between the measurements of phase, modulation and relative intensity and the predicted values from diffusion theory. Future developments in this area will probably be in fluorescence based imaging algorithms, and fluorescence lifetime detection to monitor chemical changes subcutaneously.

The imaging work presented in this thesis was an initial examination of frequency-domain measurements for optical coefficient reconstruction imaging. Overall the attempt to produce an optical imaging algorithm for scattering media was successful. The iterative reconstruction algorithm was able to calculate images which were representative of the original object. The resolution of the system tested here was limited by the chosen grid size (6.25 mm) and the diffuse spread of the photon path (approximately 0.2d, where d is the depth into the medium). Measurements at higher frequencies can improve the

resolution of the photon path slightly. The contrast of heterogeneties or objects reconstructed is linked to their position, size and number. The algorithm presented here has some systematic errors in the image reconstructions which were associated with the coarse grid size chosen. A further examination of the reconstruction artifacts should be done once specific applications/geometries are chosen. Future algorithms may take advantage of the multigrid finite difference solver used in this study, since it provides a very fast forward calculation of the diffusion equation. The goal of this study has been to examine the physical and mathematical basis for the diffuse optical tomographic algorithm without focusing on one particular application.

References

Andersson-Engels S, Ankerst J, Johansson J, Svanberg K, Svanberg S 1993 Laser induced fluorescence in malignant and normal tissue of rats injected with benzoporphyrin derivative *Photochem. Photobiol.* **57** 978-983

Arnfield M R, Chapman J D, Tulip J, Fenning M C, McPhee M S 1993 Optical properties of experimental prostate tumours in vivo *Photochem. Photobiol.* **57** 306-311

Arridge S R, Cope M, Delpy D T 1992 The theoretical basis for the determination of optical pathlengths in tissue: temporal and frequency analysis *Phys. Med. Biol.* **37** 1531-1560

Barbour R L, Graber H L, Wang Y, Chang J H, Aronson R, 1993 A perturbation approach for optical diffusion tomography using continuous-wave and time resolved data, *Medical Optical Tomography: Functional Imaging and Monitoring* ed. G Muller (SPIE Press, Bellingham) 87-120

Bayes R 1995 private comm.

Beauvoit B, Evans S M, Jenkins T W, Miller E E, Chance B 1995 Correlation between scattering and the mitochondrial content of normal tissue and transplantable rodent tumors *Analytical Biochem.* **226** 167-174

Beauvoit B, Liu H, Kang K, Kaplan P D, Miwa M, Chance B 1993 Characterization of the absorption and scattering properties for various yeast strains by time-resolved spectroscopy *Cell Biophys.* **23** 91-109

Benaron D A 1995 Laser imaging for clinical applications *SPIE conference* **2390**

Bohren C F, Huffman D R Absorption and Scattering of Light by Small Particles John Wiley and sons (Toronto: 1983)

Boas D A, O'Leary M A, Chance B, Yodh A G 1994 Scattering of diffuse photon density waves by spherical inhomogeneities within turbid media: analytic solution and applications

Brazy J E, Lewis D V, Mitnick M H, Jobsis F F 1985 Noninvasive monitoring of cerebral oxygenation in preterm infants: preliminary observations *Pediatrics* **75** 217-225

Carslaw H S, Jaeger J C Conduction of Heat in Solids Oxford Press (London, 1959)

Case K M, Zweifel P F Linear Transport Theory Addison-Wesley (Reading, MA 1967)

Chance B, Nioka S, Kent J, McCully K, Fountain M, Greenfield R, Holtom G 1988 Time-resolved spectroscopy of haemoglobin in resting and ischemic muscle *Anal. Biochem.* **174** 698-707

Chance B, Alfano R, ed. 1994 *Photon Migration and Imaging in Random Media and Tissues* Proceedings of SPIE Vol. 1888

Cheong W, Prahl S A, Welch A J 1990 A review of the optical properties of biological tissues *IEEE J. Quant. Elec.* **26** 2166-2185

Cope M, Delpy D T 1988 System for long-term measurement of cerebral blood and tissue oxygenation on newborn infants by near infra-red transillumination *Med. & Biol. Eng. & Comp.* **26** 289-294

Cope M, van der Zee P, Essenpreis M, Arridge S R, Delpy D T 1991 Data analysis for near infrared spectroscopy of tissue: problems in determining the relative cytochrome aa_3 concentration *Proc. SPIE* **1431** 251-262

Coulton D, Kress R Inverse acoustic and electromagnetic scattering theory Springer-Verlag (New York: 1992)

Delpy D T, Cope M, van der Zee P, Arridge S, Wray S, Wyatt J S 1988 Estimation of optical pathlength through tissue by direct time of flight measurement *Phys. Med. Biol.* **33** 1433-1442

Dougherty T J 1993 Yearly Review Photodynamic Therapy *Photochem. Photobiol.* **58** 895-900

Duncan A, Whitlock T L, Cope M, Delpy D T, 1993 A multiwavelength, wideband, intensity modulated optical spectrometer for near infrared spectroscopy and imaging *Proc. SPIE* **1888** 248-257

Durkin A J, Jaikumar S, Ramanujam N, Richards-Kortum R 1994 Relation between fluorescence spectra of dilute and turbid samples *Appl. Optics* **33** 414-423

Ediger M N, Pettit G H. Hahn D W 1994 Enhanced ArF laser absorption in a collagen target under ablative conditions *Lasers in Surgery and Medicine* **15** 107-111

Fantini S, Franceschini M A, Gratton E 1995 Semi-infinite geometry boundary problem for light migration in highly scattering media: a frequency-domain study in the diffusion approximation *J. Opt. Soc. Am.*

Farrell T J, Patterson M S, Wilson B C 1991 A diffusion theory model of spatially resolved, steady-state diffuse reflectance for the non-invasive determination of tissue optical properties in vivo *Med. Phys.* **19**, 879-888

Farrell T, Wilson B C, Patterson M S 1992 The use of a neural network to determine optical properties from spatially resolved diffuse reflectance measurements *Phys. Med. Biol.* **37** 2281-2286

Ferrari M, Wei Q, Carraresi L, De Blasi R, Zaccanti G 1992 Time-resolved spectroscopy

of the human forearm *J. Photochem. Photobiol. B: Biol.* **16** 141-153

Firbank M, Delpy D T 1994 A design for a stable and reproducible phantom for use in near infra-red imaging and spectroscopy *Phys. Med. Biol.* **38** 847-853

Fishkin J, Gratton E, 1993 Propagation of photon-density waves in strongly scattering media containing an absorbing semi-infinite plane bounded by a straight edge, *J. Opt. Soc. Am. A* **10** 127-140

Fishkin J B, 1994 Imaging and spectroscopy of tissue-like phantoms using photon density waves: Theory and Experiments Ph.D. Thesis, University of Illinios

Flock S T, Patterson M S, Wilson B C, Wyman D R 1989 Monte Carlo modeling of light propagation in highly scattering tissues-I: Model predictions and comparison with diffusion theory *IEEE trans. Biomed. Eng.* **36** 1162-1168

Flock S T, Jacques S J, Wilson B C, Star W M, van Gemert M J C 1992 Optical properties of Intralipid: A phantom medium for light propagation studies *Lasers Surg. Med.* **12**, 510-519

Franceschini M A, Fantini S, Gratton E 1993 LEDs in frequency-domain spectroscopy of tissues *Proc. SPIE* **2389**

Fulton S R, Ciesielski C E, Schubert W H, 1986 Multigrid methods for elliptic problems: A Review *Monthly Weather Review* **114**, 943-959

Gandjbankhche A H, Nossal R, Bonner R F 1993 Scaling relationships for theories of anisotropic random walks applied to tissue optics *Applied Optics* **32** 504-516

Gijsbers G H, Selten F M, van Gemert M J 1991 CW laser ablation velocities as a function of absorption in an experimental one-dimensional tissue model *Lasers Surg. Med.* **11** 287-296

Gratton E, Limkeman M 1983 A continuously variable frequency cross-correlation phase fluorometer with picosecond resolution *Biophys. J.* **44** 315-324

Gratton E, 1995 *SPIE conference* presentation in the optical tomography session.

Gros C, Quenville Y, Hummel Y, 1972 *J. Radiol. Electrol.* **53** 297

Hale G M, Querry M R 1973 Optical constants of water in the 200 nm to 200 µm wavelength region *Appl. Opt.* **12** 555-563

Haskell R C, Svaasand L O, Tsay T T, Feng T C, McAdams M, Tromberg B J 1995 *Journ. of Opt. Soc. Am.*

Haskell R C 1995 Phase velocity limit of high-frequency photon density waves *SPIE proc.*

2389

Henderson B W, Dougherty T J How does photodynamic therapy work? *Photochem. Photobiol.* **55** 145-157

Hielscher A H, Liu H, Chance B, Tittel T K, Jacques S L 1995 Frequency resolved reflectance spectroscopy on composite tissue structures *SPIE proc.* **2389**

Ishimaru A 1978 Diffusin of a pulse in densely distributed scatters *J. Opt. Soc. Am.* **68** 1045-1049

Ishimaru A 1989 Diffusion of light in turbid material *Appl. Opt.* **28** 2210-2215

Jaywant S, Wilson B, Patterson M, Lilge L, Flotte T, Woolsey J, McColloch C 1992 Temperature dependent changes in the optical absorption and scattering spectra of tissues: correlation with ultrastructure *Proc. SPIE* **1888**

Jobsis F F, 1977 Non-invasive, infrared monitoring of cerebral and myocardial oxygen sufficiency and circulatory parameters *Science* **198** 1264-1267

Kang 1993 *Proc. SPIE* **1888**

Kaltenbach J M, Kaschke M 1993 Frequency and time-domain modelling of light transport in random media *Medical Optical Tomography: Functional Imaging and Monitoring* ed. G Muller (SPIE Press, Bellingham)

Keene J P, Kessel D, Land E J, Redmond R W, Truscott T G 1986 Direct detection of singlet oxygen sensitized by haematoporphyrin and related compounds *Photochem. Photobiol.* **43** 117-120

Keijzer M, Star W M, Storchi P 1988 Optical diffusion in layered media *Appl. Opt.* **27** 1820-1824

Kessel D, Woodburn K 1993 Biodistribution of photosensitizing agents *Int. J. Biochem.* **25** 1377-1383

Kohl M, Essenpreis M, Bocker D, Cope M 1995 Influence of Glucose concentration upon light scattering in tissue simulating phantoms

Kyriacou G A, Koukourlis C S, Sahalos J N 1993 A Reconstruction algorithm of electrical impedance tomography with optimal configuration of the driven electrodes *IEEE Trans. Med. Imag.* **12** 430-438

Lackowicz J R, Szmacinski H, Nowaczyk K, Berndt K W, Johnson M, 1992 Fluorescence Lifetime Imaging *Anal. Biochem.* **202** 316-330

Lamarsh J R 1966 *Introduction to Nuclear Reactor Theory* (Massacheusetts: Addison-

Wesley)

Maier J S, Gratton E 1993 Frequency-domain methods in optical tomography: detection of localized absorbers and a backscattering reconstruction scheme *Proc. SPIE* **1888** 440-451

Maier J S, Walker S A, Fantini S, Franceschini M A, Gratton E 1995 Possible correlation between glucose concentration and reduced scattering coefficient of tissues in the near-infrared *Opt. Letters*

Madsen S J 1992 Experimental studies of time-resolved light propagation in turbid media *Ph.D. Thesis* McMaster University

Madsen S J, Wilson B C, Patterson M S, Park Y D, Jacques S L, Hefez Y 1992 Experimental tests of a simple diffusion model for the estimation of scattering and absorption coefficients of turbid media from time-resolved diffuse reflectance measurements *Appl. Opt.* **31** 3509-3517

Madsen S J, Patterson M S, Wilson B C 1992 The use of india ink as an optical absorber in tissue-simulating phantoms *Phys. Med. Biol.* **37** 985-993

Madsen S J, Wyss P, Svaasand L O, Haskell R C, Tadir Y, Tromberg B J 1994(a) Determination of the optical properties of the human uterus using frequency-domain photon migration and steady-state techniques *Phys. Med. Biol.* **39**, 1191-1202

Madsen S J, Anderson E R, Haskell R C, Tromberg B J 1994(b) Portable high-bandwidth frequency-domain photon migration instrument for tissue spectroscopy *Opt. Lett.* **19**, 1934-1936

Mengelkoch L J, Martin D, Lawler J 1994 A Review of the principles of pulse oximetry and accuracy of pulse oximeter estimates during exercise *Physical Therapy* **74** 40-49

Moulton J D 1990 Diffusion modelling of picosecond laser pulse propagation in turbid media *M.Eng. Thesis* McMaster University

Navarro G, Profio A E 1988 Contrast in diaphanography of the breast *Med. Phys.* **15** 181

O'Leary M A, Boas D A, Chance B, Yodh A G 1994 Images of inhomogeneous turbid media using photon density waves OSA: Advances in optical imaging and photon migration ed. R R Alfano **21** 106-115

Pass H I 1993 Photodynamic therapy in oncology: mechanisms and clinical use *J. Nat. Canc. Inst.* **85** 443-456

Patterson M S, Chance B, Wilson B C 1989 Time resolved reflectance and transmittance for the non-invasive measurement of tissue optical properties *Appl. Opt.* **28** 2331-2336

Patterson M S, Moulton J D, Wilson B C, Chance B 1990 Applications of time-resolved light scattering measurements to photodynamic therapy dosimetry *Proc. SPIE* **1203** 62-74

Patterson M S, Moulton J D, Wilson B C, Berndt K W, Lakowicz J R 1991(a) Frequency-domain reflectance for the determination of the scattering and absorption properties of tissue *Appl. Opt.* **30** 4474-4476

Patterson M S, Madsen S J, Moulton J D, Wilson B C 1991(b) Diffusion equation representation of photon migration in tissue *IEEE Microwave Theory and Techniques Symposium Digest* 905-908

Patterson M S, Wilson B C, Wyman D R 1991(c) The propagation of optical radiation in tissue I: Models of radiation transport and their application *Lasers Med. Sci.* **6**, 155-168

Patterson M S, Wilson B C, Wyman D R 1991(d) The propagation of optical radiation in tissue II: Optical properties of tissue and resulting fluence distributions *Lasers Med. Sci.* **6**, 379-390

Peters V G, Wyman D F, Patterson M S, Frank G L 1990 Optical properties of normal and diseased breast tissues in the visible and near infrared *Phys. Med. Biol.* **35** 1317-1334

Pettit G H, Ediger M N 1993 Pump/probe transmission measurements of corneal tissue during excimer laser ablation *Lasers in Surgery and Medicine* **13** 363-367

Pickering J W, Prahl S A, van Wieringen N, Beek J F, Sterenborg H, van Gemert M J C, 1993 Double-integrating-sphere system for measuring the optical properties of tissue *Appl. Opt.* **32** 399-410

Poets C F, Southall D P 1994 Noninvasive monitoring of infants and children: Practical considerations and areas of concern *Pediatrics* **93** 737-746

Press W H, Teukolsky S A, Vetterling W T, Fannery B P, 1992 *Numerical Recipes in Fortran* 2nd Ed. (Cambridge U. Press, New York) pp 816-862

Profio A E, Navarro G A 1989(a) Scientific basis of breast diaphanography *Med. Phys.* **16** 60-65

Profio A E 1989(b) Light transport in tissue *Appl. Opt.* **28** 2216-2222

Senz R, Muller G 1988 Laser in medicine *Proc. Duetsche Bunsen-Gesellschaft Phys. Chem.* **E6960**, 269-277

Sevick E M, Chance B, Leigh J, Nioka S, Maris M 1991 Quantitation of time and frequency-resolved optical spectra for the determination of tissue oxygenation *Anal. Biochem.* **195** 330-351

Sevick E M, Lakowicz J R, Szmacinski H, Nowaczyk K, Johnson M L 1992 Frequency

domain imaging of absorbers obscured by scattering *J. Photochem. Photobiol. B: Biol.* **16** 169-185

Sevick E M, Suddeath L F, Burch C L 1994 The origin of fluorescence and phosphorescence signals re-emitted from tissues *Proc. SPIE* **2137**

Sinaasappel M, Sterenborg H J 1993 Quantification of the hematoporphyrin derivative by fluorescence measurement using dual-wavelength excitation and dual-wavelength detection *Appl. Optics* **32** 541-548

Star W M, Marijnissen P A, van Gemert M J C 1988 Light dosimetry in optical phantoms and in tissues: I. Multiple flux and transport theory *Phys. Med. Biol.* **33** 437-454

Tromberg B J, Orenstien A, Kimel S, Barker S J, Hyatt J, Nelson J S, Berns M W 1990 In vivo tumour oxygen tension measurements for the evaluation of the efficiency of photodynamic therapy *Photochem Photobiol* **52** 375-385

Tromberg B J, Svaasand L O, Tsay T T, Haskell R C 1993 Properties of photon density waves in multiple-scattering media *Appl. Opt.* **32** 607-616

Wagnieres G, 1995 private comm.

Walsh J T, Cummings J P 1994 Effect of the dynamic optical properties of water on midinfrared laser ablation *Laser in Surgery and Medicine* **15** 295-305

Welch A J, Motamedi M, Rastegar S, LeCarpentier G L, Jansen D 1991 Laser thermal ablation: Review *Photochem. Photobiol* **53** 815-823

Wilson B C, Patterson M S 1990 The determination of light fluence distributions in photodynamic therapy in Photodynamic therapy of neoplastic disease Vol. 1, ed. Kessel D, CRC Press (Boston)

Wilson B, Farrell T, Patterson M S 1990 An optical fiber-based diffuse reflectance spectrometer for non-invasive investigation of photodynamic sensitizers *in vivo* in *Future Directions and Applications in Photodynamic Therapy* (SPIE Inst. series) 219-232

Wilson B C, Sevick E, Patterson M S, Chance B 1992 Time-dependent optical spectroscopy and imaging for biomedical applications *Proc. IEEE* **80** 918-930

Wilson B C, Patterson M S, Pogue B W 1993 Instrumentation for *in vivo* tissue spectroscopy and imaging *Proc. SPIE* **1892** 132-147

Wilson D F, Rumsey W L, Vanderkooi J M 1989 Oxygen distribution in isolated perfused liver observed by phosphorescence imaging *Adv. Expl. Med. Biol.* **248** 109-115

Wray S, Cope M, Delpy T D, Wyatt J S, Reynolds E 1988 Characterization of the near infrared spectra of cytochrome aa_3 and haemoglobin for the non-invasive monitoring of

cerebral oxygenation *Biochim Biophys Acta* 933 184-192

Wyatt J, Cope M, Delpy D, van der Zee P, Arridge S, Edwards A, Reynolds E 1990 Measurement of optical path length for cerebral near-infrared spectroscopy in newborn infants *Dev. Neurosci.* 12 140-144

van Staveren H J, Moes C J M, van Marle J, Prahl A, van Gemert M J C 1991 Light scattering in Intralipid-10% in the wavelength range of 400-1100 nm *Appl. Opt.* 30 4507-4514

Yoo K M, Liu F, Alfano R R 1990 When does the diffusion approximation fail to describe photon transport in random media *Phys. Rev. Lett.* 64 2647-2650

Hamilton Regional Cancer Centre
699 CONCESSION STREET, HAMILTON, ONTARIO L8V 5C2 • TEL: (416) 387-9495
Centre Régional de Cancérologie de Hamilton

February 24, 1995

Managing Editor
Institute of Physics Publishing
Techno House Redcliffe Way
Bristol BS1 6NX England
Dear Madam/Sir:

I am completing a Ph.D. thesis at McMaster University entitled "Frequency-domain optical spectroscopy and imaging of biological tissue." I would like your permission to reprint the following journal article in my thesis:

Pogue B W and Patterson M S 1994 Frequency domain optical absorption spectroscopy of finite tissue volumes using diffusion theory *Physics in Medicine and Biology* **39** 1157-1180

Please note that I am co-author of this work.

I am also requesting that you grant an irrevocable, non-exclusive licence to McMaster University and the National Library of Canada to reproduce this material as part of the thesis. Proper acknowledgement of your copyright of the reprinted material will be given in the thesis.

If these arrangements meet with your approval, please sign where indicated below and return this letter to me. Thank you.

Sincerely,

Brian Pogue
Medical Physics,
Hamilton Regional Cancer Centre
and McMaster University

PERMISSION GRANTED FOR THE USE REQUESTED ABOVE :

Institute of Physics Publishing

Authorized by : _____

Title : _____

Date : _____

Signature : _____

PERMISSION TO REPRODUCE AS REQUESTED IS GIVEN PROVIDED THAT:

(a) the consent of the author(s) is obtained
(b) the source of the material including author/editor, title, date and publisher is acknowledged.

IOP Publishing Limited
Techno House,
Redcliffe Way,
Bristol
~~BS1 6NX~~

4/3/95
Date

Rights & Permission

Hamilton Regional Cancer Centre
699 CONCESSION STREET, HAMILTON, ONTARIO L8V 5C2 • TEL: (416) 387-9495
Centre Régional de Cancérologie de Hamilton

February 24, 1995

The Society of Photo-Optical Instrumentation Engineers
PO Box 10
Bellingham, Washington 98227-0010
Dear Madam/Sir:

I am completing a Ph.D. thesis at McMaster University entitled "Frequency-domain optical spectroscopy and imaging of biological tissue." I would like your permission to reprint the following journal article in my thesis:

B. W. Pogue, M. S. Patterson and T. J. Farrell, "Forward and inverse calculations for 3-D frequency-domain diffuse optical tomography" Proceedings of SPIE 2389, (in press) 1995

Please note that I am co-author of this work.

I am also requesting that you grant an irrevocable, non-exclusive licence to McMaster University and the National Library of Canada to reproduce this material as part of the thesis. Proper acknowledgement of your copyright of the reprinted material will be given in the thesis.

If these arrangements meet with your approval, please sign where indicated below and return this letter to me. Thank you.

Sincerely,

Brian Pogue
Medical Physics,
Hamilton Regional Cancer Centre
and McMaster University

PERMISSION GRANTED FOR THE USE REQUESTED ABOVE :

Publisher's permission is hereby granted under the following conditions: (1) you obtain permission of the author(s); (2) the material to be used has appeared in our publication without credit or acknowledgment to another source; and (3) you credit the original SPIE publication. Include the authors' names, title of paper, volume title, SPIE volume number, and year of publication in your credit statement.

OFFICE OF RIGHTS AND PERMISSIONS
Society of Photo-Optical Instrumentation Engineers (SPIE)
P.O. Box 10 Bellingham, Washington 98227-0010 USA
Telephone 206/676-3290 (Pacific Time) Telex 46-7053
FAX 206/647-1445

Eric A. Pepper, SPIE Publications — 2/24/95 Month/day/year

The Optical Society of America is the copyright owner of the material you have cited herein. Permission is granted to reproduce said material as described, provided permission is also obtained from one of the original authors, if reasonably practicable, and provided a proper citation is included. A proper citation consists of author(s), journal, volume, page, and year.

Ghassan Rassam

Ghassan Rassam
Director of Publications
Optical Society of America

2/23/95
Date

Hamilton Regional Cancer Centre
699 CONCESSION STREET, HAMILTON, ONTARIO L8V 5C2 • TEL: (416) 387-9495
Centre Régional de Cancérologie de Hamilton

February 24, 1995

Publisher of Applied Optics
Optical Society of America
2010 Massachusetts Avenue, NW,
Washington DC 20036-1023
Dear Madam/Sir:

I am completing a Ph.D. thesis at McMaster University entitled "Frequency-domain optical spectroscopy and imaging of biological tissue." I would like your permission to reprint the following journal article in my thesis:

M. S. Patterson and B. W. Pogue, "Mathematical model for time-resolved and frequency-domain fluorescence spectroscopy in biological tissues," Applied Optics 33 (10) 1963-1974 (1994)

Please note that I am co-author of this work.

I am also requesting that you grant an irrevocable, non-exclusive licence to McMaster University and the National Library of Canada to reproduce this material as part of the thesis. Proper acknowledgement of your copyright of the reprinted material will be given in the thesis.

If these arrangements meet with your approval, please sign where indicated below and return this letter to me. Thank you.

Good Luck!

Sincerely, Brian Pogue

Brian Pogue
Medical Physics,
Hamilton Regional Cancer Centre
and McMaster University

PERMISSION GRANTED FOR THE USE REQUESTED ABOVE :

Optical Society of America

Authorized by : See reverse

Title : _____

Date : _____

Signature : _____

Hamilton Regional Cancer Centre
699 CONCESSION STREET, HAMILTON, ONTARIO L8V 5C2 • TEL: (416) 387-9495
Centre Régional de Cancérologie de Hamilton

June 9, 1995

Managing Editor
Institute of Physics Publishing
Techno House Redcliffe Way
Bristol BS1 6NX England
Dear Madam/Sir:

I am completing a Ph.D. thesis at McMaster University entitled "Frequency-domain optical spectroscopy and imaging of biological tissue." I would like your permission to reprint the following journal article in my thesis:

Pogue B W, M S Patterson, H Jiang, K D Paulsen 1995 Initial Assessment of a simple system for frequency domain diffuse optical tomography *Physics in Medicine and Biology* (to be published)

Please note that I am co-author of this work.

I am also requesting that you grant an irrevocable, non-exclusive licence to McMaster University and the National Library of Canada to reproduce this material as part of the thesis. Proper acknowledgement of your copyright of the reprinted material will be given in the thesis.

If these arrangements meet with your approval, please sign where indicated below and return this letter to me. Thank you.

Sincerely,

Brian Pogue
Medical Physics,
Hamilton Regional Cancer Centre
and McMaster University

PERMISSION GRANTED FOR THE USE REQUESTED ABOVE:

Institute of Physics Publishing

Authorized by : _____

Title : _____

Date : _____

Signature : _____

PERMISSION TO REPRODUCE AS REQUESTED IS GIVEN PROVIDED THAT:
(a) the consent of the author(s) is obtained
(b) the source of the material including author/editor, title, date and publisher is acknowledged.

IOP Publishing Limited
Techno House,
Redcliffe Way,
Bristol
BS1 6NX

9/6/95
Date

Rights & Permission